Functional characterization of Nodal receptors during early embryonic development in zebrafish

Dissertation

der Mathematisch-Naturwissenschaftlichen Fakultät

der Eberhard Karls Universität Tübingen

zur Erlangung des Grades eines

Doktors der Naturwissenschaften

(Dr. rer. nat.)

vorgelegt von

M. Sc. Hannes Preiß

aus Heilbronn

Tübingen

2020

Gedruckt mit Genehmigung der Mathematisch-Naturwissenschaftlichen Fakultät der Eberhard Karls Universität Tübingen

Tag der mündlichen Qualifikation:	09.12.2020
Stellvertretender Dekan:	Prof. Dr. József Fortágh
1. Berichterstatter:	Prof. Dr. Patrick Müller
2. Berichterstatter:	Prof. Dr. Erik Schäffer

Table of Contents

List of Figures

List of Supplementary Figures

List of Tables

Acknowledgements

First and foremost, I would like to thank Prof. Dr. Patrick Müller for providing me with the possibility of doing my PhD in his lab and for his support and scientific guidance throughout the years. I am grateful for his help with the design of experiments and their analysis, and for his input on the presentation of my findings. Further I am very grateful that he supported new experimental directions and ideas.

I am thankful to Prof. Dr. Birte Höcker and Prof. Dr. Erik Schäffer for their guidance, support and flexibility as part of my Thesis Advisory Committee. I thank the International Max Planck Research School “From Molecules to Organisms” for their funding and valuable trainings and workshops. Personal thanks to the PhD program coordinators Dr. Sarah Danes, Dr. Dagmar Sigurdottir and Sibylle Patheiger for their always open doors.

I thank all current and former members of the Müller lab for their company, constant readiness to help and for providing a productive working environment. Especially the lab management and technical support by Christine Henzler, Maria Langegger and Catrin Weiler helped me a lot. Additionally, I would like to thank Christine Henzler for her help with receptor cloning. I am especially indebted to her, Jens-Dominik Maile and Hannah Wild for their help with genotyping of a myriad of receptor mutants. Furthermore, I am very grateful to our animal care take Dieter Labbusch for always providing the best care for our fish and keeping an eye on our aquaria. Although she has left the lab already, I would like to thank Sarah Keim for her early cloning of *acvr1c* and her technical support in the lab, domo arigato. During my time in the lab, I had many wonderful scientific discussions, and I would like to thank Dr. Luciano Marcon, Dr. Jelena Marcon-Raspopovic, Dr. Daniel Čapek and Dr. Murat Ünalan for expanding my knowledge of signaling pathways and patterning in the embryo. Big thanks to my fellow PhD students Autumn Pomreinke, Gary H. Soh and Dr. Alexander Bläßle for helping me with SPIM imaging, staining protocols for pSMAD, receptor *in situs* and assisting me with pyFRAP and pyFDAP data analysis. Moreover, I would like to thank Dr. Maria Almuedo-Castillo for her initial work on sequencing and identifying *acvr1c,* cloning *acvr1b-a* and for her introduction in and help with the generation of receptor mutants. A big “Dankeschön” also to Dr. David Mörsdorf, who was always open for discussions and

helped me tremendously with my zebrafish and the interpretation of FRAP data. Last but not least, I cannot thank Dr. Katherine W. Rogers enough for her help with staining protocols, YSL injections and her thorough feedback on the thesis manuscript; I hope you get all your puppies through customs once you have your own lab.

I am very happy, that during my time at the FML I also had the possibility to exchange and collaborate with other scientists outside of the Müller lab. I am very appreciative to Prof. Dr. Michael Schindler, Ramona Businger and Rebecca Böffert for the opportunity to contribute to their research into human CMV inhibitors. Furthermore, I would like to thank Dr. Anastasia Eskova for including my requests in the development of the software “hetindel”, which helped me tremendously to identify Nodal receptor alleles. Without the help and support of our Light microscopy facility, many of my experiments would not have been possible. Thanks to Dr. Christian Feldhaus, Aurora Panzera and Dr. Vanessa de Oliveira Carlos for their great support.

While working at the FML, I also had the opportunity to organize and perform several science communication events over the years. I am very grateful to all the event organizers. I especially want to thank Prof. Dr. Patrick Müller, Dr. David Mörsdorf, Laura Reinke, Christine Henzler, Dr. Christian Feldhaus and Dr. Daniel Fleiter.

I would also like to thank my parents and brothers for always being supportive and for pretending to understand what I am actually doing in the lab. Furthermore, I would like to thank Reimara and Otto Rössler for providing me with a warm and friendly home in Tübingen.

Finally, I especially want to thank Michal Rössler for her support throughout the years. She gave me crucial feedback on the thesis manuscript and helped me keep focus. Thank you for taking me with you on all our travels and being my constant source of motivation.

Abbreviations

aa	Amino acids
Acvr1b-a	Activin receptor Type I ba
Acvr1b-b	Activin receptor Type I bb
Acvr1c/Alk7	Activin receptor Type I c
Acvr2a-a	Activin receptor Type II aa
Acvr2a-b	Activin receptor Type II ab
Acvr2b-a	Activin receptor Type II ba
Acvr2b-b	Activin receptor Type II bb
BLAST	Basic Local Alignment Search Tool
BMP	Bone morphogenic protein
Ca	Constitutively active
cDNA	Coding deoxyribonucleic acid
Cre/LoxP	Cyclization recombination/Locus of X-over P1
CRISPR/Cas9	Clustered regularly interspaced short palindromic repeats/CRISPR-associated 9
Cyc/cyc	Cyclops/cyclops
DAPI	4′,6-diamidino-2-phenylindole
DIG	Digoxigenin
Dn	Dominant negative
DNA	Deoxyribonucleic acid
dpf	Day(s) post fertilization
Dvr1	Decapentaplegic and Vg-related 1
EGF	Epidermal growth factor
EGF-CFC	Containing an EGF-like and CFC (Cripto, FRL-1, Cryptic) motif
EZRC	European zebrafish research center
FCS	Fluorescence correlation spectroscopy
FDAP	Fluorescence decay after photoconversion
FGF	Fibroblast growth factor
FRAP	Fluorescence recovery after photobleaching
Gdf3	Growth and differentiation factor 3

GFP	Green fluorescent protein
hpf	Hour(s) post fertilization
hpi	Hour(s) post injection
MeOH	Methanol
MO	Morpholino
mRNA	Messenger ribonucleic acid
MZsqt-/-;cyc-/-	Maternal-zygotic *sqt-/-;cyc-/-*
oep/Oep	*one-eyed pinhead*/One-eyed pinhead
PBS	Phosphate-buffered saline
PBST	Phosphate-buffered saline with 0.1 % Tween-20
PCR	Polymerase chain reaction
pSmad2/3	Phosphorylated Smad2/3
qRT-PCR	Quantitative reverse-transcriptase PCR
RFP	Red fluorescent protein
RNA	Ribonucleic acid
RT	Room temperature
SDS-PAGE	Sodium dodecyl sulfate polyacrylamide gel electrophoresis
sgRNA	Single guide RNA
SHH	Sonic hedgehog
Smad	Sma- and Mad-related protein
sqt/Sqt	*squint*/Squint
SW-FCCS	single wavelength fluorescence cross-correlation spectroscopy
TGF-β	Transforming growth factor-β
TPM	Transcripts per million
Tris	Tris(hydroxymethyl)aminomethane
TSA	Tyramide Signal Amplification
Xnr1	*Xenopus* nodal-related 1
YSL	Yolk syncytial layer

Summary

Understanding the robust control mechanisms that steer the development of a single cell into a complex organism remains one of the most central challenges in developmental biology. A crucial factor for the coordination of cell fates in the developing embryo is the intercellular communication mediated by different signaling pathways and their respective activity levels. The complex interplay of these pathways successively determines distinct cell fates. However, the mechanisms that control signal dispersal in the embryo are not fully understood.

In vertebrates, the Nodal signaling pathway is crucial for mediating germ layer patterning. The secreted transforming growth factor beta (TGF-β) ligand Nodal activates downstream transcriptional regulation by recruiting a receptor complex comprised of Type I and Type II Activin receptors and an EGF-CFC co-receptor. Previous studies in human, mouse, *Xenopus* and zebrafish have identified several of these receptors that mediate Nodal signaling. While in mouse several Nodal receptor mutants show severe developmental defects, in zebrafish only mutants of the co-receptor *one-eyed pinhead* (*oep*) recapitulate a Nodal loss-of-function phenotype. Here, I systematically identified and characterized three Type I and four Type II Activin receptor homologs in zebrafish. Temporal and spatial expression analysis demonstrated that, except for the Type I receptor *acvr1c*, all investigated putative Nodal receptors are maternally deposited and continuously expressed during germ layer patterning. To assess the role of the putative Nodal receptors during germ layer patterning in zebrafish, I generated receptor mutants and used them in a combinatorial knockdown assay with receptor targeting morpholinos. Using this approach, I could show that the two Type I receptors *acvr1b-a* and *acvr1b-b* redundantly mediate early Nodal signaling in zebrafish.

Measurements in zebrafish suggest that the secreted Nodal ligands have a lower diffusivity and a shorter range than their long-range antagonist Lefty. Both, Nodal and Lefty belong to the TGF-β superfamily and are similar in size and structure. Interaction of Nodal with extracellular binding partners, so called diffusion regulators, has been proposed to explain their different mobility. To elucidate whether the Nodal receptors can function as such diffusion regulators, I used quantitative approaches to analyze their effect on Nodal distribution and diffusion. My results show that range and shape of the Nodal distribution gradient can be influenced by receptor and co-receptor levels. These findings highlight the potential of Nodal-receptor interaction as a mechanism for restricting Nodal dispersal during germ layer patterning.

In summary, my thesis contributes to a more detailed understanding of the role of Nodal receptors during early germ layer patterning in zebrafish. My findings emphasize the importance of receptor redundancy in zebrafish and reinforce the ability of receptors to influence signal propagation in ways that go beyond signal transduction.

Zusammenfassung

Eine der zentralsten Herausforderungen der Entwicklungsbiologie ist die Frage, wie die Entwicklung einer einzigen Zelle zu einem komplexen Organismus robust gesteuert wird. Für die Koordination der Zelldifferenzierung im sich entwickelnden Embryo ist die interzelluläre Kommunikation, die durch verschiedene Signalwege und deren jeweilige Aktivitätsniveaus vermittelt wird, essenziell. Die Mechanismen, die die Signalverteilung im Embryo steuern, sind jedoch noch nicht vollständig verstanden.

Bei Wirbeltieren ist der Nodal Signalweg entscheidend für die Vermittlung der Keimblattentwicklung. Der sezernierte Transforming growth factor beta (TGF-β) Ligand Nodal rekrutiert zur Signaltransduktion einen Rezeptorkomplex aus Typ I und Typ II Aktivinrezeptoren und einem EGF-CFC Korezeptor. Obwohl Rezeptormutanten in der Maus schwere Entwicklungsstörungen aufweisen, zeigt im Zebrafisch nur die Mutante des Korezeptors one-eyed pinhead (oep) einen Nodal Knockout Phänotyp. In dieser Arbeit identifiziere und charakterisiere Ich systematisch drei Typ I und vier Typ II Aktivinrezeptor-Homologe in Zebrafisch. Die zeitliche und räumliche Expressions-analyse zeigt, dass alle untersuchten mutmaßlichen Nodal-Rezeptoren, mit Ausnahme des Typ I Rezeptors acvr1c, maternal vorhanden und während der Keimblatt-entwicklung weiter exprimiert sind. Zusätzlich habe ich mehrere Rezeptormutanten generiert und sie mit Morpholinos in einem kombinierten Rezeptorknockdown-Assay verwendet, um die Rolle der mutmaßlichen Nodal-Rezeptoren während der Keimblattentwicklung zu bewerten. Hierdurch konnte ich zeigen, dass im Zebrafisch die beiden Typ I Rezeptoren acvr1b-a und acvr1b-b redundant Nodal Signal vermitteln.

Messungen in Zebrafisch haben gezeigt, dass sekretiertes Nodal eine geringere Diffusionsfähigkeit und eine kürzere Reichweite aufweist als sein Antagonist Lefty. Nodal und Lefty gehören beide zur TGF-β Superfamilie und besitzen ein ähnliches Molekulargewicht. Man vermutet, dass ihre unterschiedliche Mobilität durch die Interaktion von Nodal mit extrazellulären Bindungspartnern zustande kommt. Um zu untersuchen, ob Nodal-Rezeptoren als Diffusionsregulatoren fungieren können, habe ich den Verteilungsgradienten und die Diffusion von Nodal unter manipulierten Rezeptor Dosis quantifiziert. Meine Ergebnisse zeigen, dass die Menge an vorhandenem Rezeptor und Co-Rezeptor die Reichweite und Form des Nodal-Gradienten beeinflussen können. Dies unterstreicht das Potenzial der Nodal-Rezeptor-Interaktion zur Steuerung der Nodal Ausbreitung im Embryo während der Keimblattdifferenzierung.

Zusammenfassend trägt meine Arbeit zu einem detaillierteren Verständnis der Rolle von Nodal-Rezeptoren während der frühen Keimblatt Differenzierung im Zebrafisch bei. Meine Ergebnisse betonen die Rolle von Rezeptorredundanz im Zebrafisch und machen deutlich, dass Rezeptoren die Ausbreitung von Entwicklungssignalen auf eine Weise beeinflussen können, die über die reine Signalübertragung hinausgeht.

1. Publications within this Thesis and Author Contributions

1.) Bläßle A., Soh G., Braun T., Mörsdorf D., **Preiß H.**, Jordan B. M., and Müller P. (2018). “Quantitative diffusion measurements using the open-source software PyFRAP.” *Nature Communications* **9**(1): 1582.

Alexander Bläßle, Ben Jordan and Patrick Müller conceived the study. Alexander Bläßle and Patrick Müller developed the software. Experiments were performed by Alexander Bläßle, Gary Soh, Theresa Braun, David Mörsdorf and I. Data analysis was done by Alexander Bläßle and Patrick Müller. I provided FRAP datasets for analysis and tested PyFRAP implementation before publication. And I provided feedback on the manuscript.

Author	**Author position**	**Scientific ideas %**	**Data generation %**	**Analysis & Interpretation %**	**Paper writing %**
Bläßle A G.	1	30		60	35
Soh G.	2	10	50	5	10
Braun T.	3	10	30	5	5
Mörsdorf D.	4		10	5	5
Preiß H.	5		10	5	5
Jordan B. M.	6	15		5	5
Müller P.	7	35		15	35
Title of Paper		Quantitative diffusion measurements using the open-source software PyFRAP.			
Status in publication process		published			

2.) **Preiß H.**, Mörsdorf D., Soh G., Almuedo-Castillo M., and Müller P. “Regulation of Nodal signaling propagation by receptor 1 interactions and positive feedback” unpublished manuscript.

Patrick Müller, David Mörsdorf and I initiated and outlined the project. Margin to margin transplantations were performed and analyzed by David Mörsdorf. *In situs* were performed by Gary Soh and I. Maria Almuedo-Castillo designed *acvr1b-a* sgRNAs and cloned the zebrafish *acvr1b-a* and *acvr1c* receptors. I performed all other experiments. Experimental results were analyzed by Patrick Müller, David Mörsdorf and me. The first manuscript draft was written by David Mörsdorf and I. Revisions were done with the help of Patrick Müller.

Authors	**Author position**	**Scientific ideas %**	**Data generation %**	**Analysis & Interpretation %**	**Paper writing %**
Preiß H.,	1	50	65	50	50
Mörsdorf D.,	2	20	20	20	20
Soh G.,	3		10		
Almuedo-Castillo M.,	4		5		
Müller P.	5	30		30	30
Title of Paper		Regulation of Nodal signaling propagation by receptor 1 interactions and positive feedback			
Status in publication process		submitted			

2. Introduction

2.1 Historical perspective on embryonic development

During development, cells differentiate into specialized cell types and organize into intricate tissues that form functional organs and make up whole organisms. Understanding how complex multicellular organisms develop from a single cell has been a major question in the field of developmental biology for centuries. Already in ancient Greece, philosophers like Hippocrates and Aristotle studied animal embryogenesis. Aristotle's observations of chicken embryo development gave rise to his theory of epigenesis, the formation of plants and animals from a seed, spore or egg following hierarchical steps of differentiation (Horder 2010). This theory persisted throughout antiquity and the Middle Ages. Observations that were made possible by the invention of microscopy in the 17th century led to the formulation of the preformationist theory of development. Antoni van Leeuwenhoek, one of the first microscopists to observe spermatozoa, described seeing vessels resembling nerves, arteries, and veins in the spermatozoa. This led to the idea that the embryo grows from miniature humans, so called homunculi, which are already present in the father's semen. Although preformism became the dominant theory for almost 200 years, detailed embryological studies in the 18th century by Caspar Friedrich Wolf and the investigation of successive leaf development in flowering plants by Johann Wolfgang von Goethe reintroduced epigenesis as a theory of development.

While preformism seems to offer a clear explanation for how different cells, organs and tissues are formed, this was less well described by the epigenesis theory. At the end of the 19th century, August Weismann proposed two theories that had a major impact on developmental biology. With his theory of germ plasm, he distinguished between somatic cells and germ cells. Only germ cells can pass on hereditary information to the next generation, while information acquired by the somatic cells will not be inherited (Weismann 1890, 1892). Weismann's other theory of mosaic development was one of the first theories to address early embryonic patterning. He suggested that nuclear determinants in the cell are unevenly split between the two daughter cells during division,

specifying different cell fates. Experiments by Wilhelm Roux supported this theory. Roux ablated one cell in a two-cell stage frog embryo, which resulted in only half an embryo being formed during later developmental stages. However, similar experiments by Hans Driesch in sea urchin larvae produced conflicting results: Driesch separated embryonic cells at the two-cell stage and found that, while often only one cell survived, embryos still developed into smaller, but perfectly normal larvae (Driesch 1891). Driesch's results later also were reproduced in frog embryos, showing that the development of sea urchin and frog embryos is guided by similar principles. The discrepancy between Roux's and Driesch's finding was probably due to an inhibitory effect that resulted from the fact that Roux ablated one of the first two cells embryo and left the destroyed cell in place (McClendon 1910). These experiments gave some of the first compelling examples that not only cell-intrinsic factors determine correct embryonic development, but that extrinsic regulation also plays a pivotal role during embryogenesis (Morgan 1924).

Another key discovery for developmental biology was published in 1924 by Hilde Mangold and Hans Spemann. Using transplantation experiments in amphibians, they showed that specific cells from donor embryos could induce the formation of a secondary axis in host embryos (Spemann & Mangold 1924). For these regions, which drive the development of the surrounding tissue, they coined the term "organizer". With the advent of molecular biology methods, we now know that these findings also emphasize that the differentiation of cells in a developing embryo is highly dependent on cell-cell communication through secreted signaling factors.

At the same time as the experiments by Mangold and Spemann, the theory of chromosomal inheritance was established and the term "genes" was designated to describe the fundamental physical and functional unit of heredity (Johannsen 1909). One of the first theories to accommodate the roles of genes and organizers was suggested by Conrad Waddington (Waddington 1940). He proposed that cells and tissues can react to an inducing signal, and that, during differentiation, cells undertake several path-determining decisions that are genetically controlled. Together, the inducing factors and genes determine the epigenetic landscape of cellular differentiation (Waddington 1957; Slack 2002). With the decryption of DNA in the 1950s and advances in molecular

biology, research started to focus on identifying and understanding the impact of individual genes on morphological changes during development.

Developmental biologists also began to consider the mechanisms underlying the patterning of the early embryo, and how this patterning is regulated during the major changes that happen during early development, such as cell divisions and movement. At the beginning of the 20th century, molecular gradients were proposed that span the developing tissue and coordinate development (Morgan & Moszkowski 1901; Boveri 1902). This idea was expanded by Albert Dalcq, who came up with the concept of a threshold mechanism by which cells interpret the graded distribution of a material and differentiate into different cell fates (Dalcq 1938; Thieffry 2001). The British mathematician, computer scientist and theoretical biologist Alan Turing coined the term "morphogen" for substances which function as such "form producing" materials in the developing tissue (Turing 1952).

2.2 Morphogen-mediated embryonic patterning

To explain, how a non-uniform distribution of morphogens during morphogenesis arises, Alan Turing proposed a mathematical model that describes how a periodic pattern can emerge within a field of cells. Turing's idea was that initially homogeneously distributed substances can generate a pattern or structure due to randomly introduced small disturbances in the system. He showed that for such a patterning to occur, two or more morphogens need to be able to diffuse through the system at different speeds and undergo chemical reactions with each other. He therefore provided one of the first mechanistic explanations for pattern formation (Turing 1952). Turing's reaction-diffusion model was further developed into an activator-inhibitor reaction-diffusion system by Hans Meinhardt and Alfred Gierer in 1972. In their proposed system of two morphogens, which has a higher biological relevance than Turing's original model, one morphogen functions as an activator and the other one as an inhibitor. For pattern formation to occur, it is crucial that the short-range activator can activate itself as well as the production of its long-range inhibitor, fulfilling the rule of local self-activation and lateral inhibition (Gierer & Meinhardt 1972).

In 1969 Lewis Wolpert also worked on differential cell differentiation. To visualize this concept, he suggested to think of a field of cells which assume different colors, thereby recreating a flag pattern, memorably naming it the “French Flag” problem (Figure 1) (Wolpert 1969). By first defining the question, he came up with mechanisms allowing for cells to know what color to adopt. In his most famous “gradient” model he introduced the concept of positional information. This proposed that cells in a tissue obtain a “positional value” relative to one or more points in the embryo. Depending on this value they then differentiate into specific cell fates. Cells obtain the positional information by a spatial gradient over the tissue and positional information is dependent on different concentration thresholds in the spatial gradient (Sharpe 2019).

To explain the formation of such a spatial gradient, Francis Crick later proposed the source-sink model, in which a morphogen is produced by a localized source and spreads from there into the surrounding tissue (Crick 1970). Importantly, diffusion needs to be coupled with molecular decay or clearance of the morphogen by a “sink”, so that a stable gradient forms and the morphogen does not spread uniformly over the whole embryo (Kicheva et al. 2007; Lander et al. 2007; Wartlick et al. 2009; Drocco et al. 2011; Rogers & Schier 2011).

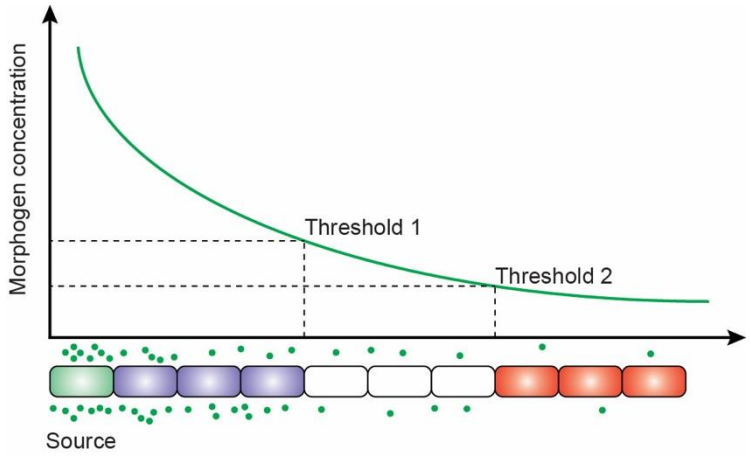

Figure 1: Positional information model illustrated by the “French Flag” problem. A morphogen is produced by a source (green), and from there forms a graded distribution over a field of cells. Cells interpret their positional information within the tissue by differentiating into different cell fates (blue, white and red) depending on the morphogen concentration exposure above or below different thresholds (Figure based on (Rogers & Schier 2011)).

One of the first morphogen gradients to be discovered is the Bicoid protein gradient in *Drosophila melanogaster* (Driever & Nüsslein-Volhard 1988a, 1988b). In this case, *bicoid* mRNA is maternally deposited in the anterior tip of the *D. melanogaster* oocyte and is then transcribed during development. It subsequently forms an anterior-posterior gradient in the embryo (Driever & Nüsslein-Volhard 1988b; St Johnston et al. 1989). Today, many more molecules have been suggested to act as morphogens, for example protein ligands like fibroblast growth factor (FGF), sonic hedgehog (SHH), Wnt and the TGF-β factors Activin, bone morphogenic protein (BMP) and Nodal, but also small molecules like retinoic acid (Wolpert 1989; Nellen et al. 1996; Zecca et al. 1996; Neumann & Cohen 1997; Strigini & Cohen 1997; Gurdon et al. 1999; Briscoe et al. 2001; Chen & Schier 2001; Müller et al. 2003; Shen 2007; Schier 2009; Umulis et al. 2009; Kam et al. 2012; Shimozono et al. 2013; van Boxtel et al. 2015).

2.3 Morphogen propagation in the embryo

During development, morphogens are generally thought to be produced by a local source from where they spread into the surrounding tissue by diffusion. The diffusion of morphogen's resembles a more or less random walk, based on Brownian motion, until the morphogens are cleared from the extracellular space, either by decay or cellular uptake (Crick 1970; Lander et al. 2007; Rogers & Schier 2011; Müller et al. 2013). The activity range of a morphogen strongly depends on its diffusivity and stability. The lower a morphogen's diffusivity and stability are in its environment, the shorter their activity range. And, vice versa, the activity range of a morphogen increases with increased diffusivity and stability (Rogers & Schier 2011).

To describe morphogen behavior, several studies have measured the diffusion constants of potential morphogens (Gregor et al. 2007; Kicheva et al. 2007; Müller et al. 2012; Wang et al. 2016; Pomreinke et al. 2017; Almuedo-Castillo et al. 2018; Mörsdorf 2019). To determine the diffusion coefficient of a morphogen, fluorescence correlation spectroscopy (FCS) measurements provide a suitable tool (Magde et al. 1972; Magde et al. 1974; Schwille et al. 1997; Haustein & Schwille 2007; Müller et al. 2013). FCS assesses the mobility of fluorescently tagged molecules in very small volumes, and can determine their

unhindered diffusivity, the so-called “free diffusivity”. However, in a complex biological environment such as that of a living embryo, propagation over longer distances often appears to be much slower than would be expected from the free diffusivity (Müller et al. 2013; Bläßle et al. 2018). Measurement of this “effective diffusivity” in the tissue context is possible through a technique called fluorescent recovery after photobleaching (FRAP) (Poo & Cone 1973; Liebman & Entine 1974; Müller et al. 2012; Bläßle et al. 2018). In this technique, the fluorescent signal in a region of interest is bleached using a strong laser. Then, the subsequent restoration of fluorescent signal in this area is measured, which stems from fluorescently tagged molecules from unbleached regions that diffuse into the area of interest. The resulting recovery curve can then be used to calculate the effective diffusivity. The difference between free and effective diffusivity can arise from several factors, such as tortuous movements of the molecule due to the tissue architecture (Müller et al. 2013; Bläßle et al. 2018). For example, recombinant GFP has a diffusion coefficient of approximately 90 $\mu m^2/s$ in water, but its diffusion coefficient decreases to approximately 40 $\mu m^2/s$ in the extracellular space of zebrafish embryos (Müller et al. 2013; Bläßle et al. 2018). The propagation of a morphogen through a tissue can also be hindered by transient interactions with immobilized extracellular binding partners, so-called diffusion regulators (Crank 1975; Miura et al. 2009; Müller et al. 2013). Several components of the extracellular space have been proposed to play a role in constraining and modulating the signaling range of morphogens in a tissue. Likely candidates are Heparan sulfate proteoglycans, membrane-bound receptors, and other components of the extracellular matrix (Lander et al. 2007; Shorten et al. 2007; Miura et al. 2009; Müller et al. 2013; Wang et al. 2016).

Protein stability can be accessed using the fluorescence decay after photoconversion (FDAP) technique (Zhang et al. 2007; Müller et al. 2012; Bläßle & Müller 2015; Rogers et al. 2015). In FDAP, the protein of interest is tagged with a photoconvertible fluorescent tag, such as Dendra2 (Gurskaya et al. 2006). Dendra2 is a green fluorescent protein, which upon exposure to a strong UV light pulse can be photoconverted from green to red fluorescence. Changes in the intensity of the red fluorescent signal over time then directly correspond with the decay of the photoconverted molecules, without any interference from the fluorescence that is emitted by newly produced tagged proteins of interest, which

have not been photoconverted. Measurements of the red fluorescent signal can then be used to calculate protein half-live and clearance rate (Bläßle & Müller 2015; Rogers et al. 2015).

2.4 Nodal signaling in zebrafish germ layer patterning

One of the first and most central steps during vertebrate embryonic development is the patterning of the germ layers into endoderm, mesoderm, and ectoderm. The formation of mesoderm and endoderm (collectively called mesendoderm) is mediated by the highly conserved TGF-β superfamily member Nodal (Shen 2007; Schier 2009; Hill 2017). Upon secretion, the Nodal pro-protein is proteolytically cleaved by convertases (Constam 2014; Tessadori et al. 2015). Its mature form needs to form heterodimers with the TGF-β ligand Vg-1/Dvr1/Gdf3 in the extracellular space for functional Nodal signaling (Bisgrove et al. 2017; Montague & Schier 2017; Pelliccia et al. 2017). Nodal signaling is mediated through a heteromeric complex of Type I and Type II Activin receptors (Wrana et al. 1992). In contrast to other members of the TGF-β superfamily, Nodal signaling additionally requires the presence of an EGF-CFC co-receptor to activate signaling (Gritsman et al. 1999; Yan et al. 1999; Reissmann et al. 2001; Shen 2007; Schier 2009). The assembled receptor complex phosphorylates the signal transducer Smad2/3 (pSmad2/3), which then associates with Smad4 and subsequently translocates into the nucleus. There, it interacts with other transcription factors to induce Nodal target gene expression (Figure 2 A) (Dick et al. 2000; Bennett et al. 2007; Ross & Hill 2008; Hata & Chen 2016).

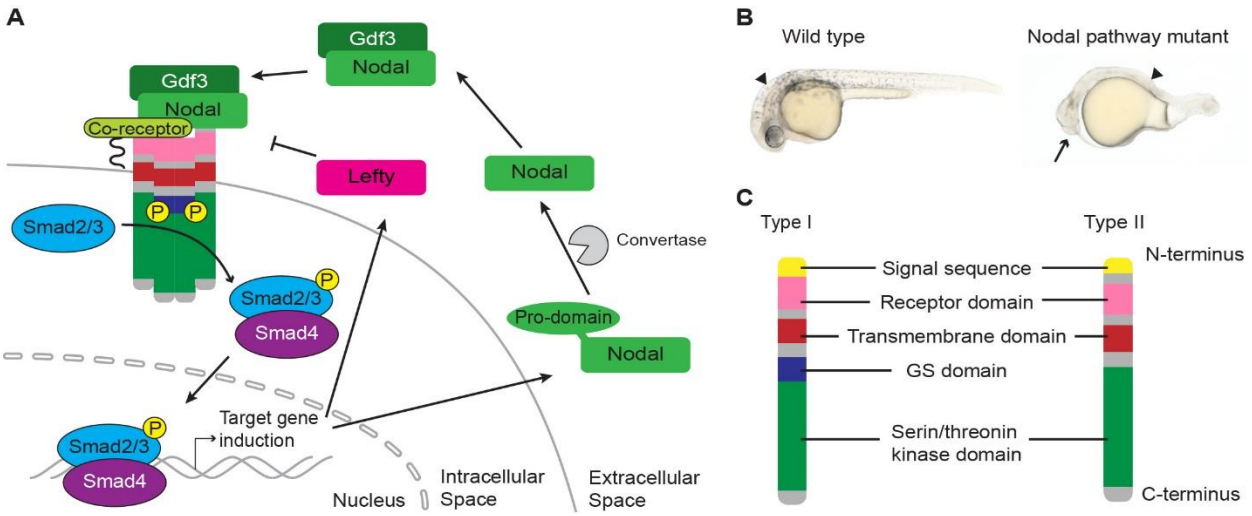

Figure 2: Nodal signaling pathway. (A) Upon the formation of a heterodimer with Gdf3, Nodal recruits the heteromeric Activin receptor complex consisting of Type I and Type II receptors. The activated receptor complex phosphorylates the signal transducer Smad2/3, which translocates into the nucleus after binding to Smad4, where it induces target gene expression. Amongst others, Nodal induces its own expression. During secretion, the pro-domain of the Nodal protein is cleaved off by convertases. The TGF- β superfamily member Lefty antagonizes Nodal signaling and its transcription is also induced by Nodal signaling. **(B)** Comparison of wild type and Nodal loss-of-function phenotype in one day old zebrafish embryos. Loss-of-function zebrafish mutants for Nodal signaling (here MZ*oep* mutants) exhibit disruption of mesoderm and endoderm development, missing notochord, somites, heart, pronephros, blood, and gut. Arrow marks fusion of the eye fields, arrowhead indicates the otic vesicle, which is located far more posteriorly in the mutant embryo compared to the wild type. **(C)** Overview of Type I and Type II Activin receptor structures. Both, Type I and Type II receptors possess a transmembrane domain, an extracellular receptor domain and an intracellular serine/threonine kinase. Type I receptors additionally possess a GS domain, which is the proposed phosphorylation site for phosphorylation and activation of the Type II receptor mediated by Type II receptors. The N-terminal signal sequence is cleaved of during protein maturation.

In zebrafish, the two Nodal ligands Squint and Cyclops mediate induction of mesendoderm starting approximately 5 hours post fertilization (hpf) at 40% epiboly of zebrafish development (Feldman et al. 1998; Rebagliati et al. 1998a; Dougan et al. 2003; Shen 2007; Rogers & Müller 2019). While *squint* transcripts are maternally deposited, *cyclops* expression is induced by signals from the yolk syncytial layer (YSL), an extraembryonic structure, after the mid-blastula transition. *Cyclops* expression peaks at the shield stage at approximately 6 hpf (Erter et al. 1998; Rebagliati et al. 1998b; Hong et al. 2011; White et al. 2017). In zebrafish, both *squint* and *cyclops* are first expressed in

the dorsal margin of the embryo and are thought to spread from there into the embryo during gastrulation, resulting in a Nodal short- to mid-range signaling gradient (Rebagliati et al. 1998a; Chen & Schier 2001; Müller et al. 2012).

Due to its localized expression, its non-uniform distribution, and its ability to induce different cell fates during germ layer patterning, Nodal was proposed as a classical secreted morphogen (Chen & Schier 2001; Schier 2009; Müller et al. 2012; Wang et al. 2016). Specifically, the Nodal gradient is thought to be translated into different mesendodermal cell fates depending on the signaling level and duration (Dubrulle et al. 2015). For example, experiments using ectopic Nodal expression from a localized source showed that target gene expression can be induced in tissue surrounding the source (Chen & Schier 2001; Jing et al. 2006; Tian et al. 2008; Müller et al. 2012).

However, recent experiments have shown that both, the distribution of the activated Nodal signal transducer pSmad2/3 and a Nodal-specific transcriptional reporter, show a strong overlap with the endogenous Nodal expression domain. Instead, mesoderm induction outside of this domain seems to be at least partly mediated by FGF signaling, (Rodaway et al. 1999; van Boxtel et al. 2015; van Boxtel et al. 2018). Therefore, it is currently under debate whether Nodal propagation via extracellular diffusion is indeed needed for the induction of a mesendodermal cell fate in target cells, which would be described by the concept of diffusion driven patterning (Figure 3 A) (Chen & Schier 2001; Müller et al. 2012). The alternative mechanism would be a relay mediated patterning, meaning that secreted Nodal only induces mesendodermal fate in directly adjacent cells, and that mid-range mesoderm induction instead is mediated by Nodal-induced FGF signaling (Figure 3 B) (van Boxtel et al. 2015; Hill 2017; van Boxtel et al. 2018).

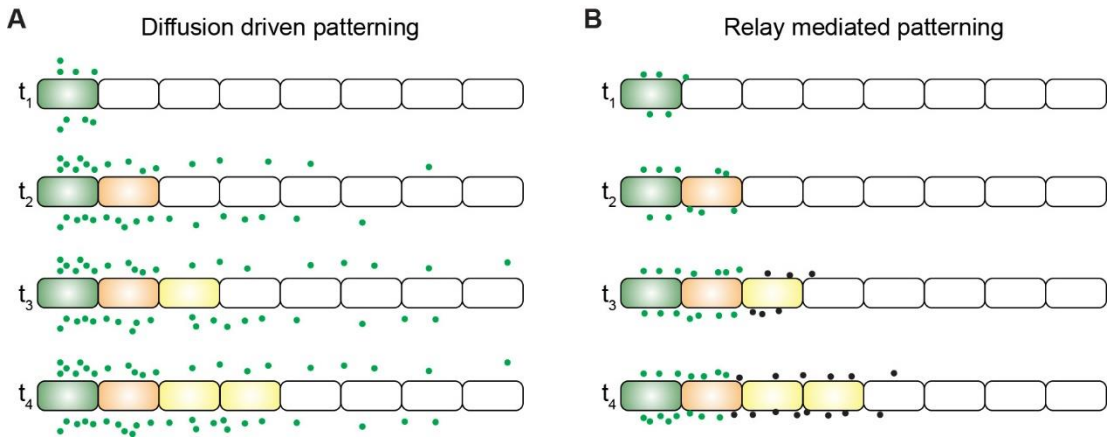

Figure 3 The two proposed modes of mesendodermal cell fate induction by Nodal signaling (A) In the diffusion driven patterning model, Nodal ligand (green dots) spreads from a source (green cell) into the embryo and forms a distribution gradient. This gradient then gets translated into a mesendodermal cell fate (orange and yellow cells). **(B)** In the relay mediated patterning model, Nodal ligand only induces an endodermal cell fate (orange cell) in directly adjacent cells, and activates long-range FGF signaling (black dots) that induces mesodermal cell fates (yellow cells) in cells further away.

While the mode of Nodal signal propagation is under debate, the secreted Nodal antagonist Lefty is well known to play a pivotal role in the regulation of the Nodal signaling domain (Rogers et al. 2017; Almuedo-Castillo et al. 2018). Lefty ligands act as long-range inhibitors of Nodal signaling and restrict Nodal signaling in the embryo (Chen & Schier 2002; Sakuma et al. 2002). Because Nodal signaling induces both, its own transcription and that of its antagonist Lefty, an auto-induction and feedback regulation of the Nodal signaling pathway exists (Meno et al. 1999; Bennett et al. 2007; Dubrulle et al. 2015). Therefore, the Nodal-Lefty signaling system has been proposed to form an activator-inhibitor reaction-diffusion system (Chen & Schier 2002; Nakamura et al. 2006; Marjoram & Wright 2011; Müller et al. 2012; Sekine et al. 2018). The longer range of Lefty was attributed to its almost 5- to 6-fold higher diffusivity compared to that of Nodal in zebrafish embryos (Sakuma et al. 2002; Müller et al. 2012). Since mature Nodal and Lefty proteins both belong to the TGF-β superfamily and have similar molecular masses, the cause of their differing diffusivity is unclear. It might however be due to binding interactions between Nodal and diffusion regulators in the extracellular space, hindering Nodal diffusion while Lefty protein can move more freely in the extracellular space (Müller et al. 2012; Müller et al. 2013; Rogers & Müller 2019).

2.5 The role of receptors in Nodal signaling

Nodal is thought to directly bind to Type II receptors and the EGF-CFC co-receptor, which in turn mediates the recruitment of the Type I receptor. Upon oligomerization of the receptor complex, the Type II receptors are thought to phosphorylate the Type I receptors in their GS-domain (Figure 2 C), which in turn leads to the recruitment of the receptor-regulated Smad proteins Smad2 and Smad3 and phosphorylation of their C-terminal SSXS motif by the Type I receptor (Wrana et al. 1992; Attisano et al. 1996; Attisano & Wrana 2002; Groppe et al. 2008). The activated pSmad2/3 proteins associate with the co-factor Smad4 and translocate into the nucleus where they, in combination with other transcription factors, activate target gene expression (Figure 2 A) (Macias-Silva et al. 1996; Dick et al. 2000; Yeo & Whitman 2001; Shi & Massague 2003; Bennett et al. 2007; Ross & Hill 2008; Hata & Chen 2016).

Even though the importance of Nodal signaling for early embryonic patterning was already shown shortly after its discovery (Conlon et al. 1991; Zhou et al. 1993; Conlon et al. 1994; Jones et al. 1995; Toyama et al. 1995; Lowe et al. 1996; Erter et al. 1998; Feldman et al. 1998), the identity of Nodal receptors was unclear initially. Even though the Type I receptor Acvr1b and the Type II receptor Acvr2b were known to induce mesoderm when overexpressed, or hinder mesoderm induction when truncated, their role in Nodal signal transduction remained elusive (de Vries et al. 1996; De Winter et al. 1996; Renucci et al. 1996; Armes & Smith 1997; Chang et al. 1997; Peyrieras et al. 1998). Only with the identification of the *one-eyed pinhead* (*oep*) mutant in zebrafish, which recapitulates the Nodal phenotype (Figure 2 B), the EGF-CFC co-receptor of Nodal was discovered (Hammerschmidt et al. 1996; Schier et al. 1997; Strähle et al. 1997; Zhang et al. 1998). Subsequently, using *in vitro* binding and target-induction assays in mouse and *Xenopus*, the Type I receptors Acvr1b and Acvr1c as well as the Type II receptors Acvr2a and Acvr2b were identified as transmitters of Nodal signaling (Table 1) (Gritsman et al. 1999; Reissmann et al. 2001; Munir et al. 2004). Additionally, mouse mutants for these putative Nodal receptors exhibit varying degrees of malformation similar to Nodal mutants, with some of the mutants arresting in their development as early as during gastrulation (Matzuk et al. 1995; Oh & Li 1997; Gu et al. 1998; Song et al. 1999). All

receptors that were identified in mouse and human have zebrafish orthologs, which are present during germ layer patterning (de Vries et al. 1996; Renucci et al. 1996; Garg et al. 1999; Nagaso et al. 1999; White et al. 2017). While mutations of *Acvr1b*, *Acvr2a* and *Acvr2b* in mouse phenocopy the severe phenotypes of Nodal loss-of-function mutants (Matzuk et al. 1995; Oh & Li 1997; Gu et al. 1998; Song et al. 1999), no zebrafish Nodal Type I and Type II receptor mutants exist that have a similar effect. And, although zebrafish is widely used to investigate Nodal signaling during development, it is unknown which of the receptor paralogs are the main mediators of endogenous Nodal signaling in zebrafish.

Table 1: Identification and characterization of putative Nodal Type I and Type II receptors in different model systems. Dn: Dominant-negative; Ca: Constitutively-active. Alternative receptor names are in parentheses.

Receptor homologs	**Zebrafish paralogs**	**Mutant phenotypes**	**Association with Nodal signaling**
Human ***ACVR1B*** (*ACTRIB, ACVRLK4, ALK4, SKR2*) (Attisano et al. 1993)	***acvr1b-a*** (acvr1b, alk4, taram-a) (Renucci et al. 1996) ***acvr1b-b***	Mouse (Gu et al. 1998) • Early embryonic lethality • defects in egg cylinder organization • gastrulation defects	(Chang et al. 1997) • Dn-xALK4 blocks mesoderm induction (Armes & Smith 1997) • Ca-xALK4 induces mesendoderm and secondary axis (Gu et al. 1998) • Receptor mutant phenocopy mouse Nodal mutant (Reissmann et al. 2001; Yeo & Whitman 2001; Bianco et al. 2002) • Direct binding to Nodal co-receptor Cripto • Mediates Nodal SMAD2 phosphorylation (Sakuma et al. 2002) • Dn-Alk4 (mouse) inhibits Nodal signaling in *Xenopus* (Aoki et al. 2002) • Zebrafish Squint + Cyclops interact with Taram-a • Dn-Taram-a inhibits Nodal signaling
Mouse ***Acvr1b*** (*ActR, ActR-IB, Alk4*) (Mathews & Vale 1991)			
Xenopus ***acvr1b*** (*xalk4, xALK4, alk4*) (Chang et al. 1997)			
Human ***ACVR1C*** (*ALK7*, *ACVRLK7*)	***acvr1c***	Mouse (Jornvall et al. 2004)	(Reissmann et al. 2001) • Ca-xAlk7 induces mesendoderm

(Bondestam et al. 2001; Roberts et al. 2003) Mouse / Rat ***Acvr1c*** (*Alk7*) (Ryden et al. 1996; Tsuchida et al. 1996) *Xenopus* ***acvr1c*** (*xAlk7*, *ALK7*) (Reissmann et al. 2001)		• Viable • Fertile • No left-right patterning defects	• Alk7 + ActRIIB form functional receptor complex for Xnr1 and mouse Nodal signaling • Alk7 binds directly to Xnr1 • Alk7 binds directly toNodal co-receptor Cripto (Munir et al. 2004) • hALK7 + Nodal induce apoptosis and inhibit proliferation of trophoblast cells
Human *ACVR2A* (*ACTRII*, *ACVR2*) (Matzuk & Bradley 1992a) Mouse ***Acvr2a*** (*Acvr2, ActRIIa*) (Mathews & Vale 1991; Matzuk & Bradley 1992b) *Xenopus* ***acvr2a*** (*acvr2, actrii, XAR7*) (Kondo et al. 1991)	***acvr2a-a*** (*acvr2a*) (Nagaso et al. 1999) **acvr2a-b**	Mouse (Matzuk et al. 1995) • Develop to term • Hypoplasia of mandibles • Delayed testes maturation • Female sterility	(Song et al. 1999) • *Acvr2a/Acvr2b* double mouse mutant phenocopy mouse Nodal mutant (Sakuma et al. 2002) • Dn-ActRIIA (mouse) inhibits Nodal signaling in *Xenopus* animal cap assay • Overexpression of *ActRIIA* can rescue lefty-induced Nodal inhibition
Human ***ACVR2B*** (*ACTRIIB, ActR-IIB*) (Hilden et al. 1994) Mouse ***Acvr2b*** (*ActRIIB*) (Attisano et al. 1992); *Xenopus* ***acvr2b*** (*actriib*, *XAR1*) (Mathews et al. 1992)	***acvr2b-a*** (*acvr2b*) (Garg et al. 1999; Nagaso et al. 1999) ***acvr2b-b***	Mouse (Oh & Li 1997) • Die postnatally • Defective axial patterning • Right isomerism • Cardiac defects	(Song et al. 1999) • *Acvr2a / Acvr2b* double mouse mutant phenocopy mouse Nodal mutant (Nagaso et al. 1999) • *acvr2b* overexpression in zebrafish causes dorsalization of embryos (Reissmann et al. 2001) • ActRIIB binds directly to Xnr1 • Alk7 + ActRIIB form functional receptor complex for Xnr1 and mouse Nodal signaling (Sakuma et al. 2002) • Dn-ActRIIB inhibits Nodal signaling in *Xenopus* • Overexpression of ActRIIB can rescue lefty-induced Nodal inhibition

Receptors have also been proposed to impact signal propagation and patterning in the embryo beyond their role as signal transducers, for example as diffusion regulators (Shorten et al. 2007; Miura et al. 2009; Marcon et al. 2016). Assessment of their potential role as diffusion regulators for Nodal propagation during zebrafish development is especially important since a decrease in mobility of over 90% has been shown between the free (Squint-GFP: D_{free} = ~39 µm^2/s; Cyclops-GFP: D_{free} = ~37 µm^2/s) and effective diffusivity (Squint-GFP: $D_{eff.}$ = ~3.2 µm^2/s; Cyclops-GFP: $D_{eff.}$ = ~0.7 µm^2/s) of the Nodals Squint and Cyclops in the embryo (Müller et al. 2012; Müller et al. 2013). Furthermore, fluorescently tagged Cyclops forms membrane-associated clusters in zebrafish embryos, while tagged Squint is more diffusely distributed in the extracellular space, suggesting a strong interaction of Cyclops with diffusion regulators (Müller et al. 2012; Rogers 2015). Co-localization studies in zebrafish have shown that Cyclops-GFP can cluster with the membrane-localized glycoprotein Knypek, making it a likely extracellular diffusion regulator for Cyclops (Rogers 2015). Furthermore, co-immunoprecipitation (co-IP) assays have identified a secreted Lectin as a potential extracellular interaction partner for Nodal ligands in zebrafish; however, overexpression of this lectin does not seem to impact Nodal diffusivity (Mörsdorf 2019).

Nodal receptors might also impact Nodal mobility in zebrafish. Specifically, the co-receptor *oep* has been shown to impact Nodal propagation. For example, overexpression of *oep* can decrease Squint-GFP diffusivity and causes it to form membrane-associated clusters similar to those of Cyclops-GFP in untreated embryos (Rogers 2015). Further experiments showed that the Nodal signaling range is strongly increased in MZ*oep* mutants (Lord et al. 2019). However, Nodal diffusivity is not increased in embryos missing Oep (Rogers 2015), indicating that other mechanisms such as changes in degradation dynamics could also account for the increased signaling range. Furthermore, FCS measurements have shown that Nodal strongly binds to the Type II receptor Acvr2b-a in zebrafish *in vivo* (Wang et al. 2016), suggesting that this interaction could also impact Nodal propagation in the embryo. However, it is unclear whether this strong interaction with the receptor influences Nodal diffusion and stability in the embryo.

3. Aims of this work

In my doctoral research I investigate the role of different putative Nodal receptors in germ layer patterning and examine their impact on the distribution of Nodal protein in the tissue.

In the first part of my thesis, I identify and characterize several putative Nodal receptors in zebrafish (chapter 4.1). Nodal signaling is crucial for the establishment of mesendodermal cell fate during germ layer patterning (Feldman et al. 1998; Shen 2007; Schier 2009). Previous experiments have identified various receptors that can mediate Nodal signaling in mouse, rat, *Xenopus* and zebrafish. However, due to an additional genome duplication event in teleosts (Meyer & Van de Peer 2005), several uncharacterized paralog receptors are present in zebrafish. To determine whether the identified receptors play a role in mediating Nodal signaling during early embryogenesis, I characterize their temporal and spatial expression, their subcellular localization, and the effect of increased receptor levels on embryo development. Furthermore, I use combinatorial receptor knockdown using morpholinos and CRISPR/Cas9-generated receptor mutants.

In the second part of my thesis, I include collaborative work on measuring the diffusivity of biological molecules (chapter 4.2). In a biological context, the spreading of molecules can be hindered by unspecific factors such as tissue tortuosity or by direct interaction with diffusion regulators (Müller et al. 2013). Diffusivity can be measured using fluorescence recovery after photobleaching (FRAP) assays. The publication “Quantitative diffusion measurements using the open-source software PyFRAP” introduces an accessible software that allows for the flexible analysis of FRAP diffusion measurements in different systems (Bläßle et al. 2018). Here, I provide several FRAP measurements of GFP-tagged Nodal which were used for testing software implementation and that highlight the impact that biological tissues can have on molecule mobility.

Thirdly, I address the idea that receptors act as Nodal diffusion regulators in the embryo (chapter 4.3). In zebrafish, Nodal signaling first occurs at the boundary between embryo and yolk, and from there it spreads into the embryo. Currently, the mechanism that regulates Nodal dispersal through the embryo is being debated. However, previous

measurements in zebrafish have shown a clear difference between the localized mobility and the diffusivity of Nodal on a tissue level. This could play an essential role in constraining Nodal signaling to the embryonic margin (Müller et al. 2013). To determine whether this difference is caused by receptor interactions with Nodal ligands in the extracellular space, I use a direct readout of Nodal gradient formation. Furthermore, I measure the impact of modulated receptor levels on Nodal localization, diffusivity, and stability.

In summary, my thesis will add to a better understanding of Nodal signaling during early embryogenesis in zebrafish. Furthermore, my research addresses the potential of Nodal receptors to modulate Nodal propagation into the embryo during germ layer patterning, elucidating the idea that the transient binding of Nodal ligand to its receptors is strong enough to hinder its diffusivity in the embryo.

4. Results and Discussion

4.1 Functional analysis of Nodal receptors in zebrafish

Here, I present the functional characterization of putative zebrafish Nodal receptors. The following results are in part from the manuscript in preparation “Regulation of Nodal signaling propagation by receptor 1 interactions and positive feedback”. This applies to the following paragraphs: “Nodal Type I and Type II receptors have several paralogs in zebrafish”; “Most Nodal receptor paralogs are present during mesendoderm formation”; “*acvr1b-a* expression is regulated by Nodal signaling”; “Single receptor mutants do not recapitulate Nodal loss-of-function phenotypes” and “The Type I receptors *acvr1b-a* and *acvr1b-b* function redundantly in early Nodal signaling”.

4.1.1 Nodal Type I and Type II receptors have several paralogs in zebrafish

To systematically identify and characterize zebrafish Nodal receptors, I used the amino acid sequences of the human and mouse Type I receptors ACVR1B and ACVR1C and Type II receptors ACVR2B and ACVR2B as queries for homology searches in the UniProt database. In addition to previously described zebrafish Type I (Renucci et al. 1996) and Type II (Garg et al. 1999; Nagaso et al. 1999) receptor orthologs, our analysis identified additional potential paralog sequences for the receptors Acvr1b-a, Acvr2a-a and Acvr2b-a – named Acvr1b-b, Acvr2a-b and Acvr2b-b (Funkenstein et al. 2012), respectively. Reconstruction of a putative phylogenetic tree shows a close clustering of the zebrafish receptors with their human and mouse paralogs, and the highest sequence similarity was found between the zebrafish Type I receptors Acvr1b-a and Acvr1b-b (Figure 4). Most putative receptor paralogs have the typical characteristics of Type I and Type II receptors, including a signal sequence, the TGF-β receptor domain, a transmembrane domain, a cytosolic kinase domain and, in case of the Type I receptors, a GS domain. Acvr2a-b is the only exception since it is missing a classical signal sequence (Supplementary **Figure 1**).

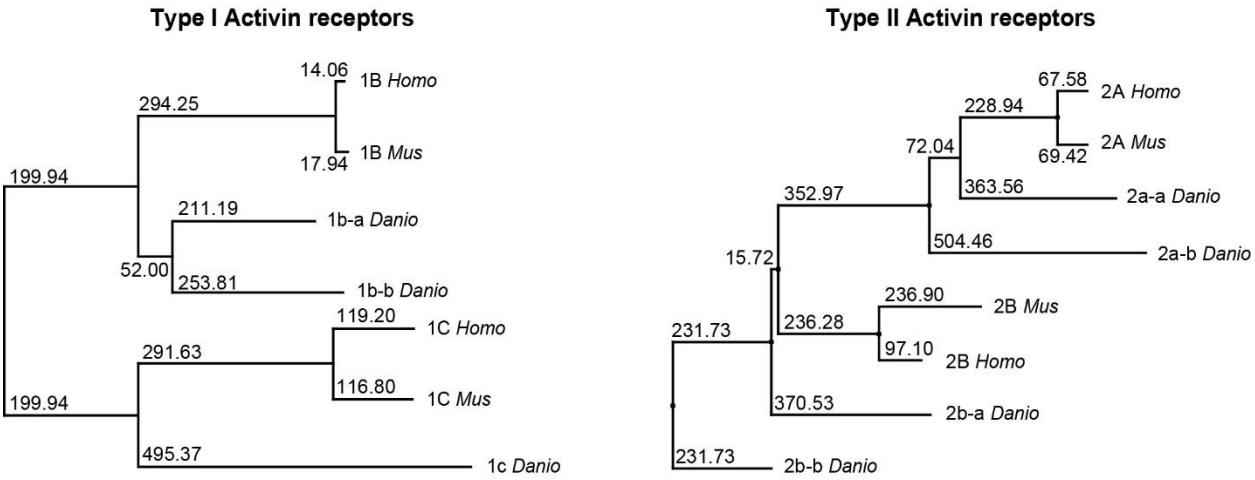

Figure 4: Multiple putative Nodal receptor paralogs are present in zebrafish. Phylogenetic neighbor-joining alignment tree of Type I and Type II receptor amino acid sequences of human (*Homo*), mouse (*Mus*) and zebrafish (*Danio*). Bootstrap values are listed at the nodes, indicating relative evolutionary distance.

4.1.2 Most Nodal receptor paralogs are present during mesendoderm formation

Germ layer patterning takes place during early blastula and gastrula stages. Analysis of the published developmental transcriptome (White et al. 2017) indicates that the transcripts of most receptor paralogs are present before the mid-blastula transition at approximately 3 hpf, suggesting that they might be maternally deposited (Figure 5 A). Expression of the identified receptors persists throughout larval development up until 4 days post-fertilization (dpf), similar to Nodal expression. The only receptor without detectable expression during early development is the Type I receptor *acvr1c*, which is first detected at 4 dpf (Figure 5 A).

To also determine the spatial expression patterns of the receptors, we used *in situ* hybridization in wild type zebrafish embryos. Consistent with the transcriptome analysis, we found that transcripts of all putative Nodal Type I and II receptors – with the exception of *acvr1c* – are present as early as the two-cell stage (approximately 40 minutes post fertilization) (Figure 5 B). During early gastrulation (shield stage; approximately 6 hpf), most receptors retain their ubiquitous expression throughout the embryo. However, expression of the Type II receptors *acvr2a-a* and *acvr2a-b* seems less prominent than

expression of *acvr2b-a* and *acvr2b-b*. While the expression of the Type I receptor *acvr1b-a* is constrained to the embryonic margin during shield stage (Renucci et al. 1996), *acvr1b-b* shows a strong ubiquitous expression similar to that of the Type II receptors *acvr2b-a* and *acvr2b-b* (Figure 5 B) (Garg et al. 1999; Nagaso et al.). The marginal expression of *acvr1b-a* during shield stage is very similar to the spatial expression dynamics of the co-receptor *oep* (Renucci et al. 1996; Vopalensky et al. 2018). Consistent with the apparent onset of *acvr1c* expression at 4 dpf in the transcriptome data, no staining was observed for *acvr1c* at shield stage, suggesting that this Type I receptor does not play a role for Nodal signaling during early development.

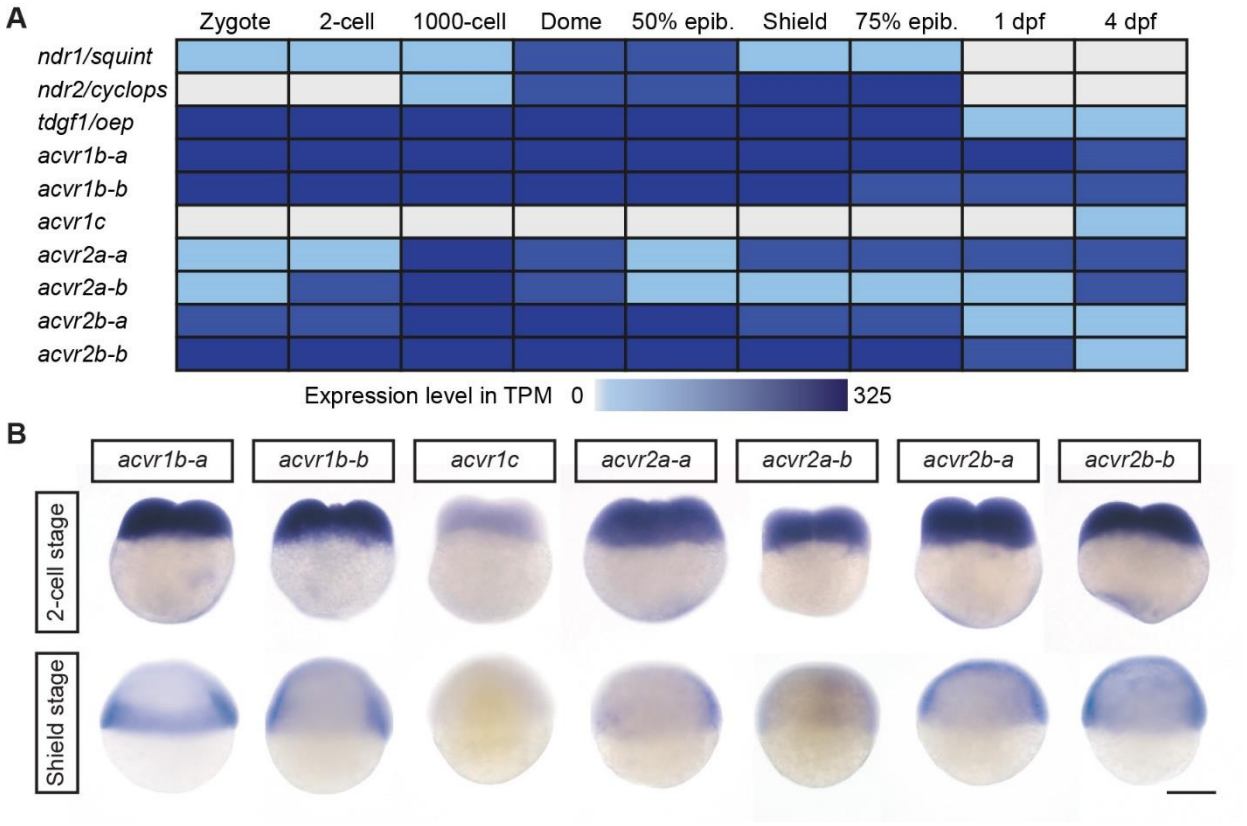

Figure 5: Spatio-temporal expression analysis of putative Nodal receptors during early zebrafish development. (A) Temporal expression analysis of transcriptomic data. Zebrafish *nodal* (*squint* and *cyclops*), its co-receptor *oep*, and putative Nodal receptors are expressed during different developmental time points. TPM: Transcripts per million. Data from (White et al. 2017). **(B)** Spatial expression analysis of Type I and Type II receptors during the two-cell and shield stage using *in situ* hybridization. Except for *acvr1c*, all receptors are maternally deposited. During shield stage, all receptors except for *acvr1c* and

acvr1b-a are expressed throughout the embryo. *acvr1b-a* is the only receptor of which the expression is restricted to the embryonic margin, where Nodal signaling is active.

4.1.3 Putative receptors exhibit unique expression profiles after 24 hours

At shield stage, expression of all Type II receptors and the Type I receptor *acvr1b-b* is ubiquitous in the embryo. However, the expression patterns diversify after one day (Figure 6). Analysis of *acvr1c* expression using *in situ* hybridization shows only light unspecific staining in the head region of the 24 hpf embryo (Figure 6 C), while the other putative Nodal receptors exhibit a strong staining in all head structures (Albertson et al. 2005). Interestingly, the Type I receptor *acvr1b-a* is strongly expressed at the tip of the developing tail (Figure 6 A), while *acvr1b-b* mRNA is mainly present in the head region (Figure 6 B), hinting at differing roles for the receptors during later development. Previous studies have shown that *acvr1b-a* plays a pivotal role in fin regeneration (Jaźwińska et al. 2007), it might also play a similar role during fin development. In contrast to the Type I receptors, the Type II receptors *acvr2a-a* and *acvr2b-a* are additionally expressed in the somites and the tail tip region of the embryo (Figure 6 D,E).

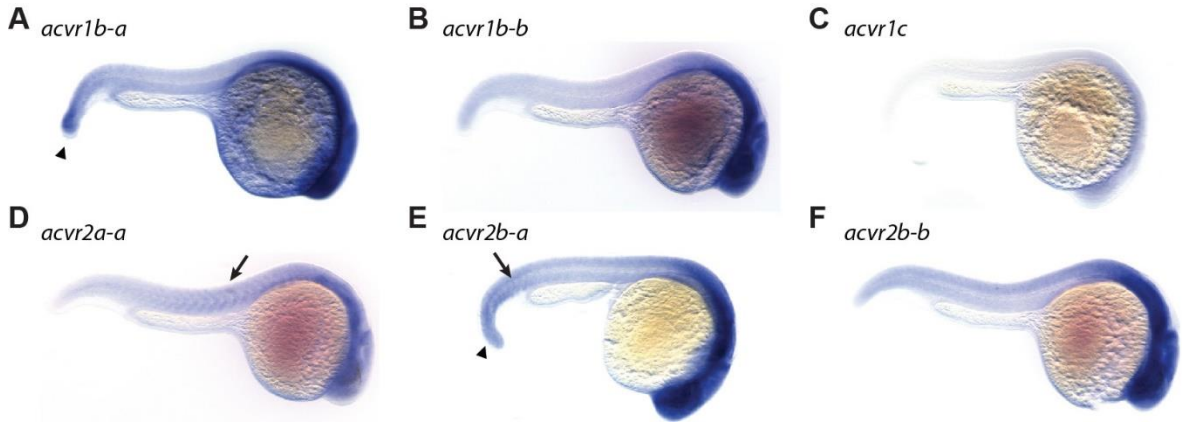

Figure 6: Spatial expression of putative Nodal receptor expression in 24 hpf embryos. Spatial expression of Type I and Type II receptors in 24 hpf embryos using *in situ* hybridization. Arrowheads mark expression in the tail bud. Arrows indicate somite staining.

4.1.4 acvr1b-a expression is regulated by Nodal signaling

Nodal signaling is well known to induce several of its own signaling pathway components, including *squint*, *cyclops*, *lefty1*, *lefty2* and *oep* (Meno et al. 1999; Feldman et al. 2002; Bennett et al. 2007; Dubrulle et al. 2015). To systematically assess potential receptor regulation by Nodal signaling, I used qRT-PCR to measure receptor expression levels in embryos with increased (injection of 30 pg *squint-GFP* mRNA or 30 pg *cyclops-GFP* mRNA) or decreased (injection of 30 pg *lefty2-Dendra2* mRNA or treatment with 10 µM of the Nodal inhibitor SB-505124 (DaCosta Byfield et al. 2004)) Nodal activity. *acvr1c* was excluded from this analysis due to its low expression level at shield stage.

In agreement with previous studies (Dubrulle et al. 2015), Nodal overexpression led to increased expression of the co-receptor *oep* and the Type I receptor *acvr1b-a* (Figure 7 A), whereas the presence of Nodal inhibitors causes decreased expression of *acvr1b-a* and *oep* compared to untreated embryos (Figure 7 A). While *acvr1b-a* mRNA is maternally ubiquitously deposited in the embryo, its expression domain is increasingly restricted to the embryonic margin during development (Figure 5 B). Upon Nodal overexpression, *acvr1b-a* expression is strongly increased throughout the embryo (Figure 7 B), whereas treatment with the Nodal inhibitor SB-505124 leads to a loss of the marginal restriction of *acvr1b-a* expression at shield stage. In contrast, none of the other putative Nodal receptors exhibit a significant change in expression upon Nodal overexpression or inhibition in comparison to untreated embryos (Figure 7).

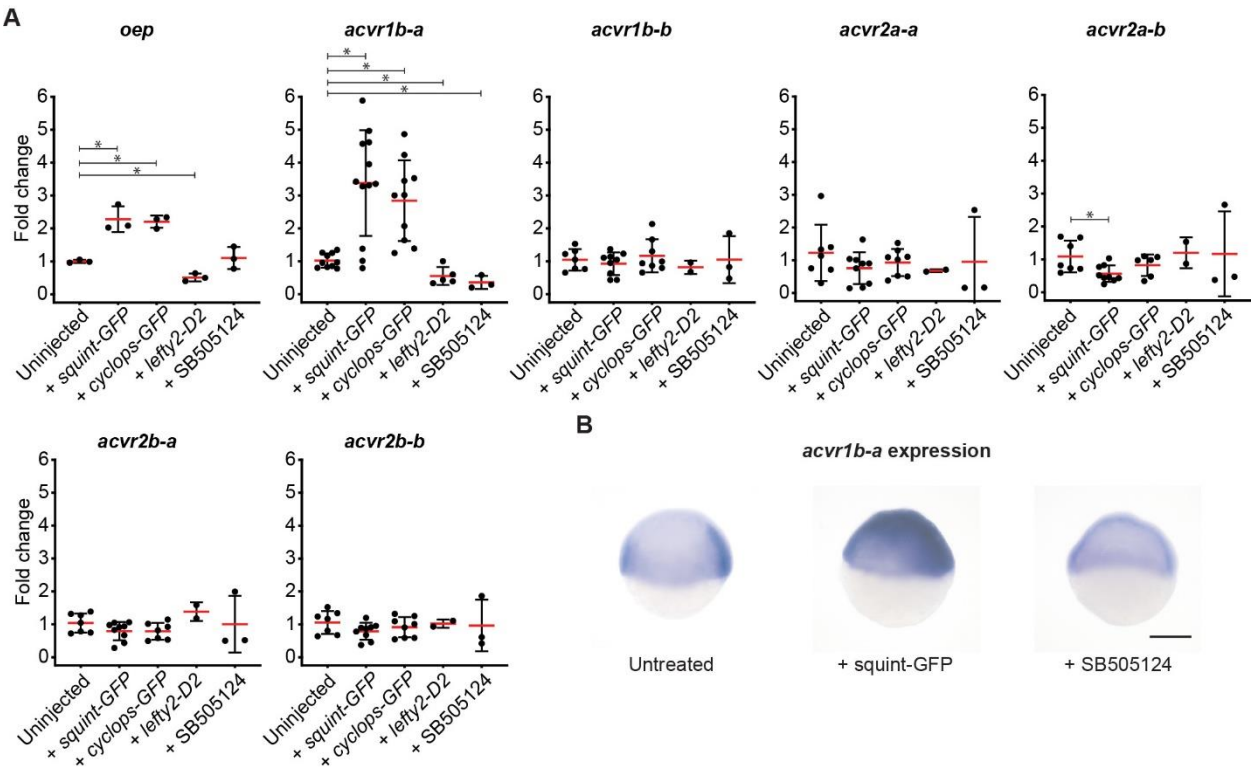

Figure 7: Nodal signaling controls the expression of *acvr1b-a* and *oep*. (A) Fold change of Nodal receptor expression calculated from qRT-PCR experiments comparing the injection of 30 pg *squint-GFP* mRNA, 30 pg *cyclops-GFP* mRNA, 30 pg *lefty2-Dendra2* mRNA and exposure to 10 µM SB505124 Nodal inhibitor to untreated embryos at 6 hpf. Each dot is the mean fold change of an individual embryo compared to an individual untreated embryo. Error bars represent the standard deviation. **(B)** *In situ* hybridization analysis of *acvr1b-a* in the presence of excessive Nodal signaling (30 pg *squint-GFP* mRNA injection) and the absence of Nodal signaling (treatment with 10 µM SB505124).

4.1.5 Most fluorescently tagged putative Nodal receptors localize to the cellular membrane

To determine whether the putative Nodal receptors localize to the cell membrane as expected, we generated receptor constructs with either mCherry or GFP fused to the C-terminal intracellular domain of the receptor. Wild type embryos were injected with 100 pg of fluorescently tagged receptor mRNA at the one-cell stage. Subcellular localization of the receptor constructs was assessed at approximately 6 hpf using confocal microscopy. Most receptors clearly localized to the cell membrane and some intracellular puncta, possibly receptor-containing vesicles originating either from the Golgi

complex or endocytosis (Figure 8). The only exceptions were *acvr1c*, which gave a weak intracellular signal, and *acvr2a-b,* which showed a lot of diffuse signal in the intracellular space with only little signal at the membrane, probably due to lacking a conserved N-terminal signaling sequence (Figure 8; Supplementary Figure 1). Interestingly, the Oep-RFP is not uniformly distributed across the cell membrane, but instead forms puncta on the membrane and within the intracellular space. However, despite the punctated distribution of Oep fluorescent signal, *oep-RFP* mRNA injection can rescue MZ*oep* mutants, indicating that the construct is functional.

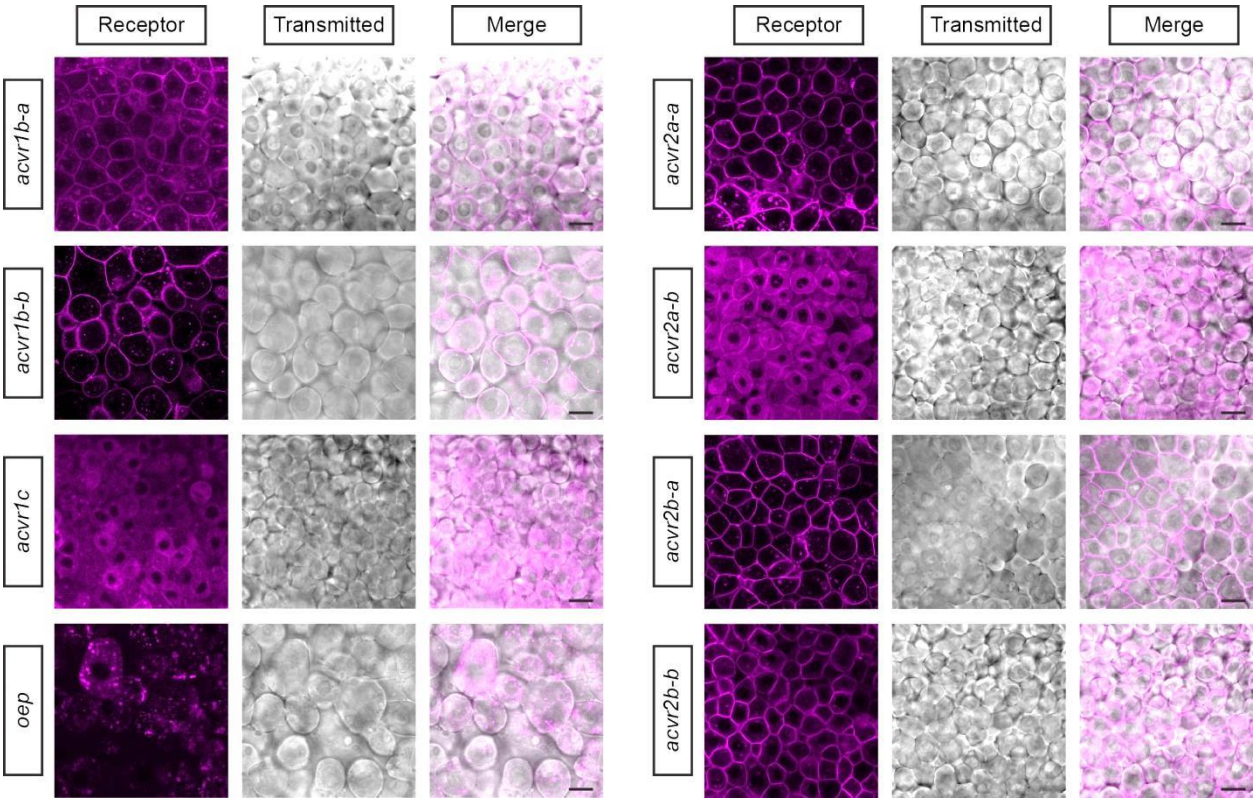

Figure 8: Receptor localization in the embryo. Embryos were injected with 100 pg C-terminally fluorescently tagged receptor construct mRNA. Distribution was assessed using confocal microscopy at 6 hpf. Intensities were adjusted for each receptor individually. Scale bars represent 20 µm.

4.1.6 Receptor overexpression can phenocopy Nodal gain-of-function

Overexpression of Nodal mRNA in zebrafish embryos leads to severe gastrulation defects which prevent epiboly and often result in embryo death by 24 hpf (Toyama et al. 1995). Mutants lacking Nodal inhibitors, like *lefty1*$^{-/-}$; *lefty2*$^{-/-}$ mutants, have increased Nodal

signaling and exhibit milder, but still lethal, phenotypes (Rogers et al. 2017). While single Lefty mutants still develop mostly normally, *lefty1*$^{+/-}$; *lefty2*$^{-/-}$ and *lefty1*$^{-/-}$; *lefty2*$^{+/-}$ mutants show what appears to be accumulation of blood progenitors in the tail region of the embryo (Rogers et al. 2017). Double homozygous Lefty mutants exhibit more severe patterning defects, like loss of the heart, eyes and tail structures. Some mutants also exhibit axis bifurcations (Rogers et al. 2017). Interestingly, injection of low amounts of constitutively active *smad2* mRNA into wild type embryos causes axis curvature, reduction of the eyes and an apparent accumulation of blood precursors in the tail area (Rogers et al. 2017). Previous characterizations of mouse, *Xenopus* and zebrafish Nodal receptor homologs of Acvr1b and Acvr2b have shown that overexpression of the receptors in *Xenopus* and zebrafish embryos can induce phenotypes that are similar to those caused by increased Nodal expression (Armes & Smith 1997; Feldman et al. 1998; Nagaso et al. 1999).

Injection of 100 pg of putative zebrafish Nodal receptor mRNA caused a broad range of receptor-specific phenotypes (Figure 9). Of the Type I receptors, overexpression of *acvr1b-a* caused the most severe phenotypes, recapitulating increased Nodal signaling in *lefty1*$^{-/-}$; *lefty2*$^{-/-}$ double mutants. *acvr1b-b* overexpression caused a range of milder phenotypes, with many embryos exhibiting malformations of the tail region and an apparent accumulation of blood next to the yolk extension. Interestingly, overexpression of the *acvr1c* receptor caused a delayed brain development in some 22 hpf embryos (Figure 9 B). Of the Type II receptors, *acvr2b-a* overexpression caused the most severe phenotypes with approximately 80% of the embryos dying due to problems during epiboly, and the surviving embryos lacking a defined body axis or mesendodermal tissue, similar to Nodal overexpression phenotypes. The paralog Type II receptor *acvr2b-b* also caused a wide range of Nodal overexpression phenotypes when overexpressed, such as head and tail defects, blood accumulation and the induction of ectopic tissue in the tail region, resembling the induction of a secondary axis (Rogers et al. 2017). In contrast, the overexpression of *acvr2a-a* mainly caused weak Nodal gain-of-function phenotypes, such as head defects and blood accumulations. The only receptor of which the overexpression did not phenocopy Nodal overexpression is *acr2a-b* (Figure 9 C).

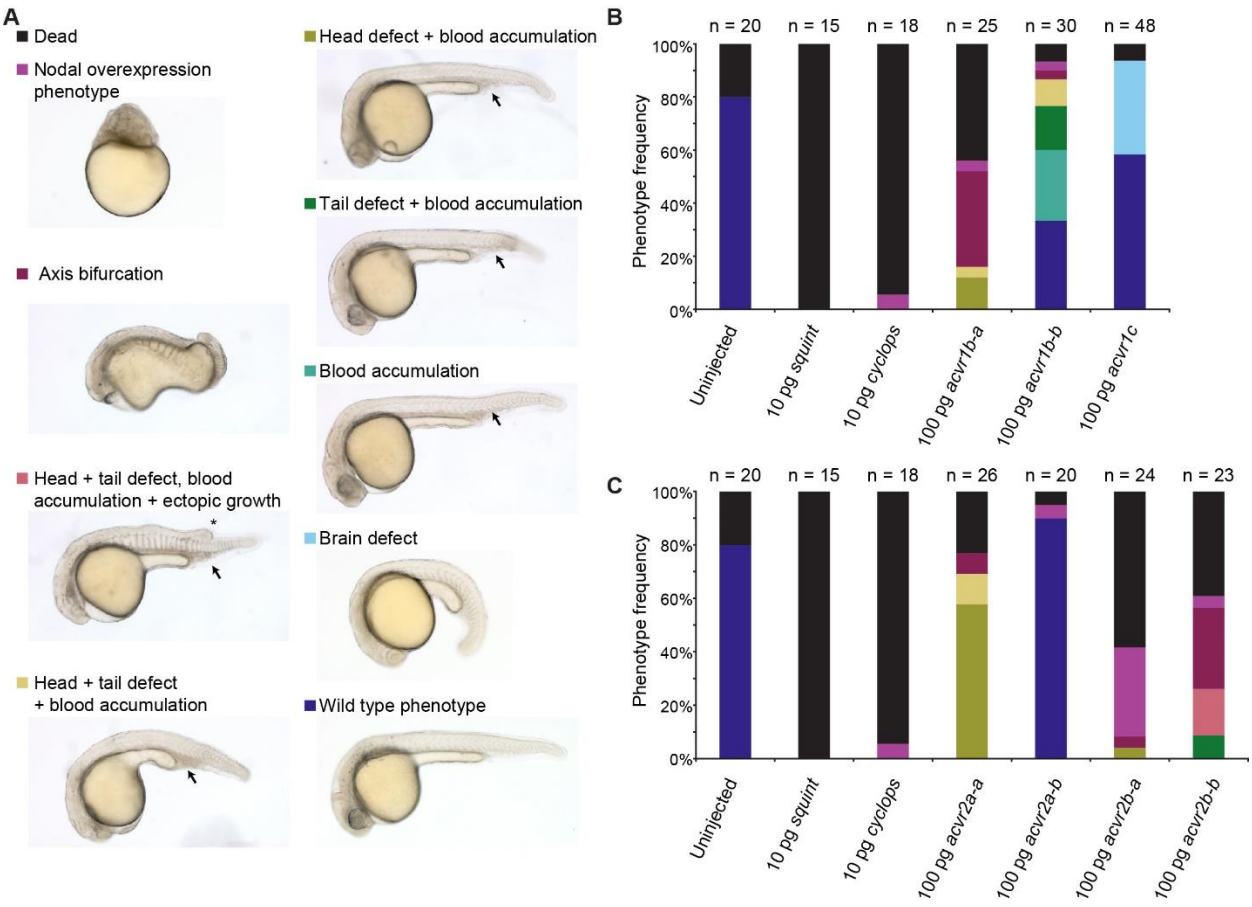

Figure 9: Overexpression of receptor mRNA can phenocopy Nodal overexpression. To compare phenotypes, wild type embryos were either injected with 100 pg of respective receptor mRNA or with 10 pg of *squint* or *cyclops* mRNA. Phenotypes were assessed after 24 hpf (or 22 hpf for *acvr1c* mRNA injection). **(A)** Phenotype classification categories. **(B)** Phenotypes of 24 hpf or 22 hpf (*acvr1c*) wild type embryos injected with 100 pg of Type I receptor mRNA. **(C)** Phenotypes of 24 hpf wild Type II embryos injected with 100 pg of Type II receptor mRNA.

4.1.7 Single receptor mutants do not recapitulate Nodal loss-of-function phenotypes

In order to better understand the role of the identified receptors in development, I used a complementary approach of morpholino-mediated knockdown and mutant generation (Rossi et al. 2015; El-Brolosy et al. 2019). I generated mutants for *acvr1b-a*, *acvr1c* and *acvr2b-a* using CRISPR/Cas9 targeting the 5' end of the respective coding sequences. The specific mutations were subsequently identified by sequencing of the genomic DNA.

The mutations caused frameshifts through insertion or deletion of base pairs, resulting in premature stop codons. Sequencing of the targeted first exons showed a 4 bp deletion for *acvr1b-a*, a 2 bp deletion for *acvr1c* and a 4 bp deletion for *acvr2b-a* (Figure 10 B,C,F). Furthermore, I obtained *acvr2a-a* and *acvr2a-b* mutants from the European Zebrafish Resource Center (EZRC). These single nucleotide mutations cause alternative splicing and a premature stop codon for *acvr2a-a* and *acvr2a-b,* respectively (Figure 10 D,E). Most mutations caused the signal sequence to be incomplete, making it highly unlikely that the mutant protein is transported to the cellular membrane to function there as a Nodal receptor.

Unlike expected, none of the single maternal-zygotic homozygous receptor mutants displayed obvious patterning defects at 1 dpf (Figure 10 B-G). This contrasts mouse receptor mutants, which exhibit severe phenotypes during early embryonic development (Oh & Li 1997; Gu et al. 1998; Song et al. 1999). Since the analysis of mutants can be impeded by genetic compensation that might mask potential patterning defects (Rossi et al. 2015; El-Brolosy et al. 2019), I also assessed the effect of knocking down gene activity using antisense morpholino oligonucleotides targeting the ATG start codons or splice sites of the putative receptor mRNAs. Morphants had non-specific head or tail defects similar to a standard control morpholino (Supplementary Figure 2), but no Nodal-specific patterning defects typical for loss-of-function mutants of other signaling pathway components were observed (Feldman et al. 1998; Gritsman et al. 1999; Dubrulle et al. 2015).

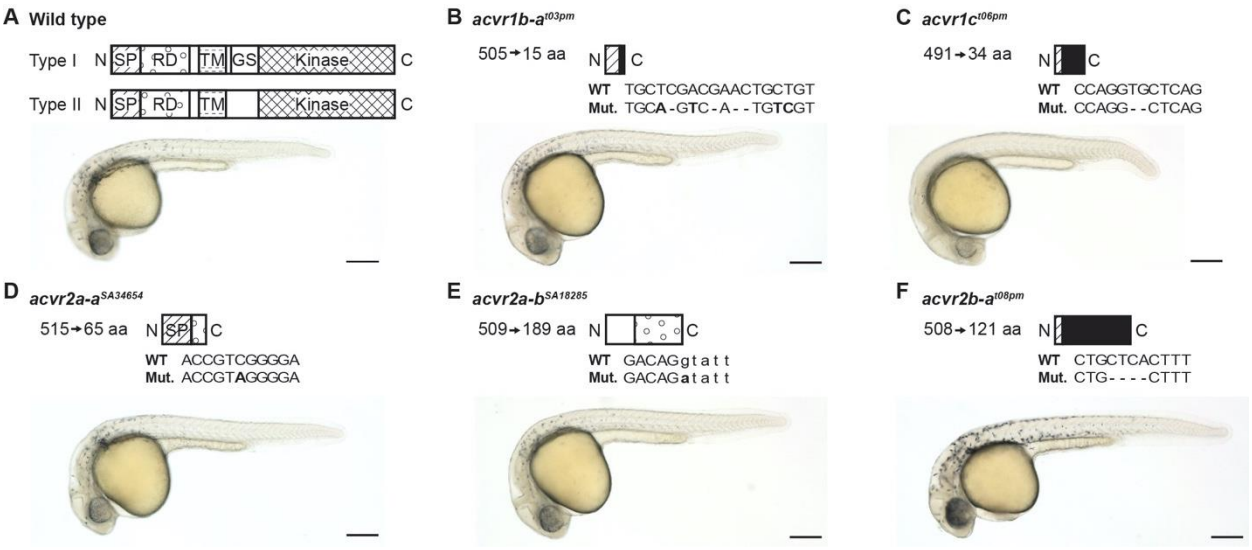

Figure 10: Single putative Nodal receptor mutants have no obvious patterning defects and are viable. (A-F) Schematic diagram of typical full-length Type I and Type II receptor proteins and predicted receptor protein truncations resulting from the *acvr1b-a*^{t03pm}, *acvr1c*^{t06pm}, *acvr2a-a*^{SA34654}, *acvr2a-b*^{SA18285}, and *acvr2b-a*^{t08pm} alleles. Mutated nucleic acid sequence and resulting protein length in amino acids (aa) are indicated. Lateral views of 1 dpf embryos are shown for wild type and single receptor maternal-zygotic homozygous mutants. Scale bars represent 250 µm. Uppercase letters indicate exon sequences; lowercase letters indicate intron sequence; aa: amino acids; SP: signal peptide; RD: receptor domain; TM: transmembrane domain; GS: GS domain; Kinase: kinase domain; Black: Nonsense sequence between frameshift mutation and new stop site.

4.1.7 The Type I receptors acvr1b-a and acvr1b-b function redundantly in early Nodal signaling

Teleosts like zebrafish have undergone an additional genome duplication following the two vertebrate-specific rounds of whole-genome duplications (Meyer & Van de Peer 2005). Partial redundancy of paralogs can underlie the lack of abnormal phenotypes in single mutants (Feldman et al. 1998; Rogers et al. 2017; Leerberg et al. 2019). I therefore tested receptor redundancy during early Nodal signaling using combinatorial receptor loss-of-function approaches.

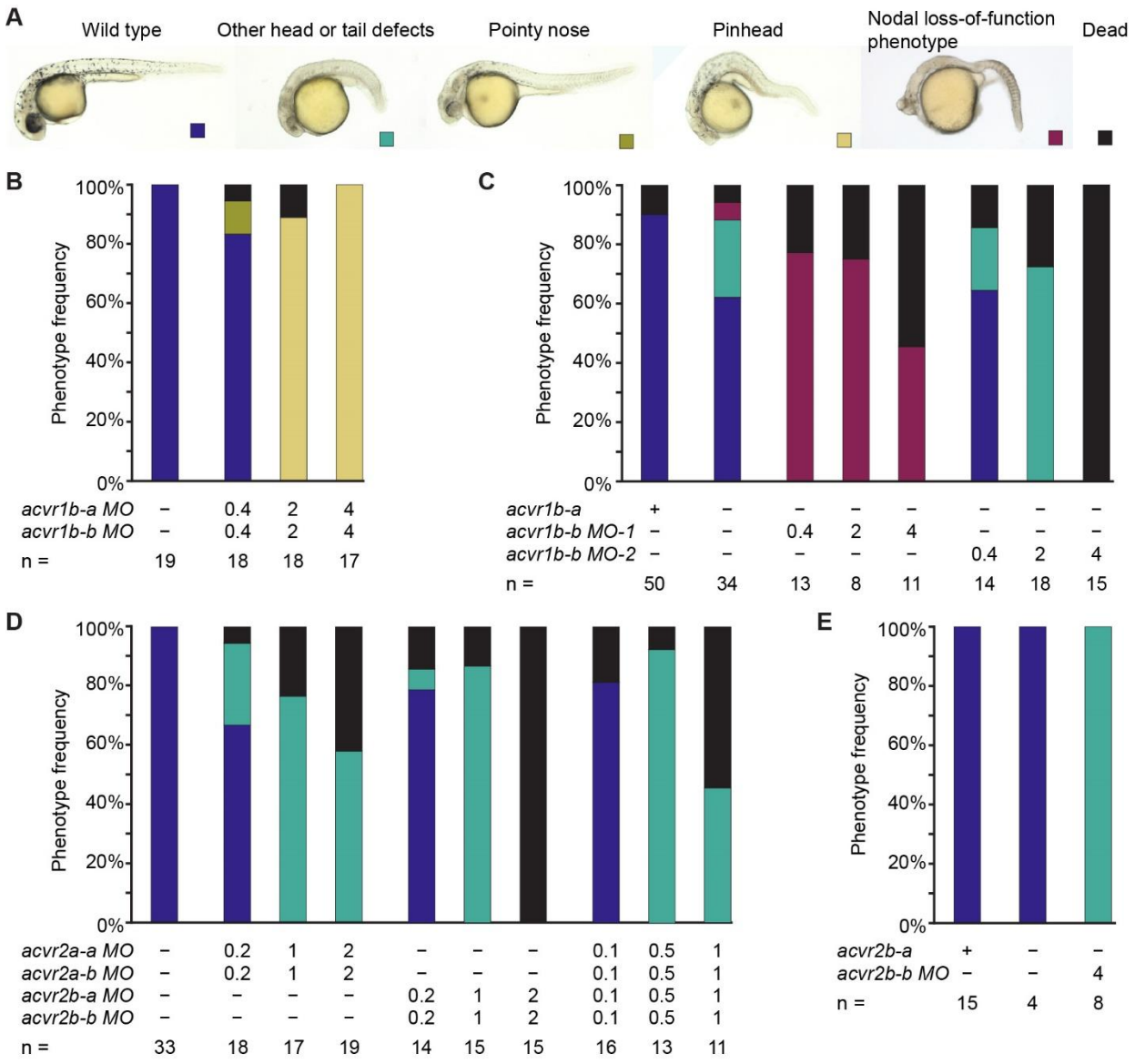

Figure 11: Phenotypes of 1 dpf zebrafish embryos with combinatorial knockdown of different putative Nodal receptors. If not indicated otherwise, embryos were injected with a mix of transcription start site and splice site targeting morpholinos (see Table 5 for morpholino sequences used). Final morpholino concentrations are indicated in the figure. **(A)** Phenotype classification categories. **(B)** Observed phenotypes after injection of different combinations of morpholinos targeted against *acvr1b-a* and *acvr1b-b* into wild type embryos. **(C)** Injection of *acvr1b-b* transcriptional start site (MO-1) and *acvr1b-b* splice site (MO-2) targeting morpholinos into maternal zygotic *acvr1b-a*$^{t03pm/t03pm}$ embryos. **(D)** Injection of Type II receptors *acvr2a-a*, *acvr2a-b*, *acvr2b-a* and *acvr2b-b* morpholino combinations into wild type embryos. **(E)** Injection of *acvr2b-b* morpholino into maternal zygotic *acvr2b-a*$^{t08pm/t08pm}$ mutant embryos.

Morpholino-mediated double knockdown of *acvr1b-a* and *acvr1b-b* leads to a clear loss of head mesoderm resulting in the distinctive fused-eye “pinhead” phenotype associated

with loss-of-Nodal signaling at 1 dpf (Figure 11 A,B). However, somites still formed in the trunk region (Figure 11 A,B) similar to the phenotype of zygotic rather than maternal-zygotic *oep* (MZ*oep*) mutants (Gritsman et al. 1999), suggesting an incomplete loss of Nodal signaling. I therefore injected *acvr1b-b*-targeting morpholinos into maternal-zygotic *acvr1b-a*$^{t03pm/t03pm}$ mutant embryos. Injection of 0.4 ng *acvr1b-b* targeting morpholinos (*acvr1b-b* MO-1) into *acvr1b-a* mutants at the one-cell stage lead to a recapitulation of the full Nodal loss-of-function phenotype at 1 dpf (Figure 3A,C; Figure 4A). Interestingly, knockdown of *acvr1b-b* using morpholinos in *acvr1b-a* mutants only resulted in Nodal loss-of-function phenotypes when using ATG targeting morpholinos, but not splice site targeting morpholinos (Figure 3A,C). This indicates that maternally deposited *acvr1b-b* receptor-encoding mRNA is sufficient for proper early germ layer differentiation.

The specificity of the morphant/mutant double-knockdown approach was assessed by rescuing the loss-of-function phenotype with *acvr1b-a* and *acvr1b-b* mRNA. At 1 dpf up to 60% of the embryos displayed normal or partially rescued phenotypes depending on the mRNA concentration (Figure 12 A). To test whether restored Nodal signaling rescues the loss-of-function phenotype, I quantified the range of phosphorylated Smad2/3 (pSmad2/3) as a direct readout of Nodal signaling during early gastrulation at 5 hpf. *acvr1b-a*$^{t03pm/t03pm}$ mutants and embryos injected with *acvr1b-b*-targeting morpholinos show a Nodal signaling range that is very similar to untreated wild type embryos, whereas double-knockdown of both Type I receptors almost completely abolishes pSmad2/3 signal throughout the embryo (Figure 12 B). The range of pSmad2/3-positive nuclei could be restored to a near-normal extent by injection of 50 pg *acvr1b-a* or 25 pg *acvr1b-b* mRNA.

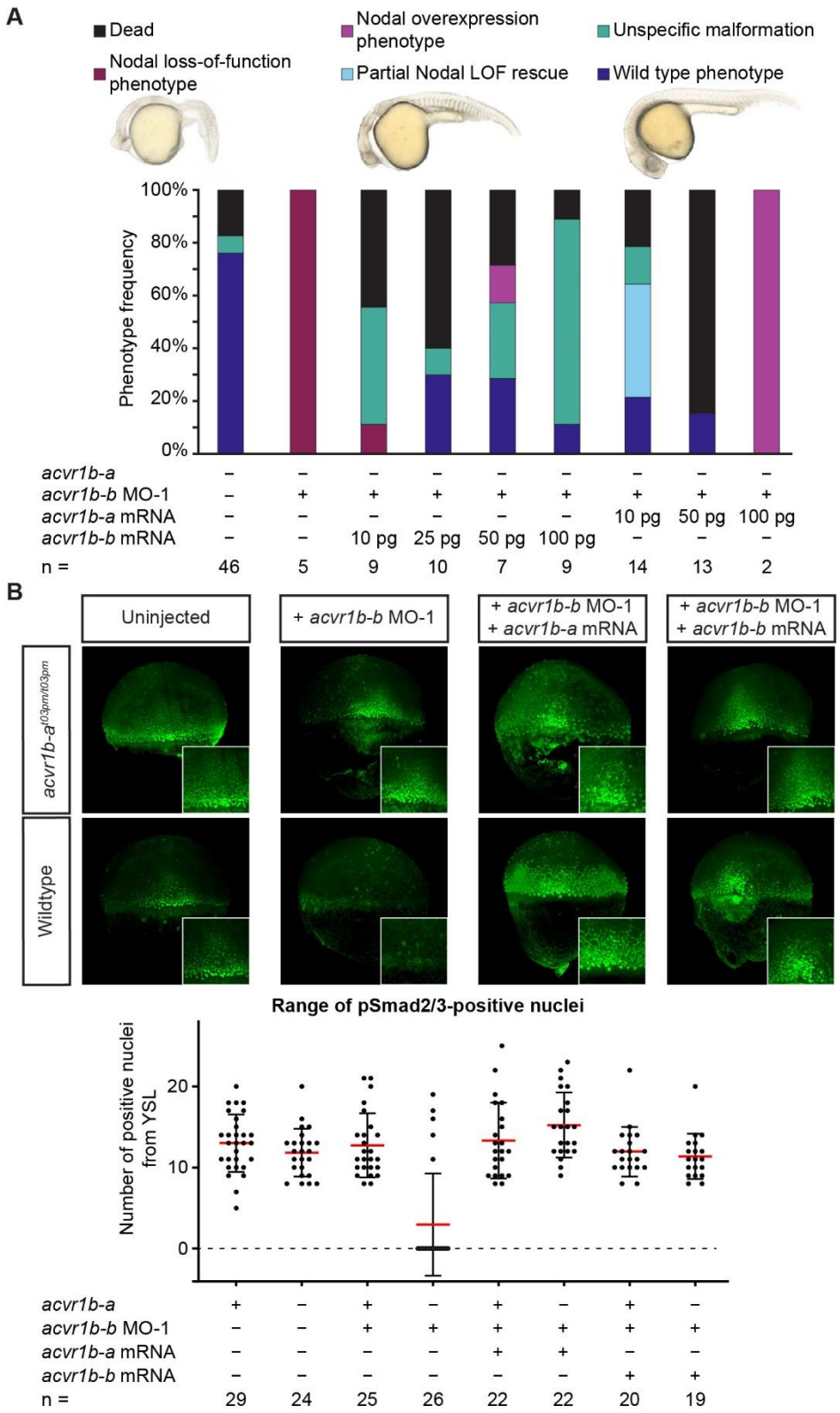

Figure 12: The Type I receptors Acvr1b-a and Acvr1b-b redundantly mediate Nodal signaling. **(A)** Rescue of Type I receptor double knockdown using *acvr1b-a* and *acvr1b-b* receptor mRNA. For

knockdown of *acvr1b-a*, the *acvr1b-a*$^{t03pm/t03pm}$ mutant was used in combination with 0.4 ng *acvr1b-b* MO-1 injections. **(B)** Influence of *acvr1b-a* and *acvr1b-b* on the Nodal signaling range at shield stage. The range of Nodal signaling was determined by counting the maximum number of rows of nuclei that are positive for pSmad2/3 immunostaining, counting from the embryonic margin towards the animal pole. *acvr1b-a*$^{t03pm/t03pm}$ mutants and 0.4 ng *acvr1b-b* MO-1 were used for receptor knockdown. They were rescued with 50 pg of *acvr1b-a* or 25 pg of *acvr1b-b* mRNA. Data was obtained from 3 independent experiments. n indicates the number of analyzed embryos. Averages are displayed in red. Error bars show standard deviation.

While these findings clearly demonstrate a redundant function of the Type I receptors *acvr1b-a* and *acvr1b-b* in mediating Nodal signaling during early zebrafish development, the role of the Type II receptors is less clear. Similar to the approach used to generate Type I receptor loss-of-function conditions, I simultaneously targeted several Type II receptors using morpholinos and mutants. Double-knockdown of *acvr2a-a* and *acvr2a-b* as well as double-knockdown of *acvr2b-a* and *acvr2b-b* resulted each in 1 dpf embryos with what appears to be non-specific head and tail malformations (Figure 11 D,E; Supplementary Figure 3). To test whether the Type II receptor paralogs act fully redundantly in zebrafish Nodal signaling, I knocked down all four Type II receptors at the same time (Figure 11 D; Supplementary Figure 3). While head or tail tissues were strongly reduced or only rudimentarily present, features normally associated with Nodal loss-of-function mutants, such as cyclopia (Feldman et al. 1998) could not be detected. Mesendodermal tissues, such as the heart tube and somites in the head and trunk region, were also still present in the combinatorial Type II receptor knockdown embryos (Figure 11 D; Supplementary Figure 3).

Discussion

To determine which of the putative zebrafish Nodal receptors mediate Nodal signaling during germ layer patterning, I systematically identified and characterized Nodal Type I and Type II receptors during early zebrafish development. *In silico* homology analysis of human, mouse and zebrafish receptor protein sequences revealed that in zebrafish, in addition to the previously identified Type I receptor *acvr1b-a* (Renucci et al. 1996), and Type II receptors *acvr2a-a* (Nagaso et al. 1999) and *acvr2b-a* (Garg et al. 1999; Nagaso et al. 1999), the paralog receptors *acvr1b-b*, *acvr2a-b* and *acvr2a-a* as well as the Type I receptor *acvr1c* are present (Figure 4). Most of the identified putative zebrafish Nodal receptors are maternally deposited and continuously expressed during the first 24 hours of development, indicating that they might play a role in early embryogenesis. The Type I receptor *acvr1c* is the only receptor not expressed until 4 dpf (White et al. 2017), meaning that it is unlikely to be active during germ layer development.

While most other receptors are uniformly expressed at 6 hpf, expression of the Type I receptor *acvr1b-a* becomes restricted to the embryonic margin (Figure 5), similar to the expression of the Nodal co-receptor *oep* (Renucci et al. 1996; Vopalensky et al. 2018). Interestingly, at 24 hpf most of the investigated receptors are expressed in the head region of the embryo (Albertson et al. 2005), while expression domains in the rest of the embryo diversify, indicating independent roles of receptors during later developmental stages.

Previous studies have shown that Nodal signaling induces the expression of several Nodal signaling pathway components like *squint*, *cyclops*, *lefty1*, *lefty2*, *oep* and *acvr1b-a* (Meno et al. 1999; Feldman et al. 2002; Bennett et al. 2007; Dubrulle et al. 2015). Using Nodal induction assays, I found that, except for the Type I receptor *acvr1b-a* and the co-receptor *oep*, none of the receptors are involved in a similar feedback loop (Figure 7 A). It recently was proposed that the restriction of *oep* expression to the embryonic margin and the subsequent loss of Oep in the animal pole of the embryo causes the prospective ectoderm to no longer respond to Nodal signaling (Vopalensky et al. 2018). Due to the similar expression dynamics and responsiveness of the Type I receptor *acvr1b-a* and the co-receptor *oep*, *acvr1b-a* could have a similar functionality to *oep* and

restrict mesendoderm spreading through a loss of competence in prospective ectodermal tissue.

The identified receptors can only mediate signaling of the extracellular Nodal ligand during germ layer patterning if they are localized at the cell membrane. My results show that most fluorescently tagged putative Nodal receptors do indeed localize to the outer membrane of the cell (Figure 8). The only receptors that do not show a clear association with the cell membrane are *acvr1c* and *acvr2a-b*. These receptors also have the least impact on embryonic development when overexpressed (Figure 9). Usually, overexpression of Nodal receptors can induce severe developmental phenotypes, which recapitulate Nodal gain-of-function phenotypes (Toyama et al. 1995; Armes & Smith 1997; Feldman et al. 1998; Nagaso et al. 1999; Rogers et al. 2017). In accordance with this observation, overexpression of the Type I receptors *acvr1b-a* and *acvr1b-b* as well as the Type II receptors *acvr2a-a*, *acvr2b-a* and *acvr2b-b* lead to phenotypes consistent with varying degrees of Nodal gain-of-function, substantiating their potential to mediate Nodal specific signaling during early embryogenesis.

In zebrafish, loss of the two Nodal ligands Squint and Cyclops causes severe developmental defects in the first 24 hpf: Embryos exhibit a distinct merging of the eye field causing cyclopia, and are missing mesendodermal tissue, such as notochord, somites, heart, blood, and gut (Feldman et al. 1998; Gritsman et al. 1999). These distinct phenotypes can be recapitulated by the loss of other components of the signaling pathway. This, for example, is the case for the co-receptor Oep or the signal transducer Smad2 (Figure 2 B) (Gritsman et al. 1999; Dubrulle et al. 2015). To determine whether the identified putative Nodal receptors in zebrafish are essential components of the Nodal signaling pathway during early embryogenesis, I generated several receptor mutants and assessed the effect of morpholino-mediated receptor knockdown. While single receptor mutants in mouse cause severe malformations during development and embryonic lethality (Coerver et al. 1996; Song et al. 1999; Ferguson et al. 2001; Kumar et al. 2001; Ma et al. 2001; Oh & Li 2002), surprisingly, single receptor knockdown in zebrafish does not lead to Nodal-associated loss-of-function phenotypes (Figure 10; Supplementary Figure 2).

In contrast to the two rounds of whole genome duplications during vertebrate evolution, teleosts, to which zebrafish belong, have undergone a third round of genome duplication (Meyer & Van de Peer 2005). This third round of genome duplication caused functional redundancy for several genes in zebrafish. For example, homozygous mutants of either *squint* or *cyclops* exhibit only relatively weak developmental defects (Heisenberg & Nusslein-Volhard 1997; Dougan et al. 2003), while the developmental defects of double mutants are severe (Feldman et al. 1998). Similarly, redundant functionality has been shown for receptors that are involved in other signaling pathways, such as FGF and BMP signaling (Smith et al. 2011; Leerberg et al. 2019). Using combinatorial knockdown of the Type I receptors, I found that knockdown of *acvr1b-b* in *acvr1b-a* receptor mutants perfectly recapitulates a complete Nodal loss-of-function phenotype (Figure 11 C). Further, I could verify that the two receptors have a redundant role in mediating Nodal signaling during germ layer patterning by showing that the Nodal signal transducer SMAD2/3 is not phosphorylated without functional *acvr1b-a* or *acvr1b-b* present (Figure **12**). The range of pSMAD2/3 could be rescued through the injection of functional receptor mRNA into the double knockdown embryo (Figure 12 B). It is notable that the knockdown of *acvr1b-b* in *acvr1b-a* mutant embryos only fully recapitulates Nodal loss-of-function phenotypes if the used morpholino is targeted against the ATG start site of the *acvr1b-b* mRNA, but not when it is targeted against the splice site (Figure 11 C). This indicates that maternally deposited *acvr1b-b* mRNA is at least partially sufficient to mediate Nodal signaling during germ layer patterning.

Surprisingly, combinatorial knockdown of the putative Nodal Type II receptors *acvr2a-a*, *acvr2a-b*, *acvr2b-a* and *acvr2b-b* did not completely emulate a Nodal loss-of-function mutant (Figure 11 D,E; Supplementary Fig. 3). Although the knockdown of all four Type II receptors causes severe malformations of head and tail tissue, features such as cyclopia (Feldman et al. 1998), loss of the heart tube and loss of somites in the head and trunk region could not be observed (Supplementary Figure 3). However, knockdown of all four putative Type II receptors in zebrafish was only possible using only morpholinos. Unfortunately, since no antibodies against the putative zebrafish Nodal receptors are available, assessing the knockdown efficiency of the used morpholinos would be difficult (Eisen & Smith 2008). A possible approach to verify that the morpholinos do indeed target

the intended sequence would be to assess whether their injection inhibits the translation of their target sequence fused to a reporter sequence. Nevertheless, this cannot confirm to what extend endogenous protein expression is inhibited. Therefore, results would be more robust if quadruple mutants of *acvr2a-a*, *acvr2a-b*, *acvr2b-a* and *acvr2b-b* could be generated to review the findings of this thesis.

Other TGF-β Type II receptors that have not yet been associated with Nodal signaling could substitute for the putative Nodal Type II receptors in mediating Nodal signaling. For example, previous studies showed that in zebrafish, Acvr2b-a can mediate Activin as well as BMP signaling by interacting with either the Type I receptor Acvr1b-a or Bmpr1a, respectively (Nagaso et al. 1999). Furthermore, *in vitro* studies have shown a high binding affinity of the BMP Type II receptor Bmpr2 to Nodal, although it still an open question whether Bmpr2 can actually transduce Nodal signaling *in vivo* (Aykul et al. 2015). Also, the Type I receptor TGFβr1 has been shown to activate the Type I receptor Acvr1 via phosphorylation, suggesting that Type I receptors can substitute for Type II receptors under certain conditions (Ramachandran et al. 2018). However, if and how other Type I or Type II receptors play a role for transducing Nodal signaling requires further investigation.

In conclusion, I identified and characterized several putative Nodal Type I and Type II receptors in zebrafish. I found that the Type I receptors *acvr1b-a* and *acvr1b-b* redundantly mediate Nodal signaling during early development, while *acvr1c* does not seem to play a role during early germ layer patterning. Furthermore, I showed that none of the putative Nodal Type II receptors can mediate Nodal signaling on its own during early embryonic development, even though all the investigated Type II receptors are expressed during germ layer patterning, and most can induce Nodal-overexpression associated phenotypes.

4.2 Measuring morphogen diffusivity

Many biological processes depend on the correct dispersal of different molecules, such as hormones, neuronal transmitters, signaling pathway ligands or transcription factors (Crick 1970; Müller & Schier 2011). The reach of these molecules is often determined by their mobility in the respective biological tissue through which they move. Changes in their diffusivity can impair homeostasis and normal development (Harmansa et al. 2015; Almuedo-Castillo et al. 2018). The mobility of fluorescently tagged proteins *in vivo* can be assessed using Fluorescence Correlation Spectroscopy (FCS) (Magde et al. 1972; Magde et al. 1974) and Fluorescence Recovery After Photobleaching (FRAP) (Poo & Cone 1973; Liebman & Entine 1974). In FCS, fluctuations of the fluorescence of tagged proteins are measured in very small volumes. These fluctuations correspond to the free movement of the tagged molecules. Theoretical correlation functions can then be used to calculate the free diffusivity of a molecule. In contrast, in the FRAP technique, one measures how long it takes for a fluorescently tagged molecule to spread into a region of interest. This is done by first bleaching a region of interest using a strong laser and then measuring the recovery of fluorescence in the region of interest, which is due to movement of unbleached molecules from outside the bleached region. Using this recovery curve one can calculate the effective diffusivity of the tagged molecule within the investigated region on interest. For the calculation of the effective diffusivity, models of tissue geometry, bleaching conditions and reaction kinetics of the investigated molecule are required.

PyFRAP was developed by Alexander Bläßle and Patrick Müller as a freely available Python software package. It is designed to allow for the easy and complete analysis of the microscopical images that are generated during FRAP measurements, and to generate publication-ready figures. PyFRAP is applicable in different model systems and works for different experimental conditions. It allows for the flexible definition of three-dimensional geometries, such as a spherical zebrafish embryo. Furthermore, it includes different mathematical reaction-diffusion models and allows the user to choose the most likely model. PyFRAP was extensively tested using *in silico*, *in vitro* and *in vivo*

experimental data, showing that it could identify the known diffusivities of macromolecules.

In biological tissues, dispersal of molecules is often restricted by the complex environment in which they move. For example, tissue architecture can lead to tortuous movement, causing a lower diffusivity of signaling molecules (Shorten et al. 2007; Müller et al. 2013). Using PyFRAP, the impact of tortuosity on molecular diffusivity was assessed using *in silico* simulations of GFP dispersal in differentially packed cell environments, indicating a reduced diffusion of GFP by around 40 % in three-dimensional simulations. These findings were corroborated by *in vitro* experiments which compare the diffusivity of recombinant GFP in a restricted environment, imitated by the presence of polyacrylamide beads, with that of a bead-free environment. The reduction of diffusivity was even more prominent when the mobility of secreted and recombinant GFP was analyzed in the biological context of living zebrafish. In this setting, diffusivity was reduced by 53 % compared to the *in vitro* measurements, probably due to a more complex tissue architecture. Another important aspect hindering propagation of molecules *in vivo* is their interaction with diffusion regulators, such as membrane-bound molecules or components of the extracellular matrix (Hrabe et al. 2004). This effect was observed during measurements of the effective diffusivity of Squint-GFP in zebrafish embryos at approximately 5 hpf. Squint-GFP is approximately 1.5-times larger than GFP alone. If only the size difference between GFP and the Squint-GFP construct impacted diffusivity, one would expect a 14 % decrease in diffusivity for Squint-GFP compared to GFP (GFP diffusivity in the embryo: D(GFP) = 36 $\mu m^2/s$; Squint-GFP diffusivity expected: D(Squint-GFP) = 31 $\mu m^2/s$). In contrast, the measured diffusivity of Squint-GFP is approximately 2 $\mu m^2/s$, which is almost 90% lower than expected. These findings, together with similar results from previous studies (Müller et al. 2013) support the idea that interactions with diffusion regulators play an important role in the propagation of embryonic signaling molecules such as Nodal.

4.3 Nodal receptors act as diffusion regulators

In this chapter, I analyze the role of receptors on Nodal propagation through the embryo. In zebrafish, Nodal expression can first be observed in the embryonic margin and is thought to establish a signaling gradient from there into the embryo (Rebagliati et al. 1998a; Chen & Schier 2001). Nodal signaling can act as a short- to mid-range inducer of mesendodermal cell fate during gastrulation (Müller et al. 2012). However, the mechanisms that underlie the restriction of the Nodal signaling range remain unclear. Previous studies have speculated that Nodal diffusion is inhibited by transient interaction of Nodal with extracellular diffusion regulators (Müller et al. 2013; Bläßle et al. 2018). Nodal receptors fulfil several requirements to function as such. Firstly, their receptor domains are present extracellularly; secondly, they are bound to the cell membrane, and thirdly, they naturally interact with the Nodal ligand. This was highlighted by recent single wavelength fluorescence cross-correlation spectroscopy (SW-FCCS) measurements of Nodal and the Type II receptor Acvr2b-a in zebrafish. These show that a strong affinity between ligand and receptor exists (Wang et al. 2016). Furthermore, loss of the co-receptor *oep* drastically increases the Nodal signaling range (Lord et al. 2019) without increasing Nodal diffusivity, while overexpression of *oep* has been shown to decrease Nodal diffusivity (Rogers 2015).

To assess the impact of Nodal receptors on Nodal distribution in the embryo, I measured the distribution profiles of Nodal-GFP constructs in embryos with altered receptor levels. Furthermore, I assessed the localization of Nodal-GFP constructs in the presence of excess receptor mRNA. I used FRAP and FDAP measurements to determine whether receptors directly impact Nodal diffusivity (FRAP) or degradation (FDAP) in the embryo.

The following results are in part from the manuscript in preparation “Regulation of Nodal signaling propagation by receptor 1 interactions and positive feedback”. This applies to the following paragraphs: “Nodal receptors affect Nodal dispersal in embryos” and “Receptor binding influences signal propagation through multiple mechanisms”.

4.3.1 Nodal receptors affect Nodal dispersal in embryos

During gastrulation, the establishment of the correct range of Nodal signaling is thought to be crucial for normal germ layer patterning (Rogers & Müller 2019). It has previously been hypothesized that interaction of Nodal with its receptors might control signal propagation (Müller et al. 2012), and the strong affinity of Nodal for its receptor Acvr2b has been suggested to shape the Nodal gradient (Wang et al. 2016). To test whether Nodal receptors can indeed affect Nodal distribution in the embryo, I mimicked the secretion of endogenous Nodal from the marginal zone by injecting 100 pg *squint-GFP* or *cyclops-GFP* mRNA into the YSL at approximately 4.5 hpf (Figure 13 A,B). I then assessed the distribution of Squint-GFP and Cyclops-GFP at 2 or 4 hours post-injection (hpi), respectively in receptor knockdown conditions.

In this assay, Squint-GFP is secreted from the YSL into the extracellular space and forms a gradient with decreasing intensity towards the animal pole at 2 hpi (Figure 13 B-E), similar to the Squint-GFP distribution from localized cell clones transplanted to the animal pole of zebrafish embryos (Müller et al. 2012; Wang et al. 2016; Soh et al. 2020). Strikingly, loss-of-function conditions for the Type I receptors *acvr1b-a* and *acvr1b-b*, the Type II receptors *acvr2a-b* and *acvr2b-a* as well as the co-receptor *oep* led to a flattened Squint-GFP distribution (Figure 13 B-E). While Squint-GFP is a relatively diffuse extracellular signal, Cyclops-GFP signal is distributed in a punctate pattern in the embryo and sharply decreases with further distance from the YSL (Müller et al. 2012) (Figure 13 B,F,G). Loss-of-function conditions for the Type I receptors *acvr1b-a* and *acvr1b-b* and the co-receptor *oep* have a drastic effect on gradient formation and increase the number and distributional range of Cyclops-GFP puncta (Figure 13 F,G).

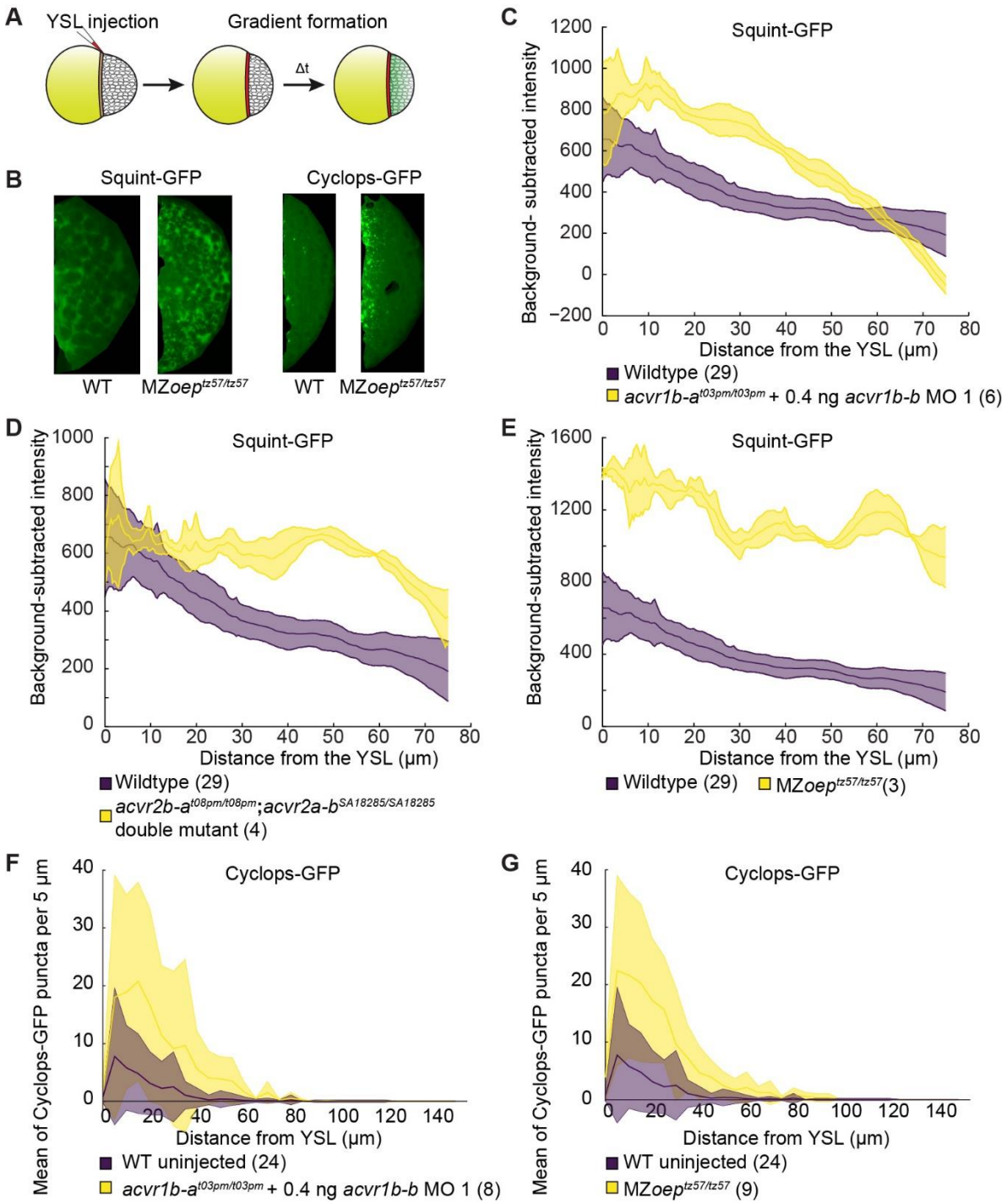

Figure 13: **Nodal receptors can shape the distribution of Nodal ligand in zebrafish embryos. (A)** Schematic illustration of the YSL injection assay to create local Nodal sources in the native context. 100 pg of *squint-GFP* or *cyclops-GFP* encoding mRNA are injected into the YSL of sphere stage embryos and subsequently imaged to measure the Nodal distribution. Embryos were imaged ~2 hpi for *squint-GFP* and ~ 4 hpi for *cyclops-GFP* mRNA injections. **(B)** Lateral views of Squint-GFP and Cyclops-GFP signals in wild type compared to *MZoep*$^{tz57/tz57}$ embryos. **(C-G)** Squint-GFP and Cyclops-GFP distributions with

modulated receptor levels. For Squint-GFP, the average background-subtracted GFP signal as a function of distance from the YSL is plotted. The shaded region indicates standard deviation. The number of measured embryos is indicated in parentheses. For Cyclops-GFP, the distance and number of puncta from the YSL were measured, and the mean number of puncta every 5 µm is plotted. Shaded regions indicate standard deviation. Distributions in wild type (purple) compared to knockdown conditions (yellow) are shown for Squint-GFP **(C-E)** and Cyclops-GFP **(F-G)** in *acvr1b-a*$^{t03pm/t03pm}$ mutant embryos injected with 0.4 ng *acvr1b-b* ATG start site targeting morpholino **(C,F)**, *acvr2b-a*$^{t08pm/t08pm}$*;acvr2a-b*$^{SA18285/SA18285}$ double mutants **(D)**, and *MZoep* mutants **(E,G)**.

4.3.2 Most receptors do not impact Nodal subcellular localization in the embryo

I investigated whether elevated receptor levels affect Nodal subcellular localization in the embryo. Nodal has been suggested to directly bind to its Type II receptors and its co-receptor (Reissmann et al. 2001). While loss of some Nodal receptors causes a change in Nodal dispersal in the embryo (Figure 13), it is unclear whether this change depends on the direct interaction of the respective receptor with Nodal. To elucidate whether receptor interaction is strong enough to change Nodal localization, I injected wild type embryos with 50 pg of receptor mRNA and 30 pg of *squint-GFP* or *cyclops-GFP* mRNA. Typically, Squint-GFP signal can be detected diffusely in the extracellular space with few membrane-associated clusters, while Cyclops-GFP signal is highly punctuate with almost no diffuse signal in the extracellular space (Figure 14 A). Interestingly, the localization of Squint-GFP and Cyclops-GFP does not change with the overexpression of most receptors, except for *oep*. Increased levels of the Nodal co-receptor *oep* caused Squint-GFP signal to cluster similarly to the punctate distribution of Cyclops-GFP. This suggests that the co-receptor Oep strongly interacts with Squint, which might have an effect on Squint diffusion.

Interestingly, the secretion of Squint-GFP is impaired in MZ*oep* mutants, and the signal appears to be cell membrane-associated (Figure 14 B) (Rogers 2015). In mouse, the *oep* orthologue *Cripto* has been shown to cause Nodal to localize to early endosomes and to be necessary for the proteolytic maturation of Nodal (Blanchet et al. 2008a; Blanchet et al. 2008b). To circumvent the clustering of Squint-GFP with Oep during maturation and exocytosis, and to assess whether puncta formation can happen in response to

extracellular interactions between Squint-GFP and Oep, I separated s*quint-GFP* and *oep-RFP* expression into different compartments of the embryo. For this purpose, I injected 50 pg of *oep-RFP* mRNA into wild type embryos at the one-cell stage, leading to its later expression in the embryonic cells, but not the YSL, and later injected 100 pg of *squint-GFP* mRNA into the YSL of the same embryos at 4.5 hpf (Supplementary Figure 4 A). The overexpression of *oep-RFP* in the embryonic cells leads to a clustered localization of extracellular Squint-GFP, similar to the puncta observed when both, *oep-RFP* and *squint-GFP*, are overexpressed in the same compartment (Figure 14 B,C; Supplementary Figure 4 B). Furthermore, Squint-GFP co-localized with Oep-RFP, indicating that, indeed, the extracellular interaction of Oep with Squint causes the puncta formation (Figure 14 C). Interestingly, loss of Oep in MZ*oep* mutants did not impair Cyclops-GFP puncta formation and secretion (Figure 14 B; Supplementary Figure 4 C). Instead, loss of Oep seems to increase the amount and range of Cyclops-GFP clusters (Figure 13 G; Supplementary Figure 4 C), while overexpression seems to decrease the amount of Cyclops-GFP puncta (Figure 14 A; Supplementary Figure 4 C). These observations indicate that, while the co-receptor Oep may play a different role for the secretion of each of the two zebrafish Nodals, Cyclops and Squint, it is one of the main receptor complex components that might impact Nodal distribution in the embryo.

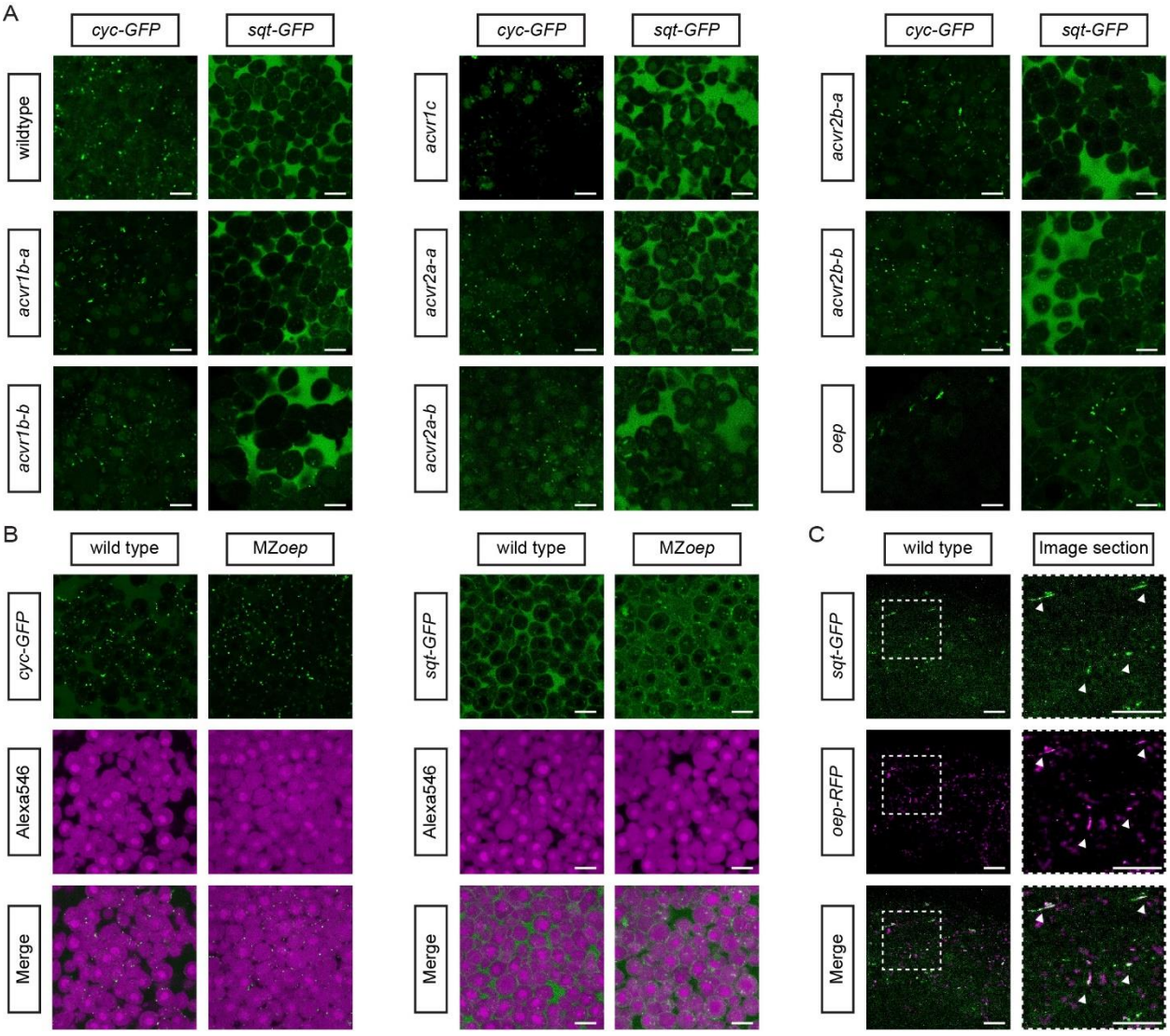

Figure 14: Impact of receptors on Nodal-GFP localization. Scale bars represent 20 µm **(A)** Localization of Squint-GFP and Cyclops-GFP in zebrafish embryos at 5-6 hpf. Wild type embryos were injected with 50 pg mRNA of the indicated receptor and 30 pg of either *squint-GFP* or *cyclops-GFP* mRNA **(B)** Localization of Squint-GFP and Cyclops-GFP in MZ*oep* mutant embryos at 5-6 hpf. Embryos were injected with 30 pg of either *cyclops-GFP* or *squint-GFP* mRNA and 0.4 ng of Alexa Fluor™ 546 dextran. **(C)** Localization of Squint-GFP in embryos that were injected with 50 pg of *oep-RFP* mRNA in the one-cell stage. Embryos were injected with 100 pg of *squint-GFP* mRNA into the YSL at 4.5 hpf. Localization was measured two hours after injection of *squint-GFP* mRNA.

4.3.3 Receptor binding influences signal propagation via multiple mechanisms

Receptors can impact signal propagation through embryonic tissues by several mechanisms. Firstly, receptor availability can affect the clearance rate of bound ligands and thereby affect signal propagation by modulating the extracellular protein stability (Rogers & Schier 2011; Rogers & Müller 2019). Secondly, transient receptor binding can slow down signal diffusion (Crank 1979; Miura et al. 2009; Müller et al. 2012; Müller et al. 2013). Thirdly, positive autoregulation through ligand-receptor interactions can extend a ligand's expression domain by relay signaling (van Boxtel et al. 2015; Rogers & Müller 2019). To determine whether the receptors affect Nodal propagation by one of these mechanisms, I measured stability and diffusion of Nodal in the presence and absence of receptors.

To measure protein stability, I used Squint-Dendra2 and Cyclops-Dendra2 in FDAP assays (Müller et al. 2012; Bläßle & Müller 2015; Rogers et al. 2015). Interestingly, overexpression of the Type II receptor *acvr2b-a* did not affect Nodal clearance (clearance rate constant k = 1.62 ± 0.41 x 10^{-4}/s for Squint-Dendra2; k = 1.97 ± 0.67 x 10^{-4}/s for Squint-Dendra2 + 100 pg *acvr2b-a* mRNA; k = 1.60 ± 0.38 x 10^{-4}/s for Cyclops-Dendra2; k = 1.88 ± 0.65 x 10^{-4}/s for Cyclops-Dendra2 + 100 pg *acvr2b-a* mRNA; Figure 15 A), suggesting that the strong interaction between Nodal and Acvr2b-a that has previously been shown *in vivo* (Wang et al. 2016) is not sufficient to modulate Nodal protein stability.

To test whether receptor interactions can affect Nodal diffusion, I focused our analysis on those receptors that had a clear influence on the Nodal propagation range, the Type II receptor Acvr2b-a as well as the feedback-regulated co-receptor Oep and the Type I receptors Acvr1b-a and Acvr1b-b (Figure 7; Figure 13). For measurements of protein diffusion, I used Squint-GFP and Cyclops-GFP in FRAP assays (Müller et al. 2012; Müller et al. 2013; Almuedo-Castillo et al. 2018; Bläßle et al. 2018; Soh & Müller 2018). Overexpression of *acvr2b-a* and *acvr1b-a* as well as knockdown of *acvr1b-a* and *acvr1b-b* did not significantly impact Nodal diffusivity (D = 2.28 ± 1.57 µm^2/s for Squint-GFP; D = 2.81 ± 2.55 µm^2/s for Squint-GFP + 100 pg *acvr2b-a* mRNA; D = 1.87 ± 1.20 µm^2/s for Squint-GFP + 100 pg *acvr1b-a* mRNA; D = 2.51 ± 1.23 µm^2/s for Squint-GFP in *acvr1b-a*$^{t03pm/t03pm}$ mutants; D = 3.96 ± 1.21 µm^2/s for Squint-GFP in *acvr1b-a*$^{t03pm/t03pm}$

mutants + 0.4 ng *acvr1b-b* MO-1; D = 1.92 ± 1.24 µm²/s for Cyclops-GFP; D = 0.79 ± 0.45 µm²/s for Cyclops-GFP + 100 pg *acvr2b-a* mRNA; D = 1.46 ± 0.51 µm²/s for Cyclops-GFP + 100 pg *acvr1b-a* mRNA; D = 1.73 ± 0.77 µm²/s for Squint-GFP in *acvr1b-a*$^{t03pm/t03pm}$ mutants; Figure 15 B). Strikingly, overexpression of the co-receptor Oep caused an almost 5-fold decrease of Squint-GFP diffusivity (D = 0.42 ± 0.36 µm²/s for Squint-GFP + 50 pg *oep-RFP* mRNA; Figure 15 B), suggesting that Oep serves as a major diffusion regulator that controls the range of Nodal signals in zebrafish embryos (Rogers 2015; Lord et al. 2019).

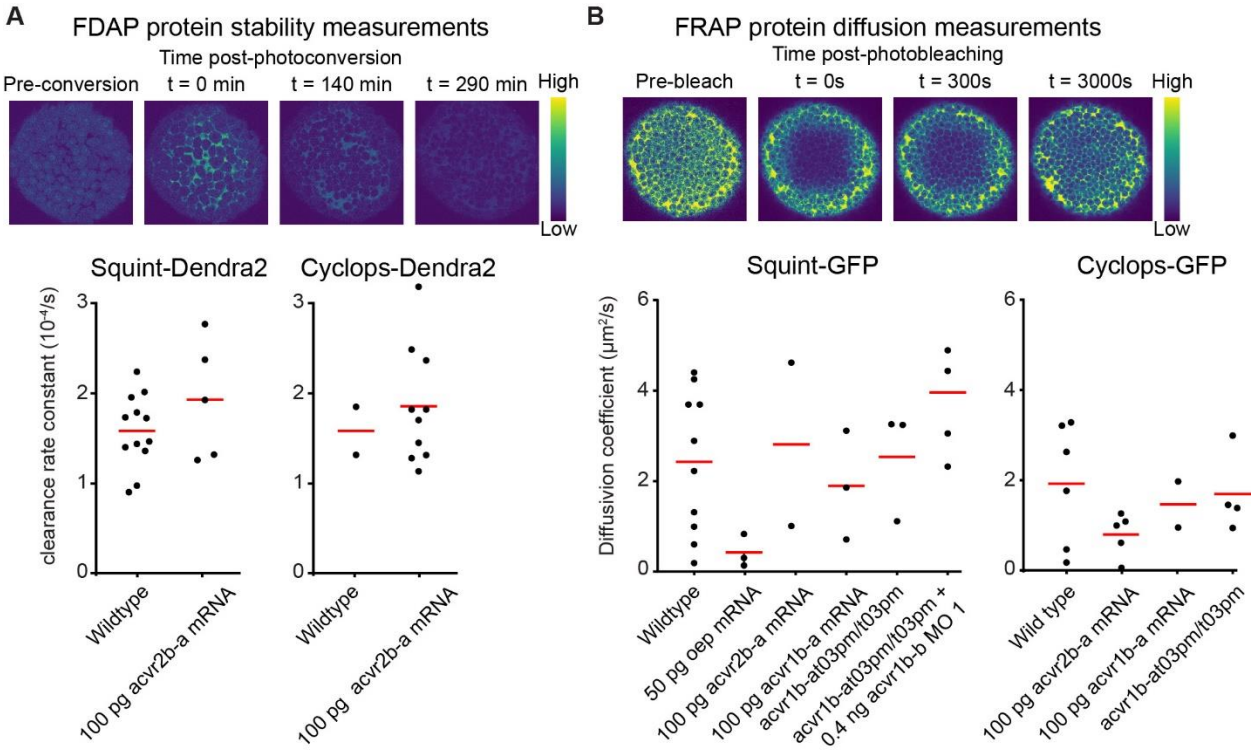

Condition	Squint-Dendra2 stability	Cyclops-Dendra 2 stability
Wildtype	1.62 ± 0.41 x 10⁻⁴/s	1.60 ± 0.38 x 10⁻⁴/s
100 pg acvr2b-a mRNA	1.97 ± 0.67 x 10⁻⁴/s	1.88 ± 0.65 x 10⁻⁴/s

Condition	Squint-GFP diffusivity	Cyclops-GFP diffusivity
Wildtype	2.28 ± 1.57 µm²/s	1.92 ± 1.24 µm²/s
50 pg oep mRNA	0.42 ± 0.36 µm²/s	-
100 pg acvr2b-a mRNA	2.81 ± 2.55 µm²/s	0.79 ± 0.45 µm²/s
100 pg acvr1b-a mRNA	1.87 ± 1.20 µm²/s	1.46 ± 0.51 µm²/s
acvr1b-a$^{t03pm/t03pm}$	2.51 ± 1.23 µm²/s	1.73 ± 0.77 µm²/s
acvr1b-a$^{t03pm/t03pm}$ + 0.4 ng acvr1b-b MO 1	3.96 ± 1.21 µm²/s	-

Figure 15: Impact of Nodal receptors on stability and diffusivity. (A) Impact of *acvr2b-a* overexpression on Squint- and Cyclops-Dendra2 clearance rate constants using FDAP measurements. For overexpression, 100 pg *acvr2b-a* mRNA was injected at the one-cell stage of wild type embryos. Mean extracellular clearance rate constants are displayed in red, and individual measurements are shown as

black dots. **(B)** Impact of receptor levels on Squint- and Cyclops-GFP diffusivity using FRAP measurements. For overexpression, either 50 pg *oep* mRNA, 100 pg *acvr2b-a* mRNA or 100 pg *acvr1b-a* mRNA were injected at the one-cell stage of wild type embryos. *acvr1b-a* mutants and 0.4 ng *acvr1b-b* MO-1 were used for receptor knockdown. The mean diffusion coefficients are displayed in red, and individual measurements are shown as black dots.

Discussion

In zebrafish, Nodal ligand is initially expressed in the YSL. From there, it is thought to spread into the embryo, forming a short- to mid-range signaling gradient (Erter et al. 1998; Hong et al. 2011; Dubrulle et al. 2015; van Boxtel et al. 2015). Interaction of Nodal with diffusion regulators in the extracellular space was proposed to explain the shorter range of Nodal and its lower diffusivity compared to its antagonist Lefty (Müller et al. 2013; Bläßle et al. 2018; Rogers & Müller 2019). Several lines of evidence indicate that Nodal receptors could fulfill the requirements for being functional Nodal diffusion regulators in the embryo. For example, strong interactions of Squint with the Type II receptor Acvr2b-a have been measured *in vivo* (Wang et al. 2016), and Nodal signaling range has been shown to be drastically increased in *oep* mutant embryos (Lord et al. 2019).

Here, I investigated the role of putative Nodal receptors on Nodal protein distribution in more detail. To study the effect of receptors on Nodal distribution in the embryo, I used an assay that imitates the endogenous Nodal dispersal from the embryonic margin. I injected fluorescently tagged Nodal mRNA into the YSL of embryos and imaged the resulting gradient of fluorescent signal within the embryo (Figure 13 A). This approach allows for a direct visualization of the effect of altered receptor levels on Nodal dispersal. Loss of Nodal receptors resulted in a flattened Nodal protein gradient, which also exhibited an increased intensity of fluorescent signal (Figure 13 C-G). These observations indicate that receptor availability can indeed impact the spreading of Nodal from a localized source. The observed increased intensity of fluorescent signal and flattening of the Nodal protein gradient could be caused by several mechanisms. On the one hand, transient binding interactions of Nodal with its receptors could be strong enough to normally retain Nodal protein close to its source and to thereby restrict its spreading into the embryo. This might explain the steeper signal intensity gradient of Nodal-GFP in untreated wild type embryos. On the other hand, Nodal protein might be more stable, and therefore able to move further, in embryos that are missing components of the Nodal signaling pathway. Besides its intrinsic stability, Nodal protein degradation kinetics can also be influenced by changes in the Nodal clearance rate via cellular uptake, which might in part be mediated by Nodal receptors (Rogers & Schier 2011; Rogers & Müller 2019).

Of the analyzed putative Nodal receptors and co-receptor, loss of the co-receptor *oep* had the highest impact on the shape of the Nodal protein gradient in the embryo (Figure 13 E,G). This suggests that Oep plays an essential role during the formation of the Nodal signaling complex (Gritsman et al. 1999; Minchiotti et al. 2001; Reissmann et al. 2001; Yeo & Whitman 2001), which makes it a likely candidate to act as a regulator of Nodal propagation *in vivo*.

The strong impact of *oep* on Nodal propagation was even more prominent when I analyzed changes in the localization of Nodal-GFP in 5 hpf embryos upon overexpression of putative Nodal receptors and *oep*. While Type I and Type II receptors do not seem to have an effect on the subcellular localization of Nodal, increased expression of *oep* lead to the apparent recruitment of Squint-GFP to membrane-associated clusters (Figure 13 B; Figure 14; Supplementary Figure 4 B) (Rogers 2015). This clustering also happens when the expression of *squint-GFP* and *oep-RFP* are spatially separated, which can be achieved by injecting *oep-RFP* mRNA into the one-cell stage embryo and later injecting *squint-GFP* mRNA into the YSL. This experimental approach demonstrates that the formation of Squint-GFP clusters upon increased o*ep* expression does not depend on their interaction during secretion (Blanchet et al. 2008a; Blanchet et al. 2008b), but rather on an extracellular interaction. Interestingly, in MZ*oep* mutant embryos, Squint-GFP secretion is impaired and fluorescent signal localizes to the cellular membrane (Figure 14 B). The localization of Cyclops-GFP, however, does not appear to be affected (Rogers 2015). In mouse, the Nodal EGF-CFC co-receptor *Cripto* has been shown to be crucial for the recruitment of convertases that mediate cleavage of the Nodal pro-domain upon secretion (Blanchet et al. 2008a). Therefore, Squint-GFP secretion in MZ*oep* mutants is likely impaired due to incomplete protein maturation, causing the secreted molecule to be retained at the cell membrane (Figure 14 B). In accordance with this idea, Squint-GFP can still move freely in the extracellular space in MZ*oep* mutants when it is expressed from the YSL, where Oep is naturally missing (Figure 13 B,E,G; Supplementary Figure 4) (Lord et al. 2019). In contrast to Squint-GFP, the clustered distribution of Cyclops-GFP In the embryo is not changed in MZ*oep* mutants, suggesting that other factors are responsible for the puncta formation of Cyclops-GFP (Figure 14 B; Supplementary Figure 4 B). However, loss of *oep* causes Cyclops-GFP puncta to spread further from a localized

source into the embryo (Figure 13 G; Supplementary Figure 4 B), indicating that the co-receptor can directly impact Cyclops propagation in the embryo.

To elucidate whether the Type I receptors Acvr1b-a and Acvr1b-b, the Type II receptor Acvr2b-a or the co-receptor Oep directly impact Nodal diffusivity, I measured the diffusion coefficients of Squint-GFP and Cyclops-GFP in correlation to receptor overexpression and knockdown, using FRAP assays (Figure 15 B). *oep* overexpression had the biggest impact on Squint-GFP diffusivity, which is in accordance with its strong impact on distribution and localization of Squint-GFP in the extracellular space. FRAP measurements showed that *oep* overexpression leads to an almost 5-fold reduction of Squint-GFP diffusivity (Figure 15 B). In contrast, overexpression of the Type I receptors *acvr1b-a*, *acvr1b-b* and the Type II receptor *acvr2b-a* does not seem to impact Nodal diffusivity (Figure 15 B).

While fluorescence measurements after the injection of *squint-GFP* and *cyclops-GFP* mRNA into the YSL indicate that Type I and Type II receptor levels impact the Nodal distribution gradient, experiments using FRAP do not show that they impair Nodal propagation through hindering diffusivity. This is surprising since a direct interaction of *Xenopus* Nodal (Xnr-1) with mouse ACVR2B had previously been demonstrated using co-IP (Reissmann et al. 2001). Furthermore, SW-FCCS measurements have shown a strong dissociation constant of Squint-GFP and the Type II receptor Acvr2b-a in the zebrafish embryo (Wang et al. 2016), indicating that Nodal directly interacts with its Type II receptor. However, previous studies using mouse Nodal and ACVR2B could not corroborate these findings, indicating species-specific interaction differences between Nodal and its Type II receptor (Yeo & Whitman 2001; Sakuma et al. 2002). Furthermore, a recent untargeted Nodal co-IP followed by mass spectroscopy could not identify Activin Type I and Type II receptors as direct binding partners. However, it is unclear whether endogenous receptor levels in the embryo are sufficient for identification in this approach (Mörsdorf 2019). To clarify whether Nodal directly interacts with its Activin receptors in zebrafish, further co-IP experiments should be conducted.

Apart from impacting Nodal diffusivity, the availability of Type I and Type II receptors could also impact Nodal propagation by modulating Nodal stability in the embryo. However,

overexpression of *acvr2b-a* did not show an increased degradation rate for zebrafish Nodal (Figure 15 A). But it is not clear whether Type II receptors alone are sufficient to induce the uptake of Nodal into the cell. This process of clearing Nodal from the extracellular space is likely to require the presence of other receptor complex components in sufficient amounts. To test this idea, Nodal stability should be assessed when several Type I and Type II receptors are overexpressed.

I could show that, in zebrafish, several Type II receptors are likely to mediate Nodal signaling (see chapter 4.1). While I assessed the impact of the Type I receptors *acvr1b-a* and *acvr1b-b*, the Type II receptor *acvr2b-a*, and the co-receptor *oep,* the influence of the other putative Nodal receptors on Nodal propagation and stability still need to be assessed in future experiments.

In contrast to the Type I and Type II receptors, the co-receptor Oep seems to directly inhibit Squint diffusivity and localization in the embryo (Rogers 2015). Consistent with my findings, previous studies also highlighted the importance of Oep for the restriction of Nodal signal to the embryonic margin and loss of mesendodermal competence in the animal pole of zebrafish embryos (Vopalensky et al. 2018; Lord et al. 2019). Additionally, the EGF-CFC co-receptor is crucial for the assembly of the Nodal receptor complex and mediates binding of Nodal to the Activin receptor complex (Gritsman et al. 1999; Reissmann et al. 2001; Yeo & Whitman 2001; Bianco et al. 2002; Yan et al. 2002; Calvanese et al. 2015).

In summary, my findings demonstrate that receptor levels can indeed function as regulators of Nodal diffusion in the developing embryo, with the co-receptor Oep likely functioning as one of the main regulators of Nodal distribution. These results emphasize that ligand-receptor interaction can function beyond simple signal transduction.

5. Conclusion and Outlook

In this thesis, I identified several so far undescribed putative Nodal receptors in zebrafish and elucidated the role of receptors on Nodal propagation during early embryonic development. Nodal signaling is a key regulator of germ layer patterning during early embryogenesis and is known to signal through a complex consisting of Activin Type I and Type II receptors and a co-receptor (Feldman et al. 1998; Shen 2007; Schier 2009; Hill 2017). While several components of the Nodal signaling pathway, such as the co-receptor *oep* or the signal transducer *smad2* have been shown to be crucial for Nodal mediated germ layer development in zebrafish (Gritsman et al. 1999; Dubrulle et al. 2015), the role of the Activin Type I and Type II receptors in zebrafish is less clear. Here, I found that, in zebrafish, early Nodal signaling is redundantly mediated by the Type I Activin receptor paralogs *acvr1b-a* and *acvr1b-b*. Furthermore, I identified several Type II receptor paralogs with the potential to mediate Nodal signaling during mesendodermal development. However, while I could demonstrate that the Type I receptors function redundantly, my knockdown experiments suggest that neither an individual nor a combination of different Type II receptors are solely responsible for mediating Nodal signaling during early germ layer patterning. The combinatorial knockdown of up to 4 Type II receptors was done using morpholinos, which is not an ideal approach since it can result in incomplete knockdown or off-target nonspecific deleterious effects. Therefore, for further investigation, directed mutagenesis with CRISPR/Cas9 should be used to generate quadruple mutants to ensure a complete knockdown of all identified putative Nodal Type II receptors. Also, previous studies have shown that Activin Type I and Type II receptors can transmit signals from different ligands (Nagaso et al. 1999; Aykul et al. 2015; Ramachandran et al. 2018). This indicates that, even if all Nodal Type II receptors are lost due to knockdown, other receptors could substitute and mediate at least some Nodal signaling during early development. Therefore, it is important to further investigate the potential role of other TGF-β pathway Type II receptors, such as the BMP receptors *bmpr2a* and *bmpr2b,* using in zebrafish embryos in which the investigated putative Nodal Type II receptors are knocked out.

Different Nodal receptors have been linked to different pathologies, such as Systemic sclerosis (Takagi et al. 2011), obesity (Andersson et al. 2008; Carlsson et al. 2009; Yogosawa & Izumi 2013; Yogosawa et al. 2013; Guo et al. 2014; Balkow et al. 2015; Bu et al. 2018), cardiovascular diseases (Ma et al. 2012; Ying et al. 2016; Chen et al. 2017; Wang et al. 2017; Wang et al. 2018) and tumorigenesis (Hempen et al. 2003; Deacu et al. 2004; Xu et al. 2004; Qiu et al. 2016; Asnaghi et al. 2019). In recent years, zebrafish has gained traction as a model organism for researching disease mechanisms and drug discovery. This led to the development of new methods and a better understanding of its physiology (Rubinstein 2003; Lieschke & Currie 2007; Gore et al. 2018; Böffert et al. 2020). However, in order to effectively use zebrafish as a clinical model system, a better understanding of the role of receptor homologs in this model organism is crucial. This will help to avoid erroneous discoveries in disease research due to potential receptor redundancies. Here, I focused on the role of putative Nodal receptors during early germ layer patterning, but their functionality during later processes, such as fin regeneration, seems to diversify (Jaźwińska et al. 2007).Therefore, it will also be important to further assess the roles of different receptors during later stages of development. To this end, one could apply induction-controlled recombination, for example by using the inducible Cre/loxP system, to abolish specific receptor activity at later time points during development (Hans et al. 2009; Ripoche et al. 2013).

During germ layer patterning in zebrafish embryos, Nodal signaling originates from the yolk syncytial layer and is thought to form a signal gradient into the embryo. It has been proposed that extracellular diffusion regulators can regulate Nodal ligand spread into the embryo (Müller et al. 2013; Rogers & Müller 2019). This idea is supported by the observations that the effective diffusivity of Nodal in a tissue is much lower than its free diffusivity in vitro (Müller et al. 2012; Müller et al. 2013), and that the short Nodal signaling range (van Boxtel et al. 2015) is extended in receptor mutants (Lord et al. 2019). Identifying the endogenous Nodal diffusion regulators in zebrafish embryos is crucial to understand the mechanisms underlying Nodal-mediated axis formation during vertebrate embryogenesis. Nodal receptors have previously been discussed as potential diffusion regulators (Müller et al. 2013; Rogers 2015; Wang et al. 2016; Rogers & Müller 2019). Here, I have examined the impact of different Nodal receptors on Nodal propagation in

the embryo. I found that decreased receptor levels can flatten the Nodal protein gradient that spreads into the embryo by increasing its dispersal range. This indicates that receptor levels can indeed impact Nodal propagation *in vivo*.

Furthermore, my analysis demonstrates that the co-receptor Oep had a bigger effect on Nodal distribution and mobility compared to the putative Type I and Type II Nodal receptors. However, although I investigated several key receptors of the Nodal signaling pathway, it is important to expand the investigation of receptor impact on Nodal propagation onto the other putative Nodal receptors that I did not focus on in the context of this thesis, like the Type II receptors *acvr2a-a* and *acvr2b-b*. Additionally, my findings highlight the redundant functionality of receptors mediating Nodal signaling during embryogenesis. Therefore, further research on the role of receptors on Nodal propagation needs to include the assessment of combinatorial effects of different receptors.

In this thesis, I used the expression of exogenous Nodal constructs to elucidate the effect of receptors on Nodal propagation through the embryo. To determine if these effects also play a role for endogenous Nodal dispersal in the zebrafish embryo, it is crucial to visualize the endogenous distribution of Nodal ligand. A new study now indicates that advances in genome editing will allow for the integration of fluorescent tags into the Nodal and Lefty loci of zebrafish (He et al. 2020). However, the functionality of these transgenic lines still needs further assessment. But, once established, these fluorescently labeled Nodal and Lefty transgenic lines would allow it to study the formation, propagation, and degradation of endogenous protein *in vivo* without the need for exogenous protein expression. Having endogenous Nodal fluorescently labeled, artificial diffusion regulators that bind to the fluorescent tag could be used to slow down Nodal diffusion in the embryo. This would allow for testing whether Nodal diffusivity is necessary for normal embryogenesis. Suitable candidates for this experimental approach would be membrane-tethered nanobodies (Harmansa et al. 2015; Mörsdorf & Müller 2019).

Mathematical models used to describe and simulate germ layer patterning require several parameters, such as protein induction kinetics, degradation rates and diffusion kinetics. But even though the degradation rates and diffusion coefficients of both, Nodal and Lefty, have been experimentally determined (Müller et al. 2012; Müller et al. 2013; Wang et al.

2016), the induction kinetics of Nodal and Lefty as well as the impact of Lefty on Nodal induction kinetics have not been characterized yet. Previous studies have used the injection of recombinant Nodal protein into embryos to measure induction kinetics on a transcription level (Dubrulle et al. 2015), but it is unclear whether they are directly translated into functional protein levels. Injecting zebrafish Nodal and Lefty protein into transgenic fluorescent Nodal and Lefty lines could expand the measurement of these induction kinetics to the translational level, either by correlating changes of fluorescence to protein levels (Soh et al. 2020) or by determining dose-dependent responses in protein levels using western blot analysis. These measurements would allow to integrate the actual induction kinetics into the theoretical models that are used to simulate the proposed mechanisms that underlie the Nodal-Lefty patterning system in greater detail. Ultimately this combination of experimental data with theoretical models could determine whether relay signaling is fast enough to establish the Nodal signaling range during development. Thereby measurements of the induction kinetics could help to distinguish between the “relay” and “hindered diffusion” model.

In summary, I identified and characterized novel putative Nodal receptors in zebrafish and investigated their role in mediating Nodal signaling during early germ layer patterning. Furthermore, this thesis provides experimental evidence that receptor levels can modulate Nodal spreading into the embryo. Taken together, these findings highlight that, although Nodal signaling has been studied in zebrafish for more than twenty years, this signaling pathway has still not been fully explored. The role of receptors needs to be investigated beyond their ability to transduce Nodal signaling into the cell. This will allow for a better understanding of the mechanisms underlying the propagation of signaling during development.

6. Supplementary figures

A **Acvr1b-a**

MLRDGNVAVMPPRRTAVALLALCGLLAVGDALKCNCTACESTGYVCETDGACMASTSYINGQEEQQVRICIPRVSLVPPGQPIYCL
SAKGLLNTHCCYTDFCNSINLQIPNGIADGKGGSWGPVELVAVIAGPVFLFCLLLIVGVLLFQHHQRNYNHRQRLDVEDPSCDHLYLA
KDKTLQDLIFDLSTSGSGSGLPLFVQRTVART*IVLQEIIGKGRFGEVWRGRWRGGDVAVKIFSSREERSWFREAEIYQTIMLRHENIL*
GFIAADNKDNGTWTQLWLVSDYHEHGSLFDYLNHYSVTIEGMIKLSLSAASGLAHLHMEILGTQGKPGIAHRDLKSKNILVKKNGTC
AIADLGLAVRHESITDTIDIAPNQRVGTKRYMAPEVLDETINMKHFDSFKCADIYALGLVYWEIARRCNAGGIHEDYQLPYYDLVPSDP
*SIEEMRKVVCDQRLRPNVPNWWQSYEALRVMGKIMRECWYANGAARLTALRIKKTLSQL*SVQEDIKI

B **Acvr1b-b**

MDPRQILRILIVLSGLNGVCDALLCNCTAPHCERDGFKCETNGACVASTSVIEGQEQHVRLCIHKEKLVPPGQPFYCLSAEGLMNTH
CCYTDYCNSIDLRLPIVTNGPGAGQDWGPVELTAVVAGPVFVLCVLVLLGLFLFQHHQRAYGHRQRLEVEDPSTEHMFLAKDKTLQ
DLIYDLSTSGSGSGLPLFVQRTVART*IVLQEIIGKGRFGEVWRGKWRGGDVAVKIFSSREERSWFREAEIYQTIMLRHENILGFIAAD*
NKDNGTWTQLWLVSDYHENGSLFDYLNRYSVTIEGMIKLALSAASGLAHLHMEILGTQGKPGIAHRDLKSKNILVKKNCTCAIADLGL
AVRHESITDTIDIAPNQRVGTKRYMAPEVLEESINMRHFDSFKCADIYALGLVYWEIARRCNAGGIHEEYQLPYYDLVPSDPSIEEMR
*KVVCDQRLRPNIPNWWQSYEALRVMGKIMRECWYANGAARLTALRIKKTL*SQLSVDEDLKI

C **Acvr1c**

MSHPRCSDAALFIFTFVQLTAALKCVCHLCVNHTCETEAEGACWNSVMLINGKEETVKSCVSPSELKGQVFCYSSRNVSKRNCCF
TDFCNNETLHLNPEQPPEDSGWSQLEVAAVILVPSCLVCVGVMLGVCAIQNLRCTHIKSLKQDPEEPLDDPTLVSPDKCLKELIYDM
STSGSGSGLPLLVQRTIART*IVLQETIGKGRFGEVWRGKWRGEDVAVKIFSSRDERSWFREAEIYQTIMLRHDNILGFIAADNKDNGS*
WTQLWLVSEYHEHGSLFDYLNRFTVSVEGMIVLALSIASGIAHLHMEIIGTQGKPAIAHRDIKSKNILVKKNGAAVIADLGLAVKHDSNT
NTIDIPINHRVGTKRYMAPEILDDSINMSSFESFKRADIYSLSLVFWELARRCSIQGIHEDFQLPYYDQVQSDPSLDDMRRVVCEQKL
*RPNIPNQWQSCEALRVMGKIMRECWHANPAARLTALRVKKTISQVTVV*KDVKE

D **Acvr2a-a**

MGPATKLAFGVFLISCSSGAILGRSETQECVFYNYNPSLENRGNRSGIEPCVGDKDKRLHCFATWRNVSGTVEIVKQGCWLDDVN
CYDSTECVEKKEDPDVFFCCCEGNMCNEKFFYNPNTAPVQTTSNPLTQKPPLFSTLLYSIVPIMGIAAIVLLSFWMYRHHKLAYPPVL
VPTQDPGPMPPSPTLVQKP*LQLLEIKARGRFGCVWKAQLLNDYVAVKIFPIQDKLSWQNEYDIYNIPGMRHENILQFIGAEKRGSNL*
DIELWLITAYHEKSSLTDYLKANVVTWNELCHIAQTMARGLAYLHSDFPGHRDGHKPAIAHRDFKSKNVLLKTNLTACIADFGLALKFE
AGKSAGDTHGQVGTRRYMAPEVLEGAINFQRDAFLRIDMYAVGLVLWELAARCTASDGPVDEYMLPFEEEVGQHPTLEDMQEVVV
*HKKLRPTLRECWQKHPGLAMLCETIEECWDHEAEARLSAGCVEERVV*QMQRQTSVSAPEEIVTVVTMVTNVDYPPKESSL

E **Acvr2a-b**

MASHWTNWKQRKYGGAILGRSETQECVYYNVSWEKDGTNRSGTESCYGEKDKRRHCFSTWKNRSGTIEMVKQGCWLDDVNCY
DSSECVERKENIDVFFCCCEGNLCNQKFHYNPETVEPTLNPVPPKPDLFPTLLYSLLPIMAVAVILFISFWMYRHLKLTYPPLLVPSQD
PGLTPPSPLLGQKP*LQLLELKARGRFGCVWKAQLLSEAVAVKIFPVQNKQSWQNEYEIYNASGMKHENLLHFIGAEKRGNGVDIEL*
WLITTYHEKGSLTDFLKANVLSWNELCLIAQTFVRGLAYLHEDIPNLKDGHKPAIAHRDIKSKNVLLKSDLTACIADFGLALKFEAGKST
GDTHGQVGTRRYMAPEVLEGAISFQRDAFLRIDMYAAGLVLWELATRCTAADGPVDEFCLPFEEEAGLHPSLEDMQDVVVHKKLR
*PIFREHWLKHTGLSLLCETMEECWDHEAEARLSAGCVEERII*SMQRSTSIISPDDILSVVTMVTNLDFPPKESSL

F **Acvr2b-a**

MFASLLTLALLLATFAADPSHGEVETRECLYYNVNWEVEKTNRSGVERCEGEKDKRSHCYASWRNNSGSIQLVKKGCWLDDFNC
YDRQECVATEENPQVFFCCCEGNFCNERFTHLPDISGPVISPPPVSPSLLNVLVYSLLPLSMLSMAVLLAFWMYRHRKPPYGHVDV
NEDPGPSPPSPLVGLKPLQLLELKARGRFGCVWKAQMINEYVAVKIFPIQDKLSWQNEREMFSTPGMKHDN*LLRFIAAEKRGSNLE*
MEFWLITEFHERGSLTDYLKGNAVSWADLCVIAESMACGLAYLHEDVPRSKGEGPKPAIAHRDFKSKNVMLKMDLTAVIGDFGLAVR
FEPGKPPGDTHGQVGTRRYMAPEVLEGAINFQRDSFLRIDMYAMGLVLWELVSRCKAADGPVDEYMLPFEEEIGQHPSLEDLQDA
*VVHKKLRPAFKDCWLKHSGLCQMCETMEECWDHDAEARLSAGCVQERISQIRRV*SSSTSDCLFSMVTSLTNVDLPPKESSI

G **Acvr2b-b**

MFVPWLAFALVWCTGVSHAEVATRECVYYNDNWRTEKTNQSGFERCEGEKDKRLHCYASWLNSTGTIRLVKKGCWLDDFNCYD
RQECVATEESPQVFFCCCEGNYCNEKFTHLPEAIAPAVKIQPPQPGPSLFGILVYSLLPLAILSLALVLACWTYHQRKPPYRHVDIGQ
DAGLPPPSPLVGLKP*LQLLELKARGRFGCVWKAQLLSEYVAVKIFPIQDKQSWQNERDIYLTEGFKHENILHYISAEKRGTNLQMEL*
WLVTEFHERGSLTDYLKGNVVSWPQLCHISASMSRGLAYLHEDLPYRAEGPKPAIAHRDFKSKNVLLKMDLTAVIADFGLAVRFEPG
KPPGDTHGQVGTRRYMAPEVLEGAINFQRDSFLRIDMYALGLVLWELVSRCTASDGPVGEYQLPFEEEVGQHPSLEDLQDAVVHK
*KMRPVFKDCWVKHQGLSQLCETIEECWDHDAEARLSAGCVEERISTI*SKSNNTLNTSTSECLLSMLTSHSDTDLPPKDSST

Supplementary Figure 1: Protein domains identified in putative Nodal receptors. (A-G) Amino acid sequences of the putative Nodal receptors Acvr1b-a, Acvr1b-b, Acvr1c, Acvr2a-a, Acvr2a-b, Acvr2b-a and Acvr2b-b. The signal sequence is marked in bold, the Activin receptor domain in red, the transmembrane domain is underlined, the GS-domain is marked in blue and the protein kinase domain is marked in italics.

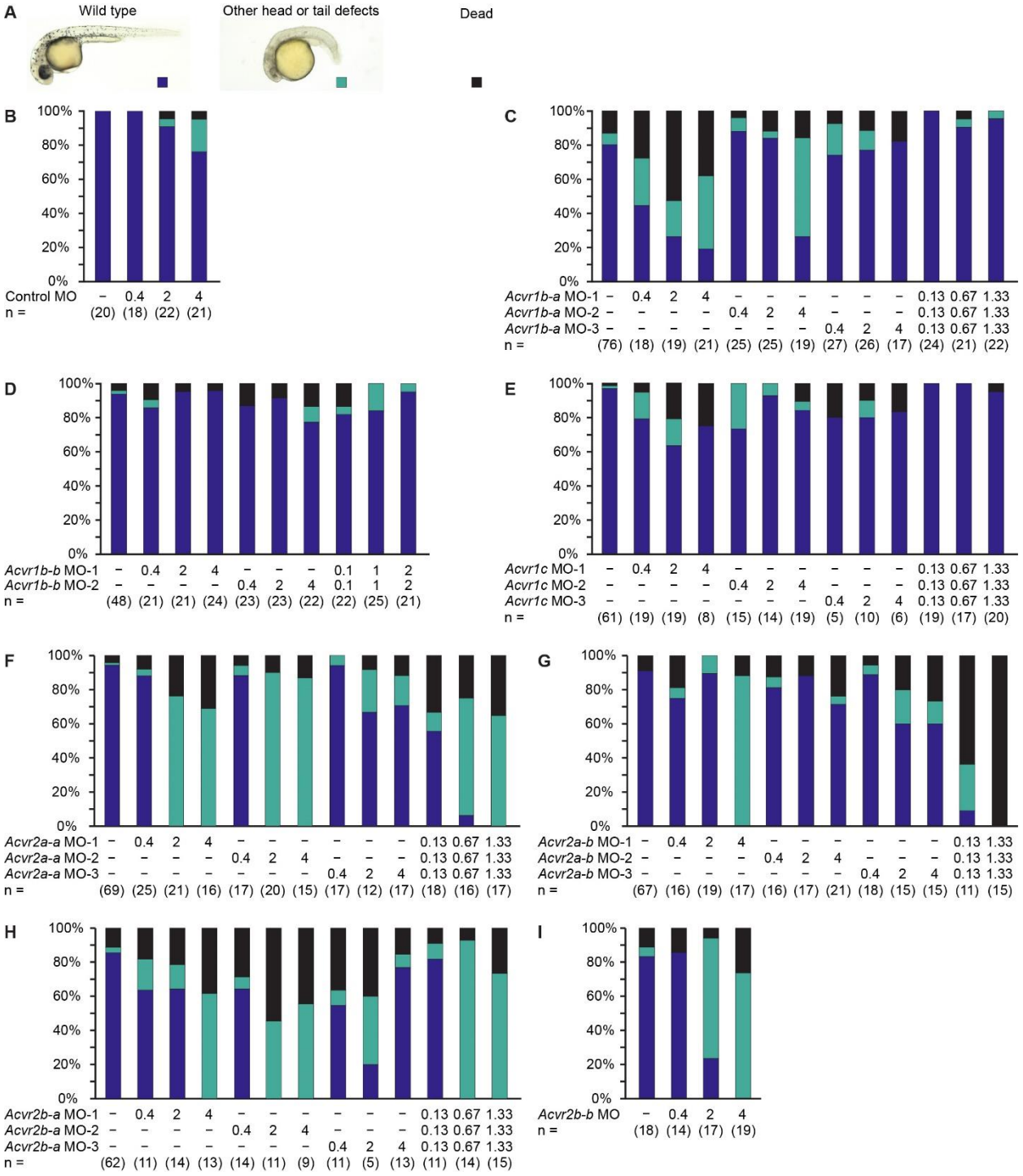

Supplementary Figure 2: Phenotypes of 1 day old embryos with morpholino mediated knockdown of Type I and Type II Nodal receptors. (A) Phenotype classification categories. **(B-I)** Phenotypes after injection of the indicated concentrations of control **(B)**, *acvr1b-a* **(C)**, *acvr1b-b* **(D)**, *acvr1c* **(E)**, *acvr2a-a* **(F),** *acvr2a-b* **(G)**, *acvr2b-a* **(H)**, and *acvr2b-b* **(I)** morpholinos into wild type embryos.

A

B

	acvr1b-a	*acvr1b-b*	*acvr1c*	*acvr2a-a*	*acvr2a-b*	*acvr2b-a*	*acvr2b-b*	*acvr2b-a; acvr2b-b*
acvr1b-a								
acvr1b-b								
acvr1c								
acvr2a-a								
acvr2a-b								
acvr2b-a								
acvr2b-b								
acvr2a-a; acvr2a-b								

Supplementary Figure 3: Summary: Phenotypes of 1 day old embryos with combinatorial knockdown of Type I and Type II receptors. (A) Phenotype classification categories. Arrow marks fusion of the eye field, arrowheads indicate the otic vesicle. **(B)** Table of phenotypes after 24 hpf for all tested receptor knockdown combinations. Light grey color indicates untested receptor combinations. Receptor phenotypes were attributed to the different classification categories depending on which phenotype was most often observed per knockdown treatment.

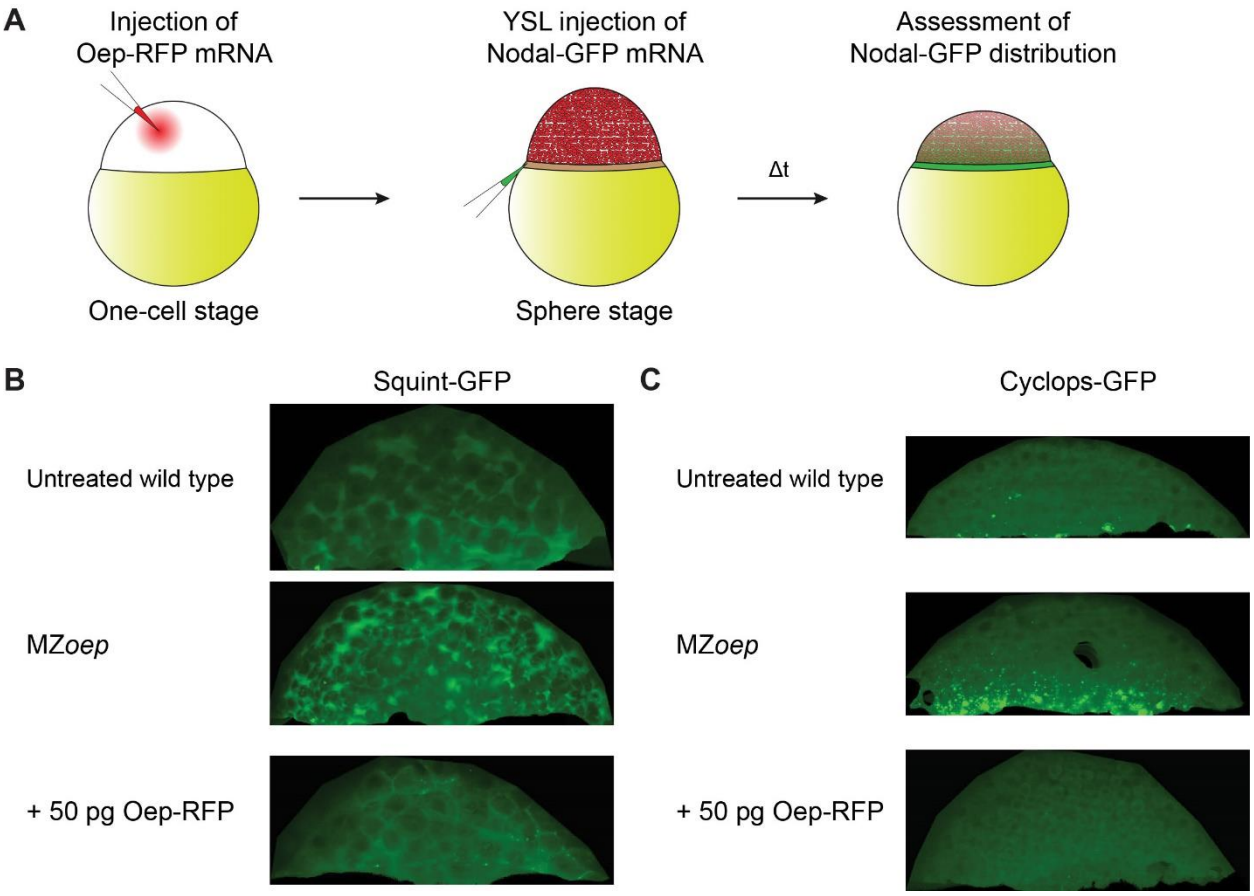

Supplementary Figure 4: Uncoupling Nodal-GFP secretion from co-receptor Oep. (A) Schematic illustration of the assay to express Nodal-GFP independently of Oep processing. One-cell stage wild type embryos were injected with 50 pg of *oep-RFP* mRNA. Later, 100 pg of *squint-GFP* or *cyclops-GFP* encoding mRNA are injected into the YSL of sphere stage embryos and subsequently imaged to measure the Nodal localization. Embryos were imaged ~2 hpi for squint-GFP and ~ 4 hpi for cyclops-GFP mRNA injections. **(B)** Localization of Squint-GFP in wild type, *MZoep*$^{tz57/tz57}$ and Oep-RFP overexpressing embryos. **(C)** Localization of Cyclops-GFP in wild type, *MZoep*$^{tz57/tz57}$ and Oep-RFP overexpressing embryos.

7. Material and Methods

Fish lines and husbandry

All procedures were executed in accordance with the guidelines of the State of Baden-Württemberg and approved by the Regierungspräsidium Tübingen (35/9185.46-5, 35/9185.81-5). MZ*oep*^{tz57} embryos were generated as previously described (Zhang et al. 1998; Gritsman et al. 1999). The wild type strain Tü was used for the generation of the *acvr1c* mutant allele. For the generation of *acvr1b-a* and *acvr2b-a* mutants, the wild type strain TE was used. *acvr2a-a*^{sa34654}, *acvr2a-b*^{sa18285} mutants were obtained from the EZRC. For all experiments, maternal-zygotic receptor mutant embryos were used. The fish strain TE was used as a wild type control in all experiments.

Phylogenetic analysis

For the phylogenetic analysis, human and mouse protein sequences of the Type I receptors ACVR1B and ACVR1C as well as protein sequences of the Type II receptors ACVR2A and ACVR2B were used for BLAST queries in the UniProt database to identify zebrafish homologs. The alignment of human, mouse and zebrafish sequences was performed using Clustal Omega (RRID: SCR 002380) (Madeira et al. 2019). The phylogenetic tree was calculated with neighbor-joining-algorithm using the blosum62 matrix. Jalview version 2.10.3b1 was used for visualization (Waterhouse et al. 2009). Branch length indicates evolutionary distance.

Whole-mount in situ hybridization

For synthesis of *acvr1b-a, acvr1b-b, acvr1c, acvr2a-a, acvr2a-b, acvr2b-a* and *acvr2b-b* probes for *in situ* hybridization assays, full-length receptor mRNA was cloned from shield stage cDNA into TOPO Blunt plasmids (primers listed in Table 1). *In situ* probes were synthesized using SP6 or T7 polymerase (Roche) and digoxigenin (DIG)-modified ribonucleotides (Roche). RNA probes were purified using the RNeasy MinElute Cleanup kit (Qiagen) according to the manufacturer's protocol. Embryos were fixed in 4% formaldehyde and transferred into methanol (MeOH) for storage. They were processed for *in situ* staining as previously described (Thisse & Thisse 2008), but without proteinase K treatment and without pre-absorption of the anti-DIG antibody (11093274910, Roche).

Table 2: Primers used for receptor cloning.

Primer name	Primer sequence (5'->3')	Digest
acvr1b-a - GFP Rev. cloning into pCS2+	GAGGCTCGAGAGGCCTTGAATTCTCACTTGTACAGCTCGTCCATG	EcoRI / XhoI
acvr1b-a - GFP splice site Forw.	CCAAGAAGACATTAAGATCTCTGCAATGGTGAGCAAGGGCGAGG	-
acvr1b-a - GFP splice site Rev.	CCTCGCCCTTGCTCACCATTGCAGAGATCTTAATGTCTTCTTGG	-
acvr1b-a - mCherry splice site Rev.	GGTGGCGACCGGTGGATCGCCCAGGATCTTAATGTCTTC	-
acvr1b-a Forw. cloning from cDNA	ATGCTAAGAGATGGGAATGTTGC	-
acvr1b-a Forw. cloning into pCS2+ vector	TCCCATCGATGCCACCATGCTAAGAGATGGGAATGTTGC	ClaI
acvr1b-a Rev. cloning from cDNA	TCAGATCTTAATGTCTTCTTGGACG	-
acvr1b-a Rev. cloning into pCS2+	AGAGGCCTTGAATTCGATCAGATCTTAATGTCTTCTTGGACG	StuI
acvr1b-a splice site	GGTGGCGACCGGTGGATCGCCCAGGATCTTAATGTCTTC	-
acvr1b-b - GFP splice site Forw.	TGGACGAGGATCTCAAAATCATGGTGAGCAAGGGC	-
acvr1b-b - GFP splice site Rev.	GCCCTTGCTCACCATGATTTTGAGATCCTCGTCCA	-
acvr1b-b - mCherry splice site Rev.	GGTGGCGACCGGTGGATCGCCCAGGATTTTGAGATCCTCGTCCA	-
acvr1b-b Forw. cloning from cDNA	ATGGACCCACGGCAAATC	-
acvr1b-b Forw. cloning into pCS2+ vector	GATTCGAATTCGCCACCATGGACCCACGGCAAATC	EcoRI
acvr1b-b Rev. cloning from cDNA	TCAGATTTTGAGATCCTCGT	-
acvr1b-b Rev. cloning into pCS2+ vector	AGAGGCTCGAGCCTTCAGATTTTGAGATCCTCGTCCA	XhoI
acvr1c - inverse pericam splice site Forw.	GTGGTCAAGGATGTTAAAGAACTGGGCGATCCACCGGTCGCCACCGGCTA	-
acvr1c - inverse pericam splice site Rev.	TAGCCGGTGGCGACCGGTGGATCGCCCAGTTCTTTAACATCCTTGACCAC	-
acvr1c Forw. cloning from cDNA	ATGTCTCATCCCAGGTGCTCAG	-
acvr1c Forw. cloning into pCS2+ vector_1	CATGGGATCCGCCACCATGTCTCATCCCAGGTGCTCAG	BamHI
acvr1c Forw. cloning into pCS2+ vector_2	GATCCGCCACCATGTCTCATCCCAGGTGCTCAG	BamHI
acvr1c Rev. cloning from cDNA	TTCTTTAACATCCTTGACCACAGTCAC	-
acvr1c Rev. cloning into pCS2+ vector _2	GAGGCTCGAGTTATTCTTTAACATCCTTGACCA	XbaI
acvr1c Rev. cloning into pCS2+ vector_1	TTCTTTAACATCCTTGACCACAGTCACCTCGAGCATG	AvaI / XhoI
acvr1c splice site Forw.	GTGGTCAAGGATGTTAAAGAACTGGGCGATCCACCGGTCGCCACCGGCTA	-
acvr1c splice site Rev.	TAGCCGGTGGCGACCGGTGGATCGCCCAGTTCTTTAACATCCTTGACCAC	-
acvr2a-a Forw. cloning from cDNA	ATGGGACCTGCAACAAAGCT	-
acvr2a-a Forw. cloning into pCS2+ vector	AGGATCCCATCGATGCCACCATGGGACCTGCAACAAAGCT	ClaI / BamHI
acvr2a-a GFP splice site Forw.	CCCCAAAGGAGTCTAGTCTAATGGTGAGCAAGGGCGAGGA	-
acvr2a-a GFP splice site Rev.	TCCTCGCCCTTGCTCACCATTAGACTAGACTCCTTTGGGG	-
acvr2a-a mCherry splice site Rev.	GGTGGCGACCGGTGGATCGCCCAGTAGACTAGACTCCTTTGGGG	-
acvr2a-a Rev. cloning from cDNA	TCATAGACTAGACTCCTTTG	-
acvr2a-a Rev. cloning into pCS2+ vector	TCTAGAGGCTCGAGAGGCCTTCATAGACTAGACTCCTTTG	StuI
acvr2a-b - GFP splice site Forw.	CTAAAGAGTCCAGCCTAATGGTGAGCAAGGGC	-
acvr2a-b - GFP splice site Rev.	GCCCTTGCTCACCATTAGGCTGGACTCTTTAG	-
acvr2a-b - mCherry splice site Rev.	GGTGGCGACCGGTGGATCGCCCAGTAGGCTGGACTCTTTAG	-
acvr2a-b Forw. cloning from cDNA	ATGGCGAGCCACTGGACAAACT	-
acvr2a-b Forw. cloning into pCS2+ vector	ATCCCATCGATGCCACCATGGCGAGCCACTGGACAAACTGGAAGCAGCGA AAATATGGAGGTGCGATTCTGGGCCGCTCG	BamHI
acvr2a-b Rev. cloning from cDNA	TCATAGGCTGGACTCTTTAG	-
acvr2a-b Rev. cloning into pCS2+ vector	CCTTGAATTCGATCATAGGCTGGACTCTTTAG	EcoRI

acvr2b-a - GFP splice site Forw.	CAAAGAGTCCAGCATCCTGGGCGATCCACCGGTCGCCACC	-
acvr2b-a - GFP/mCherry splice site Rev.	GGTGGCGACCGGTGGATCGCCCAGGATGCTGGACTCTTTG	-
acvr2b-a Forw. cloning from cDNA	ATGTTCGCTTCTCTGCTCACTTT	-
acvr2b-a Forw. cloning into pCS2+ vector	AGGATCCCATCGATGCCACCATGTTCGCTT	ClaI
acvr2b-a Rev. cloning from cDNA	TCAGATGCTGGACTCTTTGGGC	-
acvr2b-a Rev. cloning into pCS2+ vector	CACTATAGTTCTAGATCAGATGCTGGACTCTT	XbaI
acvr2b-b - GFP splice site Forw.	GCCCAAAGACTCCAGCACCATGGTGAGCAAGGGC	-
acvr2b-b - GFP splice site Rev.	GCCCTTGCTCACCATGGTGCTGGAGTCTTTGGGC	-
acvr2b-b - mCherry splice site Rev.	GGTGGCGACCGGTGGATCGCCCAGGGTGCTGGAGTCTTTGGGC	-
acvr2b-b Forw. cloning from cDNA	ATGTTTGTTCCCTGGCTGGC	-
acvr2b-b Forw. cloning into pCS2+ vector	GATCCCATCGATGCCACCATGTTTGTTCCCTGGCTGGC	ClaI
acvr2b-b Rev. cloning from cDNA	TCAGGTGCTGGAGTCTTTGG	-
acvr2b-b Rev. cloning into pCS2+ vector	GAGGCCTTGAATTCGATCAGGTGCTGGAGTCTTTGG	XhoI
GFP Rev. cloning into pCS2+ vector	GCCTTGAATTCTTACTTGTACAGCTCGTCCATGC	EcoRI
inverse pericam - zFKBP1b splice site Forw.	GGAGTACAACGGTACCGGGATGGGTGTTGAGGTTG	-
inverse pericam - zFKBP1b splice site Rev.	CAACCTCAACACCCATCCCGGTACCGTTGTACTCC	-
inverse pericam linker Forw.	CTGGGCGATCCACCGGTCGCCACCGGCTACAACAGCACC	-
mCherry Forw.	GTGAGCAAGGGCGAGGAGGATAAC	-
mCherry Rev. cloning into pCS2+ vector	TAGAGGCTCGAGTTACTTGTACAGCTCGTCCATGC	XhoI
mCherry splice site Forw.	CTGGGCGATCCACCGGTCGCCACCGTGAGCAAGGGCGAGGAG	-
zFKBP1b Rev.	CTCCAATTTCAGCAGCTCTAC	-
zFKBP1b Rev. cloning into pCS2+ vector	GGCTCGAGAGGCCTTGAATTCCTACTCCAATTTCAGCAG	EcoRI / XhoI

Plasmids and *mRNA synthesis*

Full-length receptor-encoding sequences were amplified from cDNA of shield stage wild type TE embryos and cloned into pCS2+ vectors (primers listed in Table 1, plasmids are listed in Table 3). C-terminal tagging of the receptors with mCherry was done using a splicing PCR (primers listed in Table 2) (Higuchi et al. 1988; Ho et al. 1989; Heckman & Pease 2007). For mRNA synthesis, the mMESSAGE mMACHINE® SP6 Transcription Kit (AM1340; Invitrogen) was used according to the manufacturer's protocol. Synthesized RNA was purified with the RNAeasy mini Kit (Qiagen) and dissolved in nuclease-free water.

Table 3: Plasmids used in this thesis.

Laboratory #	Gene	Backbone	Purpose	Reference
583	*acvr1b-a*	pCS2+	mRNA synthesis	cloned by myself
195	*acvr1b-a*	pCR-Blunt II-TOPO	in situ probe	cloned by Maria Almuedo-Castillo
298	*acvr1b-a mCherry*	pCS2+	mRNA synthesis	cloned by Maria Almuedo-Castillo
536	*acvr1b-b*	pCS2+	mRNA synthesis	cloned by myself
515	*acvr1b-b*	pCR-Blunt II-TOPO	in situ probe	cloned by myself
537	*acvr1b-b-GFP*	pCS2+	mRNA synthesis	cloned by myself
81	*acvr1c*	pCS2+	mRNA synthesis / in situ probe	Cloned by Sarah Keim
87	*acvr1c IP*	pCS2+	mRNA synthesis	Cloned by Sarah Keim
513	*AcvR2aa*	pCR-Blunt II-TOPO	in situ probe	cloned by myself
527	*acvR2a-a*	pCS2+	mRNA synthesis	cloned by myself
581	*acvR2a-a-mCherry*	pCS2+	mRNA synthesis	cloned by myself
528	*acvR2a-b*	pCS2+	mRNA synthesis	cloned by myself
582	*acvR2a-b-mCherry*	pCS2+	mRNA synthesis	cloned by myself
495	*acvr2b-a*	pCS2+	mRNA synthesis	cloned by myself
529	*acvR2b-b*	pCS2+	mRNA synthesis	cloned by myself
514	*acvR2b-b*	pCR-Blunt II-TOPO	in situ probe	cloned by myself
580	*acvR2b-b-mCherry*	pCS2+	mRNA synthesis	cloned by myself
80	*cyclops-GFP*	pCS2	mRNA synthesis	(Müller et al. 2012)
47	*oep-RFP*	pCS2	mRNA synthesis	
103	*squint-dendra2*	pCS2	mRNA synthesis	(Müller et al. 2012)
49	*squint-GFP*	pCS2	mRNA synthesis	(Müller et al. 2012)

Microinjections

For mRNA, sgRNA and morpholino injections, embryos were injected at the one- or two-cell stage with the indicated amounts in a total of 1 nl. Injected embryos were incubated at 28˚C, and unfertilized embryos were discarded at 4-5 hpf. For fixation, imaging and YSL injections, the embryos were dechorionated using 0.1 mg/ml Pronase (Roche) in 5 ml embryo medium (Rogers 2015).

For Nodal gradient analysis, 2 nl of an injection mix containing 100 pg of *Squint-GFP* or *Cyclops-GFP* and 0.5 ng of Alexa Fluor™ 647 dextran (D22914, Invitrogen) was injected

into the YSL of sphere stage embryos. Imaging of YSL-injected embryos was started 2 hpi for *Squint*-GFP injections and 4 hpi for *Cyclops*-GFP injections.

Mutant generation

acvr1b-a, *acvr1c* and *acvr2b-a* mutants were generated using the CRISPR/Cas9 system (Gagnon et al. 2014). Target sequences for guide RNAs were chosen using CHOP-CHOP (Montague et al. 2014). sgRNAs targeting *acvr1b-a* (mix of sgRNAs GCTACAGCAGTTCGTCGAGG and GGATTACTAGCGGTCGGCGA) and *acvr1c* (AGCGCTGCATCTGAGCACCT) were synthesized as described previously (Gagnon et al. 2014). *acvr2b-a* (GTTCGCTTCTCTGCTCACTT) sgRNA was procured from IDT. 400 pg of Cas9-encoding mRNA (from MLM3613, *Addgene*) and 150 pg of sgRNA were co-injected into one- or two-cell stage wild type embryos. CRISPR efficiency was tested using a T7 Endonuclease I digestion assay (Gagnon et al. 2014) with the primers listed in Table 4.

Table 4: Primers for mutant genotyping.

Mutant	Target	Forward primer	Reverse primer
acvr1b-a^{t03pm}	Exon 2	TCGCTTGTCAATATCACACACA	CTCTCTCTCCACACACCATCAG
acvr1c^{t06pm}	Exon 1	TCTGTCTACGTGTTGTCGCTTT	AAAGTTGGTGTGTGCTGACAGT
acvr2a-a^{sa34654}	Exon 2	AACTACAACCCCAGCTTGGAGAA	TTTGAAAATTCTTTGAAATCTTT
acvr2a-b^{sa18285}	Exon 1	TTTCCAGTTGTGTTTGATTCCATGT	ACAAGTTTCCCTCGCAGCAG
acvr2b-a^{t08pm}	Exon 1	GTGGTGTGTGAGAGTGTGTGTG	CAGGAGCATTTTAACAACACGA

Genotyping

Genomic DNA was isolated from caudal fin tissue of adult zebrafish using the “hotshot” method (Meeker et al. 2007), and regions of interest were amplified using standard PCR conditions and the primers listed in Table 4. PCR amplicons were prepared for direct use in sequencing reactions by treatment with ExoI and rSAP (NEB), and the respective amplification primers were used in separate sequencing reactions. Mutations in the first generation were identified using PolyPeakParser and Hetindel (Hill et al. 2014, RRID:SCR_018922). For later genotyping analysis, Lasergene Seqman Pro 14 was used. To reduce the likelihood of off-target-effects, mutants were outcrossed to wild type TE fish at least once before in-crossing of heterozygotes to obtain homozygous fish.

Morpholino antisense oligonucleotides

For each receptor, several morpholinos were designed that target splice sites or the region surrounding the ATG start codon (Table 5). Morpholinos were obtained from GeneTools (Philomath, OR) and injected into 20 to 30 wild type TE embryos at the one-cell stage using the amounts indicated in the figures. Embryos were assessed at shield stage and 1 dpf. After each assessment, unfertilized and dead embryos were discarded.

Table 5: Morpholino sequences used for phenotype analysis. ATG start site targets are underlined.

Receptor	Morpholino sequence (5'->3')	Target site	Reference
acvr1b-a MO-1	CTGCAACATTCCCATCTCTTAGCAT	ATG start site	(Jaźwińska et al. 2007)
acvr1b-a MO-2	GTTTGGCCTGTACTGCTACCATTG	e2i2 splice site	
acvr1b-a MO-3	ATAAACATGCAACTTACCAGACCCT	e3i3 splice site	
acvr1b-b MO-1	CATCCTTACAGGACTCCCATTGCAC	ATG start site	
acvr1b-b MO-2	CAAAGATTTGTTTTCAGCACCTCCA	e7i7 splice site	
acvr1c MO-1	GATGAGACATGACATCTGTCACTTA	ATG start site	
acvr1c MO-2	TACTATTTTGTCCTGTCTTACCTGG	e2i2 splice site	
acvr1c MO-3	TTAATGGGCACAGCCAGCTCTCACC	e3i3 splice site	
acvr2a-a MO-1	GCAGGTCCCATTTTTTCACTCTTCT	ATG start site	(Albertson et al. 2005)
acvr2a-a MO-2	AGCAGTAGGGAATACCTGTCATAGC	e2i2 splice site	
acvr2a-a MO-3	TCGCTGAATGGAGCCTTACTCTGAA	e3i3 splice site	
acvr2a-b MO-1	TCGATGGTCCCCGAGCGGTTCTTC	Putative 5'UTR	
acvr2a-b MO-2	TGGCTGCACACAAACACAGATTAAT	splice site	(Dogra et al. 2017)
acvr2a-b MO-3	TGACAGAAGTATTTACCTGTGACGG	e3i3 splice site	
acvr2b-a MO-1	GCAGAGAAGCGAACATATTCCTTT	ATG start site	(Albertson et al. 2005)
acvr2b-a MO-2	TGAGCAGAGAAGCGAACATATTCCT	ATG start site	(Dogra et al. 2017)
acvr2b-a MO-3	AATGTTTAAGAGAGTCACCTGGTTC	e3i3 splice site	
acvr2b-b MO	AGCCAGCCAGGGAACAAACATATTC	ATG start site	(Dogra et al. 2017)

qRT-PCR

For qRT-PCR experiments, single embryos were collected at shield stage and total RNA was isolated using NucleoZol (740404.200; Macherey-Nagel) according to the manufacturer's protocol. 100 ng of RNA was used for cDNA synthesis with SuperScript™ III Reverse Transcriptase (18080044, Invitrogen) according to the manufacturer's

protocol. qRT-PCR was performed with Platinum SYBR Green qPCR SuperMix-UDG (1173304, Invitrogen) on a CFX Connect Real-Time System (BIORAD). 2 µl of 1:5 diluted cDNA was used as a template. Primers for qRT-PCR analysis are listed in Table 6, and *eF1A* was used as an internal control. Technical duplicates and biological triplicates were performed for each sample.

Table 6: qRT-PCR primers.

Target	Forward primer (5'->3')	Reverse primer (5'->3')
eF1A	AGAAGGAAGCCGCTGAGATGG	TCCGTTCTTGGAGATACCAGCC
acvr1b-a	CGCCATGAAAACATCTTGG	GTGTCCATGTGCCATTGTCT
acvr1b-b	CTCTCCACCTCAGGATCAGG	GTACGAGCCACGGTCCTTT
acvr1c	GAGATTATTGGCACCCAAGG	AACCAGGATGTTCTTTGACTTTATG
acvr2a-a	GGTGTCCTCACAACATTG	TCACCGGTCACTCGACAC
acvr2a-b	GTGACACACACGGACAGGTT	AAACTGATCGCTCCTTCCAG
acvr2b-a	CAAACCAGCCATCGCACA	TCACACCAGTCTACGACC
acvr2b-b	ACACGTCGACATCGGACAG	AGGCTTCAGTCCAACCAGAG

pSmad2/3 immunostainings

For pSmad2/3 immunofluorescence stainings, embryos were fixed in 4% formaldehyde in PBS overnight at 4˚C. Embryos were dehydrated in 100% MeOH and stored at -20˚C. For staining, the embryos were incubated in acetone (Roth, 5025.5) for 7 min, washed three times for 5 min with PBST (PBS + 0.1% Tween 20), blocked for at least 1 h with 10% FBS (Biochrom) in PBST and incubated with 1:5000 rabbit anti-pSmad2/3 primary antibody (Cell Signaling Technologies, 8828) in blocking solution at 4°C overnight. The following day, embryos were washed 8 times for 15 min with PBST, blocked with blocking solution for at least 1 h, and incubated with 1:500 goat anti-rabbit HRP secondary antibody (Jackson ImmunoResearch, 111-035-003) in blocking solution at 4°C overnight. Embryos were then washed 8 times for 15 min with PBST and incubated once in TSA 1x amplification buffer (TSA Plus Fluorescein Kit, Perkin Elmer, NEL741001KT) for 15 min. For staining, embryos were incubated in 75 µl 1:75 fluorescein-TSA in 1x amplification buffer for 45 min. Embryos were washed three times for 5 min with PBST, 30 min with MeOH and washed two times more with PBST before incubation in 1:5000 DAPI in PBST at room temperature for at least 1 h, then they were washed at least three

times with PBST. Embryos were transferred into MeOH and stored at -20˚C before imaging.

Imaging

Brightfield images for phenotype documentation were taken using an Axio Zoom.V16 (ZEISS) microscope with a PlanNeoFluar Z 1x objective.

Images of fixed and live embryos were obtained using a Lightsheet Z.1 microscope (ZEISS). For mounting, the samples were taken up in 1.5 % low-melting point agarose (50080, Lonza) with a size 3 glass capillary sample holder (ZEISS). If not noted otherwise, embryos were imaged using a W Plan-Apochromat 20x objective, 0.7 zoom and 5 µm distance between z-slices. For imaging of pSmad2/3 immunostainings, embryos were imaged from different angles using a 488 nm laser at 2% power with 100 ms exposure time. For DAPI stainings, embryos were imaged using a 405 nm laser at 10% laser power with 70 ms exposure time. For YSL injections, 15 slice z-stacks were imaged using the 405 nm laser with 100% laser power and 70 ms exposure time. Additionally, embryos were imaged with a 638 nm far-red laser at 1% laser power and 20 ms exposure time for detection of Alexa Fluor 647 dextran.

FRAP and FDAP measurements were performed using a LSM 780 NLO confocal microscope (ZEISS) with an LD C-Apochromat 40x/1.1 W Korr objective. For imaging, embryos were mounted in 1.5 % low-melting point agarose in glass-bottom petri dishes (P35G-1.5-20-C, MatTek Corporation). After solidification, the agarose was covered with embryo medium to protect the embryos from drying out. FRAP and FDAP measurements were performed as previously described (Bläßle et al. 2018).

YSL injection image analysis

Images obtained from embryos that had been injected with Nodal mRNA into the YSL were analyzed using Fiji (Schindelin et al. 2012). To mask fluorescent signal in the YSL from analysis, the far-red channel was converted into a mask with the mean thresholding algorithm. 10 marginal z-slices of the GFP channel were then used for a maximum intensity projection. Before the region of interest around the embryo was defined, the maximum intensity projections were rotated, so that the YSL was on the left, parallel to the image margin. Pixels outside of the embryo were set to N/A to avoid potential dilution

effects when averaging intensities. For Squint-GFP, the “plot profile” function was used to extract the averaged intensities from the embryo. Background levels, which were determined by measuring uninjected embryos, were subtracted from the gradient profiles. The profiles were normalized following the procedure described in (Gregor et al. 2007) with the model $I_n(x) = A_n \bar{c}(x) + b_n$, relating the mean intensity profile $\bar{c}(x)$ of all data points to each embryo’s intensity profile $I_n(x)$ through the embryo-specific proportionality constant A_n and the non-specific background b_n. A_n and b_n were determined by minimizing the sum of squared differences between the model and the intensity profiles using the function *fminsearch* in MATLAB 7.10.0.

For Cyclops-GFP, the Fiji “find maxima” function was used to identify Cyclops-GFP puncta in the embryo. Uninjected embryos were used to verify that this approach only identified single maxima in order to exclude artifacts. The xy-coordinates of the puncta were extracted using the function “Measure”, and the distribution of puncta as a function of distance from the YSL was plotted.

8. References

Albertson, R. C., Payne-Ferreira, T. L., Postlethwait, J., & Yelick, P. C. (2005). Zebrafish acvr2a and acvr2b exhibit distinct roles in craniofacial development. *Dev Dyn, 233*(4), 1405-1418. doi:10.1002/dvdy.20480

Almuedo-Castillo, M., Bläßle, A., Mörsdorf, D., Marcon, L., Soh, G. H., Rogers, K. W., . . . Müller, P. (2018). Scale-invariant patterning by size-dependent inhibition of Nodal signalling. *Nat Cell Biol, 20*(9), 1032-1042. doi:10.1038/s41556-018-0155-7

Andersson, O., Korach-Andre, M., Reissmann, E., Ibanez, C. F., & Bertolino, P. (2008). Growth/differentiation factor 3 signals through ALK7 and regulates accumulation of adipose tissue and diet-induced obesity. *Proc Natl Acad Sci U S A, 105*(20), 7252-7256. doi:10.1073/pnas.0800272105

Aoki, T. O., Mathieu, J., Saint-Etienne, L., Rebagliati, M. R., Peyrieras, N., & Rosa, F. M. (2002). Regulation of nodal signalling and mesendoderm formation by TARAM-A, a TGFbeta-related type I receptor. *Dev Biol, 241*(2), 273-288. doi:10.1006/dbio.2001.0510

Armes, N. A., & Smith, J. C. (1997). The ALK-2 and ALK-4 activin receptors transduce distinct mesoderm-inducing signals during early *Xenopus* development but do not co-operate to establish thresholds. *Development, 124*(19), 3797-3804.

Asnaghi, L., White, D. T., Key, N., Choi, J., Mahale, A., Alkatan, H., . . . Eberhart, C. G. (2019). ACVR1C/SMAD2 signaling promotes invasion and growth in retinoblastoma. *Oncogene, 38*(12), 2056-2075. doi:10.1038/s41388-018-0543-2

Attisano, L., Carcamo, J., Ventura, F., Weis, F. M., Massague, J., & Wrana, J. L. (1993). Identification of human activin and TGF beta type I receptors that form heteromeric kinase complexes with type II receptors. *Cell, 75*(4), 671-680.

Attisano, L., & Wrana, J. L. (2002). Signal transduction by the TGF-beta superfamily. *Science, 296*(5573), 1646-1647. doi:10.1126/science.1071809

Attisano, L., Wrana, J. L., Cheifetz, S., & Massague, J. (1992). Novel activin receptors: distinct genes and alternative mRNA splicing generate a repertoire of serine/threonine kinase receptors. *Cell, 68*(1), 97-108.

Attisano, L., Wrana, J. L., Montalvo, E., & Massague, J. (1996). Activation of signalling by the activin receptor complex. *Mol Cell Biol, 16*(3), 1066-1073. doi:10.1128/mcb.16.3.1066

Aykul, S., Ni, W., Mutatu, W., & Martinez-Hackert, E. (2015). Human Cerberus prevents nodal-receptor binding, inhibits nodal signaling, and suppresses nodal-mediated phenotypes. *PLoS One, 10*(1), e0114954. doi:10.1371/journal.pone.0114954

Balkow, A., Jagow, J., Haas, B., Siegel, F., Kilic, A., & Pfeifer, A. (2015). A novel crosstalk between Alk7 and cGMP signaling differentially regulates brown adipocyte function. *Mol Metab, 4*(8), 576-583. doi:10.1016/j.molmet.2015.06.003

Bennett, J. T., Joubin, K., Cheng, S., Aanstad, P., Herwig, R., Clark, M., . . . Schier, A. F. (2007). Nodal signaling activates differentiation genes during zebrafish gastrulation. *Dev Biol, 304*(2), 525-540. doi:10.1016/j.ydbio.2007.01.012

Bianco, C., Adkins, H. B., Wechselberger, C., Seno, M., Normanno, N., De Luca, A., . . . Salomon, D. S. (2002). Cripto-1 activates nodal- and ALK4-dependent and -independent signaling pathways in mammary epithelial Cells. *Mol Cell Biol, 22*(8), 2586-2597. doi:10.1128/mcb.22.8.2586-2597.2002

Bisgrove, B. W., Su, Y. C., & Yost, H. J. (2017). Maternal Gdf3 is an obligatory cofactor in nodal signaling for embryonic axis formation in zebrafish. *Elife, 6*. doi:10.7554/eLife.28534

Blanchet, M. H., Le Good, J. A., Mesnard, D., Oorschot, V., Baflast, S., Minchiotti, G., . . . Constam, D. B. (2008a). Cripto recruits Furin and PACE4 and controls Nodal trafficking during proteolytic maturation. *The EMBO Journal, 27*(19), 2580-2591. doi:10.1038/emboj.2008.174

Blanchet, M. H., Le Good, J. A., Oorschot, V., Baflast, S., Minchiotti, G., Klumperman, J., & Constam, D. B. (2008b). Cripto localizes Nodal at the limiting membrane of early endosomes. *Sci Signal, 1*(45), ra13. doi:10.1126/scisignal.1165027

Bläßle, A., & Müller, P. (2015). PyFDAP: automated analysis of fluorescence decay after photoconversion (FDAP) experiments. *Bioinformatics, 31*(6), 972-974. doi:10.1093/bioinformatics/btu735

Bläßle, A., Soh, G., Braun, T., Mörsdorf, D., Preiß, H., Jordan, B. M., & Müller, P. (2018). Quantitative diffusion measurements using the open-source software PyFRAP. *Nat Commun, 9*(1), 1582. doi:10.1038/s41467-018-03975-6

Böffert, R., Businger, R., Preiß, H., Ehmann, D., Truffault, V., Simon, C., . . . Schindler, M. (2020). The human alpha-defensin-derived peptide HD5(1-9) inhibits cellular attachment and entry of human cytomegalovirus. *Antiviral Res, 177*, 104779. doi:10.1016/j.antiviral.2020.104779

Bondestam, J., Huotari, M. A., Moren, A., Ustinov, J., Kaivo-Oja, N., Kallio, J., . . . Ritvos, O. (2001). cDNA cloning, expression studies and chromosome mapping of human type I serine/threonine kinase receptor ALK7 (ACVR1C). *Cytogenet Cell Genet, 95*(3-4), 157-162. doi:59339

Boveri, T. (1902). *Über die Polarität des Seeigel-Eies: mit Tafel I*: Stuber.

Briscoe, J., Chen, Y., Jessell, T. M., & Struhl, G. (2001). A hedgehog-insensitive form of patched provides evidence for direct long-range morphogen activity of sonic hedgehog in the neural tube. *Mol Cell, 7*(6), 1279-1291. doi:10.1016/s1097-2765(01)00271-4

Bu, Y., Okunishi, K., Yogosawa, S., Mizuno, K., Irudayam, M. J., Brown, C. W., & Izumi, T. (2018). Insulin Regulates Lipolysis and Fat Mass by Upregulating Growth/Differentiation Factor 3 in Adipose Tissue Macrophages. *Diabetes, 67*(9), 1761-1772. doi:10.2337/db17-1201

Calvanese, L., Sandomenico, A., Caporale, A., Foca, A., Foca, G., D'Auria, G., . . . Ruvo, M. (2015). Conformational features and binding affinities to Cripto, ALK7 and ALK4 of Nodal synthetic fragments. *J Pept Sci, 21*(4), 283-293. doi:10.1002/psc.2733

Carlsson, L. M., Jacobson, P., Walley, A., Froguel, P., Sjostrom, L., Svensson, P. A., & Sjoholm, K. (2009). ALK7 expression is specific for adipose tissue, reduced in obesity and correlates to factors implicated in metabolic disease. *Biochem Biophys Res Commun, 382*(2), 309-314. doi:10.1016/j.bbrc.2009.03.014

Chang, C., Wilson, P. A., Mathews, L. S., & Hemmati-Brivanlou, A. (1997). A *Xenopus* type I activin receptor mediates mesodermal but not neural specification during embryogenesis. *Development, 124*(4), 827-837.

Chen, Y., & Schier, A. F. (2001). The zebrafish Nodal signal Squint functions as a morphogen. *Nature, 411*(6837), 607-610. doi:10.1038/35079121

Chen, Y., & Schier, A. F. (2002). Lefty proteins are long-range inhibitors of squint-mediated nodal signaling. *Curr Biol, 12*(24), 2124-2128. doi:10.1016/s0960-9822(02)01362-3

Chen, Y. H., Wang, Q., Li, C. Y., Hou, J. W., Chen, X. M., Zhou, Q., . . . Li, Y. G. (2017). Haplodeficiency of activin receptor-like kinase 4 alleviates myocardial infarction-induced cardiac fibrosis and preserves cardiac function. *J Mol Cell Cardiol, 105*, 1-11. doi:10.1016/j.yjmcc.2017.02.002

Coerver, K. A., Woodruff, T. K., Finegold, M. J., Mather, J., Bradley, A., & Matzuk, M. M. (1996). Activin signaling through activin receptor type II causes the cachexia-like symptoms in inhibin-deficient mice. *Mol Endocrinol, 10*(5), 534-543. doi:10.1210/mend.10.5.8732684

Conlon, F. L., Barth, K. S., & Robertson, E. J. (1991). A novel retrovirally induced embryonic lethal mutation in the mouse: assessment of the developmental fate of embryonic stem cells homozygous for the 413.d proviral integration. *Development, 111*(4), 969-981.

Conlon, F. L., Lyons, K. M., Takaesu, N., Barth, K. S., Kispert, A., Herrmann, B., & Robertson, E. J. (1994). A primary requirement for nodal in the formation and maintenance of the primitive streak in the mouse. *Development, 120*(7), 1919-1928.

Constam, D. B. (2014). Regulation of TGFbeta and related signals by precursor processing. *Semin Cell Dev Biol, 32*, 85-97. doi:10.1016/j.semcdb.2014.01.008

Crank, J. (1975). *The mathematics of diffusion* (2d ed.). Oxford, Eng: Clarendon Press.

Crank, J. (1979). *The mathematics of diffusion* (2d ed.). Oxford: Clarendon Press.

Crick, F. (1970). Diffusion in embryogenesis. *Nature, 225*(5231), 420-422. doi:10.1038/225420a0

DaCosta Byfield, S., Major, C., Laping, N. J., & Roberts, A. B. (2004). SB-505124 is a selective inhibitor of transforming growth factor-beta type I receptors ALK4, ALK5, and ALK7. *Mol Pharmacol, 65*(3), 744-752. doi:10.1124/mol.65.3.744

Dalcq, A. (1938). *Form and Causality in Early Development*: The University Press.

de Vries, C. J., de Boer, J., Joore, J., Strähle, U., van Achterberg, T. A., Huylebroeck, D., . . . Zivkovic, D. (1996). Active complex formation of type I and type II activin and TGF beta receptors in vivo as studied by overexpression in zebrafish embryos. *Mech Dev, 54*(2), 225-236. doi:10.1016/0925-4773(95)00480-7

De Winter, J. P., De Vries, C. J., Van Achterberg, T. A., Ameerun, R. F., Feijen, A., Sugino, H., . . . Van Den Eijden-Van Raaij, A. J. (1996). Truncated activin type II receptors inhibit bioactivity by the formation of heteromeric complexes with activin type I. receptors. *Exp Cell Res, 224*(2), 323-334. doi:10.1006/excr.1996.0142

Deacu, E., Mori, Y., Sato, F., Yin, J., Olaru, A., Sterian, A., . . . Meltzer, S. J. (2004). Activin type II receptor restoration in ACVR2-deficient colon cancer cells induces transforming growth factor-beta response pathway genes. *Cancer Res, 64*(21), 7690-7696. doi:10.1158/0008-5472.CAN-04-2082

Dick, A., Mayr, T., Bauer, H., Meier, A., & Hammerschmidt, M. (2000). Cloning and characterization of zebrafish smad2, smad3 and smad4. *Gene, 246*(1-2), 69-80. doi:10.1016/s0378-1119(00)00056-1

Dogra, D., Ahuja, S., Kim, H.-T., Rasouli, S. J., Stainier, D. Y. R., & Reischauer, S. (2017). Opposite effects of Activin type 2 receptor ligands on cardiomyocyte proliferation during development and repair. *Nature Communications, 8*(1), 1902. doi:10.1038/s41467-017-01950-1

Dougan, S. T., Warga, R. M., Kane, D. A., Schier, A. F., & Talbot, W. S. (2003). The role of the zebrafish nodal-related genes squint and cyclops in patterning of mesendoderm. *Development, 130*(9), 1837-1851. doi:10.1242/dev.00400

Driesch, H. (1891). Entwicklungsmechanische Studien. I–II. Der Wert der beiden ersten Furchungszellen in der Echinodermententwicklung. Experimentelle Erzeugung von Teil- und Doppelbildungen. *Zeitschrift für wissenschaftliche Zoologie*(53).

Driever, W., & Nüsslein-Volhard, C. (1988a). The bicoid protein determines position in the Drosophila embryo in a concentration-dependent manner. *Cell, 54*(1), 95-104. doi:10.1016/0092-8674(88)90183-3

Driever, W., & Nüsslein-Volhard, C. (1988b). A gradient of bicoid protein in Drosophila embryos. *Cell, 54*(1), 83-93. doi:10.1016/0092-8674(88)90182-1

Drocco, J. A., Grimm, O., Tank, D. W., & Wieschaus, E. (2011). Measurement and perturbation of morphogen lifetime: effects on gradient shape. *Biophys J, 101*(8), 1807-1815. doi:10.1016/j.bpj.2011.07.025

Dubrulle, J., Jordan, B. M., Akhmetova, L., Farrell, J. A., Kim, S. H., Solnica-Krezel, L., & Schier, A. F. (2015). Response to Nodal morphogen gradient is determined by the kinetics of target gene induction. *Elife, 4*. doi:10.7554/eLife.05042

Eisen, J. S., & Smith, J. C. (2008). Controlling morpholino experiments: don't stop making antisense. *Development, 135*(10), 1735-1743. doi:10.1242/dev.001115

El-Brolosy, M. A., Kontarakis, Z., Rossi, A., Kuenne, C., Gunther, S., Fukuda, N., . . . Stainier, D. Y. R. (2019). Genetic compensation triggered by mutant mRNA degradation. *Nature, 568*(7751), 193-197. doi:10.1038/s41586-019-1064-z

Erter, C. E., Solnica-Krezel, L., & Wright, C. V. (1998). Zebrafish nodal-related 2 encodes an early mesendodermal inducer signaling from the extraembryonic yolk syncytial layer. *Dev Biol, 204*(2), 361-372. doi:10.1006/dbio.1998.9097

Feldman, B., Concha, M. L., Saude, L., Parsons, M. J., Adams, R. J., Wilson, S. W., & Stemple, D. L. (2002). Lefty antagonism of squint is essential for normal gastrulation. *Current Biology, 12*(24), 2129-2135. doi:10.1016/S0960-9822(02)01361-1

Feldman, B., Gates, M. A., Egan, E. S., Dougan, S. T., Rennebeck, G., Sirotkin, H. I., . . . Talbot, W. S. (1998). Zebrafish organizer development and germ-layer formation require nodal-related signals. *Nature, 395*(6698), 181-185. doi:10.1038/26013

Ferguson, C. A., Tucker, A. S., Heikinheimo, K., Nomura, M., Oh, P., Li, E., & Sharpe, P. T. (2001). The role of effectors of the activin signalling pathway, activin receptors IIA and IIB, and Smad2, in patterning of tooth development. *Development, 128*(22), 4605-4613.

Funkenstein, B., Krol, E., Esterin, E., & Kim, Y. S. (2012). Structural and functional characterizations of activin type 2B receptor (acvr2b) ortholog from the marine fish, gilthead sea bream, Sparus aurata: evidence for gene duplication of acvr2b in fish. *J Mol Endocrinol, 49*(3), 175-192. doi:10.1530/JME-12-0075

Gagnon, J. A., Valen, E., Thyme, S. B., Huang, P., Akhmetova, L., Pauli, A., . . . Schier, A. F. (2014). Efficient mutagenesis by Cas9 protein-mediated oligonucleotide insertion and large-scale assessment of single-guide RNAs. *PLoS One, 9*(5), e98186. doi:10.1371/journal.pone.0098186

Garg, R. R., Bally-Cuif, L., Lee, S. E., Gong, Z., Ni, X., Hew, C. L., & Peng, C. (1999). Cloning of zebrafish activin type IIB receptor (ActRIIB) cDNA and mRNA expression of ActRIIB in embryos and adult tissues. *Mol Cell Endocrinol, 153*(1-2), 169-181. doi:10.1016/s0303-7207(99)00044-1

Gierer, A., & Meinhardt, H. (1972). A theory of biological pattern formation. *Kybernetik, 12*(1), 30-39.

Gore, A. V., Pillay, L. M., Venero Galanternik, M., & Weinstein, B. M. (2018). The zebrafish: A fintastic model for hematopoietic development and disease. *Wiley Interdiscip Rev Dev Biol*. doi:10.1002/wdev.312

Gregor, T., Wieschaus, E. F., McGregor, A. P., Bialek, W., & Tank, D. W. (2007). Stability and nuclear dynamics of the bicoid morphogen gradient. *Cell, 130*(1), 141-152. doi:10.1016/j.cell.2007.05.026

Gritsman, K., Zhang, J., Cheng, S., Heckscher, E., Talbot, W. S., & Schier, A. F. (1999). The EGF-CFC protein one-eyed pinhead is essential for nodal signaling. *Cell, 97*(1), 121-132. doi:10.1016/s0092-8674(00)80720-5

Groppe, J., Hinck, C. S., Samavarchi-Tehrani, P., Zubieta, C., Schuermann, J. P., Taylor, A. B., . . . Hinck, A. P. (2008). Cooperative assembly of TGF-beta superfamily signaling complexes is mediated by two disparate mechanisms and distinct modes of receptor binding. *Mol Cell, 29*(2), 157-168. doi:10.1016/j.molcel.2007.11.039

Gu, Z., Nomura, M., Simpson, B. B., Lei, H., Feijen, A., van den Eijnden-van Raaij, J., . . . Li, E. (1998). The type I activin receptor ActRIB is required for egg cylinder organization and gastrulation in the mouse. *Genes Dev, 12*(6), 844-857. doi:10.1101/gad.12.6.844

Guo, T., Marmol, P., Moliner, A., Bjornholm, M., Zhang, C., Shokat, K. M., & Ibanez, C. F. (2014). Adipocyte ALK7 links nutrient overload to catecholamine resistance in obesity. *Elife, 3*, e03245. doi:10.7554/eLife.03245

Gurdon, J. B., Standley, H., Dyson, S., Butler, K., Langon, T., Ryan, K., . . . Zorn, A. (1999). Single cells can sense their position in a morphogen gradient. *Development, 126*(23), 5309-5317.

Gurskaya, N. G., Verkhusha, V. V., Shcheglov, A. S., Staroverov, D. B., Chepurnykh, T. V., Fradkov, A. F., . . . Lukyanov, K. A. (2006). Engineering of a monomeric green-to-red photoactivatable fluorescent protein induced by blue light. *Nat Biotechnol, 24*(4), 461-465. doi:10.1038/nbt1191

Hammerschmidt, M., Pelegri, F., Mullins, M. C., Kane, D. A., Brand, M., van Eeden, F. J., . . . Nüsslein-Volhard, C. (1996). Mutations affecting morphogenesis during gastrulation and tail formation in the zebrafish, Danio rerio. *Development, 123*(1), 143-151.

Hans, S., Kaslin, J., Freudenreich, D., & Brand, M. (2009). Temporally-controlled site-specific recombination in zebrafish. *PLoS One, 4*(2), e4640-e4640. doi:10.1371/journal.pone.0004640

Harmansa, S., Hamaratoglu, F., Affolter, M., & Caussinus, E. (2015). Dpp spreading is required for medial but not for lateral wing disc growth. *Nature, 527*(7578), 317-322. doi:10.1038/nature15712

Hata, A., & Chen, Y. G. (2016). TGF-beta Signaling from Receptors to Smads. *Cold Spring Harb Perspect Biol, 8*(9). doi:10.1101/cshperspect.a022061

Haustein, E., & Schwille, P. (2007). Fluorescence correlation spectroscopy: novel variations of an established technique. *Annu Rev Biophys Biomol Struct, 36*, 151-169. doi:10.1146/annurev.biophys.36.040306.132612

He, X., Chen, W., Liu, Z., Yu, G., Chen, Y., Cai, Y.-J., . . . Yang, Y. (2020). Efficient and risk-reduced genome editing using double nicks enhanced by bacterial recombination factors in multiple species. *Nucleic Acids Research, 48*(10), e57-e57. doi:10.1093/nar/gkaa195

Heckman, K. L., & Pease, L. R. (2007). Gene splicing and mutagenesis by PCR-driven overlap extension. *Nat Protoc, 2*(4), 924-932. doi:10.1038/nprot.2007.132

Heisenberg, C. P., & Nusslein-Volhard, C. (1997). The function of silberblick in the positioning of the eye anlage in the zebrafish embryo. *Dev Biol, 184*(1), 85-94. doi:10.1006/dbio.1997.8511

Hempen, P. M., Zhang, L., Bansal, R. K., Iacobuzio-Donahue, C. A., Murphy, K. M., Maitra, A., . . . Kern, S. E. (2003). Evidence of selection for clones having genetic inactivation of the activin A type II receptor (ACVR2) gene in gastrointestinal cancers. *Cancer Res, 63*(5), 994-999.

Higuchi, R., Krummel, B., & Saiki, R. K. (1988). A general method of in vitro preparation and specific mutagenesis of DNA fragments: study of protein and DNA interactions. *Nucleic Acids Res, 16*(15), 7351-7367. doi:10.1093/nar/16.15.7351

Hilden, K., Tuuri, T., Eramaa, M., & Ritvos, O. (1994). Expression of type II activin receptor genes during differentiation of human K562 cells and cDNA cloning of the human type IIB activin receptor. *Blood, 83*(8), 2163-2170.

Hill, C. S. (2017). Spatial and temporal control of NODAL signaling. *Curr Opin Cell Biol, 51*, 50-57. doi:10.1016/j.ceb.2017.10.005

Hill, J. T., Demarest, B. L., Bisgrove, B. W., Su, Y. C., Smith, M., & Yost, H. J. (2014). Poly peak parser: Method and software for identification of unknown indels using sanger sequencing of polymerase chain reaction products. *Dev Dyn, 243*(12), 1632-1636. doi:10.1002/dvdy.24183

Ho, S. N., Hunt, H. D., Horton, R. M., Pullen, J. K., & Pease, L. R. (1989). Site-directed mutagenesis by overlap extension using the polymerase chain reaction. *Gene, 77*(1), 51-59. doi:10.1016/0378-1119(89)90358-2

Hong, S. K., Jang, M. K., Brown, J. L., McBride, A. A., & Feldman, B. (2011). Embryonic mesoderm and endoderm induction requires the actions of non-embryonic Nodal-related ligands and Mxtx2. *Development, 138*(4), 787-795. doi:10.1242/dev.058974

Horder, T. (2010). History of Developmental Biology *eLS*.

Hrabe, J., Hrabetova, S., & Segeth, K. (2004). A model of effective diffusion and tortuosity in the extracellular space of the brain. *Biophys J, 87*(3), 1606-1617. doi:10.1529/biophysj.103.039495

Jaźwińska, A., Badakov, R., & Keating, M. T. (2007). Activin-βA Signaling Is Required for Zebrafish Fin Regeneration. *Curr Biol, 17*(16), 1390-1395. doi:10.1016/j.cub.2007.07.019

Jing, X. H., Zhou, S. M., Wang, W. Q., & Chen, Y. (2006). Mechanisms underlying long- and short-range nodal signaling in Zebrafish. *Mech Dev, 123*(5), 388-394. doi:10.1016/j.mod.2006.03.006

Johannsen, W. (1909). *Elemente der exakten Erblichkeitslehre*. Jena: Gustav Fischer.

Jones, C. M., Kuehn, M. R., Hogan, B. L., Smith, J. C., & Wright, C. V. (1995). Nodal-related signals induce axial mesoderm and dorsalize mesoderm during gastrulation. *Development, 121*(11), 3651-3662.

Jornvall, H., Reissmann, E., Andersson, O., Mehrkash, M., & Ibanez, C. F. (2004). ALK7, a receptor for nodal, is dispensable for embryogenesis and left-right patterning in the mouse. *Mol Cell Biol, 24*(21), 9383-9389. doi:10.1128/MCB.24.21.9383-9389.2004

Kam, R. K., Deng, Y., Chen, Y., & Zhao, H. (2012). Retinoic acid synthesis and functions in early embryonic development. *Cell Biosci, 2*(1), 11. doi:10.1186/2045-3701-2-11

Kicheva, A., Pantazis, P., Bollenbach, T., Kalaidzidis, Y., Bittig, T., Jülicher, F., & Gonzalez-Gaitan, M. (2007). Kinetics of morphogen gradient formation. *Science, 315*(5811), 521-525. doi:10.1126/science.1135774

Kondo, M., Tashiro, K., Fujii, G., Asano, M., Miyoshi, R., Yamada, R., . . . Shiokawa, K. (1991). Activin receptor mRNA is expressed early in *Xenopus* embryogenesis and the level of the expression

affects the body axis formation. *Biochem Biophys Res Commun, 181*(2), 684-690. doi:10.1016/0006-291x(91)91245-8

Kumar, T. R., Varani, S., Wreford, N. G., Telfer, N. M., de Kretser, D. M., & Matzuk, M. M. (2001). Male reproductive phenotypes in double mutant mice lacking both FSHbeta and activin receptor IIA. *Endocrinology, 142*(8), 3512-3518. doi:10.1210/endo.142.8.8336

Lander, A. D., Nie, Q., & Wan, F. Y. (2007). Membrane-associated non-receptors and morphogen gradients. *Bull Math Biol, 69*(1), 33-54. doi:10.1007/s11538-006-9152-2

Leerberg, D. M., Hopton, R. E., & Draper, B. W. (2019). Fibroblast Growth Factor Receptors Function Redundantly During Zebrafish Embryonic Development. *Genetics, 212*(4), 1301-1319. doi:10.1534/genetics.119.302345

Liebman, P. A., & Entine, G. (1974). Lateral diffusion of visual pigment in photorecptor disk membranes. *Science, 185*(4149), 457-459. doi:10.1126/science.185.4149.457

Lieschke, G. J., & Currie, P. D. (2007). Animal models of human disease: zebrafish swim into view. *Nat Rev Genet, 8*(5), 353-367. doi:10.1038/nrg2091

Lord, N. D., Carte, A. N., Abitua, P. B., & Schier, A. F. (2019). The pattern of Nodal morphogen signaling is shaped by co-receptor expression. *bioRxiv*, 2019.2012.2030.891101. doi:10.1101/2019.12.30.891101

Lowe, L. A., Supp, D. M., Sampath, K., Yokoyama, T., Wright, C. V., Potter, S. S., . . . Kuehn, M. R. (1996). Conserved left-right asymmetry of nodal expression and alterations in murine situs inversus. *Nature, 381*(6578), 158-161. doi:10.1038/381158a0

Ma, G. T., Soloveva, V., Tzeng, S. J., Lowe, L. A., Pfendler, K. C., Iannaccone, P. M., . . . Linzer, D. I. (2001). Nodal regulates trophoblast differentiation and placental development. *Dev Biol, 236*(1), 124-135. doi:10.1006/dbio.2001.0334

Ma, L., Selamet Tierney, E. S., Lee, T., Lanzano, P., & Chung, W. K. (2012). Mutations in ZIC3 and ACVR2B are a common cause of heterotaxy and associated cardiovascular anomalies. *Cardiol Young, 22*(2), 194-201. doi:10.1017/S1047951111001181

Macias-Silva, M., Abdollah, S., Hoodless, P. A., Pirone, R., Attisano, L., & Wrana, J. L. (1996). MADR2 is a substrate of the TGFbeta receptor and its phosphorylation is required for nuclear accumulation and signaling. *Cell, 87*(7), 1215-1224. doi:10.1016/s0092-8674(00)81817-6

Madeira, F., Park, Y. M., Lee, J., Buso, N., Gur, T., Madhusoodanan, N., . . . Lopez, R. (2019). The EMBL-EBI search and sequence analysis tools APIs in 2019. *Nucleic Acids Res, 47*(W1), W636-W641. doi:10.1093/nar/gkz268

Magde, D., Elson, E., & Webb, W. W. (1972). Thermodynamic Fluctuations in a Reacting System---Measurement by Fluorescence Correlation Spectroscopy. *Physical Review Letters, 29*(11), 705-708. doi:10.1103/PhysRevLett.29.705

Magde, D., Elson, E. L., & Webb, W. W. (1974). Fluorescence correlation spectroscopy. II. An experimental realization. *Biopolymers, 13*(1), 29-61. doi:10.1002/bip.1974.360130103

Marcon, L., Diego, X., Sharpe, J., & Müller, P. (2016). High-throughput mathematical analysis identifies Turing networks for patterning with equally diffusing signals. *Elife, 5*. doi:10.7554/eLife.14022

Marjoram, L., & Wright, C. (2011). Rapid differential transport of Nodal and Lefty on sulfated proteoglycan-rich extracellular matrix regulates left-right asymmetry in *Xenopus*. *Development (Cambridge, England), 138*(3), 475-485. doi:10.1242/dev.056010

Mathews, L. S., & Vale, W. W. (1991). Expression cloning of an activin receptor, a predicted transmembrane serine kinase. *Cell, 65*(6), 973-982. doi:10.1016/0092-8674(91)90549-e

Mathews, L. S., Vale, W. W., & Kintner, C. R. (1992). Cloning of a second type of activin receptor and functional characterization in *Xenopus* embryos. *Science, 255*(5052), 1702-1705. doi:10.1126/science.1313188

Matzuk, M. M., & Bradley, A. (1992a). Cloning of the human activin receptor cDNA reveals high evolutionary conservation. *Biochim Biophys Acta, 1130*(1), 105-108. doi:10.1016/0167-4781(92)90472-c

Matzuk, M. M., & Bradley, A. (1992b). Structure of the mouse activin receptor type II gene. *Biochem Biophys Res Commun, 185*(1), 404-413. doi:10.1016/s0006-291x(05)81000-9

Matzuk, M. M., Kumar, T. R., & Bradley, A. (1995). Different phenotypes for mice deficient in either activins or activin receptor type II. *Nature, 374*(6520), 356-360. doi:10.1038/374356a0

McClendon, J. F. (1910). The development of isolated blastomeres of the frog's egg. *American Journal of Anatomy, 10*(1), 425-430. doi:10.1002/aja.1000100112

Meeker, N. D., Hutchinson, S. A., Ho, L., & Trede, N. S. (2007). Method for isolation of PCR-ready genomic DNA from zebrafish tissues. *Biotechniques, 43*(5), 610, 612, 614. doi:10.2144/000112619

Meno, C., Gritsman, K., Ohishi, S., Ohfuji, Y., Heckscher, E., Mochida, K., . . . Hamada, H. (1999). Mouse Lefty2 and zebrafish antivin are feedback inhibitors of nodal signaling during vertebrate gastrulation. *Mol Cell, 4*(3), 287-298. doi:10.1016/s1097-2765(00)80331-7

Meyer, A., & Van de Peer, Y. (2005). From 2R to 3R: evidence for a fish-specific genome duplication (FSGD). *Bioessays, 27*(9), 937-945. doi:10.1002/bies.20293

Minchiotti, G., Manco, G., Parisi, S., Lago, C. T., Rosa, F., & Persico, M. G. (2001). Structure-function analysis of the EGF-CFC family member Cripto identifies residues essential for nodal signalling. *Development, 128*(22), 4501-4510.

Miura, T., Hartmann, D., Kinboshi, M., Komada, M., Ishibashi, M., & Shiota, K. (2009). The cyst-branch difference in developing chick lung results from a different morphogen diffusion coefficient. *Mech Dev, 126*(3-4), 160-172. doi:10.1016/j.mod.2008.11.006

Montague, T. G., Cruz, J. M., Gagnon, J. A., Church, G. M., & Valen, E. (2014). CHOPCHOP: a CRISPR/Cas9 and TALEN web tool for genome editing. *Nucleic Acids Res, 42*(Web Server issue), W401-407. doi:10.1093/nar/gku410

Montague, T. G., & Schier, A. F. (2017). Vg1-Nodal heterodimers are the endogenous inducers of mesendoderm. *Elife, 6*. doi:10.7554/eLife.28183

Morgan, T. H. (1924). Two Embryos from One Egg. *The Scientific Monthly, 18*(5), 529-546.

Morgan, T. H., & Moszkowski, M. (1901). *Regeneration*. New York: Wilhelm Engelmann.

Mörsdorf, D. (2019). *Quantifying and perturbing the movement of extracellular proteins in zebrafish embryos.* Eberhad Karls Universität Tübingen.

Mörsdorf, D., & Müller, P. (2019). Tuning Protein Diffusivity with Membrane Tethers. *Biochemistry, 58*(3), 177-181. doi:10.1021/acs.biochem.8b01150

Müller, B., Hartmann, B., Pyrowolakis, G., Affolter, M., & Basler, K. (2003). Conversion of an extracellular Dpp/BMP morphogen gradient into an inverse transcriptional gradient. *Cell, 113*(2), 221-233.

Müller, P., Rogers, K. W., Jordan, B. M., Lee, J. S., Robson, D., Ramanathan, S., & Schier, A. F. (2012). Differential diffusivity of Nodal and Lefty underlies a reaction-diffusion patterning system. *Science, 336*(6082), 721-724. doi:10.1126/science.1221920

Müller, P., Rogers, K. W., Yu, S. R., Brand, M., & Schier, A. F. (2013). Morphogen transport. *Development, 140*(8), 1621-1638. doi:10.1242/dev.083519

Müller, P., & Schier, A. F. (2011). Extracellular movement of signaling molecules. *Dev Cell, 21*(1), 145-158. doi:10.1016/j.devcel.2011.06.001

Munir, S., Xu, G., Wu, Y., Yang, B., Lala, P. K., & Peng, C. (2004). Nodal and ALK7 inhibit proliferation and induce apoptosis in human trophoblast cells. *J Biol Chem, 279*(30), 31277-31286. doi:10.1074/jbc.M400641200

Nagaso, H., Suzuki, A., Tada, M., & Ueno, N. (1999). Dual specificity of activin type II receptor ActRIIb in dorso-ventral patterning during zebrafish embryogenesis. *Dev Growth Differ, 41*(2), 119-133. doi:10.1046/j.1440-169x.1999.00418.x

Nakamura, T., Mine, N., Nakaguchi, E., Mochizuki, A., Yamamoto, M., Yashiro, K., . . . Hamada, H. (2006). Generation of Robust Left-Right Asymmetry in the Mouse Embryo Requires a Self-Enhancement and Lateral-Inhibition System. *Developmental Cell, 11*(4), 495-504. doi:10.1016/j.devcel.2006.08.002

Nellen, D., Burke, R., Struhl, G., & Basler, K. (1996). Direct and long-range action of a DPP morphogen gradient. *Cell, 85*(3), 357-368. doi:10.1016/s0092-8674(00)81114-9

Neumann, C. J., & Cohen, S. M. (1997). Long-range action of Wingless organizes the dorsal-ventral axis of the Drosophila wing. *Development, 124*(4), 871-880.

Oh, S. P., & Li, E. (1997). The signaling pathway mediated by the type IIB activin receptor controls axial patterning and lateral asymmetry in the mouse. *Genes Dev, 11*(14), 1812-1826. doi:10.1101/gad.11.14.1812

Oh, S. P., & Li, E. (2002). Gene-dosage-sensitive genetic interactions between inversus viscerum (iv), nodal, and activin type IIB receptor (ActRIIB) genes in asymmetrical patterning of the visceral organs along the left-right axis. *Dev Dyn, 224*(3), 279-290. doi:10.1002/dvdy.10103

Pelliccia, J. L., Jindal, G. A., & Burdine, R. D. (2017). Gdf3 is required for robust Nodal signaling during germ layer formation and left-right patterning. *Elife, 6*. doi:10.7554/eLife.28635

Peyrieras, N., Strähle, U., & Rosa, F. (1998). Conversion of zebrafish blastomeres to an endodermal fate by TGF-beta-related signaling. *Curr Biol, 8*(13), 783-786. doi:10.1016/s0960-9822(98)70303-3

Pomreinke, A. P., Soh, G. H., Rogers, K. W., Bergmann, J. K., Bläßle, A. J., & Müller, P. (2017). Dynamics of BMP signaling and distribution during zebrafish dorsal-ventral patterning. *Elife, 6*. doi:10.7554/eLife.25861

Poo, M. M., & Cone, R. A. (1973). Lateral diffusion of phodopsin in Necturus rods. *Exp Eye Res, 17*(6), 503-510. doi:10.1016/0014-4835(73)90079-1

Qiu, W., Tang, S. M., Lee, S., Turk, A. T., Sireci, A. N., Qiu, A., . . . Su, G. H. (2016). Loss of Activin Receptor Type 1B Accelerates Development of Intraductal Papillary Mucinous Neoplasms in Mice With Activated KRAS. *Gastroenterology, 150*(1), 218-228 e212. doi:10.1053/j.gastro.2015.09.013

Ramachandran, A., Vizan, P., Das, D., Chakravarty, P., Vogt, J., Rogers, K. W., . . . Hill, C. S. (2018). TGF-beta uses a novel mode of receptor activation to phosphorylate SMAD1/5 and induce epithelial-to-mesenchymal transition. *Elife, 7*. doi:10.7554/eLife.31756

Rebagliati, M. R., Toyama, R., Fricke, C., Haffter, P., & Dawid, I. B. (1998a). Zebrafish nodal-related genes are implicated in axial patterning and establishing left-right asymmetry. *Dev Biol, 199*(2), 261-272. doi:10.1006/dbio.1998.8935

Rebagliati, M. R., Toyama, R., Haffter, P., & Dawid, I. B. (1998b). cyclops encodes a nodal-related factor involved in midline signaling. *Proc Natl Acad Sci U S A, 95*(17), 9932-9937. doi:10.1073/pnas.95.17.9932

Reissmann, E., Jörnvall, H., Blokzijl, A., Andersson, O., Chang, C., Minchiotti, G., . . . Brivanlou, A. H. (2001). The orphan receptor ALK7 and the Activin receptor ALK4 mediate signaling by Nodal proteins during vertebrate development. *Genes Dev, 15*(15), 2010-2022. doi:10.1101/gad.201801

Renucci, A., Lemarchandel, V., & Rosa, F. (1996). An activated form of type I serine/threonine kinase receptor TARAM-A reveals a specific signalling pathway involved in fish head organiser formation. *Development, 122*(12), 3735-3743.

Ripoche, D., Gout, J., Pommier, R. M., Jaafar, R., Zhang, C. X., Bartholin, L., & Bertolino, P. (2013). Generation of a conditional mouse model to target Acvr1b disruption in adult tissues. *Genesis, 51*(2), 120-127. doi:10.1002/dvg.22352

Roberts, H. J., Hu, S., Qiu, Q., Leung, P. C., Caniggia, I., Gruslin, A., . . . Peng, C. (2003). Identification of novel isoforms of activin receptor-like kinase 7 (ALK7) generated by alternative splicing and expression of ALK7 and its ligand, Nodal, in human placenta. *Biol Reprod, 68*(5), 1719-1726. doi:10.1095/biolreprod.102.013045

Rodaway, A., Takeda, H., Koshida, S., Broadbent, J., Price, B., Smith, J. C., . . . Holder, N. (1999). Induction of the mesendoderm in the zebrafish germ ring by yolk cell-derived TGF-beta family signals and discrimination of mesoderm and endoderm by FGF. *Development, 126*(14), 3067-3078.

Rogers, K. W. (2015). *Mesendoderm patterning by the Nodal/Lefty activator/inhibitor system*. FAS Theses and Dissertations.

Rogers, K. W., Bläßle, A., Schier, A. F., & Müller, P. (2015). Measuring protein stability in living zebrafish embryos using fluorescence decay after photoconversion (FDAP). *J Vis Exp*(95), 52266. doi:10.3791/52266

Rogers, K. W., Lord, N. D., Gagnon, J. A., Pauli, A., Zimmerman, S., Aksel, D. C., . . . Schier, A. F. (2017). Nodal patterning without Lefty inhibitory feedback is functional but fragile. *Elife, 6*. doi:10.7554/eLife.28785

Rogers, K. W., & Müller, P. (2019). Nodal and BMP dispersal during early zebrafish development. *Dev Biol, 447*(1), 14-23. doi:10.1016/j.ydbio.2018.04.002

Rogers, K. W., & Schier, A. F. (2011). Morphogen gradients: from generation to interpretation. *Annu Rev Cell Dev Biol, 27*(1), 377-407. doi:10.1146/annurev-cellbio-092910-154148

Ross, S., & Hill, C. S. (2008). How the Smads regulate transcription. *Int J Biochem Cell Biol, 40*(3), 383-408. doi:10.1016/j.biocel.2007.09.006

Rossi, A., Kontarakis, Z., Gerri, C., Nolte, H., Holper, S., Kruger, M., & Stainier, D. Y. (2015). Genetic compensation induced by deleterious mutations but not gene knockdowns. *Nature, 524*(7564), 230-233. doi:10.1038/nature14580

Rubinstein, A. L. (2003). Zebrafish: from disease modeling to drug discovery. *Curr Opin Drug Discov Devel, 6*(2), 218-223.

Ryden, M., Imamura, T., Jornvall, H., Belluardo, N., Neveu, I., Trupp, M., . . . Ibanez, C. F. (1996). A novel type I receptor serine-threonine kinase predominantly expressed in the adult central nervous system. *J Biol Chem, 271*(48), 30603-30609.

Sakuma, R., Ohnishi Yi, Y., Meno, C., Fujii, H., Juan, H., Takeuchi, J., . . . Hamada, H. (2002). Inhibition of Nodal signalling by Lefty mediated through interaction with common receptors and efficient diffusion. *Genes Cells, 7*(4), 401-412.

Schier, A. F. (2009). Nodal morphogens. *Cold Spring Harb Perspect Biol, 1*(5), a003459. doi:10.1101/cshperspect.a003459

Schier, A. F., Neuhauss, S. C., Helde, K. A., Talbot, W. S., & Driever, W. (1997). The one-eyed pinhead gene functions in mesoderm and endoderm formation in zebrafish and interacts with no tail. *Development, 124*(2), 327-342.

Schindelin, J., Arganda-Carreras, I., Frise, E., Kaynig, V., Longair, M., Pietzsch, T., . . . Cardona, A. (2012). Fiji: an open-source platform for biological-image analysis. *Nature Methods, 9*(7), 676-682. doi:10.1038/nmeth.2019

Schwille, P., Bieschke, J., & Oehlenschlager, F. (1997). Kinetic investigations by fluorescence correlation spectroscopy: the analytical and diagnostic potential of diffusion studies. *Biophys Chem, 66*(2-3), 211-228. doi:10.1016/s0301-4622(97)00061-6

Sekine, R., Shibata, T., & Ebisuya, M. (2018). Synthetic mammalian pattern formation driven by differential diffusivity of Nodal and Lefty. *Nat Commun, 9*(1), 5456. doi:10.1038/s41467-018-07847-x

Sharpe, J. (2019). Wolpert's French Flag: what's the problem? *Development, 146*(24). doi:10.1242/dev.185967

Shen, M. M. (2007). Nodal signaling: developmental roles and regulation. *Development, 134*(6), 1023-1034. doi:10.1242/dev.000166

Shi, Y., & Massague, J. (2003). Mechanisms of TGF-beta signaling from cell membrane to the nucleus. *Cell, 113*(6), 685-700. doi:10.1016/s0092-8674(03)00432-x

Shimozono, S., Iimura, T., Kitaguchi, T., Higashijima, S., & Miyawaki, A. (2013). Visualization of an endogenous retinoic acid gradient across embryonic development. *Nature, 496*(7445), 363-366. doi:10.1038/nature12037

Shorten, P. R., McMahon, C. D., & Soboleva, T. K. (2007). Insulin transport within skeletal muscle transverse tubule networks. *Biophys J, 93*(9), 3001-3007. doi:10.1529/biophysj.107.107888

Slack, J. M. (2002). Conrad Hal Waddington: the last Renaissance biologist? *Nat Rev Genet, 3*(11), 889-895. doi:10.1038/nrg933

Smith, K. A., Noel, E., Thurlings, I., Rehmann, H., Chocron, S., & Bakkers, J. (2011). Bmp and nodal independently regulate lefty1 expression to maintain unilateral nodal activity during left-right axis specification in zebrafish. *PLoS Genet, 7*(9), e1002289. doi:10.1371/journal.pgen.1002289

Soh, G. H., & Müller, P. (2018). FRAP Analysis of Extracellular Diffusion in Zebrafish Embryos. *Methods Mol Biol, 1863*, 107-124. doi:10.1007/978-1-4939-8772-6_6

Soh, G. H., Pomreinke, A. P., & Müller, P. (2020). Integration of Nodal and BMP Signaling by Mutual Signaling Effector Antagonism. *Cell Rep, 31*(1), 107487. doi:10.1016/j.celrep.2020.03.051

Song, J., Oh, S. P., Schrewe, H., Nomura, M., Lei, H., Okano, M., . . . Li, E. (1999). The type II activin receptors are essential for egg cylinder growth, gastrulation, and rostral head development in mice. *Dev Biol, 213*(1), 157-169. doi:10.1006/dbio.1999.9370

Spemann, H., & Mangold, H. (1924). über Induktion von Embryonalanlagen durch Implantation artfremder Organisatoren. *Archiv für mikroskopische Anatomie und Entwicklungsmechanik, 100*(3-4), 599-638. doi:10.1007/bf02108133

St Johnston, D., Driever, W., Berleth, T., Richstein, S., & Nüsslein-Volhard, C. (1989). Multiple steps in the localization of bicoid RNA to the anterior pole of the Drosophila oocyte. *Development, 107 Suppl*, 13-19.

Strähle, U., Jesuthasan, S., Blader, P., Garcia-Villalba, P., Hatta, K., & Ingham, P. W. (1997). one-eyed pinhead is required for development of the ventral midline of the zebrafish (Danio rerio) neural tube. *Genes Funct, 1*(2), 131-148.

Strigini, M., & Cohen, S. M. (1997). A Hedgehog activity gradient contributes to AP axial patterning of the Drosophila wing. *Development, 124*(22), 4697-4705.

Takagi, K., Kawaguchi, Y., Kawamoto, M., Ota, Y., Tochimoto, A., Gono, T., . . . Yamanaka, H. (2011). Activation of the activin A-ALK-Smad pathway in systemic sclerosis. *J Autoimmun, 36*(3-4), 181-188. doi:10.1016/j.jaut.2010.09.004

Tessadori, F., Noel, E. S., Rens, E. G., Magliozzi, R., Evers-van Gogh, I. J., Guardavaccaro, D., . . . Bakkers, J. (2015). Nodal signaling range is regulated by proprotein convertase-mediated maturation. *Dev Cell, 32*(5), 631-639. doi:10.1016/j.devcel.2014.12.014

Thieffry, D. (2001). Rationalizing early embryogenesis in the 1930s: Albert Dalcq on gradients and fields. *J Hist Biol, 34*(1), 149-181. doi:10.1023/a:1010389907221

Thisse, C., & Thisse, B. (2008). High-resolution in situ hybridization to whole-mount zebrafish embryos. *Nat Protoc, 3*(1), 59-69. doi:10.1038/nprot.2007.514

Tian, J., Andree, B., Jones, C. M., & Sampath, K. (2008). The pro-domain of the zebrafish Nodal-related protein Cyclops regulates its signaling activities. *Development, 135*(15), 2649-2658. doi:10.1242/dev.019794

Toyama, R., O'Connell, M. L., Wright, C. V., Kuehn, M. R., & Dawid, I. B. (1995). Nodal induces ectopic goosecoid and lim1 expression and axis duplication in zebrafish. *Development, 121*(2), 383-391.

Tsuchida, K., Sawchenko, P. E., Nishikawa, S., & Vale, W. W. (1996). Molecular cloning of a novel type I receptor serine/threonine kinase for the TGF beta superfamily from rat brain. *Mol Cell Neurosci, 7*(6), 467-478.

Turing, A. M. (1952). The chemical basis of morphogenesis. *Philos Trans R Soc Lond B Biol Sci, 237*(641), 37-72. doi:10.1098/rstb.1952.0012

Umulis, D., O'Connor, M. B., & Blair, S. S. (2009). The extracellular regulation of bone morphogenetic protein signaling. *Development, 136*(22), 3715-3728. doi:10.1242/dev.031534

van Boxtel, A. L., Chesebro, J. E., Heliot, C., Ramel, M. C., Stone, R. K., & Hill, C. S. (2015). A Temporal Window for Signal Activation Dictates the Dimensions of a Nodal Signaling Domain. *Dev Cell, 35*(2), 175-185. doi:10.1016/j.devcel.2015.09.014

van Boxtel, A. L., Economou, A. D., Heliot, C., & Hill, C. S. (2018). Long-Range Signaling Activation and Local Inhibition Separate the Mesoderm and Endoderm Lineages. *Dev Cell, 44*(2), 179-191 e175. doi:10.1016/j.devcel.2017.11.021

Vopalensky, P., Pralow, S., & Vastenhouw, N. L. (2018). Reduced expression of the Nodal co-receptor Oep causes loss of mesendodermal competence in zebrafish. *Development, 145*(5). doi:10.1242/dev.158832

Waddington, C. H. (1940). *Organisers and Genes*. Cambridge: Cambridge University Press.

Waddington, C. H. (1957). *The strategy of the genes*. London: Geo Alen & Unwin.

Wang, Q., Chen, Y., Zhang, D., Li, C., Chen, X., Hou, J., . . . Li, Y. (2018). Activin Receptor-Like Kinase 4 Haplodeficiency Mitigates Arrhythmogenic Atrial Remodeling and Vulnerability to Atrial Fibrillation in Cardiac Pathological Hypertrophy. *J Am Heart Assoc, 7*(16), e008842. doi:10.1161/JAHA.118.008842

Wang, Q., Yu, Y., Zhang, P., Chen, Y., Li, C., Chen, J., . . . Li, Y. (2017). The crucial role of activin A/ALK4 pathway in the pathogenesis of Ang-II-induced atrial fibrosis and vulnerability to atrial fibrillation. *Basic Res Cardiol, 112*(4), 47. doi:10.1007/s00395-017-0634-1

Wang, Y., Wang, X., Wohland, T., & Sampath, K. (2016). Extracellular interactions and ligand degradation shape the nodal morphogen gradient. *Elife, 5*, e13879. doi:10.7554/eLife.13879

Wartlick, O., Kicheva, A., & Gonzalez-Gaitan, M. (2009). Morphogen gradient formation. *Cold Spring Harb Perspect Biol, 1*(3), a001255. doi:10.1101/cshperspect.a001255

Waterhouse, A. M., Procter, J. B., Martin, D. M., Clamp, M., & Barton, G. J. (2009). Jalview Version 2--a multiple sequence alignment editor and analysis workbench. *Bioinformatics, 25*(9), 1189-1191. doi:10.1093/bioinformatics/btp033

Weismann, A. (1890). Prof. Weismann's Theory of Heredity. *Nature, 41*(1058), 317-323. doi:10.1038/041317g0

Weismann, A. (1892). *Das Keimplasma; eine Theorie der Vererbung*: Jena, Fischer.

White, R. J., Collins, J. E., Sealy, I. M., Wali, N., Dooley, C. M., Digby, Z., . . . Busch-Nentwich, E. M. (2017). A high-resolution mRNA expression time course of embryonic development in zebrafish. *Elife, 6*. doi:10.7554/eLife.30860

Wolpert, L. (1969). Positional information and the spatial pattern of cellular differentiation. *J Theor Biol, 25*(1), 1-47. doi:10.1016/s0022-5193(69)80016-0

Wolpert, L. (1989). Positional information revisited. *Development, 107 Suppl*(Supplement), 3-12.

Wrana, J. L., Attisano, L., Carcamo, J., Zentella, A., Doody, J., Laiho, M., . . . Massague, J. (1992). TGF beta signals through a heteromeric protein kinase receptor complex. *Cell, 71*(6), 1003-1014. doi:10.1016/0092-8674(92)90395-s

Xu, G., Zhong, Y., Munir, S., Yang, B. B., Tsang, B. K., & Peng, C. (2004). Nodal induces apoptosis and inhibits proliferation in human epithelial ovarian cancer cells via activin receptor-like kinase 7. *J Clin Endocrinol Metab, 89*(11), 5523-5534. doi:10.1210/jc.2004-0893

Yan, Y. T., Gritsman, K., Ding, J., Burdine, R. D., Corrales, J. D., Price, S. M., . . . Shen, M. M. (1999). Conserved requirement for EGF-CFC genes in vertebrate left-right axis formation. *Genes Dev, 13*(19), 2527-2537. doi:10.1101/gad.13.19.2527

Yan, Y. T., Liu, J. J., Luo, Y., E, C., Haltiwanger, R. S., Abate-Shen, C., & Shen, M. M. (2002). Dual roles of Cripto as a ligand and coreceptor in the nodal signaling pathway. *Mol Cell Biol, 22*(13), 4439-4449.

Yeo, C., & Whitman, M. (2001). Nodal signals to Smads through Cripto-dependent and Cripto-independent mechanisms. *Mol Cell, 7*(5), 949-957. doi:10.1016/s1097-2765(01)00249-0

Ying, S., Cao, H., Hu, H., Wang, X., Tang, Y., & Huang, C. (2016). Alk7 Depleted Mice Exhibit Prolonged Cardiac Repolarization and Are Predisposed to Ventricular Arrhythmia. *PLoS One, 11*(2), e0149205. doi:10.1371/journal.pone.0149205

Yogosawa, S., & Izumi, T. (2013). Roles of activin receptor-like kinase 7 signaling and its target, peroxisome proliferator-activated receptor gamma, in lean and obese adipocytes. *Adipocyte, 2*(4), 246-250. doi:10.4161/adip.24974

Yogosawa, S., Mizutani, S., Ogawa, Y., & Izumi, T. (2013). Activin receptor-like kinase 7 suppresses lipolysis to accumulate fat in obesity through downregulation of peroxisome proliferator-activated receptor gamma and C/EBPalpha. *Diabetes, 62*(1), 115-123. doi:10.2337/db12-0295

Zecca, M., Basler, K., & Struhl, G. (1996). Direct and long-range action of a wingless morphogen gradient. *Cell, 87*(5), 833-844. doi:10.1016/s0092-8674(00)81991-1

Zhang, J., Talbot, W. S., & Schier, A. F. (1998). Positional cloning identifies zebrafish one-eyed pinhead as a permissive EGF-related ligand required during gastrulation. *Cell, 92*(2), 241-251.

Zhang, L., Gurskaya, N. G., Merzlyak, E. M., Staroverov, D. B., Mudrik, N. N., Samarkina, O. N., . . . Lukyanov, K. A. (2007). Method for real-time monitoring of protein degradation at the single cell level. *Biotechniques, 42*(4), 446, 448, 450. doi:10.2144/000112453

Zhou, X., Sasaki, H., Lowe, L., Hogan, B. L., & Kuehn, M. R. (1993). Nodal is a novel TGF-beta-like gene expressed in the mouse node during gastrulation. *Nature, 361*(6412), 543-547. doi:10.1038/361543a0

9. Original publications

This chapter contains the original publications that are part of this thesis:

1.) Bläßle A., Soh G., Braun T., Mörsdorf D., **Preiß H.**, Jordan B. M. and Müller P. (2018). “Quantitative diffusion measurements using the open-source software PyFRAP.” *Nature Communications* **9**(1): 1582.

2.) **Preiß H.**, Mörsdorf D., Soh G., Almuedo-Castillo M. and Müller P. “Regulation of Nodal signaling propagation by receptor 1 interactions and positive feedback” unpublished manuscript; State of manuscript is from the 15-01-2021

nature COMMUNICATIONS

ARTICLE

DOI: 10.1038/s41467-018-03975-6 OPEN

Quantitative diffusion measurements using the open-source software PyFRAP

Alexander Bläßle[1], Gary Soh[1], Theresa Braun[1,3], David Mörsdorf[1], Hannes Preiß[1], Ben M. Jordan[2] & Patrick Müller[1]

Fluorescence Recovery After Photobleaching (FRAP) and inverse FRAP (iFRAP) assays can be used to assess the mobility of fluorescent molecules. These assays measure diffusion by monitoring the return of fluorescence in bleached regions (FRAP), or the dissipation of fluorescence from photoconverted regions (iFRAP). However, current FRAP/iFRAP analysis methods suffer from simplified assumptions about sample geometry, bleaching/photoconversion inhomogeneities, and the underlying reaction-diffusion kinetics. To address these shortcomings, we developed the software PyFRAP, which fits numerical simulations of three-dimensional models to FRAP/iFRAP data and accounts for bleaching/photoconversion inhomogeneities. Using PyFRAP we determined the diffusivities of fluorescent molecules spanning two orders of magnitude in molecular weight. We measured the tortuous effects that cell-like obstacles exert on effective diffusivity and show that reaction kinetics can be accounted for by model selection. These applications demonstrate the utility of PyFRAP, which can be widely adapted as a new extensible standard for FRAP analysis.

[1] Friedrich Miescher Laboratory of the Max Planck Society, Max-Planck-Ring 9, 72076 Tübingen, Germany. [2] Department of Organismic and Evolutionary Biology, Harvard University, 26 Oxford Street, Cambridge, MA 02138, USA. [3] Present address: University of Konstanz, Universitätsstraße 10, 78457 Konstanz, Germany. Correspondence and requests for materials should be addressed to P.Mül. (email: patrick.mueller@tuebingen.mpg.de)

The diffusion of molecules is important for almost any process across all scales of biological organisation, from transcription factors finding their targets on DNA to signalling molecules spreading through tissues during development and homoeostasis[1–3]. The biological function of a molecule is affected by its action range and therefore its mobility; however, effective diffusion of molecules moving through complex tissues is difficult to measure quantitatively. More than 40 years ago, Poo & Cone[4] and Liebman & Entine[5] developed a method to assess the diffusivities of fluorescent molecules. In these fluorescence recovery after photobleaching (FRAP) experiments, the fluorescence of molecules in a small region of the sample is bleached by exposure to a strong laser pulse[6]. The dynamics of fluorescence recovery in the bleached region can then be used to infer the mobility of the fluorescent molecules (Fig. 1a). Inverted FRAP (iFRAP) assays have recently been developed as an extension of FRAP experiments[7–10], which eliminate the often harsh bleaching conditions used in FRAP experiments. iFRAP assays utilise photoconvertible molecules that can be induced to alter their fluorescence excitation/emission properties after exposure to 'photoconverting' light. In iFRAP experiments, the spread of signal from a small photoconverted domain into the neighbouring regions of the sample is monitored over time and thus represents an experimental mirror image of FRAP (Fig. 1b).

Diffusion coefficients are commonly extracted from FRAP experiments by fitting analytical solutions computed from theoretical models to the measured recovery curves[11–18], and a few simulation-based analysis methods have been developed[19–21]. Although this allows for a rapid assessment of qualitative mobility differences in identical experimental settings, current approaches rely on several assumptions that can affect the accuracy of the analysis. First, most current methods reduce the FRAP analysis to one-dimensional or two-dimensional simplifications[11–21], often assuming that the fluorescent pool is infinitely large[11–14,16,17], or ignoring more complex geometries of biological samples that could play important roles in molecule movement (Fig. 1c). Recent studies have argued that geometry is crucial for dynamic biological processes[22,23], and must be taken into account for accurate analysis of FRAP data. Indeed, false assumptions about the FRAP sample geometry can drastically affect diffusion coefficient estimates (Fig. 1d).

Second, the bleaching process in FRAP experiments is often inaccurately modelled. Bleaching is posited to be homogeneous or to follow a Gaussian distribution throughout bleached circular or rectangular regions, while the molecules outside of the bleached region are assumed to remain unbleached[11–13, 15–18]. However, molecules diffusing during the bleaching process can create inhomogeneities both inside and outside of the bleached region; moreover, a delay between bleaching and the start of the recovery measurement can lead to further inhomogeneities (Fig. 1c). Incorrect assumptions about the bleaching process can thus lead to a severe misestimation of diffusion coefficients[14, 24–27] (Fig. 1e).

Third, in vivo FRAP experiments can be strongly influenced by reaction kinetics such as production or degradation of fluorescent molecules, which can contribute to the observed recovery curve (Fig. 1c). However, this is mostly neglected in classical FRAP analysis models and can lead to erroneous diffusion estimates (Fig. 1f)[11–17].

To address these shortcomings, we developed the versatile Python-based FRAP analysis software PyFRAP (available at https://mueller-lab.github.io/PyFRAP). To facilitate data analysis, PyFRAP is equipped with an intuitive graphical user interface (GUI, Fig. 2a), which gives users without a computational background access to a sophisticated FRAP data analysis workflow from image analysis to statistical model comparison methods (Fig. 2b). PyFRAP applies the first post-bleach image as initial condition (Fig. 2c), and numerically simulates the FRAP experiment in realistic two-dimensional or three-dimensional experiment geometries (Fig. 2d, e); the solution from this simulation is then fitted to the experimental data. Furthermore, PyFRAP can accurately account for both uniform production and degradation during FRAP experiments. PyFRAP saves all analysed data and settings in a logical data structure that can be shared with collaborators or re-used for later analyses (Fig. 2f). The software is freely available, and the open-source environment allows for rapid expansion through collaborative work[28] to adjust analysis methods to the users' needs.

To demonstrate the utility of PyFRAP, we conducted several typical in vitro and in vivo FRAP experiments (Supplementary Fig. 1). PyFRAP accurately determines the diffusion coefficients of fluorescent molecules ranging from 3 to 500 kDa in both artificial and biological contexts. In contrast to currently available software, PyFRAP's flexible initial conditions also allow analysis of iFRAP experiments, producing results comparable to FRAP. We used PyFRAP to measure the influence that obstacles such as cells exert on the movement of diffusing molecules, and found that such geometric hindrance decreases diffusivity by about one-third. Moreover, PyFRAP provides accurate modelling of reaction kinetics, including production and degradation. Finally, to test the impact of extracellular binding on protein diffusivity, we measured the diffusion of signalling molecules in living zebrafish embryos. We found that the effective diffusivity of a signalling molecule in developing zebrafish was reduced to about one-tenth of its predicted value, in agreement with hindered diffusion models postulating interactions of embryonic signals with diffusion regulators[22,29]. Altogether, our analyses highlight how detailed examination of FRAP data can be used to determine the contribution of individual factors to the movement of molecules in controlled artificial and biological contexts[30].

Results

PyFRAP is a versatile FRAP/iFRAP analysis package. Current FRAP analysis methods often make simplified assumptions about FRAP experimental conditions to aid in the derivation of analytical solutions[11–16,18], and to facilitate numerical simulations[20,21]. Such assumptions include reducing complex sample geometries to lower dimensions, idealising the initial bleaching profile, or ignoring additional reaction kinetics potentially underlying fluorescence recovery (Fig. 1c). Unless the experiment is well approximated by these assumptions (e.g., simple geometry, small bleach spot compared to a large sample volume, sharp bleach profile, no reactions), this can lead to erroneous diffusion estimates (Fig. 1d–f). To address these shortcomings, we developed PyFRAP. PyFRAP numerically simulates FRAP experiments in realistic three-dimensional geometries using an interpolation of the first post-bleach image as initial condition. This simulation is then fitted to the experimental data, incorporating reaction kinetics such as uniform production and degradation.

PyFRAP is an open-source Python-based FRAP analysis software that runs on the major operating systems Microsoft Windows, Mac OSX and Linux. Over the past 20 years, Python has become the standard programming language for scientific research because of the availability of versatile add-on packages and its intuitive and simple syntax[31]. Building on the resourcefulness of Python, PyFRAP is based on commonly used packages such as PyQT, SciPy and FiPy[32–36]. PyFRAP comes with an intuitive graphical user interface (GUI, Fig. 2a) and a fully documented application programming interface (API) allowing

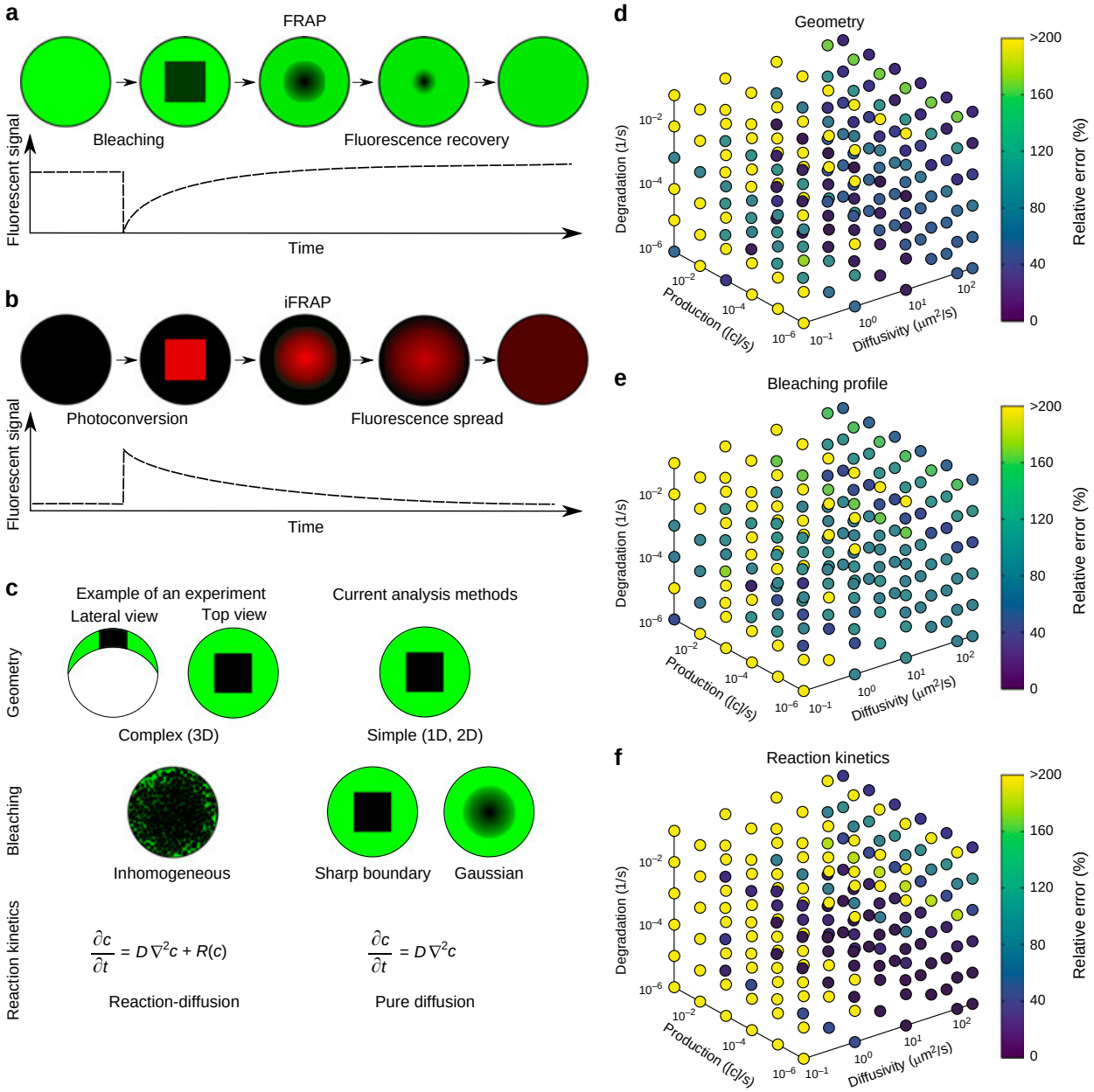

Fig. 1 Fluorescence perturbation techniques used for effective diffusion measurements, and drawbacks of current analysis methods. **a** In fluorecence recovery after photobleaching (FRAP) experiments, a small region in the sample is bleached. After bleaching, the diffusion-driven recovery in the bleached region is monitored. **b** Inverse FRAP (iFRAP) is an experimental mirror image of FRAP: Molecules in a given region are photoconverted and then spread throughout the sample, resulting in the loss of fluorescent signal in the region of photoconversion. **c** Drawbacks of current analysis methods exemplified with zebrafish development at late blastula stages. Current analysis methods simplify sample geometry, idealise bleaching profiles, or ignore underlying reaction kinetics. **d**–**f** Possible relative error in diffusion coefficient estimates that can occur if false assumptions are made about sample geometry (**d**), bleaching conditions (**e**), or reaction kinetics (**f**), respectively. The maximum displayed error was capped to a value of 200%, but can be up to 1000%

quick development of scripts or modifications of the PyFRAP code. PyFRAP's functionalities include sophisticated image processing functions useful for FRAP analysis, customisable geometry and analysis region definitions, a finite element partial differential equation (PDE) solver that simulates FRAP/iFRAP experiments with adjustable options, statistical tools for averaging and model comparison, and multiple plotting and input/output functions (see Methods section and Supplementary Note 1 for details). To make the software easily accessible, dialogue boxes (software wizards) guide the user step-by-step through data import, image analysis, simulation and fitting.

We programmed PyFRAP to import image data from most common microscope formats, such as .tif, .lsm and .czi. Users can define arbitrary regions of interests (ROIs) that are then used for image analysis, simulation and fitting (Supplementary Fig. 2a). For some experimental setups, the imaged sample might be larger than the field of view. In these cases, the concentration of molecules in regions outside of the image can be estimated from selected areas in the first image of the recovery image series (Supplementary Fig. 2b). Uneven illumination is a common artefact in FRAP experiments. PyFRAP can correct this artefact by normalisation using pre-bleach images or using a correction matrix computed from a secondary data set generated with a

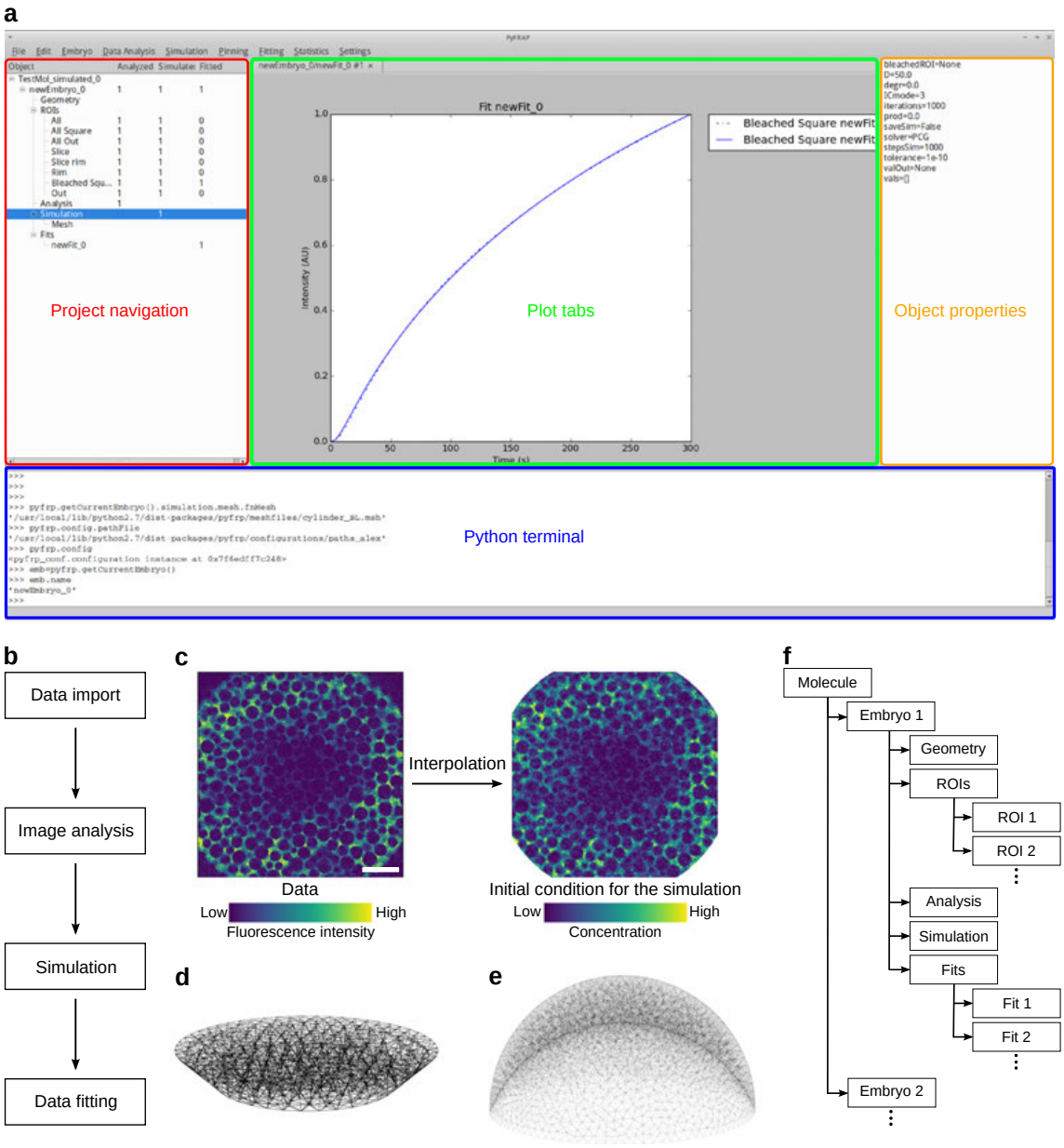

Fig. 2 The PyFRAP software package. **a** Annotated snapshot of the PyFRAP main GUI with project navigation tree (red), plot tabs (green), object property display (orange), and integrated Python terminal (blue). **b** PyFRAP work flow. **c** PyFRAP's interpolation of the first post-bleach image as initial condition for FRAP simulations. The length of the white scale bar represents 100 µm. **d**, **e** Spatial discretisation of geometries resembling **d** a frustum and **e** a zebrafish embryo at late blastula stages (dome stage). **f** PyFRAP's data structure

homogeneously distributed fluorophore[37–39] (see Methods section and Supplementary Fig. 2c for details). To avoid numerical instabilities, PyFRAP allows the user to smooth or denoise the image data using a Gaussian or median filter (see Methods section, Supplementary Note 1, Supplementary Fig. 3, and Supplementary Table 1 for details).

FRAP and iFRAP experiments have been performed in a variety of contexts, from the cigar-shaped *Drosophila* embryo and the relatively flat *Drosophila* wing disc to the dome-shaped pre-gastrula stage zebrafish embryo[10,22,29, 40–42]. These structures have distinct geometries that could impact fluorescence recovery. In fact, we found that simplifying the three-dimensional zebrafish embryo to a two-dimensional disc can frequently lead up to a >200% error in estimated diffusion coefficients (Fig. 1d). In PyFRAP, users can define arbitrary two-dimensional and three-dimensional geometries using Gmsh[43] or CAD STereoLithography (.stl) files that are then spatially discretised into tetrahedral meshes by Gmsh in combination with TetGen[44]. PyFRAP provides various meshing options, such as local mesh refinements, boundary layer meshes and attractor meshes, allowing users to adapt the mesh to experimental details (see Fig. 2d, e and Supplementary Fig. 4c for example geometries and meshes).

In current FRAP analysis methods, the initial condition of the FRAP experiment is often simplified to a simple rectangular function or a Gaussian profile to approximate sharp or blurred bleach boundaries, respectively[11,12, 14–18, 45–47]. However, light scattering, imperfect bleaching and diffusion during the bleaching process can lead to more complex bleaching profiles and thus need to be considered during FRAP analysis to avoid misestimation of diffusion coefficients[24,25,30,48]. To overcome this issue, PyFRAP uses a bilinear interpolation between pixels of the first

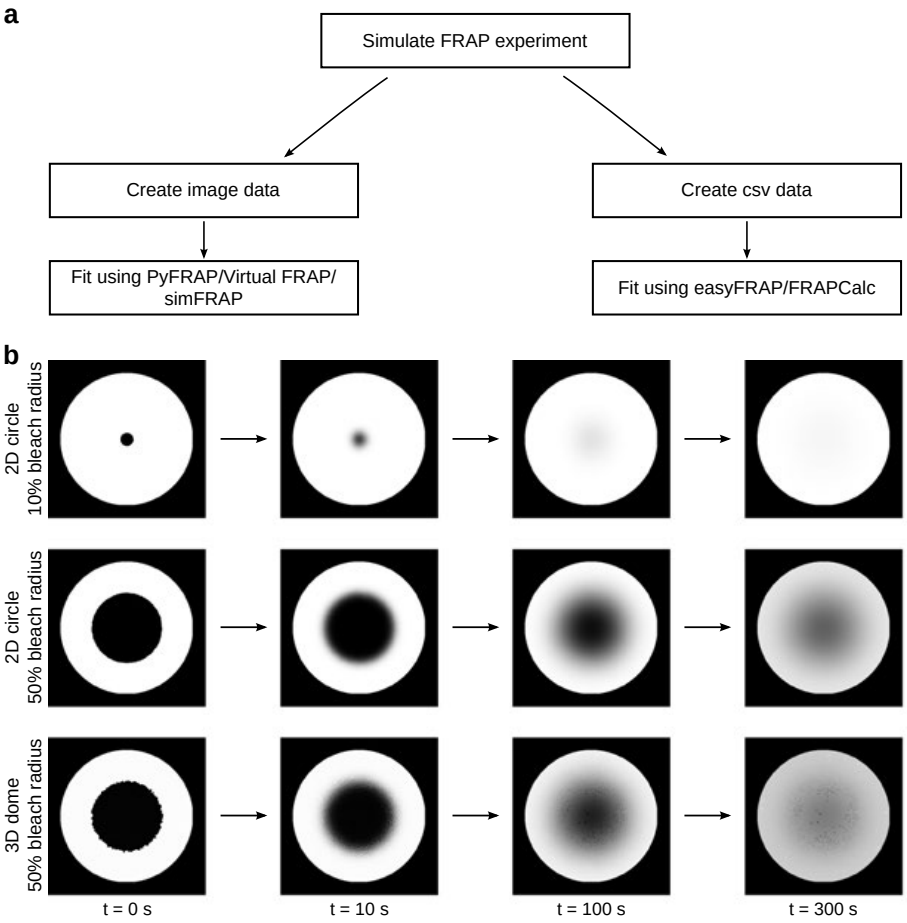

c

Geometry	Bleach domain radius (%)	Simulated D (μm²/s)	PyFRAP D (μm²/s)	FrapCalc D (μm²/s)	easyFRAP* D (μm²/s)	simFRAP D (μm²/s)	virtualFRAP D (μm²/s)
2D circle	5	10	9.8	9.0	14.0	9.3	9.1
2D circle	10	10	9.7	9.7	21.5	9.5	9.1
2D circle	50	10	9.8	10.4	89.1	13.1	10.3
2D circle	5	50	47.5	37.2	38.2	39.8	44.2
2D circle	10	50	49.5	45.2	70.7	47.9	44.3
2D circle	50	50	48.4	63.6	260.5	19.0	42.0
2D circle	5	200	245.0	112.7	67.3	n.a.	39.3
2D circle	10	200	179.0	157.6	161.0	8.7	177.8
2D circle	50	200	197.1	503.1	910.0	n.a.	191.7
3D dome	5	10	11.9	n.a.	17.2	9.7	11.3
3D dome	10	10	9.0	n.a.	23.8	10.1	9.0
3D dome	50	10	10.3	24.0	83.3	12.7	13.3
3D dome	5	50	56.9	n.a.	61.5	47.7	41.8
3D dome	10	50	44.2	n.a.	90.7	49.5	43.4
3D dome	50	50	47.4	n.a.	310.4	48.7	34.1
3D dome	5	200	211.6	n.a.	139.2	185.6	40.5
3D dome	10	200	172.4	n.a.	264.5	192.5	188.0
3D dome	50	200	191.1	n.a.	1021.9	177.3	113.5

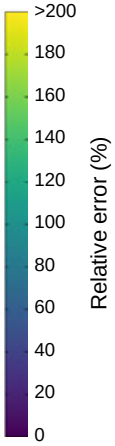

Fig. 3 PyFRAP benchmarking simulation experiment. **a** Workflow of PyFRAP benchmarking. **b** Examples of simulated data sets for different bleach spot sizes and geometries. **c** Benchmarking results of PyFRAP against currently available software packages using simulated FRAP experiments. Simulation experiments varied in bleached region size, diffusion coefficient and experiment geometry. All diffusion coefficients and estimates are given in units of μm²/s. n.a. indicates that the software was not able to fit the simulated data. Colours indicate relative estimation error in %. Diffusion coefficients determined by easyFRAP (asterisk) were computed in combination with an equation providing a relationship between recovery rate, bleached domain size and diffusivity[45]

post-bleach image to estimate the initial condition for mesh cells. This initial condition closely resembles initial experimental bleaching profiles and concentration distributions (Fig. 2c). Moreover, in contrast to most current FRAP analysis methods[11–18,46,47], PyFRAP does not fit a mathematical expression based on simplified assumptions to the data; instead, PyFRAP uses FiPy[32] to simulate the experiment numerically, resulting in a solution that incorporates the realistic three-dimensional geometry and initial conditions. The numerical simulation is then fitted to the FRAP data by minimising the sum of squared differences using classical optimisation algorithms[49–51] (see Methods section for details).

In typical FRAP and iFRAP experiments, a protein of interest is tagged with a fluorescent protein and expressed within a tissue. In such an experiment, the fusion protein is often actively produced at the same time that FRAP is carried out; additionally, fusion proteins undergo degradation over time. Depending on how the fusion protein is expressed (promoter-driven expression, mRNA injection, etc.), its degradation kinetics, and the timescale of the FRAP/iFRAP experiment, production and degradation can dramatically influence recovery curves. Ignoring reaction kinetics in FRAP experiments could therefore lead to erroneous diffusion coefficient estimates. Indeed, recovery curves with pure diffusion fitted to a simulated reaction-dominant data set often resulted in a >200% error in the estimated diffusion coefficients (Fig. 1f). To ensure that the appropriate reaction kinetics are considered when analysing FRAP data, PyFRAP is equipped with four models: (1) Pure diffusion, (2) diffusion with production, (3) diffusion with degradation and (4) diffusion with production and degradation (see Methods section for details). The model can be constrained with previous reaction rate measurements from assays such as fluorescence decay after photoconversion (FDAP) [52,53]; alternatively, production and degradation rates can be directly obtained from fitting the FRAP data. Below, we discuss methods to determine which approaches are most appropriate for a given data set.

An advantage of PyFRAP is its ability to assess FRAP data using multiple models of varying complexity, from pure diffusion to combined reaction-diffusion kinetics. However, determining which model is appropriate for a given data set can be challenging. Choosing the incorrect model can lead to overfitting and potentially false diffusion coefficients[54]. The Akaike information criterion (AIC) is a statistical tool that can aid in model selection[55]. PyFRAP's implementation of the AIC allows users to compare the models mentioned above and determines the most likely model based on a relative weighted measure that includes both the model's log-likelihood and its degrees of freedom, i.e., the number of model parameters. Moreover, PyFRAP provides several statistical tests (Supplementary Table 2) to assess differences between measurements and obtained fits, such as Student's *t*-test[56] for normally distributed data or the Mann–Whitney-U-test[57], which does not require normally distributed data. The Shapiro–Wilk-test can be used to assess whether the measured diffusivities follow a normal distribution[58] and whether application of Student's *t*-test or the Mann–Whitney-U-test is justified.

PyFRAP's object-oriented data structure (Fig. 2f) can be saved into serialised objects and easily loaded for further analysis or shared with collaborators. In addition, PyFRAP lets users visualise every aspect of PyFRAP's analysis work flow and save plots and images into publication-ready figures.

Benchmarking PyFRAP. To validate PyFRAP, we first determined whether it can recover true diffusion coefficients and reaction kinetics from simulated data. We used our previous in-house solution[22,29,42] based on the commercial programs MATLAB and COMSOL multiphysics to simulate 24 FRAP experiments with different reaction kinetics and diffusion coefficients. Using PyFRAP, the simulated data sets were fitted with all four possible reaction-diffusion models (see above). We determined a maximal error of 10% (average error: 2%, Supplementary Table 3) between simulated and estimated diffusion coefficients, demonstrating that PyFRAP recovers correct diffusion coefficients within the error tolerance of the numerical simulations.

Next, we tested whether PyFRAP's implementation of the AIC allows identification of the models used to create the simulated data. When the data were simulated with models describing either pure diffusion, diffusion and degradation, or diffusion and production, the AIC predicted the correct underlying model (Supplementary Table 3). However, the model selection based on the AIC did not favour the correct model for data sets that included diffusion combined with both production and degradation, since models with fewer degrees of freedom provided smaller Akaike weight values. Simulations involving diffusion, production and degradation can generate data effectively indistinguishable from data simulated with only diffusion and production or diffusion and degradation, explaining why the AIC cannot predict the correct model in this case.

To assess PyFRAP's performance in comparison with other available software packages based on analytical[17,46,47,59] or numerical[20,21,60] approaches (Supplementary Table 4), we used easyFRAP[47], Virtual FRAP[20], FrapCalc[46], simFRAP[21] and PyFRAP itself to analyse simulated FRAP experiments (Supplementary Note 2, Fig. 3). We simulated 18 experiments in which geometry, relative bleach window size, and diffusion coefficients differed. Simulations were conducted either in a simple circular two-dimensional domain or a complex three-dimensional zebrafish embryo-like geometry (Fig. 2e). FrapCalc and easyFRAP assume circular bleach windows[12,46,47]; to facilitate comparison, we therefore simulated FRAP experiments with circular bleach windows. Bleach window sizes comprised 5, 10 or 50% of the slice diameter, representing different proportions between fluorescent and bleached pools (Fig. 3b). Simulations were performed with three biologically relevant diffusion coefficients: 10, 50 and 200 $\mu m^2/s$.

Simulation-based programs (PyFRAP, virtualFRAP and simFRAP) generally provided better results than analytical solutions (easyFRAP and FrapCalc): FrapCalc and easyFRAP were either unable to determine diffusion coefficients, or provided diffusivities that were off by at least 20% for most experiments (Fig. 3c). Fast recovery dynamics were challenging for all tested software. One reason for this is that fewer data points were recorded during the actual recovery process of highly diffusive molecules due to a fixed frame rate of 1 frame/s in the simulated test data sets, leading to larger errors; moreover, for fast recovery dynamics errors from interpolating simulations onto images are more severe. The analytical software packages provided better results for the two-dimensional compared to three-dimensional geometries, while simulation-based approaches showed no clear trend regarding geometry. In terms of bleach window radius, the analytical solutions performed worst if the window diameter was 50% of the slice diameter. This effect might be due to the assumption of an infinite pool of fluorescent molecules outside of the bleached region[12]—when the bleach window is very large, the pool of unbleached fluorescent molecules is small, which conflicts with the assumption of an infinite pool. In contrast, PyFRAP outperformed all current software packages and exhibited the smallest error between predicted and simulated diffusion coefficients (Fig. 3c).

Applications of PyFRAP to measure diffusion hindrance. In vivo, it is thought that the overall movement of molecules is affected by binding interactions and by the presence of obstacles such as cells, resulting in a reduced effective diffusion coefficient of secreted proteins that move through tissues[22]. However, the effects of these interactions have not been rigorously tested experimentally. We therefore employed PyFRAP to examine the effects of obstacles and binding partners on the effective diffusivity of dextrans and proteins in experimentally controlled in vitro geometries and in living zebrafish embryos.

First, we measured diffusion coefficients of a wide range of differently sized molecules (Supplementary Table 5) in a simple in vitro context in the absence of binding partners or obstacles. We performed FRAP experiments with different bleach

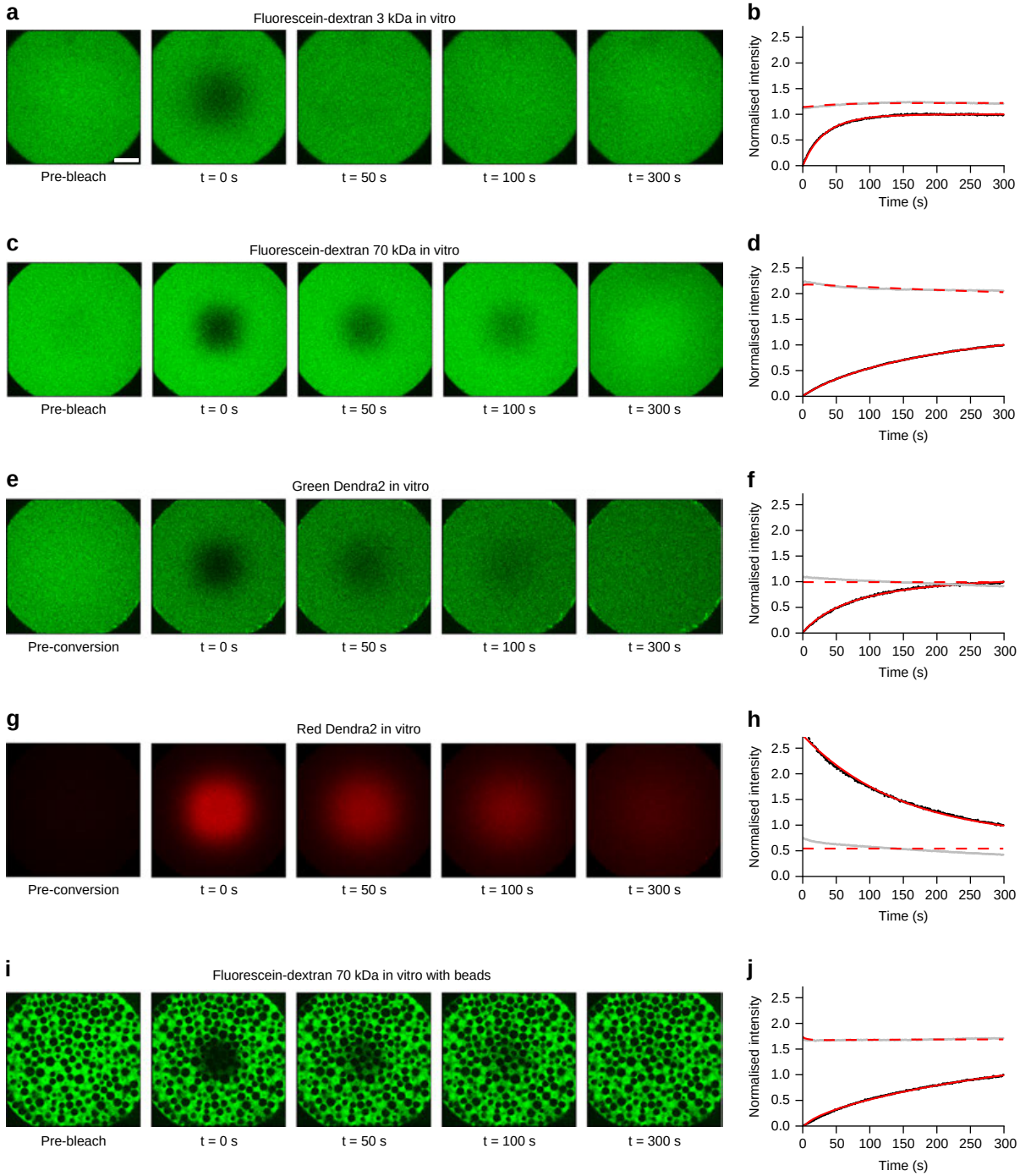

Fig. 4 Examples of in vitro FRAP and iFRAP experiments and the resulting fits to measure free diffusion. **a**, **c**, **e**, **g**, **i** In vitro FRAP and iFRAP experiment images and **b**, **d**, **f**, **h**, **j** fits with PyFRAP. Black and grey dots represent data points of bleached and slice ROI, respectively. Red solid and dashed lines show the respective fits. **a**–**d** FRAP experiments with 3 and 70 kDa fluorescent dextrans (see Supplementary Fig. 5 for the full data set with fluorescent dextrans between 3 and 500 kDa). **e**–**h** iFRAP experiment with photoconverted Dendra2 protein showing data for the green (**e**, **f**) and the red (**g**, **h**) channel. **i**, **j** FRAP experiment with 70 kDa fluorescent dextran in the presence of polyacrylamide beads. Recovery curves were normalised between 0 (intensity in the bleached ROI at the first post-bleach time point) and 1 (intensity in the bleached ROI at the last post-bleach time point) to allow comparison across data sets. The length of the white scale bar in **a** represents 100 μm, and all images were acquired with the same magnification

geometries using fluorophore-coupled dextrans ranging from 3 to 500 kDa in molecular weight (Fig. 4a–d, Supplementary Figs. 5 and 6), and compared the results with theoretical predictions and literature values. Fluorescence recovery in these in vitro experiments should be purely defined by diffusion, and the theoretical diffusivities D of spherical molecules can be calculated from their radii r based on the relationship $D \sim 1/r$ as postulated by the Einstein–Stokes equation (Supplementary Note 3). The diffusion coefficients determined by PyFRAP were in good agreement with literature values and theoretical predictions (Fig. 5a, Supplementary Tables 6 and 7).

A variant of FRAP that allows exclusion of reaction kinetics, such as production, and thus decrease the number of unknown experimental parameters is iFRAP (Fig. 1b). To perform in vitro iFRAP experiments, we used the green-to-red photoconvertible protein Dendra2[61]. Since photoconverting Dendra2 from green to red can also be interpreted as bleaching the original green fluorescence, measuring unconverted and converted protein distributions produces both FRAP and iFRAP experiments at the same time. To test whether PyFRAP correctly analyses iFRAP data, we used the experimental FRAP and iFRAP sets independently and assessed whether the obtained diffusion values are equal (Fig. 4e–h). Using FRAP we measured a Dendra2 diffusivity of 52.9 ± 5.2 (standard deviation) $\mu m^2/s$, and using iFRAP we obtained a similar value of $53.3 \pm 3.1\ \mu m^2/s$ (Fig. 5b, average difference between the two diffusivities per data set: $2.6 \pm 1.5\ \mu m^2/s$).

Next, we examined the effect of tortuosity on diffusion. In biological samples, the path length that molecules take increases as they move around obstacles such as cells. The effect of this

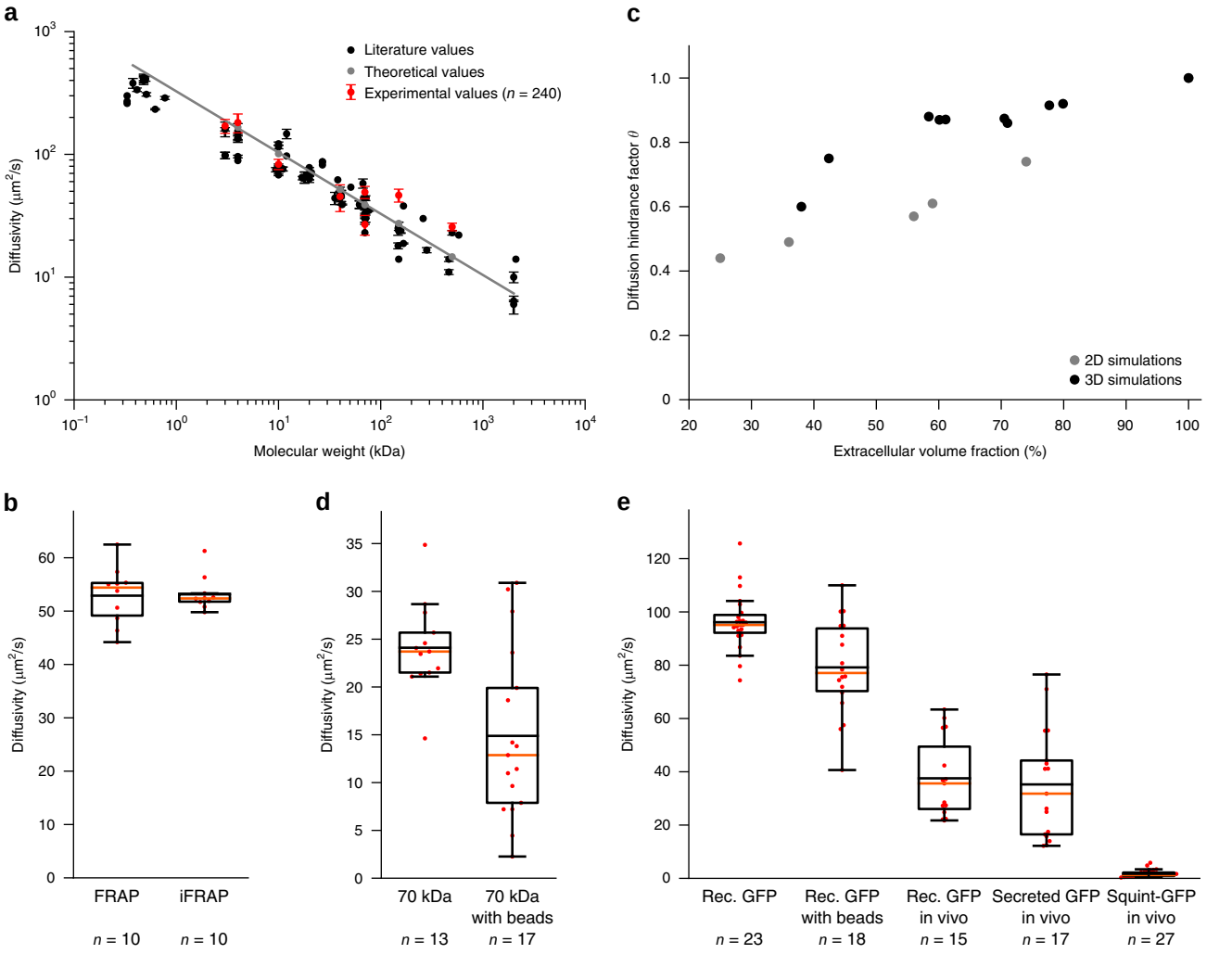

Fig. 5 Effective diffusion coefficients determined by PyFRAP. **a** Results of in vitro experiments and PyFRAP analysis for freely diffusing fluorescent dextrans of different molecular weights. Black markers indicate literature values for fluorescent dextrans, red markers the mean effective diffusion estimates obtained by in vitro experiments and PyFRAP analysis, and grey markers the theoretical estimates derived from the Einstein-Stokes equation (see Supplementary Note 3). Red error bars show the standard deviation of PyFRAP's effective diffusion estimates, and black error bars show the standard deviation of the literature values listed in Supplementary Table 7. The grey line represents a linear regression fit to the theoretical values. **b** Results of FRAP/iFRAP experiments for the photoconvertible protein Dendra2. **c** Results of simulations investigating the influence of tortuosity on effective diffusion for differently packed bead experiments. Grey and black markers indicate 2D and 3D simulation results, respectively. **d** Results of fluorescent dextran experiments demonstrating the impact of tortuosity on effective diffusivities. **e** Results of GFP experiments to analyse the impact of tortuosity, embryonic extracelluar environment, protein production, and extracellular binding on effective diffusion estimates. Box plots in **b**, **d**, **e** show median (orange line), mean (black horizontal line inside box), 25% quantiles (box), and all included data points (red markers). Whiskers extend to the smallest data point within the 1.5 interquartile range of the lower quartile, and to the largest data point within the 1.5 interquartile range of the upper quartile

tortuous movement can be described by the diffusion hindrance factor (also known as diffusion permeability[62]) $\theta = 1/\lambda^2 = D^*/D$, where λ is the tortuosity, D^* is the effective diffusion coefficient (with obstacles), and D is the free diffusion coefficient (without obstacles). To assess the expected magnitude of tortuosity on altering effective diffusivity, we first performed numerical simulations of FRAP experiments with and without radial obstacles in two- and three-dimensional geometries. Radial obstacles were either placed regularly, randomly, or following a nearly-ideal packing scheme, resulting in an extracellular volume fraction (EVF, i.e., the space available for molecules to diffuse) ranging from 78% down to 25% (Supplementary Fig. 7). These simulations demonstrated that recovery rates are slowed down as the EVF decreases (Fig. 5c, Supplementary Table 8). If the geometry is two-dimensional, an EVF of 25% results in an expected reduction in effective diffusivity of approximately 66%. In three-dimensional simulation experiments, we obtained a reduction of effective diffusion coefficients by 40% when the EVF was decreased to 38% (Supplementary Note 3).

To determine whether the presence of obstacles decreases effective diffusivity as predicted by our simulations, we performed FRAP assays in vitro with a fluorescein-coupled 70 kDa dextran (Fig. 4i, j) or recombinant GFP (Supplementary Fig. 8) in the presence of polyacrylamide beads. Consistent with our predictions, recovery was slower in the presence of beads, and the effective diffusivity of fluorescein-coupled 70 kDa dextran dropped from 24.1 ± 0.4 (standard error) μm^2/s to 14.9 ± 0.5 μm^2/s, suggesting an EVF of 39% ($\theta = 0.61$) (Fig. 5c, d, Supplementary Tables 8 and 9). Similarly, for recombinant GFP effective diffusivity dropped by 18% (Fig. 5e, Supplementary Table 10, Supplementary Fig. 8a–d).

To assess diffusion hindrance in vivo, we injected recombinant GFP protein into the extracellular space of living zebrafish embryos. We found that the effective diffusivity in vivo was 60% lower than for freely diffusing GFP, and 53% lower than in in vitro experiments with beads (Fig. 5e, Supplementary Table 10, Supplementary Fig. 8e, f). This suggests that tortuosity in zebrafish embryos is higher than in the in vitro bead assay. Importantly, we found similar diffusion coefficients of 36 μm^2/s in vivo for extracellularly injected recombinant GFP and secreted GFP constantly produced from injected mRNA, showing that PyFRAP can properly account for both diffusion and production (Fig. 5e, Supplementary Table 10, Supplementary Fig. 8g, h).

Finally, we examined the effects of binding interactions on effective diffusivity. GFP presumably does not experience significant binding interactions with extracellular molecules in zebrafish embryos, although its movement is affected by obstructions like cells and cellular extensions. In contrast, secreted signalling molecules are expected to interact with extracellular molecules such as receptors and extracellular matrix components[22]. To assess the effect that interactions with extracellular molecules might have on secreted signalling molecules, we injected mRNA encoding the TGFβ-superfamily member Squint fused to GFP into zebrafish embryos[29]. Squint-GFP is approximately 1.5 times larger than GFP and according to the Einstein-Stokes equation (Supplementary Note 3) would be predicted to have an approximately 1.14 times smaller diffusion coefficient than GFP (effective diffusivity D(GFP) = 36 μm^2/s, expected effective diffusivity D(Squint-GFP) = 31 μm^2/s). However, we measured an effective diffusion coefficient of approximately 2 μm^2/s for Squint-GFP in living zebrafish embryos, ~90% lower than the predicted diffusion coefficient (Fig. 5e, Supplementary Table 10, Supplementary Figs. 8i, j and 9). These findings are consistent with previous measurements[29] and with the idea that interactions with so far unidentified binding partners slow down the effective diffusion of embryonic signalling molecules like Squint-GFP[22,29].

Discussion

Although FRAP analyses have long been used to measure relative differences in mobilities between macromolecules, analysis tools to accurately and quantitatively determine effective diffusion coefficients from FRAP data are lacking. Current analysis tools impose several simplifications including one-dimensional or two-dimensional reductions of complex three-dimensional geometries, idealised bleaching conditions, and the absence of important reaction kinetics. When the experimental conditions closely resemble the simplified assumptions, e.g., small bleach domains and negligible reaction kinetics, these tools can rapidly provide reasonable diffusion estimates (Fig. 3c). However, experimental conditions are often more complex, and the use of simplified assumptions may yield drastically divergent diffusion coefficients (Fig. 1d–f). PyFRAP addresses these shortcomings by providing a simulation-based analysis that incorporates realistic geometries, bleaching conditions and reaction kinetics.

We found that PyFRAP's data analysis pipeline is numerically reliable, recovered the correct diffusion coefficients and reaction kinetics, and additionally predicted the correct underlying reaction-diffusion models for simulated test data sets with known diffusion, production, and degradation parameters. PyFRAP consistently outperformed all other tested software packages, demonstrating its strength as a novel FRAP analysis method. Furthermore, PyFRAP was able to determine diffusion coefficients comparable to both theoretical and previously experimentally measured estimates for macromolecules with molecular weights ranging over two orders of magnitude. Since PyFRAP can analyse data independently of any assumptions about the initial conditions, it is suitable to analyse both FRAP and iFRAP experiments. iFRAP has recently been developed as an alternative to FRAP due the increasing availability of photoconvertible proteins and allows ignoring reaction kinetics such as production. We performed tandem FRAP/iFRAP experiments to analyse the diffusion of the photoconvertible protein Dendra2 and found equal diffusion coefficients in vitro with both methods.

FRAP experiments are typically performed in tissues in which macromolecules need to move around cellular obstacles, resulting in slower fluorescence recovery. To determine how this tortuosity might affect diffusion coefficients estimated from FRAP experiments, we first simulated FRAP experiments in two- and three-dimensional geometries introducing radial beads at different densities to vary the extracellular volume fraction (EVF). Our simulations showed a strong correlation between tortuosity and effective diffusivity and agree with previous theoretical work including Monte-Carlo simulations and homogenisation theory[62–65]. We then tested the predictions from these simulations with in vitro experiments using polyacrylamide beads to mimic cells. Compared to experiments without beads, the effective diffusion coefficient decreased by 39% (diffusion hindrance factor $\theta = 0.61$) for 70 kDa fluorescein-dextran and 18% ($\theta = 0.82$) for recombinant GFP. In living zebrafish embryos, effective diffusivity is much further reduced (Fig. 5e). It is unlikely that this is due to different viscosity of the extracellular medium in vivo, since free GFP diffusion is only marginally reduced in zebrafish embryos[22]. Instead, it is plausible that the complex geometries of real extracelluar environments—which include filopodia, extracellular matrix, and cavities that might act as dead end pores—could further increase tortuosity[62]. Finally, most in vivo FRAP experiments are affected by biochemical reactions such as

production and degradation of proteins, which must be taken into account for accurate diffusion coefficient estimates (Fig. 1c, f). PyFRAP offers various models for different reaction kinetics and can accurately estimate diffusion coefficients from data sets that include constant production and degradation.

PyFRAP measures effective diffusion, but due to its built-in PDE solver it could be extended in the future to consider spatially inhomogeneous kinetics and advective fluxes and to perhaps even determine the diffusivities of individual species in polydisperse mixtures of fluorescent molecules[66,67]. While PyFRAP can simulate three-dimensional FRAP experiments, FRAP data is currently almost exclusively obtained from two-dimensional confocal microscopy. In recent years, the development of light-sheet microscopy made fast three-dimensional imaging with low phototoxicity feasible[68]. In the future, PyFRAP's image analysis tools could be extended to fit light-sheet microscopy data, which might provide deeper insights into the three-dimensional dynamics of molecule movement including convective flows or spatially inhomogeneous diffusion.

Methods

FRAP/iFRAP experiments in vitro. FRAP experiments to measure pure diffusion and tortuosity effects were conducted in a frustum-like plexiglass hole. Holes around 700 µm in diameter and about 100 µm in depth were drilled into a plexiglass block using a dental drill. Due to the small depth, the resulting shape was frustum-like with an upper base of 510 µm diameter.

Holes were filled with aqueous solutions of FITC-/fluorescein-labelled dextrans of different sizes, recombinant GFP, or Dendra2 protein (Supplementary Table 5) using a micro-pipette. Dendra2 protein was centrifuged at 16,000 × *g* for 30 min at 4 °C to remove protein aggregates. Excess liquid was removed from the hole by pipetting under observation with a stereo microscope.

To model the effect of tortuosity in the in vitro FRAP experiments, polyacrylamide beads were added to the sample solution. The microbeads (Bio-Gel P-2 Gel, <45 µm wet bead size) were first soaked in distilled water overnight for hydration. The beads were then centrifuged at 300 × *g*, the supernatant removed, and the required quantity of beads transferred to another tube for resuspension in fluorescein-dextran or GFP+BSA solution. This was repeated and followed by removal of the supernatant, leaving a concentrated slurry of beads and fluorescent solution for the experiments. The beads were transferred into the plexiglass template and settled within 1–2 min.

To prevent evaporation, mineral oil (Sigma) was placed around the solution before sealing the hole with a cover slip (No 1.5). Supplementary Fig. 1a outlines the sample preparation process for in vitro experiments. The sample was upended carefully and mounted on an inverted confocal microscope. Images were taken using an LSM 780 NLO microscope (ZEISS) with an LD LCI Plan-Apochromat 25×/0.8 Imm Korr DIC objective (ZEISS) and immersion oil (Immersol TM W, n = 1.334 at 23 °C, ZEISS). First, a plane approximately in the middle of the hole was chosen and the z-position set to zero. Then, the position of the highest and lowest point was determined. Cuboid volumes (141.42 µm × 141.42 µm × 100 µm) were bleached by imaging a z-stack at highest laser power (488 nm) or photoconverted at moderate laser power. Time series of 300 images (512 pixels × 512 pixels) were taken with a speed of 1 frame/s (pixel dwell time: 3.15 µs) over a duration of 5 min. The zoom was set to 0.7, and the resulting images had a size of 566.79 µm × 566.79 µm.

After the FRAP experiment, the template was cleaned using distilled water, soap, and an interdental toothbrush.

FRAP experiments in vivo. Zebrafish embryos (*Danio rerio*) were collected 10 min after mating and proteolytically dechorionated[22,29,42]. For the experiments with recombinant GFP, 100 pg of recombinant GFP were injected into the extracelluar space when zebrafish embryos reached high stage[22,29,69] (Supplementary Table 10). For experiments with secreted GFP[29], 100 pg of the mRNA encoding the fluorescent protein were injected at the one-cell stage. For experiments with Squint-GFP[29], either 30 or 200 pg of mRNA were injected at the one-cell stage. At dome stage, embryos were mounted in drops of 1% low-melting-point agarose animal pole down onto a glass-bottom dish (MatTek Corp. P35G-1.5-20-C), and as soon as the drops solidified covered with Danieau's medium[29,42] to prevent the embryos from drying out. Supplementary Fig. 1b outlines the in vivo sample preparation process.

Confocal images were taken roughly at a depth of 40 µm from the animal pole into the embryo. For data sets injected with 200 pg of Squint-GFP-encoding mRNA, images were acquired with the same settings as described for the in vitro experiments either with 1 frame/s for 300 s, or 1 frame/10 s for 3000 s. Images of embryos injected with 30 pg of Squint-GFP-encoding mRNA were taken with a spatial resolution of 340.08 µm × 340.08 µm and 1 frame/10 s for 3000 s. Data sets for recombinant GFP in vivo were acquired with the same microscope settings as the experiments conducted in vitro.

ROI selection. PyFRAP's image analysis depends on defining specific ROIs for the experimental data and simulations. Users can define multiple different geometrical shapes of ROIs in three-dimensional space such as cylinders, prisms, and any kind of addition or subtraction between ROIs. The specified ROIs are then used for image analysis, estimating concentrations outside the field of view, evaluating the simulation, and fitting to the analysed data. PyFRAP is equipped with an ROI manager and wizards for several standard sets of ROIs.

Image analysis. Let Ω_i (with $i \in \{1, 2, \ldots, n_\Omega\}$ and n_Ω the number of ROIs) be the list of ROIs specified for PyFRAP's analysis. The mean intensity over the ROI Ω_i at time t_j (with $j \in \{1, 2, \ldots, n_t\}$ and n_t the number of images) is then calculated by

$$\bar{I}_{\Omega_i}(t_j) = \frac{1}{A_i} \sum_{(x_k, y_l) \in \Omega_i} I(x_k, y_l, t_j) \quad (1)$$

where A_i is the area of Ω_i, and $I(x_k, y_l, t_j)$ is the intensity at pixel (x_k, y_l) (with $k \in \{1, 2, \ldots, n_x\}$ and n_x the number of rows in the images, and with $l \in \{1, 2, \ldots, n_y\}$ and n_y the number of columns in the images).

FRAP image data were analysed within the ROIs Ω_{bleached} and Ω_{slice}. Ω_{slice} was defined as a circular domain with centre C_{slice} and radius r_{slice}. Since the imaging depth varied between experiments, both C_{slice} and r_{slice} were cropped for each data set. The bleached ROI Ω_{bleached} was defined as a square with sidelength s_{bleached} and left-lower corner at $O_{\text{bleached}} = C_{\text{slice}} - \frac{1}{2}(s_{\text{bleached}}, s_{\text{bleached}})$. The definition of both ROIs is shown in Supplementary Fig. 2a.

Accounting for uneven illumination. Uneven imaging due to inhomogeneous sample illumination is a common problem in microscopy[37–39]. We implemented two solutions in PyFRAP to address this problem: (1) Normalisation by an image acquired before bleaching, and (2) applying a flattening mask derived from imaging a homogeneous fluorescent sample. The pixel-wise mean image over n_t images can be defined as

$$M(x_k, y_l, t_j) = \frac{1}{n_t} \sum_{j=1}^{n_t} I(x_k, y_l, t_j) \quad (2)$$

To avoid noise-induced singularities when normalising, PyFRAP computes a mean normalisation mask M_{pre} over multiple pre-bleach images, and then divides each image of the recovery time series pixel-wise by the computed mask

$$\tilde{I}(x_k, y_l, t_j) = \frac{I(x_k, y_l, t_j) + O_{\text{norm}}}{M_{\text{pre}}(x_k, y_l) + O_{\text{norm}}} \quad (3)$$

where O_{norm} is the optimal data offset computed via

$$O_{\text{norm}} = \max\left\{ \min_{k,j}\left(I(x_k, y_l, t_j)\right), \min_{k,j}\left(M_{\text{pre}}(x_k, y_l, t_j)\right) \right\} + 1 \quad (4)$$

Similarly, the flattening mask F is computed using the mean over multiple images of a fluorophore spread homogeneously across a cover slip, M_{flat}:

$$F(x_k, y_l) = \frac{\max_k(M_{\text{flat}}(x_k, y_l)) + O_{\text{flat}}}{M_{\text{flat}}(x_k, y_l) + O_{\text{flat}}} \quad (5)$$

Similar to the normalisation in Eq. (4), the optimal data offset O_{flat} is obtained by taking the maximum over all minimum intensities of images in both recovery and flattening data sets. The recovery data set is obtained by pixel-wise multiplication of the recovery image with the flattening mask obtained in Eq. (5):

$$\tilde{I}(x_k, y_l, t_j) = F(x_k, y_l) \cdot I(x_k, y_l, t_j) \quad (6)$$

An outline of both correction methods is shown in Supplementary Fig. 2c.

In the present study, two pre-bleach images were acquired per sample for the normalisation mask, and two images of fluorescein conjugated to a 40 kDa dextran or recombinant GFP homogeneously spread on a cover slip were acquired for the flattening approach. The effects of flattening and normalisation on data analysis are described in Supplementary Note 1.

Accounting for background fluorescence. Background subtraction is a standard procedure to extract the true signal of microscope images[38,39]. Similar to the flattening and normalisation masks, PyFRAP takes the average over multiple pixels to obtain a background mask and then subtracts it pixel-wise[38,39]:

$$\tilde{I}(x_k, y_l, t_j) = I(x_k, y_l, t_j) - M_{\text{bkgd}}(x_k, y_l) \quad (7)$$

The mean of two images without a sample was determined to compute a background mask. The effect of background subtraction is discussed in Supplementary Note 1.

Application of filters for noise reduction. Microscope data sets are often noisy, causing problems for normalisation and simulation. PyFRAP smooths noisy pixels by either applying a Gaussian blur with standard deviation σ_{gauss}, or a median filter with filter window radius r_{median}. We found that $\sigma_{gauss} = 2$ and $r_{median} = 5$ provided good results for the data in the present study (see Supplementary Note 1).

Accounting for fluorescence outside of the imaging view. In some cases it is not possible to capture the whole sample in one field of view under the microscope, and the concentration in the non-imaged regions needs to be estimated. PyFRAP solves this by letting users define an ROI Ω_{rim} to select an approximation of the average unbleached intensity from the first image of the recovery image series:

$$c_{rim} = \frac{1}{A_{rim}} \sum_{(x_k, y_l) \in \Omega_{rim}} I(x_k, y_l, t_0) \tag{8}$$

Ω_{rim} is defined by $\Omega_{rim} = \Omega_{slice} - \Omega_{centre}$, where

$$\Omega_{center} = \left\{ (x_k, y_l) | \sqrt{(x_k - x_c)^2 + (y_l - yc)^2} < \rho_{rim} r_{slice} \right\} \tag{9}$$

with (x_c, y_c) the centre pixel coordinates of the image. Ω_{rim} thus defines a small annulus comprising all pixels (x_k, y_l) inside Ω_{slice} that have a distance of at least $\rho_{rim} r_{slice}$ from the centre of the image (Supplementary Fig. 2b). $\rho_{rim} = 0.66$ and $\rho_{rim} = 0.4585$ were found to provide good values for the in vitro and in vivo experiments, respectively.

Simulations. PyFRAP simulates FRAP experiments numerically. Ignoring reaction kinetics, a FRAP experiment can be described by the diffusion equation

$$\frac{\partial c(\mathbf{x}, t)}{\partial t} = D \nabla^2 c(\mathbf{x}, t), \mathbf{x} \in \Omega \tag{10}$$

where $c(\mathbf{x}, t)$ is the concentration of the measured molecule at position $\mathbf{x} = \langle x, y, z \rangle$ and time t inside the domain Ω, and D is its scalar diffusion coefficient. The diffusion coefficient is assumed to be constant and homogeneous.

Since the sample is assumed to be a closed system, no-flux Neumann boundary conditions were defined as

$$\frac{\partial c(\mathbf{x}, t)}{\partial \mathbf{n}} = 0, \mathbf{x} \in \partial\Omega \tag{11}$$

where $\mathbf{n}$ is the normal vector of the boundary $\partial\Omega$ at position $\mathbf{x}$.

Initial conditions for simulations. The initial conditions are given by the bilinear interpolation P between pixels of the initial post-bleaching image:

$$P(x, y) = \frac{(x_2 - x, x - x_1)}{(x_1 - x_2)(y_2 - y_1)} \cdot \begin{pmatrix} I(x_1, y_1) & I(x_1, y_2) \\ I(x_2, y_1) & I(x_2, y_2) \end{pmatrix} \cdot \begin{pmatrix} y_2 - y \\ y - y_1 \end{pmatrix} \tag{12}$$

$I(x_{k'}, y_{l'})$ with $k', l' \in \{1, 2\}$ represents the intensities in the initial image of the four pixels surrounding (x, y). If (x, y) is outside of the visible ROI in the initial image (Ω_1), the rim concentration c_{rim} given in Eq. (8) is combined piece-wise with Eq. (12) to give the initial condition

$$c(\mathbf{x}, 0) = \begin{cases} P(x, y) & \text{if} (x, y) \in \Omega_1 \forall z \\ c_{rim} & \text{otherwise} \end{cases} \tag{13}$$

Simulation geometry. PyFRAP comes with its own geometry definition tool. Geometry definitions can then be converted into the Gmsh format[43] for meshing. PyFRAP can read Gmsh's geometry definition files, use Gmsh's mesh files, or import STereoLithography (.stl) files, allowing users to define arbitrary two- and three-dimensional geometries. This gives users the ability to describe a realistic FRAP experiment geometry with the necessary precision.

The simulation geometry Ω for the in vitro experiments was a conical frustum with upper radius $r_{upper} = 317.65$ pixels, lower radius $r_{lower} = 224.25$ pixels, and height $h \approx 90.33$ pixels (Supplementary Fig. 4b). For the in vivo experiments, the simulation geometry resembled a zebrafish embryo at dome stage, i.e., the intersection of two hemispheres intersecting each other at the equator of the outer hemisphere. Since the geometry depends on the radius of the embryo in the initial image, $r_{imaging}$ was calculated separately for each experiment[29,70]. Assuming that the radius of the inner hemisphere r_{inner} is 10% larger than the one of the outer hemisphere, r_{outer}, the geometry can be computed by

$$\begin{aligned} r_{outer} &= \frac{r_{imaging}^2 + h_{imaging}^2}{-2h_{imaging}} \\ r_{inner} &= 1.1 \cdot r_{outer} \\ d_{center} &= \sqrt{r_{inner}^2 - r_{outer}^2} \end{aligned} \tag{14}$$

where d_{centre} is the distance between the two centres of the hemispheres. Supplementary Fig. 4a shows a schematic of the zebrafish dome stage geometry.

Meshing for simulations. PyFRAP discretises simulation geometries using Gmsh[43] in combination with TetGen[44] into tetrahedral meshes. PyFRAP utilises almost all functionalities of Gmsh—such as boundary layer meshes, attractor meshes, mesh merging and mesh refinement—allowing users to apply fine meshes where they are needed.

The overall default element size in the present study was $\nu = 25$ pixels^3. To overcome numerical instabilities, such as Gibbs phenomena at the boundary of $\Omega_{bleached}$, the mesh around the bleached area boundary was refined using a boundary layer mesh of thickness $w_{BL} = 30$ pixels and element size $\nu_{BL} = 15$ pixels^3. Since only the simulation inside Ω_{slice} and $\Omega_{bleached}$ is used to fit the FRAP experiments, the mesh inside Ω_{slice} was also refined to an element size of $\nu_{slice} = 15$ pixels^3. Supplementary Fig. 4c, e shows an example of a tetrahedral mesh with both slice refinement and boundary layer meshes for the zebrafish dome geometry described in the previous section.

PDE solver. All partial differential equations (PDEs) were simulated using the FiPy toolbox[32]. The LU factorisation algorithm or the Preconditioned-Conjugated-Gradient algorithm implemented in PySparse were used to solve the linear system at each time step.

Simulation parameters. All simulations were performed with a reference diffusion coefficient of $D = 50$ pixels^2/s. To ensure that the simulations run long enough to capture the full recovery of the FRAP experiment, the end time point of the simulation was set to $t_{sim,end} = 1680$ s for experiments conducted with an acquisition interval of $\Delta t = 1$ s. Since the recovery is steepest at the beginning of the simulations, a logarithmic time-stepping scheme was used, making early time steps shorter to achieve greater accuracy. A summary of all simulation parameters used to analyse the FRAP data in the present study is given in Supplementary Table 11.

Fitting. To avoid the need to re-simulate the FRAP experiment for each choice of diffusion coefficient D, PyFRAP uses the self-similarity property of the solution to Eq. (10). For example, a simulated FRAP experiment with the diffusion coefficient $D = 50$ pixels^2/s results in the same recovery behaviour as an experiment with the diffusion coefficient $D = 200$ pixels^2/s, just four times slower. This can be described as

$$c(\mathbf{x}, t, D) = c\left(\mathbf{x}, \frac{D_{ref}}{D} t, D_{ref}\right) \tag{15}$$

where D_{ref} is the reference diffusion coefficient, i.e., the diffusion coefficient used for the simulation of Eq. (10). Supplementary Fig. 4d shows simulated recovery curves for various diffusion coefficients illustrating this self-similarity property.

PyFRAP allows users to fit four different models to FRAP data: (1) Pure diffusion, (2) diffusion and production, (3) diffusion and degradation, (4) diffusion with degradation and production, and each of these models with an additional set of equalisation parameters (see below). In case of pure diffusion, the solution for the diffusion coefficient D over a given ROI Ω_i is simply given by the volume integral of the solution in Eq. (15):

$$\bar{c}(\Omega_i, t, D) \equiv \int_{\mathbf{x} \in \Omega_i} c(\mathbf{x}, t, D) \mathrm{d}V \tag{16}$$

A summary of all parameters used to fit the FRAP data in the present study is given in Supplementary Table 12.

Extending the diffusion model with reaction kinetics. Spatially uniform production was added to the scaled FRAP model defined in Eq. (15) or in Eq. (20) by

$$\bar{c}(\Omega_i, t, D) = c(\Omega_i, t, D) + k_2 t \tag{17}$$

where k_2 is the production rate. To add spatially uniform degradation, the resulting solution is given by

$$\bar{c}(\Omega_i, t, D) = c(\Omega_i, t, D) e^{-k_1 t} \tag{18}$$

The parameter k_1 represents the degradation rate constant. Adding both degradation and production to the system results in the following superposition of solutions:

$$\bar{c}(\Omega_i, t, D) = c(\Omega_i, t, D) e^{-k_1 t} + \left(1 + e^{-k_1 t}\right) \frac{k_2}{k_1} \tag{19}$$

Accounting for varying fluorophore fractions by equalisation. FRAP experiments can vary in intensity during the experiment due to, for example, an increase or decrease in extracellular volume fraction, due to molecules moving in and out of the imaging plane, or due to an immobile fraction of fluorescent molecules. These effects are accounted for by equalisation, which normalises both simulation and data recovery curves to an equivalent scale between 0 and 1. During

the fitting process, the simulated recovery curves are slightly lifted or lowered to better resemble overall fluorescence levels. This can be written as

$$\tilde{c}(\Omega_i, t, D) = \frac{1}{\bar{c}_{\max} E_i}\left(\int_{\mathbf{x}\in\Omega_i} \bar{c}(\mathbf{x}, t, D)\mathrm{d}V - \bar{c}_{\min}\right) \quad (20)$$

where E_i is the equalisation factor for ROI Ω_i. The background $\bar{c}_{\min}$ was chosen to be the smallest concentration of the bleached ROI inside the imaging region (Ω_{bleached}), over the whole time series

$$\bar{c}_{\min} = \min_t \int_{\mathbf{x}\in\Omega_{\text{bleached}}} \bar{c}(\mathbf{x}, t)\mathrm{d}V \quad (21)$$

and the normalisation value $\bar{c}_{\max}$ to be the maximum concentration inside the whole imaging ROI (Ω_{slice}), over the whole time series

$$\bar{c}_{\max} = \max_t \int_{\mathbf{x}\in\Omega_{\text{slice}}} \bar{c}(\mathbf{x}, t)\mathrm{d}V \quad (22)$$

Minimisation and parameter estimation. Choosing one of the models defined in Eqs. (15), (16), (17), (18) and (19), the sum of squared differences, SSD, was calculated by

$$\mathrm{SSD} = \sum_{\mathrm{i}}\sum_{\mathrm{t_j}}\left(\mathfrak{e}\left(\Omega_{\mathrm{i}}, \mathrm{t_j}, \mathrm{D}\right) - \mathrm{I}_{\Omega_{\mathrm{i}}}\left(\mathrm{t_j}\right)\right)^2 \quad (23)$$

where $t_j \in 0, .., T$ are all time points of the FRAP data set, and $\Omega_i \in \Omega_{\text{bleached}}, \Omega_{\text{slice}}$ are the two ROIs of interest yielding a mean optimal fit between all fitted ROIs. The minimisation of Eq. (23) was carried out using a constrained Nelder–Mead algorithm[49]. Since especially for a larger number of degrees of freedom the minimisation algorithm tended to stop in local minima, initial guesses for the diffusion coefficient D were tested over two orders of magnitude, and the fit yielding the minimum SSD was considered optimal.

Analysis speed. Details of the method to determine PyFRAP's performance in terms of analysis speed are described in Supplementary Note 4 and Supplementary Tables 13 and 14.

Statistics. PyFRAP offers four statistical tools (Supplementary Table 2) allowing users to test whether the estimated diffusion coefficient for one experimental group is significantly different from another one. The statistical tools include the two most prominent parametric significance tests, the Student's t-test[56] and a modification of this test, Welch's t-test[71], which both assume normally distributed test groups. PyFRAP also provides the Shapiro–Wilk test, allowing PyFRAP users to quickly assess whether the estimated diffusion coefficients follow a normal distribution. The Shapiro–Wilk test was recently found to have the best sensitivity compared to other common normality tests[72]. If normality cannot be guaranteed, PyFRAP offers two non-parametric ranked hypothesis tests: The Wilcoxon signed-rank test[73] and the Mann–Whitney U test[57].

Often, the underlying reaction kinetics of FRAP experiments or the relevance of their contribution might be unknown[54]. However, models with more parameters generally provide better fits than simpler models. The AIC[55] allows users to evaluate which model fits the data the best while keeping model complexity low. For this, let

$$\Theta := (k_1, k_2, D, E_1, E_2, \dots) \quad (24)$$

be the vector of unknown diffusion coefficient D, reaction rates k_1 and k_2, and E_1, E_2, … a list of equalisation factors. Moreover, let $m = m(\Theta)$ be the model prediction using Θ. Assuming that the data is distributed normally around the model

$$d_i - m_i \sim \mathcal{N}(\mu, \sigma) \quad (25)$$

the log-likelihood function at data point i, L_i becomes

$$L_i(\Theta|d_i - m_i) = (d_i - m_i)^2 \quad (26)$$

and is thus identical with the sum of squared differences used for optimisation in Eq. (23):

$$L(\Theta) = \sum_i L_i(\Theta) = \mathrm{SSD} \quad (27)$$

The AIC is then given by

$$\mathrm{AIC} = 2\mathrm{k} - 2\mathrm{L}\left(\hat{\Theta}\right) \quad (28)$$

where k is the number of parameters of model m and

$$\hat{\Theta} = \mathrm{argmin}(L(\Theta|d_i - m_i, i = 1\ldots n)) \quad (29)$$

is the parameter configuration Θ minimising the log-likelihood function (Eq. (27)), i.e., the parameter configuration returned from fitting the model to data. The best model according to the AIC is then $m(\mathrm{argmin}(\mathrm{AIC}_i - \mathrm{AIC}_{\min}))$. If the number of sample points is small, the corrected AIC (AICc) provides a more accurate model selection technique:

$$\mathrm{AICc} = \mathrm{AIC} + \frac{2\mathrm{k}(\mathrm{k}+1)}{\mathrm{n}-\mathrm{k}-1} \quad (30)$$

where n is the number of data points. A rule of thumb for when the AIC (Eq. (28)) or its corrected version (Eq. (30)) should be used is

$$\frac{n}{k} > 40 \quad (31)$$

PyFRAP automatically selects which statistical model is more appropriate if not specified differently.

PyFRAP also provides R^2-values for each fit: An R^2-value for each fitted ROI and the product and mean of these values. In general, PyFRAP computes an R^2-value of an ROI by

$$R^2 = 1 - \frac{\sum_i m_i - d_i}{\sum_i d_i - \bar{d}} \quad (32)$$

where m_i and d_i are model and data at time i, and $\bar{d}$ is the mean over all data points.

Data exclusion. We performed a rigorous screen of all data sets, and we excluded data sets that showed strong radial inhomogeneities in the first post-bleach image due to inhomogeneous distribution of fluorescent molecules. Moreover, we excluded in vitro data sets that showed unstable distributions in the overall fluorescence intensity levels, indicating incomplete bleaching through the depth of the sample.

Code availability. PyFRAP is freely available from https://mueller-lab.github.io/PyFRAP.

Data availability. All data is available from the corresponding author upon request.

Received: 24 September 2017 Accepted: 26 March 2018
Published online: 20 April 2018

References

1. Crick, F. Diffusion in embryogenesis. *Nature* **255**, 420–422 (1970).
2. Lander, A. D., Nie, Q. & Wan, F. Y. M. Do morphogen gradients arise by diffusion? *Dev. Cell.* **2**, 785–796 (2002).
3. Müller, P. & Schier, A. F. Extracellular movement of signaling molecules. *Dev. Cell.* **21,**145-158 (2011).
4. Poo, M. M. & Cone, R. A. Lateral diffusion of rhodopsin in Necturus rods. *Exp. Eye Res.* **17**, 503–507 (1973).
5. Liebman, P. A. & Entine, G. Lateral diffusion of visual pigment in photoreceptor disk membranes. *Science* **185**, 457–459 (1974).
6. Loren, N. et al. Fluorescence recovery after photobleaching in material and life sciences: putting theory into practice. *Q. Rev. Biophys.* **48**, 323–387 (2015).
7. Lippincott-Schwartz, J., Altan-Bonnet, N. & Patterson, G. H. Photobleaching and photoactivation: following protein dynamics in living cells. *Nat. Cell Biol.* **5**, S7–S14 (2003).
8. Bancaud, A., Huet, S., Rabut, G. & Ellenberg, J. Fluorescence perturbation techniques to study mobility and molecular dynamics of proteins in live cells: FRAP, photoactivation, photoconversion, and FLIP. *Cold Spring Harb. Protoc.* **12**, 1303–1325 (2010).
9. Griffin, E. E., Odde, D. J. & Seydoux, G. Regulation of the MEX-5 gradient by a spatially segregated kinase/phosphatase cycle. *Cell* **146**, 955–958 (2011).
10. Zhou, S. et al. Free extracellular diffusion creates the Dpp morphogen gradient of the *Drosophila* wing disc. *Curr. Biol.* **22**, 668–675 (2012).
11. Axelrod, D., Koppel, D. E., Schlessinger, J., Elson, E. & Webb, W. W. Mobility measurement by analysis of fluorescence photobleaching recovery kinetics. *Biophys. J.* **16**, 1055–1069 (1976).

12. Soumpasis, D. Theoretical analysis of fluorescence photobleaching recovery experiments. *Biophys. J.* **41**, 95–97 (1983).
13. Sprague, B. L. & McNally, J. G. FRAP analysis of binding: proper and fitting. *Trends Cell Biol.* **15**, 84–91 (2005).
14. Kang, M., Day, C. A., Drake, K., Kenworthy, A. K. & DiBenedetto, E. A generalization of theory for two-dimensional Fluorescence Recovery After Photobleaching applicable to confocal laser scanning microscopes. *Biophys. J.* **97**, 1501–1511 (2009).
15. Deschout, H. et al. Straightforward FRAP for quantitative diffusion measurements with a laser scanning microscope. *Opt. Express* **18**, 22886–22905 (2010).
16. Kang, M., Day, C. A., Kenworthy, A. K. & DiBenedetto, E. Simplified equation to extract diffusion coefficients from confocal FRAP data. *Traffic* **13**, 1589–1600 (2012).
17. Kraft, L. J., Dowler, J. & Kenworthy, A. K. *Frap-toolbox: Software for the Analysis of Fluorescence Recovery after Photobleaching*. http://www.fraptoolbox.com Accessed 12 Dec 2016 (2014).
18. Lin, L. & Othmer, H. G. Improving parameter inference from FRAP data: an analysis motivated by pattern formation in the *Drosophila*wing disc. *Bull. Math. Biol.* **79**, 448–497 (2017).
19. Beaudouin, J., Mora-Bermúdez, F., Klee, T., Daigle, N. & Ellenberg, J. Dissecting the contribution of diffusion and interactions to the mobility of nuclear proteins. *Biophys. J.* **90**, 1878–1894 (2006).
20. Schaff, J. C., Cowan, A. E., Loew, L. M. & Moraru, I. I. Virtual FRAP-an experiment-oriented simulation tool. *Biophys. J.* **96**, 30a (2009).
21. Blumenthal, D., Goldstien, L., Edidin, M. & Gheber, L. A. Universal approach to FRAP analysis of arbitrary bleaching patterns. *Sci. Rep.* **5**, 11655 (2015).
22. Müller, P., Rogers, K. W., Yu, S. R., Brand, M. & Schier, A. F. Morphogen transport. *Development* **140**, 1621–1638 (2013).
23. Umulis, D. M. & Othmer, H. G. The importance of geometry in mathematical models of developing systems. *Curr. Opin. Genet. Dev.* **22**, 547–552 (2012).
24. Weiss, M. Challenges and artifacts in quantitative photobleaching experiments. *Traffic* **5**, 662–671 (2004).
25. Mazza, D., Cella, F., Vicidomini, G., Krol, S. & Diaspro, A. Role of three-dimensional bleach distribution in confocal and two-photon fluorescence recovery after photobleaching experiments. *Appl. Opt.* **46**, 7401–7411 (2007).
26. Machán, R., Foo, Y. H. & Wohland, T. On the equivalence of FCS and FRAP: simultaneous lipid membrane measurements. *Biophys. J.* **111**, 152–161 (2016).
27. Braga, J., Desterro, J. M. & Carmo-Fonseca, M. Intracellular macromolecular mobility measured by Fluorescence Recovery After Photobleaching with confocal laser scanning microscopes. *Mol. Biol. Cell.* **10**, 4749–4760 (2004).
28. Blischak, J. D., Davenport, E. R. & Wilson, G. A quick introduction to version control with Git and GitHub. *PLoS. Comput. Biol.* **12**, e1004668 (2016).
29. Müller, P. et al. Differential diffusivity of Nodal and Lefty underlies a reaction-diffusion patterning system. *Science* **336**, 721–724 (2012).
30. Sigaut, L., Ponce, M. L., Colman-Lerner, A. & Dawson, S. P. Optical techniques provide information on various effective diffusion coefficients in the presence of traps. *Phys. Rev. E* **82**, 051912 (2010).
31. Millman, K. J. & Aivazis, M. Python for scientists and engineers. *Comput. Sci. Eng.* **13**, 9–12 (2011).
32. Guyer, J. E., Wheeler, D. & Warren, J. A. FiPy: partial differential equations with Python. *Comput. Sci. Eng.* **11**, 6–15 (2009).
33. van der Walt, S. et al. scikit-image: Image processing in Python. *PeerJ* **2**, e453 (2014).
34. Jones, E. et al. *SciPy: Open source scientific tools for Python* (2001). http://www.scipy.org/
35. van der Walt, S., Colbert, C. & Varoquaux, G. The numpy array: a structure for efficient numerical computation. *Comput. Sci. Eng.* **13**, 22–30 (2011).
36. Hunter, J. D. Matplotlib: a 2D graphics environment. *Comput. Sci. Eng.* **9**, 90–95 (2007).
37. Lindblad, J. & Bengtsson, E. in *Proceedings of the 12th Scandinavian Conference on Image Analysis (SCIA)*, 264–271 (2001).
38. Waters, J. C. Accuracy and precision in quantitative fluorescence microscopy. *J. Cell. Biol.* **185**, 1135–1148 (2009).
39. Schwarzfischer, M. et al. in *Proceedings of Microscopic Image Analysis with Applications in Biology* (2011).
40. Gregor, T., Bialek, W., de Ruyter van Steveninck, R. R., Tank, D. W. & Wieschaus, E. F. Diffusion and scaling during early embryonic pattern formation. *Proc. Natl Acad. Sci. USA* **102**, 18403–18407 (2005).
41. Kicheva, A. et al. Kinetics of morphogen gradient formation. *Science* **5811**, 521–525 (2007).
42. Pomreinke, A. P. et al. Dynamics of BMP signaling and distribution during zebrafish dorsal-ventral patterning. *eLife* **6**, e25861 (2017).
43. Geuzaine, C. & Remacle, J.-F. Gmsh: a 3-D finite element mesh generator with built-in pre- and post-processing facilities. *Int. J. Numer. Methods Eng.* **79**, 1309–1331 (2009).
44. Si, H. Tetgen, a delaunay-based quality tetrahedral mesh generator. *ACM Trans. Math. Softw.* **41**, 11:1–11:36 (2015).
45. Sprague, B. L., Pego, R. L., Stavreva, D. A. & McNally, J. G. Analysis of binding reactions by fluorescence recovery after photobleaching. *Biophys. J.* **86**, 3473–3495 (2004).
46. Miura, K. *Frapcalc*. http://wiki.cmci.info/downloads/frap_analysis Accessed 12 Dec 2016 (2016).
47. Rapsomaniki, M. A. et al. EasyFRAP: an interactive, easy-to-use tool for qualitative and quantitative analysis of FRAP data. *Bioinformatics* **28**, 1800–1801 (2012).
48. Castle, B. T., Howard, S. A. & Odde, D. J. Assessment of transport mechanisms underlying the Bicoid morphogen gradient. *Cell. Mol. Bioeng.* **4**, 116–121 (2011).
49. Nelder, J. A. & Mead, R. A simplex method for function minimization. *Comput. J.* **7**, 308–313 (1965).
50. Nash, S. G. Newton-type minimization via the Lanczos method. *SIAM J. Numer. Anal.* **21**, 770–788 (1984).
51. Nocedal, J. & Wright, S. J. *Numerical optimization*. 2nd edn, (Springer, NY, 2006).
52. Bläßle, A. & Müller, P. PyFDAP: automated analysis of fluorescence decay after photoconversion (FDAP) experiments. *Bioinformatics* **6**, 972–974 (2015).
53. Rogers, K. W., Bläßle, A., Schier, A. F. & Müller, P. Measuring protein stability in living zebrafish embryos using fluorescence decay after photoconversion (FDAP). *J. Vis. Exp.* **95**, e52266 (2015).
54. Mai, J. et al. Are assumptions about the model type necessary in reaction-diffusion modeling? A FRAP application. *Biophys. J.* **100**, 1178–1188 (2011).
55. Akaike, H. A new look at the statistical model identification. *IEEE Trans. Autom. Control* **19**, 716–723 (1974).
56. Student. The probable error of a mean. *Biometrika* **6**, 1–25 (1908).
57. Mann, H. B. & Whitney, D. R. On a test of whether one of two random variables is stochastically larger than the other. *Ann. Math. Stat.* **18**, 50–60 (1947).
58. Shapiro, S. S. & Wilk, M. B. An analysis of variance test for normality (complete samples). *Biometrika* **52**, 591–611 (1965).
59. Aaron, J. *FRAP* https://de.mathworks.com/matlabcentral/fileexchange/47327-frap-zip Accessed 12 Dec 2016 (2016).
60. Ulrich, M. et al. Tropical-parameter estimation and simulation of reaction-diffusion models based on spatio-temporal microscopy images. *Bioinformatics* **22**, 2709–2710 (2006).
61. Gurskaya, N. G. et al. Engineering of a monomeric green-to-red photoactivatable fluorescent protein induced by blue light. *Nat. Biotechnol.* **24**, 461–465 (2006).
62. Hrabe, J., Hrabetová, S. & Segeth, K. A model of effective diffusion and tortuosity in the extracellular space of the brain. *Biophys. J.* **87**, 1606–1617 (2004).
63. Tao, L. & Nicholson, C. Maximum geometrical hindrance to diffusion in brain extracellular space surrounding uniformly spaced convex cells. *J. Theor. Biol.* **229**, 59–68 (2004).
64. Novak, I. L., Kraikivski, P. & Slepchenko, B. M. Diffusion in cytoplasm: effects of excluded volume due to internal membranes and cytoskeletal structures. *Biophys. J.* **97**, 758–767 (2009).
65. Donovan, P., Chehreghanianzabi, Y., Rathinam, M. & Zustiak, S. P. Homogenization theory for the prediction of obstructed solute diffusivity in macromolecular solutions. *PLoS ONE* **11**, e0146093 (2016).
66. Periasamy, N. & Verkman, A. S. Analysis of fluorophore diffusion by continuous distributions of diffusion coefficients: application to photobleaching measurements of multicomponent and anomalous diffusion. *Biophys. J.* **75**, 557–567 (1998).
67. Xiong, R. et al. Sizing nanomaterials in bio-fluids by cFRAP enables protein aggregation measurements and diagnosis of bio-barrier permeability. *Nat. Commun.* **7**, 12982 (2016).
68. Höckendorf, B., Thumberger, T. & Wittbrodt, J. Quantitative analysis of embryogenesis: a perspective for light sheet microscopy. *Dev. Cell.* **23**, 1111–1120 (2012).
69. Yu, S. R. et al. Fgf8 morphogen gradient forms by a source-sink mechanism with freely diffusing molecules. *Nature* **461**, 533–536 (2009).
70. Kimmel, C. B., Ballard, W. W., Kimmel, S. R., Ullmann, B. & Schilling, T. F. Stages of embryonic development of the zebrafish. *Dev. Dyn.* **203**, 253–310 (1995).
71. Welch, B. L. The generalisation of Student's problems when several different population variances are involved. *Biometrika* **34**, 28–35 (1947).
72. Razali, N. M. & Wah, Y. B. Power comparisons of Shapiro-Wilk, Kolmogorov-Smirnov, Lilliefors and Anderson-Darling tests. *J. Stat. Model. Anal.* **2**, 21–33 (2011).
73. Wilcoxon, F. Individual comparisons by ranking methods. *Biom. Bull.* **1**, 80–83 (1945).

Acknowledgements

We thank Ekkehard Kröwerath (University Hospital Tübingen, Centre for Dentistry, Oral Medicine, and Maxillofacial Surgery) for the preparation of plexiglass holes, Katherine Rogers and Fabian Fröhlich for discussions and suggestions, and Sarah Keim and Katherine Rogers for testing PyFRAP. This work was supported by the Emmy Noether Programme of the Deutsche Forschungsgemeinschaft, the Max Planck Society, and an ERC Starting Grant to P.M.

Author contributions

A.B., B.M.J. and P.M. conceived the study. A.B. and P.M. designed the software and performed data analysis and simulations. A.B. implemented the software. G.S., T.B., D.M. and H.P. conducted experiments. A.B. and P.M. wrote the manuscript.

Additional information

Supplementary Information accompanies this paper at https://doi.org/10.1038/s41467-018-03975-6.

Competing interests: The authors declare no competing interests.

Reprints and permission information is available online at http://npg.nature.com/reprintsandpermissions/

Publisher's note: Springer Nature remains neutral with regard to jurisdictional claims in published maps and institutional affiliations.

Supplementary Information for

Quantitative diffusion measurements using the open-source software PyFRAP

Alexander Bläßle[1], Gary Soh[1], Theresa Braun[1,2], David Mörsdorf[1], Hannes Preiß[1], Ben M. Jordan[3], and Patrick Müller[1,*]

[1]Friedrich Miescher Laboratory of the Max Planck Society, Tübingen, Germany
[2]Present address: University of Konstanz, Konstanz, Germany
[3]Department of Organismic and Evolutionary Biology, Harvard University, Cambridge, USA

[*]Correspondence to: patrick.mueller@tuebingen.mpg.de (P.M.)

This PDF includes:
Supplementary Notes 1-4
Supplementary Tables 1-14
Supplementary Figures 1-9
Supplementary References 1-43

Supplementary Note 1: Analysis method selection

To assess how image correction by flattening, normalisation, background subtraction, Gaussian blur, and median filter application affects effective diffusion estimates from FRAP experiments, we tested the 24 analysis combinations listed in Supplementary Table 1. We assessed whether 1) the resulting diffusion estimate D is affected, 2) the standard deviation σ of the estimated diffusion coefficients is affected (i.e. whether correcting and smoothing the images makes the diffusion estimates more exact), and 3) the goodness of the fits (i.e. R^2-values) is affected. We quantified the effect of an analysis option by

$$H(v, \alpha) = \frac{v(\alpha)}{v(\alpha_0)} \tag{1}$$

where $\alpha = \{n, f, b, g, m\}$ represents an analysis option defined by five binary entries indicating whether normalisation n, flattening f, background subtraction b, Gaussian blur g, or a median filter m was used. If we did not correct images, we denote this by α_0. The variable v describes the quantified result, such as the mean diffusion coefficient. Supplementary Fig. 3 shows a subset of this analysis for three different variables v: The mean diffusion coefficient D, the variance of diffusion coefficients σ, and the fit quality R^2. FRAP experiments performed in the present study were grouped by condition (*in vitro* experiments with free diffusion, *in vitro* experiments with beads, and *in vivo* experiments) to isolate condition-specific effects. We did not correct for potential illumination inhomogeneities in *in vivo* experiments, since these only covered a small centered area of the total image, and illumination is homogeneous in this region. Moreover, normalisation cannot be used for the analysis of *in vitro* experiments containing beads, since normalisation would introduce artificially high intensity areas at the locations of the beads.

If only normalisation and flattening were applied, we observed an increase of the apparent diffusion coefficients and an improvement in fit quality for free diffusion (Supplementary Fig. 3a,c). Both techniques only mildly affected the variance of diffusion coefficients (Supplementary Fig. 3b). Background subtraction had no effect on any measure (Supplementary Fig. 3a-c). Moreover, noise reduction or smoothing via median filter or Gaussian blur application tended to decrease the variance in all conditions (Supplementary Fig. 3b) and improve the fits for free diffusion (Supplementary Fig. 3b).

We also tested whether a combination of an illumination correction technique (n or f) with the remaining three manipulation techniques (b, g and m) can further improve the analysis. Supplementary Fig. 3d shows that this can lead to an increase in mean apparent diffusion estimates similar to those observed in Supplementary Fig. 3a. Moreover, applying a median filter or Gaussian blur in combination with flattening improves fit quality and decreases diffusion estimate variance (Supplementary Fig. 3e,f).

To keep the extent of image manipulation as minimal as possible while obtaining comparable low-variance estimates from high-quality fits, we only applied flattening to correct the images from *in vitro* experiments. Since both Gaussian blur and median filter treatments appeared to stabilise diffusion coefficient estimates (i.e. reducing their variance) to a similar extent, we restricted image smoothing to the application of a median filter for all other analyses.

Supplementary Note 2: Comparison of PyFRAP to other FRAP analysis software

We selected four current FRAP analysis software packages for comparison with PyFRAP: The two analytical programs easyFRAP[1] and FrapCalc[2], and the two numerical packages virtualFRAP[3] and simFRAP[4] (Supplementary Table 4).

To assess the performance of PyFRAP in comparison with other FRAP analysis software solutions, we created simulated FRAP data sets using PyFRAP's simulation toolbox. We found that PyFRAP and our in-house software based on MATLAB and COMSOL Multiphysics[5–7] produced identical simulated data, and we subsequently chose to use PyFRAP to simulate the experiments due to the ease of PyFRAP's scripting abilities. We simulated two-dimensional or three-dimensional FRAP experiments with circular bleaching spots of various sizes for a 300 s time-course. Two-dimensional simulated experiments were conducted in a circle with radius 215 μm, and three-dimensional experiments resembled a zebrafish at dome stage with $r_{\text{imaging}} = 215$ μm and $h_{\text{imaging}} = 80$ μm (see Methods section for details). Molecules were allowed to move with diffusion coefficients of 10 μm^2/s, 50 μm^2/s, or 200 μm^2/s, covering a range of typical diffusivities in biological samples. Bleached spots were placed in the center of the simulation geometry and comprised 5%, 10%, or 50% of the slice radius. We chose the boundary layer mesh described in the Methods section to envelope the bleached spot, guaranteeing numerical accuracy of the simulation experiments. PDEs were simulated over 4000 logarithmically-spaced time steps. The simulations were saved in a csv sheet specifically formatted for the use of easyFRAP or FrapCalc, or in 301 images by interpolation of the numerical solution onto a 512 μm $\times$ 512 μm grid. We then either imported and analysed the csv sheet using FrapCalc (`https://github.com/miura/FrapCalc` for IgorPro7) or easyFRAP, or read in and analysed the simulated images using simFRAP or virtualFRAP. The benchmarking analysis was performed using Microsoft Windows 8.1.

In contrast to other programs that determine absolute diffusion coefficients, easyFRAP only provides recovery half times ($1/\tau_{\frac{1}{2}}$). Thus, to compute diffusion coefficients from easyFRAP, we used the well-established[8] equation

$$D = \frac{-\omega^2 \ln\left(\frac{1}{2}\right)}{\tau_{\frac{1}{2}}}$$

with various dimensions of the bleached spot ω.

We used PyFRAP's standard pipeline to analyse the saved simulated FRAP images files in an unbiased manner, only constraining imaging depth and radius.

As mentioned in the main text, PyFRAP outperformed all tested software packages and exhibited the smallest error between predicted and simulated diffusion coefficients (Fig. 3c).

Supplementary Note 3: Data analysis and control experiments

Computation of theoretical diffusion coefficients

We compared our *in vitro* FRAP results for differently sized fluorescein-labeled dextrans to predictions derived from the Einstein-Stokes equation

$$D = \frac{k_{\mathrm{B}}T}{6\pi\eta r} \tag{2}$$

where $k_{\mathrm{B}} = 1.380\,648\,52 \times 10^{-23}\ \mathrm{m^2\,kg\,s^{-2}\,K^{-1}}$ is the Boltzmann constant. The FRAP experiments were conducted in an aqueous solution with viscosity $\eta = 0.9321 \times 10^{-3}\ \mathrm{kg\,s^{-1}\,m^{-1}}$ at $T = 296\ \mathrm{K}$. Stokes radii r of the fluorescent molecules were obtained from the manufacturers' websites and are listed along with the calculated theoretical diffusion coefficients in Supplementary Table 5.

FRAP experiments with different bleach window sizes

To test whether different bleach window size might lead to different diffusion coefficient estimates, we performed FRAP experiments with three different bleach window sizes: 34.01 $\mu\mathrm{m}$, 141.7 $\mu\mathrm{m}$, and 242.91 $\mu\mathrm{m}$. Using fluorescein-labeled dextrans of 40 kDa and 70 kDa molecular weight, we found that different bleach window sizes do not affect diffusion coefficient estimates determined by PyFRAP (Supplementary Fig. 6).

FRAP experiments can be executed over different spatial scales, from subcellular to tissue-level measurements. Our experiments were performed on spatial scales that are three orders of magnitude larger than the microscope's resolution limit. However, it is possible that FRAP experiments in very small samples with subcellular bleach areas may be affected by the imaging resolution, and future deconvolution-based approaches could be helpful to improve the measurement accuracy of PyFRAP in these cases.

Simulating tortuosity

The movement of molecules during FRAP experiments in biological samples is affected by obstacles such as cells, nuclei, or filopodia, and such tortuous molecule movements have been suggested to alter recovery rates and diffusion estimates[6].

To obtain a better understanding of how obstacles alter effective diffusion coefficients, we performed a simulation study in two- and three-dimensional geometries. We placed objects with a radius of $r_{\mathrm{Bead}} \approx 20\ \mu\mathrm{m}$ (similar to the dimensions of cells and beads used in the present study) in each geometry in three different ways: 1) Equally sized beads aligned as a regular grid (Supplementary Fig. 7a), 2) randomly placed within the domain with radii drawn from a cut-off normal distribution (Supplementary Fig. 7b,d), and 3) equally sized beads placed according to a hexagonal close-packing (Supplementary Fig. 7c). Beads were placed with different minimal gaps between them, ranging from 0.05 $\mu\mathrm{m}$ to 10 $\mu\mathrm{m}$. For 2D simulations, the overall geometry was a circle with radius 300 $\mu\mathrm{m}$. We chose a cylinder with equal radius and height of 100 $\mu\mathrm{m}$ or a cuboid with dimensions 600 $\mu\mathrm{m} \times 600\ \mu\mathrm{m} \times 100\ \mu\mathrm{m}$ for all 3D simulations experiments. The combination between various placement methods and gap sizes allowed us to vary the extracellular volume fraction (EVF) – i.e. the space available for the diffusing molecules – from 25% to 78%.

Confirming previous analyses[9–12], we found that the introduction of beads delayed molecule recovery in the bleached ROI, and the effect of tortuosity increased as the EVF decreased (Fig. 5b, Supplementary Fig. 7e,f, Supplementary Table 8). Moreover, the effect in two-dimensional experiments was more severe. For example, FRAP simulations with EVF $= 36\%$ reduced diffusion by 51% compared to only 40% for EVF $= 38\%$ in a three-dimensional simulation. Both observations are in line with theoretical predictions and previous results[9–12].

BSA does not affect fluorophore diffusivity

We found a stronger effect of bead-mediated tortuosity on 70 kDa fluorescein-labeled dextran molecules than on GFP *in vitro* (Fig. 5d,e). BSA was added to the aqueous solution with GFP to prevent the fluorescent protein from interacting with the plexiglass surface of the drilled hole in the *in vitro* experiments. To test whether BSA might also interact with the polyacrylamide beads and thus distort FRAP results, we repeated the experiments with 70 kDa fluorescein-labeled dextran both for pure diffusion with beads in addition to experiments with 70 kDa fluorescein-labeled dextran + BSA + beads. We found that BSA had no influence on the recovery rates, yielding equal results within standard error, i.e. 14.9 ± 2.1 μm^2/s for bead experiments and 15.1 ± 2.4 μm^2/s for experiments with additional BSA (Supplementary Fig. 9a).

Varying the experimental settings for Squint-GFP FRAP experiments does not consistently affect measured diffusion coefficients

For the FRAP experiments with Squint-GFP produced from injected mRNA, we acquired data sets varying the amount of injected mRNA, the frame rate and length of image acquisition, and the zoom factor of the microscope. Results were partitioned into three experimental groups, i.e. images recorded with 1) a frame rate of 1 frames/10 s for 3000 s with 30 pg of injected mRNA and a spatial resolution of 340.08 $\mu m \times 340.08$ μm, 2) a frame rate of 1 frame/10 s for 3000 s with 200 pg of injected mRNA and a spatial resolution of 566.79 $\mu m \times 566.79$ μm, and 3) a frame rate of 1 frame/s for 300 s with 200 pg of injected mRNA and a spatial resolution of 566.79 $\mu m \times 566.79$ μm.

There were no clear trends between different acquisition methods (Supplementary Fig. 9b). However, acquiring images at a higher frame rate for a shorter period of time appeared to make experiments and thus apparent diffusion coefficients more noisy, possibly resulting from the slow transport process underlying Squint-GFP diffusion.

Supplementary Note 4: PyFRAP analysis speed

To evaluate PyFRAP's analysis speed, we tested several analysis settings on different operating systems and computers. We designed three test cases: 1) A two-dimensional circular geometry similar to those used for the benchmarking simulations described in Supplementary Note 2, 2) a three-dimensional frustum geometry identical to the ones used to analyse the *in vitro* FRAP experiments described in the present work, and 3) a three-dimensional geometry resembling a zebrafish embryo at dome stage similar to our analysis of the *in vivo* experiments. The test data sets had identical properties as the data described for the respective experiments. A summary of all relevant test parameters can be found in Supplementary Table 13. All cases were tested on the three common operating systems Mac OSX, Microsoft Windows, and Ubuntu Linux, and the time from analysing the image data to mesh generation, simulation, and model fitting was measured for each test case. The results of these tests are summarised in Supplementary Table 14.

Note that PyFRAP does not allow parallel processing and only uses a single core of a CPU.

Supplementary Table 1. Combinations of image correction and smoothing methods used to analyse FRAP experiments. See Supplementary Fig. 3 for the results of this analysis. Note that flattening and normalisation were never applied at the same time since this would have distorted the image data.

Combination	Normalisation	Flattening	Background subtraction	Gaussian filter	Median filter
1	Off	Off	Off	Off	Off
2	Off	Off	Off	Off	On
3	Off	Off	Off	On	Off
4	Off	Off	Off	On	On
5	Off	Off	On	Off	Off
6	Off	Off	On	Off	On
7	Off	Off	On	On	Off
8	Off	Off	On	On	On
9	Off	On	Off	Off	Off
10	Off	On	Off	Off	On
11	Off	On	Off	On	Off
12	Off	On	Off	On	On
13	Off	On	On	Off	Off
14	Off	On	On	Off	On
15	Off	On	On	On	Off
16	Off	On	On	On	On
17	On	Off	Off	Off	Off
18	On	Off	Off	Off	On
19	On	Off	Off	On	Off
20	On	Off	Off	On	On
21	On	Off	On	Off	Off
22	On	Off	On	Off	On
23	On	Off	On	On	Off
24	On	Off	On	On	On

Supplementary Table 2. Statistical tools available in PyFRAP.

Method	Purpose	Type	Publication
Student's t-test	Significance testing	Parametric	[13]
Welch's t-test	Significance testing	Parametric	[14]
Wilcoxon signed-rank test	Significance testing	Non-parametric	[15]
Mann-Whitney U test	Significance testing	Non-parametric	[16]
Shapiro-Wilk test	Normality testing	Parametric	[17]
Akaike Information Criterion (AIC)	Model comparison	Parametric	[18]

Supplementary Table 3. Benchmarking PyFRAP against an in-house software combination of MATLAB and COMSOL Multiphysics. Data was simulated with MATLAB and COMSOL Multiphysics[5–7], and then fitted with PyFRAP for each of the four available reaction-diffusion models.

MATLAB + COMSOL Multiphysics			***PyFRAP***			***R^2-value***		***AIC***
D (μm^2/s)	**Degradation (10^{-4}/s)**	**Production (10^{-4} [c]/s)**	**D (μm^2/s)**	**Degradation (10^{-4}/s)**	**Production (10^{-4} [c]/s)**	**Bleached window**	**Slice**	**Correct model prediction**
Pure diffusion								
1	0	0	1.0	0	0	0.998	0.972	yes
5	0	0	4.8	0	0	1.000	0.910	yes
10	0	0	9.5	0	0	1.000	0.932	yes
40	0	0	39.1	0	0	0.999	0.870	yes
110	0	0	109.4	0	0	0.999	0.984	yes
200	0	0	199.1	0	0	0.999	0.990	yes
Diffusion + degradation								
1	5.0	0	1.0	5.8	0	0.998	0.921	yes
5	5.0	0	4.9	5.5	0	1.000	0.959	yes
10	5.0	0	9.7	5.4	0	1.000	0.972	yes
40	5.0	0	39.0	5.0	0	0.999	0.950	yes
110	5.0	0	108.1	4.9	0	0.999	0.943	yes
200	5.0	0	198.0	5.0	0	0.999	0.982	yes
Diffusion + production								
1	0	5.0	1.0	0	4.4	0.999	0.950	yes
5	0	5.0	5.0	0	4.6	1.000	0.972	yes
10	0	5.0	9.8	0	4.7	1.000	0.978	yes
40	0	5.0	38.9	0	5.0	1.000	0.991	yes
110	0	5.0	108.3	0	5.1	1.000	0.998	yes
200	0	5.0	198.4	0	5.0	1.000	0.999	yes
Diffusion + production + degradation								
1	5.0	7.0	1.1	4.8	6.2	0.992	0.845	no
5	5.0	7.0	5.0	4.8	6.4	1.000	0.894	no
10	5.0	7.0	9.5	5.9	7.5	1.000	0.910	no
40	5.0	7.0	39.2	4.1	6.3	1.000	0.979	no
110	5.0	7.0	105.2	9.7	12.0	0.999	0.995	no
200	5.0	7.0	192.6	11.6	13.3	1.000	0.996	no

Supplementary Table 4. Selection of current FRAP analysis software packages.

Software	Fit type	Result type	Input data	Publication	Platform	Tested	Comments
easyFRAP	Analytical	Qualitive	CSV	[1]	Windows, Mac OSX	Yes	Requires MATLAB Runtime, only produces $\tau_{1/2}$
FrapCalc	Analytical	Qualitive	CSV	[2]	Windows, Mac OSX	Yes	Requires IgorPro
FRAP	Analytical	Qualitive	Image files	[19]	Cross-platform	No	Requires specialised MATLAB toolboxes
simFRAP	Simulation	Quantitive	Image files	[4]	Cross-platform	Yes	Fiji Plugin
virtualFRAP	Simulation	Quantitive	Image files	[3]	Windows	Yes	
FRAPToolbox	Simulation	Quantitive	Image files	[20]	Cross-platform	No	Unable to read non-OME formats
Tropical	Simulation	Quantitive	Image files	[21]	Windows, Linux	No	Software unavailable

Supplementary Table 5. Fluorescent samples used for *in vitro* experiments, and their calculated theoretical diffusion coefficients. Theoretical values were only computed if an estimate of the molecule's Stokes radius could be found (see Supplementary Note 3 for details).

Fluorophore	**Molecular weight (kDa)**	**Concentration (µM)**	**Manufacturer**	**Stokes radius (nm)**	**Theoretical D ($\mu m^2/s$)**
Fluorescein-dextran	3	1	Thermo Fisher	1.36	171
Fluorescein-dextran	4	1, 15, 100	Sigma-Aldrich	1.4	166
Fluorescein-dextran	10	1	Thermo Fisher	2.3	101
Fluorescein-dextran	40	1	Thermo Fisher	4.5	52
Fluorescein-dextran	70	1	Sigma-Aldrich	6.0	39
Fluorescein-dextran	70	1	Thermo Fisher	6.0	39
Fluorescein-dextran	150	1	Sigma-Aldrich	8.5	27
Fluorescein-dextran	500	1	Thermo Fisher	15.8	15
GFP	32.7	4	Biovision	n.a.	n.a.
Dendra2	27.5	0.5	Hoelzel Diagnostics	n.a	n.a.

Supplementary Table 6. Diffusion coefficients determined by *in vitro* experiments and PyFRAP analysis. Theoretical values were only computed if an estimate of the molecule's Stokes radius could be found. Mean D values determined by PyFRAP as well as literature values are given with standard deviation.

			PyFRAP		***Literature***		
Dextran size (kDa)	**Manufacturer**	**D (µm²/s) theoretical**	**D (µm²/s) experimental**	**n**	**D (µm²/s) experimental**	**Technique**	**Reference**
3	Thermo Fisher	171	170.3 ± 21.9	19	161 ± 22	FCS	[22]
4	Sigma-Aldrich	166	181.1 ± 31.6	44	135 ± 10	FRAP	[23]
10	Thermo Fisher	101	83.1 ± 8.0	12	122 ± 4	FCS	[22]
40	Thermo Fisher	52	45.3 ± 11.1	57	47 ± 2	FCS	[22]
70	Thermo Fisher	39	26.9 ± 4.9	35	37 ± 7	FCS	[22]
70	Sigma-Aldrich	39	49.2 ± 5.6	31	30 ± 2	FRAP	[24]
150	Sigma-Aldrich	27	46.4 ± 5.6	31	26 ± 2	FRAP	[24]
500	Thermo Fisher	15	25.7 ± 1.8	11	23.2 ± 1.1	FRAP	[25]

Supplementary Table 7. Literature values used for Fig. 5.

Molecule	MW (kDa)	Temperature during measurement (°C)	Manufacturer	D ($\mu m^2/s$)	Stdev ($\mu m^2/s$)	Technique	Reference
Fluorescein	0.33	22	Sigma-Aldrich	300	n.a.	FCS	[24]
Fluorescein	0.33	23	n.a.	270	n.a.	FRAP	[26]
Fluorescein	0.33	23	n.a.	260	n.a.	FRAP	[26]
Na2-Fluorescein	0.376	25	Fluka	380	35	FRAP	[27]
Oregon Green 488 carboxylic acid	0.41230	23	Thermo Fisher	336	11	FCS	[22]
Rhodamine B	0.47901	23	Fluka	420	20	FCS	[22]
Rhodamine B	0.47901	22.5	Sigma-Aldrich	420	30	FCS	[28]
Rhodamine 6 G	0.47901	22.5	Molecular Probes	400	30	FCS	[28]
Rhodamine 6 G	0.47901	23	Thermo Fisher	400	20	FCS	[22]
Tetramethyl-Rhodamine methyl ester	0.50093	23	Thermo Fisher	412	18	FCS	[22]
Oregon Green 488 carboxylic acid succinimidyl ester	0.50938	23	Thermo Fisher	308	10	FCS	[22]
Rhodamine green succinimidyl ester	0.621	20	Molecular Probes	233	3	FCS	[29]
Alexa488 alkyne	0.774	32	Life Technologies	288	8	FCS	[30]
Fluorescent dextran	3	23	Thermo Fisher	161	22	FCS	[22]
Alexa488-dextran	3	32	Life Technologies	160	5	FCS	[30]
FITC-dextran	3	22	Pharmacia	98	6	FRAP	[31]
FITC-dextran	3	n.a.	Pharmacia	98	6	FRAP	[32]
FITC-dextran	4	25	Sigma-Aldrich	149	n.a.	FRAP	[33]
FITC-dextran	4	25	Sigma-Aldrich	135	10	FRAP	[23]
FITC-dextran	4	32	Sigma-Aldrich	135	6	FCS	[30]
FITC-dextran	4	20	Sigma-Aldrich	96	2.4	FCS	[34]
FITC-dextran	4	22	Sigma-Aldrich	89	n.a.	FRAP	[35]
FITC-dextran	4	19	Sigma-Aldrich	155	23	FRAP	[36]
FITC-dextran	9.4	20	Sigma-Aldrich	75	3	FRAP	[37]
Fluorescent dextran	10	23	Thermo Fisher	122	4	FCS	[22]
Rhodamine green dextran	10	20	Molecular Probes	115	4	FCS	[29]
Alexa488-dextran	10	32	Life Technologies	82	1.4	FCS	[30]
FITC-dextran	10	22	Sigma-Aldrich	76	n.a.	FRAP	[31]
FITC-dextran	10	20	Sigma-Aldrich	68	1	FCS	[34]
FITC-dextran	11	n.a.	Sigma-Aldrich	76	2.5	FRAP	[32]
FITC-dextran	11	22	Sigma-Aldrich	76	3	FRAP	[31]
FITC-dextran	12	25	Sigma-Aldrich	97	n.a.	FRAP	[33]
FITC-Insulin	12	25	Sigma-Aldrich	147	13	FRAP	[33]
FITC-dextran	17	22	Sigma-Aldrich	65	n.a.	FRAP	[31]
FITC-dextran	17.2	20	Sigma-Aldrich	64	2	FRAP	[37]
FITC-dextran	18	22	Sigma-Aldrich	65	7	FRAP	[31]
FITC-dextran	18	n.a.	Sigma-Aldrich	65	6.5	FRAP	[32]
FITC-dextran	20	22	Sigma-Aldrich	78	n.a.	FCS	[24]
FITC-dextran	20	22	Sigma-Aldrich	64	2	FRAP	[24]
FITC-dextran	20	29	Sigma-Aldrich	70	8	FRAP	[36]
FITC-dextran	20	22	Sigma-Aldrich	63	4	FRAP	[25]
FITC-dextran	21	25	Sigma-Aldrich	71	n.a.	FRAP	[33]
GFP	26.9	25	custom-made	87	n.a.	FCS	[38]
GFP	26.9	n.a.	custom-made	87	n.a.	FRAP	[39]
GFP	26.9	22	Clontech	82	n.a.	FCS	[24]

FITC-dextran	35.6	20	Sigma-Aldrich	44	5	FRAP	[37]
FITC-dextran	38	25	Sigma-Aldrich	62	n.a.	FRAP	[33]
Fluorescent dextran	40	23	Thermo Fisher	47	2	FCS	[22]
FITC-dextran	40	22	Sigma-Aldrich	45	n.a.	FCS	[40]
FITC-dextran	40	22	Sigma-Aldrich	45	n.a.	FCS	[24]
FITC-dextran	40	32	Sigma-Aldrich	45	1.1	FCS	[30]
FITC-dextran	40	22	Sigma-Aldrich	44	5	FRAP	[24]
FITC-dextran	40	22	Sigma-Aldrich	52	2	FRAP	[25]
FITC-dextran	41	22	Sigma-Aldrich	46	5	FRAP	[31]
FITC-dextran	41	n.a.	Sigma-Aldrich	46	4.6	FRAP	[32]
FITC-dextran	42	20	Sigma-Aldrich	39	0.4	FCS	[34]
FITC-dextran	51	25	Sigma-Aldrich	54	n.a.	FRAP	[33]
FITC-dextran	62	n.a.	Sigma-Aldrich	39	2.6	FRAP	[32]
FITC-dextran	62	22	Sigma-Aldrich	39	3	FRAP	[31]
FITC-BSA	67	25	n.a.	58	5	FRAP	[33]
FITC-dextran	70	22	Sigma-Aldrich	38	n.a.	FCS	[24]
FITC-dextran	70	22	Sigma-Aldrich	38	n.a.	FCS	[40]
Fluorescent dextran	70	23	Thermo Fisher	37	7	FCS	[22]
FITC-dextran	70	n.a.	Fluka	33	2.1	FCS	[41]
FITC-dextran	70	22	Sigma-Aldrich	30	2	FRAP	[24]
FITC-dextran	70	25	Thermo Fisher	30	3.1	FRAP	[27]
FITC-dextran	70	23	n.a.	23	n.a.	FRAP	[26]
FITC-dextran	70	22	Sigma-Aldrich	44	1	FRAP	[25]
FITC-dextran	71	25	Sigma-Aldrich	44	2	FRAP	[23]
FITC-dextran	71.2	20	Sigma-Aldrich	30	2	FRAP	[37]
FITC-dextran	77	20	Sigma-Aldrich	35	0.6	FCS	[34]
FITC-dextran	148	20	Sigma-Aldrich	25	3.1	FCS	[34]
FITC-dextran	148	20	Sigma-Aldrich	18	1	FRAP	[37]
FITC-dextran	150	22	Sigma-Aldrich	26	2	FRAP	[24]
FITC-dextran	150	22	Sigma-Aldrich	24	n.a.	FCS	[40]
FITC-dextran	150	22	Sigma-Aldrich	24	n.a.	FCS	[24]
FITC-dextran	150	20	Sigma-Aldrich	14	n.a.	FRAP	[42]
FITC-dextran	157	n.a.	Sigma-Aldrich	24	1.3	FRAP	[32]
FITC-dextran	157	22	Sigma-Aldrich	24	1	FRAP	[31]
FITC-dextran	167	25	Sigma-Aldrich	38	n.a.	FRAP	[33]
FITC-dextran	167	n.a.	Sigma-Aldrich	18.8	0.2	FRAP	[43]
FITC-dextran	260	25	Sigma-Aldrich	30	n.a.	FRAP	[33]
FITC-dextran	282	20	Sigma-Aldrich	16.6	0.8	FCS	[34]
FITC-dextran	464	20	Sigma-Aldrich	14	0.6	FCS	[34]
FITC-dextran	464	n.a.	Sigma-Aldrich	11	0.5	FRAP	[43]
FITC-dextran	500	22	Sigma-Aldrich	23	1	FRAP	[25]
FITC-dextran	580	25	Sigma-Aldrich	22	n.a.	FRAP	[33]
FITC-dextran	2000	25	Sigma-Aldrich	10	1	FRAP	[23]
Fluorescent dextran	2000	23	Thermo Fisher	6	1	FCS	[22]
FITC-dextran	2000	n.a.	Sigma-Aldrich	6.4	0.09	FRAP	[43]
FITC-dextran	2101	25	Sigma-Aldrich	14	n.a.	FRAP	[33]

Supplementary Table 8. Summary of tortuosity simulations.

Dimension	Geometry	Packing	Extracelluar volume fraction (EVF) (%)	Diffusion hindrance factor θ
2D	Circle	Regular	74	0.74
2D	Circle	Regular	59	0.61
2D	Circle	Random	56	0.57
2D	Circle	Random	36	0.49
2D	Circle	Ideal	25	0.44
3D	Cylinder	Regular	71	0.86
3D	Cylinder	Random	78	0.92
3D	Cylinder	Random	58	0.88
3D	Cylinder	Ideal	78	0.92
3D	Cylinder	Ideal	71	0.874
3D	Cylinder	Ideal	61	0.871
3D	Cylinder	Ideal	60	0.870
3D	Cylinder	Ideal	42	0.75
3D	Cuboid	Ideal	38	0.60

Supplementary Table 9. Diffusion coefficients determined by *in vitro* experiments and PyFRAP analysis in the presence of polyacrylamide beads. Mean diffusion values are given with standard error.

Dextran size (kDa)	Manufacturer	Condition	D ($\mu m^2/s$)	n
70	Thermo Fisher	Free	24.1 ± 0.4	13
70	Thermo Fisher	Beads	14.9 ± 0.5	17

Supplementary Table 10. Diffusion coefficients determined by *in vitro* and *in vivo* experiments and PyFRAP analysis with GFP and GFP fusion proteins. Mean diffusion values are given with standard error.

Molecule	**Manufacturer**	**Source**	**Condition**	**Context**	**D (µm^2/s) PyFRAP**	**n**
Recombinant GFP	Biovision	Protein	Free	*In vitro*	96.1 ± 2.2	23
Recombinant GFP	Biovision	Protein	Beads	*In vitro*	79.2 ± 4.1	18
Recombinant GFP	Biovision	Injected protein	Extracelluar matrix	*In vivo*	37.6 ± 3.7	15
Secreted GFP	In-house	Injected mRNA	Extracelluar matrix + production	*In vivo*	35.3 ± 4.8	17
Squint-GFP	In-house	Injected mRNA	Extracelluar matrix + production + binding	*In vivo*	1.7 ± 0.25	27

Supplementary Table 11. Parameters used for the simulation of FRAP experiments.

Variable	Definition	Default value
	Simulation	
D	Diffusion coefficient	$D = 50$ pixels^2/s
	Time stepping	
$t_{\mathrm{sim,start}}$	Simulation start time	0 s
$t_{\mathrm{sim,end}}$	Simulation end time	1680 s
n_{sim}	Number of time steps	4000
t_{scale}	Time-stepping scheme	Logarithmic
	Geometry	
r_{upper}	Upper radius of frustum	317.65 pixels
r_{lower}	Lower radius of frustum	224.25 pixels
h	Height of frustum	90.33 pixels
	Meshing	
v	Mesh element size	25 pixels^3
v_{BL}	Boundary layer element size	15 pixels^3
v_{slice}	Slice refinement element size	15 pixels^3
w_{BL}	Boundary layer thickness	30 pixels
	Solver	
ϵ	Solver tolerance	10^{-10}
N_{iter}	Solver iterations	1000

Supplementary Table 12. Fitting and model parameters, initial guesses, and bounded ranges. Note that we tried different initial guesses for the diffusion coefficient D, which prevented the minimisation algorithm from stopping at a local minimum. We then then took the fit that yielded the global minimum SSD.

Initial guesses		
Parameter	**Initial guess**	**Allowed range**
D (pixels^2/s)	1 - 200	0.01 - 400
k_1 (1/s)	0	0 - 100
k_2 ($[c]$/s)	0	0 - 100
E_{bleached}	1	0.1 - 3
E_{slice}	1	0.1 - 3
Fitting convergence		
Parameter	**Definition**	**Default value**
$N_{\max}$	Maximum number of function calls	1000
δ	Tolerance of termination	10^{-10}

Supplementary Table 13. Test data and settings to measure PyFRAP analysis speed.

	2D	**Frustum**	**Dome**
Geometry	2D circle	3D frustum	3D zebrafish dome
Number of images	301	301	301
Number of mesh cells	7000	20000	35000
Number of time steps	1000	3000	3000
Illumination correction	No	Yes	Yes
Median filter application	No	Yes	Yes

Supplementary Table 14. PyFRAP analysis speed.

Operating system	Version	Processor	Memory	2D test (s)	Frustum test (s)	Dome test (s)
Ubuntu	14.04 LTS	Intel Core i7-3520M 2.90 GHz	8 GB	97	378	489
Ubuntu	16.04 LTS	Intel Core i5-4210 2.60 GHz	8 GB	125	521	743
Ubuntu	16.04 LTS	Intel Xeon E3-1275 3.60 GHz	64 GB	73	347	437
Mac OS X	10.13.3	Intel Core i7-4790K 4.00 GHz	32 GB	79	282	386
Windows	8.1	Intel Core i7-5600U 2.60 Ghz	8 GB	91	373	567

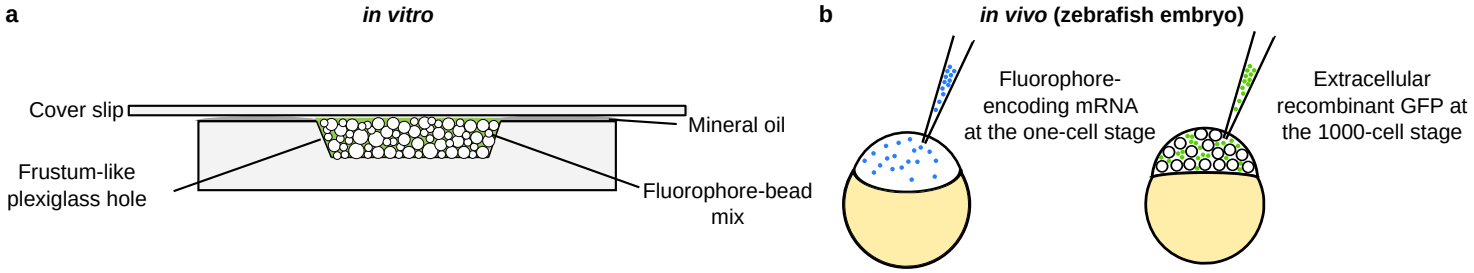

Supplementary Figure 1 | Sample preparation for *in vitro* and *in vivo* FRAP experiments. (a) *In vitro* experiments. Fluorophore solution was pipetted into a frustum-like plexiglass hole. The hole was then sealed with mineral oil and covered with a cover slip. The sample was flipped and placed under an inverted confocal microscope. **(b)** *In vivo* experiments in zebrafish embryos. mRNA encoding a fluorophore was injected into embryos at the one-cell stage, or recombinant GFP was injected into the extracellular space of embryos at the 1000-cell stage.

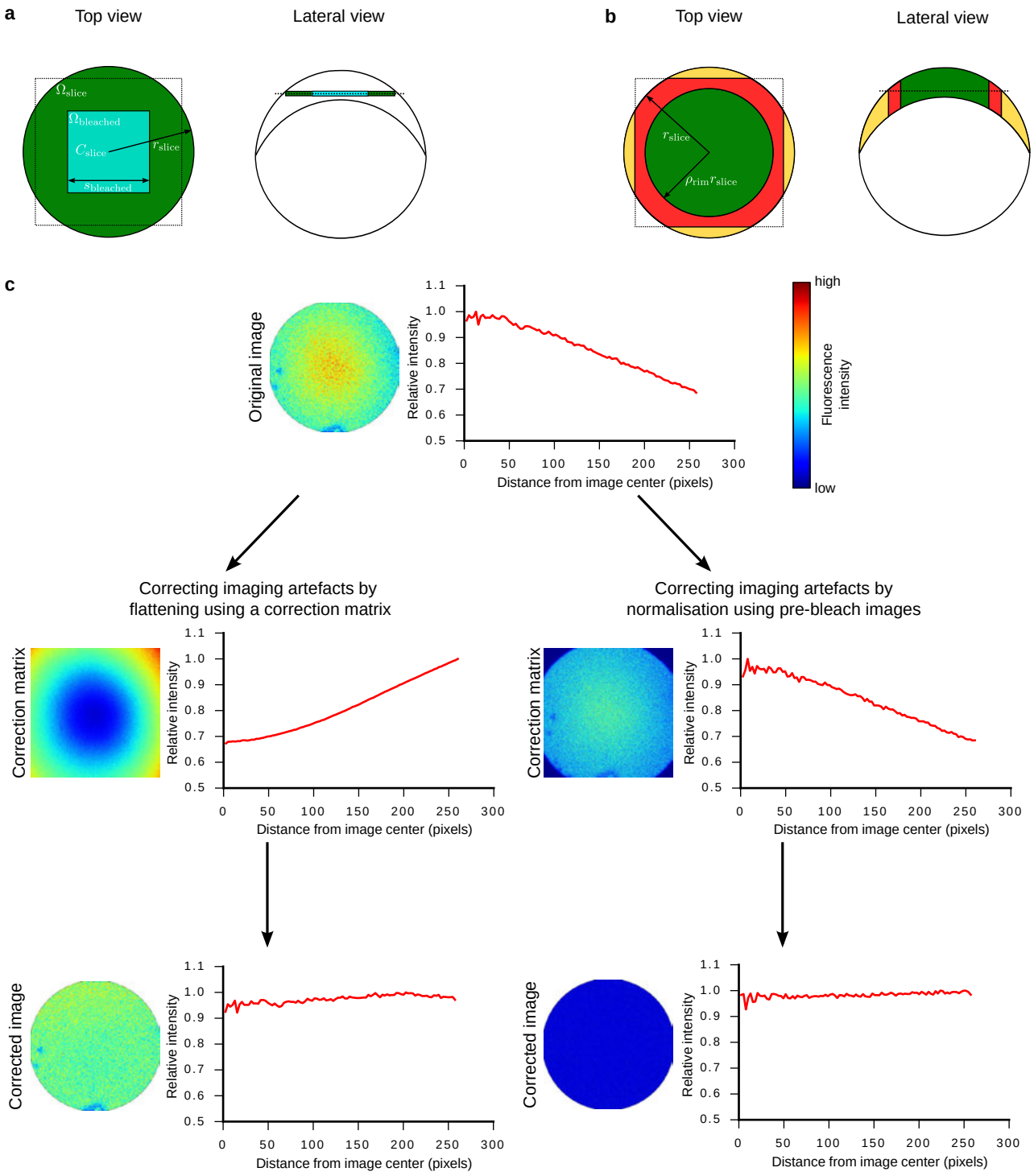

Supplementary Figure 2 | Image analysis in PyFRAP. (a) Basic regions of interest (ROIs) of FRAP analysis: The cyan square indicates the bleached region of the FRAP experiment inside the complete circular geometry within the imaging slice. The dashed lines indicate the location of the acquired image data. **(b)** Rim concentration calculation: Hypothetical data (orange) outside the acquired image (dashed line) is extrapolated through the average concentration in a slim rim of the visible fraction in the imaging slice (red). **(c)** Image manipulation techniques used to correct uneven illumination: Correction was either performed by multiplying the data with a correction matrix (flattening), or by dividing the data through an average pre-bleach image (normalisation). The original image shows a pre-bleach measurement of a uniformly distributed fluorophore. Deviations from the theoretical flat intensity profile are due to imaging artefacts.

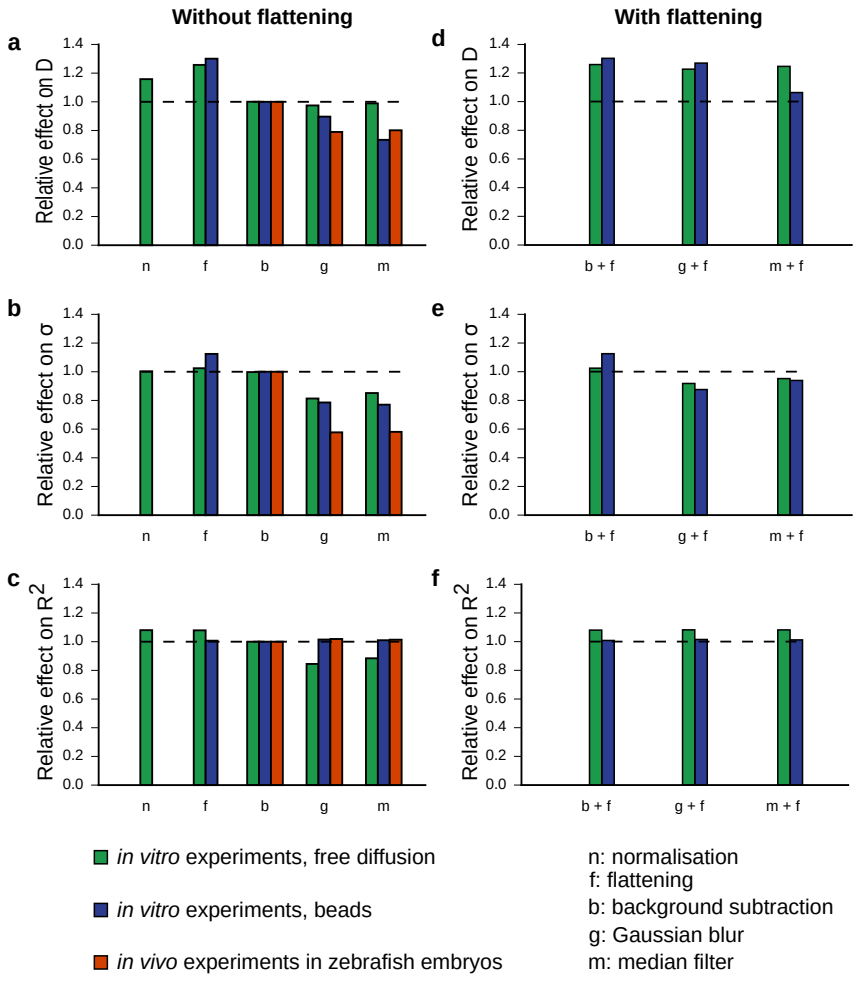

Supplementary Figure 3 | Analysis subset of image correction and smoothing techniques. Data sets were grouped by condition (*in vitro* experiments with free diffusion (green), *in vitro* experiments with beads (blue), and *in vivo* experiments in zebrafish embryos (orange)). Bar plots show the effect of each manipulation (n: normalisation, f: flattening, b: background subtraction, g: Gaussian blur, m: median filter) compared to analyses in which no manipulation was applied. Values above or below the dashed line indicate that the manipulation had an effect. **(a,b,c)** Effect on mean diffusion coefficient D, standard deviation σ, and R^2-value if only one of the five image manipulation techniques was applied, respectively. **(e,d,f)** Effect if flattening and one of the three remaining manipulation techniques was applied. *In vivo* experiments with zebrafish embryos were excluded for this analysis (see Supplementary Note 1 for details).

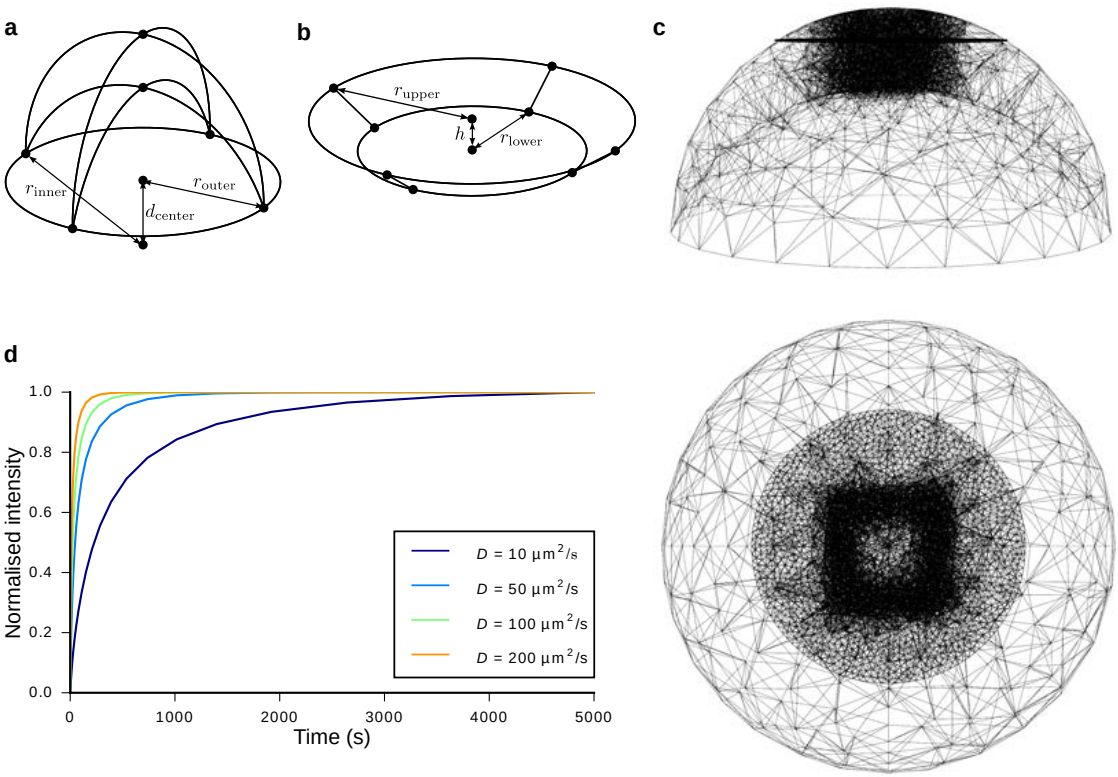

Supplementary Figure 4 | Simulation details for PyFRAP analysis. (a) The zebrafish dome geometry used to analyse *in vivo* experiments is described by the distance between the centers (d_{center}) and the radii (r_{inner}, r_{outer}) of two hemispheres. **(b)** The frustum geometry used to analyse *in vitro* experiments is described by the upper (r_{upper}) and lower (r_{lower}) radius and its height h. **(c)** Lateral and top views of tetrahedral meshes in the zebrafish dome geometry with a boundary layer mesh around the bleached area and a refined mesh in the imaging slice. **(d)** Scaling solution of a simulated FRAP recovery curve for different diffusion coefficients.

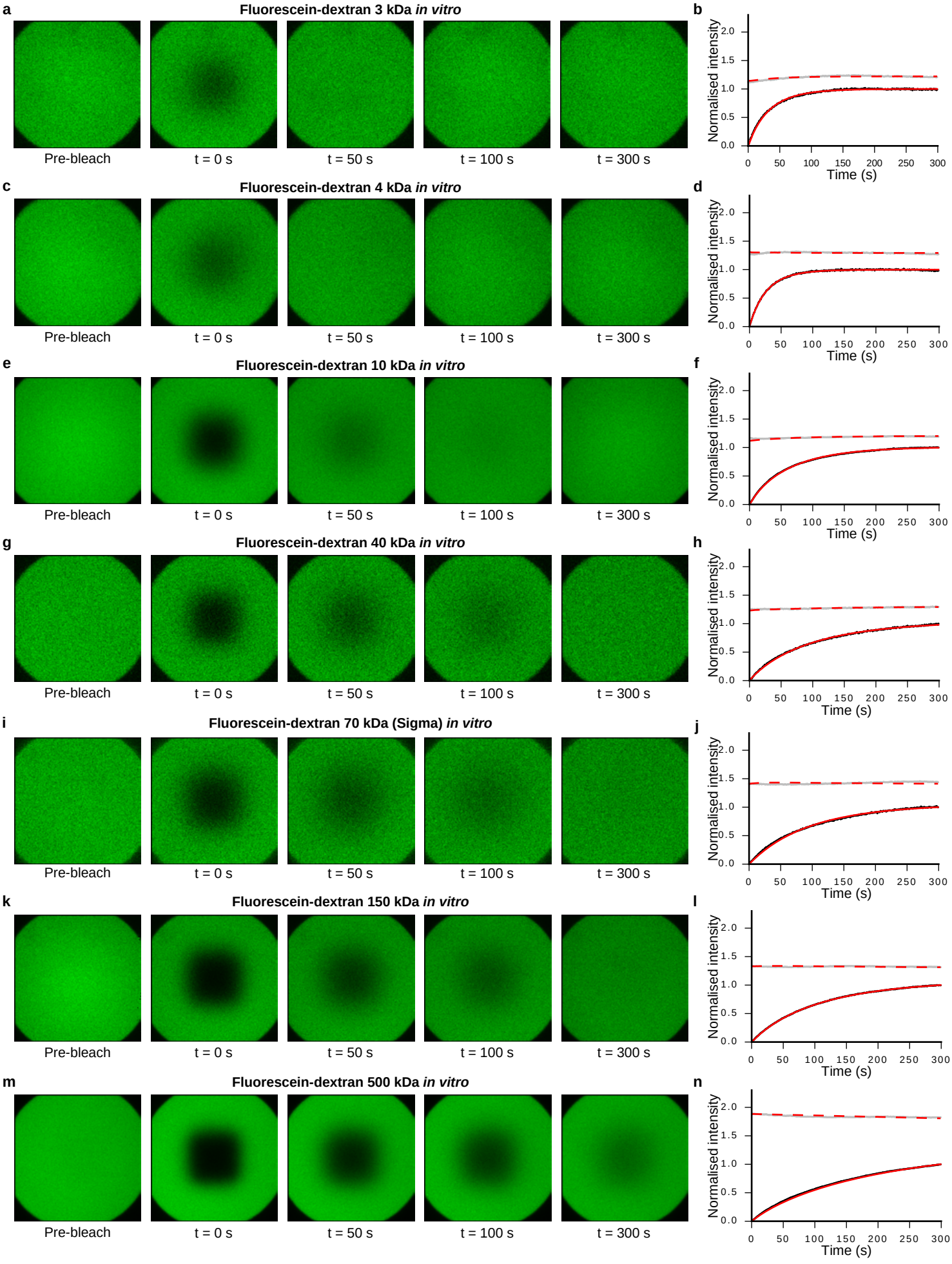

Supplementary Figure 5 | Examples of *in vitro* experiments and the resulting fits to measure free diffusion. (a,c,e,g,i,k,m) *In vitro* FRAP experiments with FITC-dextrans ranging from 3 kDa to 500 kDa. Maximum image intensities are the average pre-conversion intensities to facilitate comparison across data sets. **(b,d,f,h,j,l,n)** Black and grey dots represent data points of bleached and slice ROI, respectively. Red solid and dashed lines show the respective fits. Recovery curves were normalised between 0 (intensity in the bleached ROI at the first post-bleach time point) and 1 (intensity in the bleached ROI at the last post-bleach time point) to facilitate comparison across data sets.

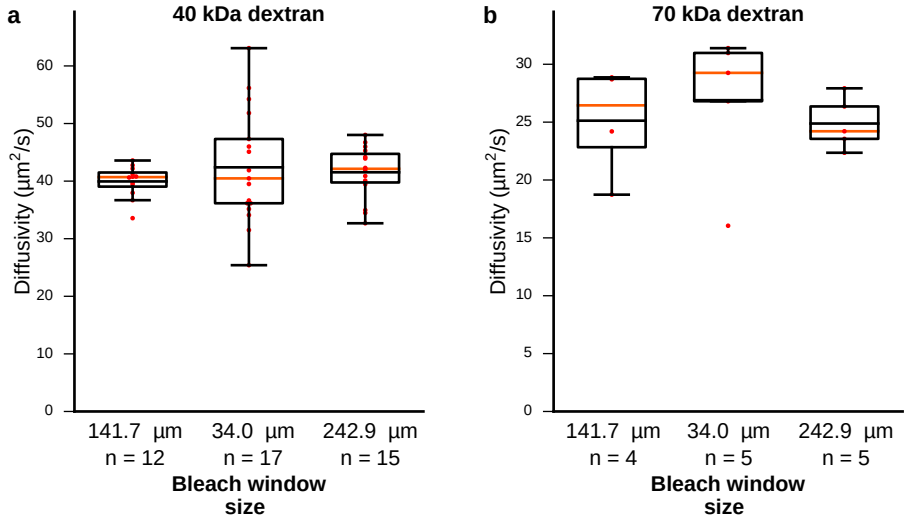

Supplementary Figure 6 | Different bleach window sizes do not affect diffusion coefficient estimates. (a) Results of control experiments with fluorescent dextran (40 kDa) for differently sized bleach windows. **(b)** Results of control experiments with fluorescent dextran (70 kDa) for differently sized bleach windows. Box plots in (a) and (b) show median (orange line), mean (black line), 25% quantiles (box), and all included data points (red markers). Whiskers extend to the smallest data point within the 1.5 interquartile range of the lower quartile, and to the largest data point within the 1.5 interquartile range of the upper quartile.

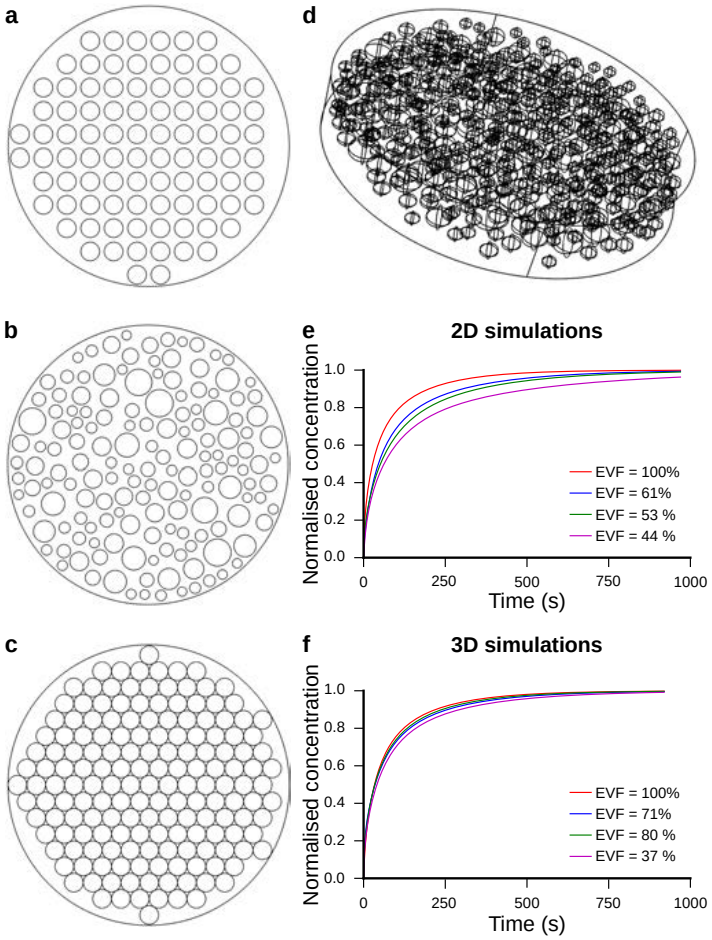

Supplementary Figure 7 | Simulations of tortuous environments in bead experiments. (a,b,c) Regularly (EVF = 59%), randomly (EVF = 56%), and ideally (EVF = 25%) placed beads in a two-dimensional circular domain. **(d)** Randomly (EVF = 78%) placed beads in a three-dimensional cylindrical domain. **(e,f)** Comparison between recovery curves in 2D and 3D bead simulations. Red lines indicate simulations without beads, blue lines indicate simulations with regularly placed beads, green lines indicate simulations with randomly placed beads, and magenta lines indicate simulations with ideally placed beads.

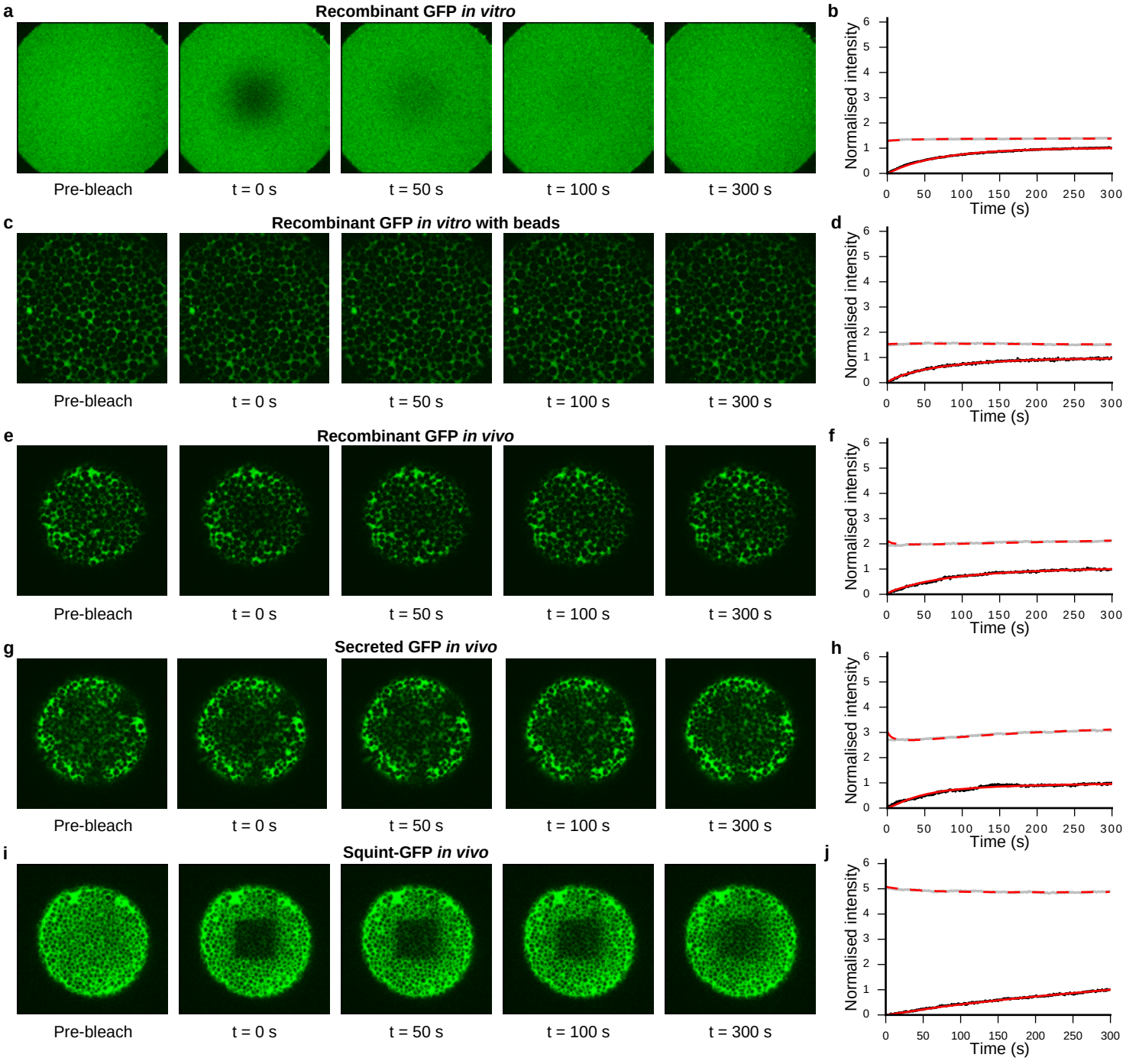

Supplementary Figure 8 | Examples of *in vitro* and *in vivo* experiments and the resulting fits. (a,b) *In vitro* FRAP experiment with recombinant GFP. **(c,d)** *In vitro* FRAP experiment with recombinant GFP mixed with polyacrylamide beads. **(e,f,g,h,i,j)** *In vivo* FRAP experiment in zebrafish embryos with recombinant GFP, secreted GFP, and Squint-GFP, respectively. **(b,d,f,h,j)** Black and grey dots represent data points of bleached and slice ROI, respectively. Red solid and dashed lines show the respective fits. Recovery curves were normalised between 0 (intensity in the bleached ROI at the first post-bleach time point) and 1 (intensity in the bleached ROI at the last post-bleach time point) to facilitate comparison across data sets.

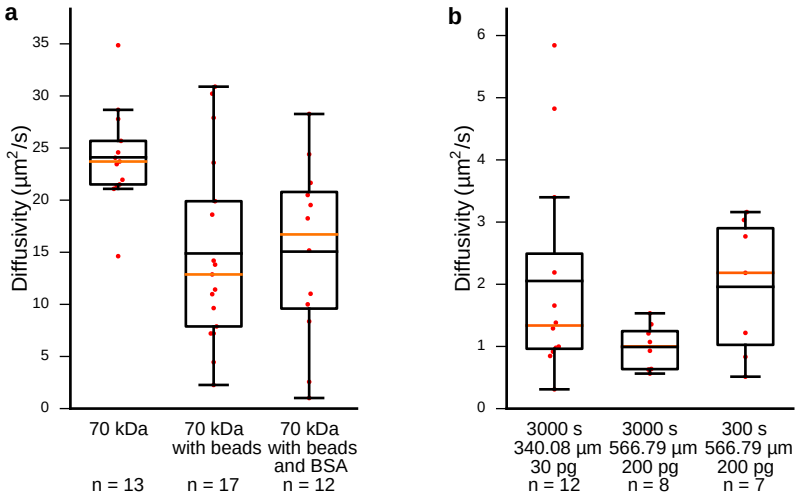

Supplementary Figure 9 | Results of control experiments for *in vitro* and *in vivo* FRAP experiments. (a) Results of control experiments with fluorescent dextran (70 kDa), and beads with or without BSA. BSA does not influence the diffusion of the fluorescent dextran. **(b)** Results of control experiments for different amounts (30 - 200 pg) of injected *Squint-GFP* mRNA, varying length of experiments (300 - 3000 s) and magnification (image size: 340.08 - 566.79 µm). Different imaging settings do not affect the measured diffusion coefficient of Squint-GFP. Box plots in (a) and (b) show median (orange line), mean (black line), 25% quantiles (box), and all included data points (red markers). Whiskers extend to the smallest data point within the 1.5 interquartile range of the lower quartile, and to the largest data point within the 1.5 interquartile range of the upper quartile.

Supplementary References

1. Rapsomaniki, M. A. *et al.* EasyFRAP: An interactive, easy-to-use tool for qualitative and quantitative analysis of FRAP data. *Bioinformatics* **28,** 1800–1801 (2012).
2. Miura, K. *FrapCalc* (accessed: 2016-12-12). `http://wiki.cmci.info/downloads/frap_analysis` (2016).
3. Schaff, J. C., Cowan, A. E., Loew, L. M. & Moraru, I. I. Virtual FRAP - an experiment-oriented simulation tool. *Biophysical Journal* **96,** 30a (2009).
4. Blumenthal, D., Goldstien, L., Edidin, M. & Gheber, L. A. Universal approach to FRAP analysis of arbitrary bleaching patterns. *Scientific Reports* **5,** 11655 (2015).
5. Müller, P. *et al.* Differential diffusivity of Nodal and Lefty underlies a reaction-diffusion patterning system. *Science* **336,** 721–724 (2012).
6. Müller, P., Rogers, K. W., Yu, S. R., Brand, M. & Schier, A. F. Morphogen transport. *Development* **140,** 1621–1638 (2013).
7. Pomreinke, A. P. *et al.* Dynamics of BMP signaling and distribution during zebrafish dorsal-ventral patterning. *Elife* **6,** e25861 (2017).
8. Sprague, B. L., Pego, R. L., Stavreva, D. A. & McNally, J. G. Analysis of binding reactions by Fluorescence Recovery After Photobleaching. *Biophysical Journal* **86,** 3473–3495 (2004).
9. Hrabe, J., Hrabetová, S. & Segeth, K. A model of effective diffusion and tortuosity in the extracellular space of the brain. *Biophysical Journal* **87,** 1606–1617 (2004).
10. Tao, L. & Nicholson, C. Maximum geometrical hindrance to diffusion in brain extracellular space surrounding uniformly spaced convex cells. *Journal of Theoretical Biology* **229,** 59–68 (2004).
11. Novak, I. L., Kraikivski, P. & Slepchenko, B. M. Diffusion in cytoplasm: Effects of excluded volume due to internal membranes and cytoskeletal structures. *Biophysical Journal* **97,** 758–767 (2009).
12. Donovan, P., Chehreghanianzabi, Y., Rathinam, M. & Zustiak, S. P. Homogenization theory for the prediction of obstructed solute diffusivity in macromolecular solutions. *PLoS ONE* **11,** e0146093 (2016).
13. Student. The probable error of a mean. *Biometrika* **6,** 1–25 (1908).
14. Welch, B. L. The generalisation of Student's problems when several different population variances are involved. *Biometrika* **34,** 28–35 (1947).
15. Wilcoxon, F. Individual comparisons by ranking methods. *Biometrics Bulletin* **1,** 80–83 (1945).
16. Mann, H. B. & Whitney, D. R. On a test of whether one of two random variables is stochastically larger than the other. *The Annals of Mathematical Statistics* **18,** 50–60 (1947).
17. Shapiro, S. S. & Wilk, M. B. An analysis of variance test for normality (complete samples). *Biometrika* **52,** 591–611 (1965).
18. Akaike, H. A new look at the statistical model identification. *IEEE Transactions on Automatic Control* **19,** 716–723 (1974).
19. Aaron, J. *FRAP* (accessed: 2016-12-12). `https://de.mathworks.com/matlabcentral/fileexchange/47327-frap-zip` (2016).
20. Kraft, L. J., Dowler, J. & Kenworthy, A. K. *Frap-Toolbox: Software for the analysis of Fluorescence Recovery After Photobleaching* (accessed: 2016-12-12). `http://www.fraptoolbox.com` (2014).

21. Ulrich, M. *et al.* Tropical-parameter estimation and simulation of reaction-diffusion models based on spatio-temporal microscopy images. *Bioinformatics* **22,** 2709–2710 (2006).

22. Zhang, Z., Nadezhina, E. & Wilkinson, K. J. Quantifying diffusion in a biofilm of Streptococcus mutans. *Antimicrobial Agents and Chemotherapy* **3,** 1075–1081 (2011).

23. Pluen, A., Netti, P. A., Jain, R. K. & Berk, D. A. Diffusion of macromolecules in agarose gels: Comparison of linear and globular configurations. *Biophysical Journal* **1,** 542–552 (1999).

24. Guiot, E. *et al.* Molecular dynamics of biological probes by Fluorescence Correlation Microscopy with two-photon excitation. *Journal of Fluorescence* **4,** 413–419 (2000).

25. Braga, J., Desterro, J. M. & Carmo-Fonseca, M. Intracellular macromolecular mobility measured by Fluorescence Recovery After Photobleaching with confocal laser scanning microscopes. *Molecular Biology of the Cell* **15,** 4749–4760 (2004).

26. Periasamy, N. & Verkman, A. Analysis of fluorophore diffusion by continuous distributions of diffusion doefficients: application to photobleaching measurements of multicomponent and anomalous diffusion. *Biophysical Journal* **1,** 557–567 (1998).

27. Schuster, E., Hermansson, A. M., Öhgren, C., Rudemo, M. & Lorén, N. Interactions and diffusion in fine-stranded β-lactoglobulin gels determined via FRAP and binding. *Biophysical Journal* **1,** 253–262 (2014).

28. Gendron, P. O., Avaltroni, F. & Wilkinson, K. J. Diffusion coefficients of several rhodamine derivatives as determined by pulsed field gradient-nuclear magnetic resonance and Fluorescence Correlation Spectroscopy. *Journal of Fluorescence* **6,** 1093–1101 (2008).

29. Visser, N. V., Hink, M. A., Hoek, A. V. & Visser, A. J. Comparison between Fluorescence Correlation Spectroscopy and time-resolved fluorescence anisotropy as illustrated with a fluorescent dextran conjugate. *Journal of Fluorescence* **3,** 251–255 (1999).

30. Kihara, T., Ito, J. & Miyake, J. Measurement of biomolecular diffusion in extracellular matrix condensed by fibroblasts using Fluorescence Correlation Spectroscopy. *PLoS ONE* **11** (2013).

31. Peters, R. Nucleo-cytoplasmic flux and intracellular mobility in single hepatocytes measured by fluorescence microphotolysis. *The EMBO Journal* **8,** 1831–6 (1984).

32. Lang, I., Scholz, M. & Peters, R. Molecular mobility and nucleocytoplasmic flux in hepatoma cells. *Journal of Cell Biology* **4,** 1183–1190 (1986).

33. Gribbon, P. & Hardingham, T. E. Macromolecular diffusion of biological polymers measured by confocal Fluorescence Recovery After Photobleaching. *Biophysical Journal* **2,** 1032–1039 (1998).

34. Gorisch, S. M. Histone acetylation increases chromatin accessibility. *Journal of Cell Science* **24,** 5825–5834 (2005).

35. Keminer, O. & Peters, R. Permeability of single nuclear pores. *Biophysical Journal* **1,** 217–228 (1999).

36. Floury, J., Madec, M. N., Waharte, F., Jeanson, S. & Lortal, S. First assessment of diffusion coefficients in model cheese by Fluorescence Recovery After Photobleaching (FRAP). *Food Chemistry* **2,** 551–556 (2012).

37. Arrio-Dupont, M., Cribier, S., Foucault, G., Devaux, P. & D'Albis, A. Diffusion of fluorescently labeled macromolecules in cultured muscle cells. *Biophysical Journal* **5,** 2327–2332 (1996).

38. Terry, B., Matthews, E. & Haseloff, J. Molecular characterization of recombinant green fluorescent protein by Fluorescence Correlation Microscopy. *Biochemical and Biophysical Research Communications* **1,** 21–27 (1995).

39. Swaminathan, R., Hoang, C. & Verkman, A. Photobleaching recovery and anisotropy decay of green fluorescent protein GFP-S65T in solution and cells: cytoplasmic viscosity probed by green fluorescent protein translational and rotational diffusion. *Biophysical Journal* **4,** 1900–1907 (1997).

40. Gulot, E. *et al.* Heterogeneity of diffusion inside microbial biofilms determined by Fluorescence Correlation Spectroscopy under two-photon excitation. *Photochemistry and Photobiology* **6,** 570–8 (2002).

41. Müller, K. P. *et al.* Multiscale analysis of dynamics and interactions of heterochromatin protein 1 by fluorescence fluctuation microscopy. *Biophysical Journal* **11,** 2876–2885 (2009).

42. Waharte, F., Steenkeste, K., Briandet, R. & Fontaine-Aupart, M. P. Diffusion measurements inside biofilms by image-based Fluorescence Recovery After Photobleaching (FRAP) analysis with a commercial confocal laser scanning microscope. *Applied and Environmental Microbiology* **17,** 5860–5869 (2010).

43. Braeckmans, K., Peeters, L., Sanders, N. N., De Smedt, S. C. & Demeester, J. Three-dimensional Fluorescence Recovery After Photobleaching with the confocal scanning laser microscope. *Biophysical Journal* **4,** 2240–2252 (2003).

Regulation of Nodal signaling propagation by receptor interactions and positive feedback

Hannes Preiß[1], David Mörsdorf[1,†], Gary Huiming Soh[1], María Almuedo-Castillo[1,‡] and Patrick Müller[1,*]

[1]Systems Biology of Development Group, Friedrich Miescher Laboratory of the Max Planck Society, 72076 Tübingen (Germany)

[†]Present address: Department of Neurosciences and Developmental Biology, University of Vienna, 1090 Vienna (Austria)

[‡] Present address: Centro Andaluz de Biología de Desarrollo, 4103 Seville (Spain)

*patrick.mueller@tuebingen.mpg.de

Abstract

During vertebrate embryogenesis, the germ layers are patterned by secreted Nodal signals. Nodals elicit signaling by binding to a complex comprising Type I/II Acvr receptors and the co-receptor Tdgf1. However, it is currently unclear whether receptor binding can also affect the propagation of Nodals themselves through the embryo, and it is unknown which of the putative Acvr paralogs mediate Nodal signaling in zebrafish. Here, we characterize three Type I and four Type II Acvr homologs and show that – except for Acvr1c – all receptor-encoding transcripts are maternally deposited and present during zebrafish embryogenesis. Using mutants and combinatorial knockdown approaches, we identified Acvr1b-a and Acvr1b-b as redundantly acting major mediators of Nodal signaling. By combining quantitative analyses with expression manipulations, we found that feedback-regulated receptors and co-receptors can directly influence the diffusion and distribution of Nodal, providing a mechanism for the spatial restriction of Nodal signaling during germ layer patterning.

Introduction

The formation of the body plan during early embryogenesis depends on the interplay between evolutionarily conserved signaling pathways. The TGF-β superfamily member Nodal is one of the key players in vertebrate development and is required to specify mesoderm and endoderm (collectively termed mesendoderm) during germ layer formation (Schier, 2009). Nodal ligands signal through a receptor complex comprising Type I and Type II single-transmembrane serine/threonine kinase receptors (Shi and Massagué, 2003; Attisano and Wrana, 2002) (Figure 1A). Unlike other members of the TGF-β superfamily, Nodal signaling additionally requires the presence of an EGF-CFC co-receptor to activate signaling. Our current understanding of Nodal signaling is that Nodal directly binds to Type II receptors and the EGF-CFC co-receptor Tdgf1, which in turn mediates the recruitment of the Type I receptors. Upon oligomerization of the receptor complex, Type II receptors phosphorylate the Type I receptors in their GS domains, leading to the recruitment and phosphorylation of the C-terminal SSXS motif of the receptor-regulated Smad (R-Smad) proteins Smad2 and Smad3 by the Type I receptor. The activated Smad2/Smad3 proteins associate with the co-factor Smad4 and translocate into the nucleus where they activate target gene expression (Hill, 2018; Shi and Massagué, 2003; Yeo and Whitman, 2001; Macias-Silva et al., 1996) (Figure 1A).

In zebrafish, mesendoderm patterning depends on the two secreted Nodal signals Squint and Cyclops (Rogers and Müller, 2019; Schier, 2009; Shen, 2007; Dougan et al., 2003). Nodal expression begins in the yolk syncytial layer at the embryonic margin during the blastula stage and then spreads into the embryo, generating a Nodal signaling gradient. This gradient

is translated into different mesendodermal cell fates depending on the signaling level and target gene induction kinetics (Dubrulle et al., 2015). Loss of Nodal signaling causes absence of endoderm as well as trunk and head mesoderm, which leads to cyclopia due to a failure to separate the eye fields, resulting in embryonic lethality (Dubrulle et al., 2015; Gritsman et al., 1999; Feldman et al., 1998). Nodal signaling is antagonized by the long-range feedback inhibitor Lefty, which is also produced at the margin (Meno et al., 1999; Thisse and Thisse, 1999). Establishment and maintenance of a correct signaling range is crucial for correct development, as excess Nodal signaling – e.g. in *lefty* mutants – can cause severe patterning defects and embryonic lethality (Almuedo-Castillo et al., 2018; Rogers et al., 2017). Measurements of active GFP-tagged fusions showed that Squint and Cyclops proteins have a lower effective diffusivity than their inhibitors Lefty1 and Lefty2 (Rogers and Müller, 2019; Müller et al., 2012). It has been proposed that this mobility difference is due to interactions between Nodals and membrane-bound diffusion regulators, whereas Lefty proteins move more freely in the extracellular space (Müller et al., 2013; Müller et al., 2012). Indeed, it has recently been shown that the Nodal signaling range dramatically increases in the absence of the zebrafish Tdgf1 co-receptor homolog Oep (Lord et al., 2019). Since Nodals strongly bind to the zebrafish Type II receptor Acvr2b-a (Wang et al., 2016), Nodal receptors themselves might also act as diffusion regulators. However, it is unclear whether this strong ligand-receptor interaction influences Nodal dispersal, whether receptor binding affects Nodal diffusion or stability in the embryo, and what role other putative Type I and Type II Acvr receptors play in the propagation of Nodal signaling through the embryo.

The two mouse, frog and human Type I receptors Acvr1b (also known as Alk4/TARAM-A) and Acvr1c (also known as Alk7) and the two Type II receptors Acvr2a and Acvr2b were identified using *in vitro* binding and target induction assays, and cause developmental defects when mutated (Reissmann et al., 2001; Gritsman et al., 1999; Kosaki et al., 1999; Gu et al., 1998; Oh and Li, 1997; Matzuk et al., 1995). Surprisingly, except for the zebrafish co-receptor Oep (Gritsman et al., 1999), no zebrafish Nodal receptor mutants are known to recapitulate Nodal loss-of-function phenotypes; and although zebrafish is widely used to investigate Nodal signaling during development, it is unknown which of the receptor paralogs mediate endogenous Nodal signaling during germ layer formation.

To understand the role of the zebrafish receptor homologs in Nodal signaling and propagation, we generated several loss-of-function mutants and used them together with combinatorial morpholino knockdown approaches to assess compound loss-of-function phenotypes. Due to the severity of single receptor knock-outs in mouse (Reissmann et al., 2001; Kosaki et al., 1999; Gu et al., 1998; Oh and Li, 1997; Matzuk et al., 1995), we expected phenotypes similar to Nodal loss-of-function mutants in zebrafish. Strikingly, loss of individual receptor function did not cause obvious patterning defects. Instead, only the combined loss of the Type I receptors *acvr1b-a* and *acvr1b-b* phenocopied known Nodal loss-of-function phenotypes (Dubrulle et al., 2015; Gritsman et al., 1999; Feldman et al., 1998), identifying these receptors as the main Type I receptors that mediate early Nodal signaling in zebrafish. Using quantitative imaging assays, we found that receptor and co-receptor levels can modulate Nodal mobility and thereby directly influence the distribution of Nodal in the embryo, providing a mechanism for the spatial restriction of Nodal signaling during germ layer patterning.

Results

Nodal Type I and Type II receptors have several putative paralogs in zebrafish

To systematically identify and characterize zebrafish Nodal receptors, we used the protein sequences of the human and mouse Type I receptors Acvr1b and Acvr1c as well as the Type

II receptors Acvr2a and Acvr2b as queries for homology searches in the Uniprot database. In addition to previously experimentally identified zebrafish Type I (Renucci et al., 1996) and Type II (Garg et al., 1999; Nagaso et al., 1999) Nodal receptor orthologs playing a role during early embryonic development, our analysis yielded further potential Nodal receptor paralogous sequences for Acvr1b-a, Acvr2a-a and Acvr2b-a – named Acvr1b-b, Acvr2a-b and Acvr2b-b (Li et al., 2019; Funkenstein et al., 2012), respectively. Reconstruction of a putative phylogenetic tree shows a close clustering of the zebrafish receptors with their human and mouse paralogs, and the highest sequence similarity was found between the zebrafish Type I receptors Acvr1b-a and Acvr1b-b (Figure 1B). Putative homologs have the typical features of Type I and Type II receptors, including a signal peptide, TGF-β receptor domain, transmembrane domain, cytosolic kinase domain and a GS domain in case of the Type I receptors; the single exception is Acvr2a-b, which is missing a classical signal peptide (Figure 1 – figure supplement 1).

Most Nodal receptor paralog transcripts are present during mesendoderm formation

To determine which of the putative Nodal receptor paralogs might have roles in germ layer patterning, we first assessed their expression during early embryogenesis. Germ layer patterning takes place during early blastula and gastrula stages (Figure 1C). Analysis of a published developmental transcriptome (White et al., 2017) indicated that the transcripts of most receptor paralogs are present at these stages and before the maternal-zygotic transition, suggesting that they are maternally deposited (Figure 1C). Expression of the identified receptors persists throughout larval development up to 4 days post-fertilization (dpf). The only receptor-encoding gene that does not seem to be expressed during early development is the Type I receptor homolog *acvr1c*, which is first detected at 4 dpf (Figure 1C). Therefore, all putative receptors except *acvr1c* are expressed at the developmental stages during which Nodal signaling patterns the germ layers.

We next used *in situ* hybridization analysis to characterize the spatial expression patterns of the putative receptors, and in particular to determine whether they are expressed at the embryonic margin, where Nodal signaling induces mesendoderm (Figure 1D). In agreement with the temporal analysis (Figure 1C), we found that transcripts of all putative Nodal Type I and II receptors – with the exception of *acvr1c* – are evenly distributed at the 2-cell stage (Figure 1D), consistent with maternal deposition. During early gastrulation (shield stage), most receptors are ubiquitously expressed throughout the embryo (Garg et al., 1999; Nagaso et al., 1999) – with the exceptions of *acvr1c*, which is not expressed, and *acvr1b-a*, which is constrained to the embryonic margin (Figure 1D), similar to the co-receptor *oep* (Vopalensky et al., 2018; Renucci et al., 1996). Together, our analyses show that, except for *acvr1c*, all putative receptors are expressed at the right time and place to potentially act as mediators of endogenous Nodal signaling during zebrafish germ layer patterning.

Nodal signaling upregulates acvr1b-a expression but does not affect other putative Nodal receptors

In zebrafish, Nodal signaling induces several of its own signaling pathway components, including *squint*, *cyclops*, *lefty1*, *lefty2* and *oep* (Dubrulle et al., 2015; Bennett et al., 2007; Feldman et al., 2002; Meno et al., 1999). To systematically assess potential receptor induction by Nodal signaling, we used qRT-PCR to measure receptor expression levels in embryos with increased Nodal signaling (injection of *squint-GFP* or *cyclops-GFP* mRNA (Müller et al., 2012)) or decreased Nodal signaling (injection of *lefty2-Dendra2* mRNA (Müller et al., 2012) or treatment with the Nodal inhibitor SB-505124 (DaCosta Byfield et al., 2004)). *acvr1c* was excluded from this analysis because its spatiotemporal expression suggests that it does not mediate endogenous Nodal signaling during germ layer patterning (Figure 1D). In agreement

with previous studies (Dubrulle et al., 2015), *oep* and *acvr1b-a* were upregulated by increased Nodal signaling and downregulated by decreased signaling (Figure 1E). Upon Nodal overexpression, *acvr1b-a* expression expanded beyond its usual domain at the margin, whereas Nodal inhibition abolished its expression (Figure 1F). In contrast, none of the other putative Nodal receptor-encoding genes exhibited a substantial change in expression upon Nodal overexpression or inhibition (Figure 1E).

Single receptor mutants do not recapitulate Nodal loss-of-function phenotypes

To elucidate the roles of the putative Nodal receptors in germ layer formation, we assessed embryonic morphologies after blocking gene activity using mutants and morpholino-mediated knockdown (El-Brolosy et al., 2019; Rossi et al., 2015). We generated mutants for *acvr1b-a*, *acvr1-c* and *acvr2b-a* using CRISPR/Cas9 by targeting the first exons of the respective genes. We recovered alleles containing indels that led to frame-shifts resulting in premature stop codons within the first exons: a 4-bp deletion for *acvr1b-a*, a 2-bp deletion for *acvr1c* and a 4-bp deletion for *acvr2b-a* (Figure 2B,C,F). Additionally, we obtained *acvr2a-a*^{SA34654} and *acvr2a-b*^{SA18285} mutants from the European Zebrafish Resource Center (EZRC), which carry single nucleotide mutations leading to alternative splicing and a premature stop codon, respectively (Figure 2D,E). Most receptor mutations disrupt the signal peptide and all downstream domains and are therefore likely to lead to a complete loss of gene function (Figure 2). Surprisingly, however, none of the maternal-zygotic homozygous receptor mutants displayed obvious patterning defects at 1 dpf (Figure 2B-F) and all were viable, unlike mouse receptor mutants that exhibit severe malformations during early embryonic development (Gu et al., 1998; Oh and Li, 1997).

Since the analysis of mutants can suffer from genetic compensation that might mask potential patterning defects (El-Brolosy et al., 2019; Rossi et al., 2015), we also assessed the effect of acutely knocking down gene activity using antisense morpholino oligonucleotides targeting the ATG start codons or splice sites of the putative receptor mRNAs. We found that morpholinos targeting the receptor-encoding mRNAs caused non-specific head or tail defects similar to a standard control morpholino (Figure 2 – figure supplement 1). Some morpholino treatments at high doses increased lethality (Figure 2 – figure supplement 1), but none of the conditions led to the Nodal-specific patterning defects that are known for loss-of-function mutants of other Nodal signaling pathway components (Dubrulle et al., 2015; Gritsman et al., 1999; Feldman et al., 1998).

The Type I receptors Acvr1b-a and Acvr1b-b redundantly mediate Nodal signaling during zebrafish germ layer patterning

Teleosts like zebrafish have undergone an additional genome duplication following the two vertebrate-specific rounds of whole-genome duplications (Meyer and Van de Peer, 2005), and partial redundancy of paralogs can underlie the lack of abnormal phenotypes in single mutants (Leerberg et al., 2019; Feldman et al., 1998). Since patterning and Nodal-dependent structures were not obviously affected by loss of individual putative Nodal receptors (Figure 2, Figure 2 – figure supplement 1), we next used combinatorial receptor loss-of-function approaches to test whether receptors may redundantly mediate Nodal signaling during germ layer patterning.

Morpholino-mediated double knockdown of *acvr1b-a* and *acvr1b-b* resulted in a clear loss of head mesoderm at 1 dpf, leading to the distinctive fused-eye “pinhead” phenotype associated with loss-of-Nodal signaling (Figure 3A,B). However, somites still formed in the trunk region, similar to the phenotype of zygotic rather than maternal-zygotic *oep* mutants (Gritsman et al., 1999), suggesting an incomplete loss of Nodal signaling possibly due to maternal deposition of receptor proteins. We therefore injected *acvr1b-b*-targeting

morpholinos into maternal-zygotic *acvr1b-a*$^{t03pm/t03pm}$ mutant embryos. Injection of 0.4 ng *acvr1b-b*-targeting morpholinos into *acvr1b-a* mutants at the one-cell stage recapitulated the full Nodal loss-of-function phenotype at 1 dpf (Figure 3C). Interestingly, knockdown of *acvr1b-b* in maternal-zygotic *acvr1b-a*$^{t03pm/t03pm}$ mutants only resulted in Nodal loss-of-function phenotypes when using ATG-targeting morpholinos ("MO-1"), but not if splice site-targeting morpholinos were used ("MO-2") (Figure 3A,C). Since splice site-targeting morpholinos do not affect maternally deposited mRNAs, this observation indicates that maternally deposited *acvr1b-b* mRNA contributes to proper germ layer formation.

The phenotypes observed in embryos lacking functional *acvr1b-a* and *acvr1b-b* suggest a loss of Nodal signaling. To test this hypothesis, we directly assessed Nodal signaling in these embryos by quantifying the range of the Nodal signal transducer phosphorylated Smad2/3 (pSmad2/3) during early gastrulation at shield stage. Similar to previous reports (Lord et al., 2019; Almuedo-Castillo et al., 2018; Rogers et al., 2017; van Boxtel et al., 2015), we observed pSmad2/3-positive cells over a distance of about 12 cell tiers at the embryonic margin of wild type embryos (Figure 4A,B). *acvr1b-a*$^{t03pm/t03pm}$ mutants and embryos injected with *acvr1b-b*-targeting morpholinos had a Nodal signaling range very similar to untreated wild type embryos. In contrast, combined mutation/knockdown of both Type I receptors almost completely abolished the pSmad2/3 signal throughout the embryo (Figure 4A,B). Importantly, the range of pSmad2/3-positive nuclei could be restored to a near-normal extent by substitution with 50 pg *acvr1b-a* or 25 pg *acvr1b-b* mRNA (Figure 4A,B), and up to 60 percent of the embryos displayed normal or partially rescued phenotypes at 1 dpf (Figure 4C).

While these results demonstrate that *acvr1b-a* and *acvr1b-b* redundantly mediate Nodal signaling during germ layer patterning, the role of the Type II receptors was less clear. Similar to the approach to generate Type I receptor loss-of-function conditions, we targeted several Type II receptors simultaneously using morpholinos and mutants. Double-knockdown of *acvr2a-a* and *acvr2a-b*, double-knockdown of *acvr2b-a* and *acvr2b-b* as well as combinatorial mutation/knockdown of *acvr2b-a* and *acvr2b-b* resulted in apparently non-specific head and tail malformations (Figure 3D,E, Figure 2 – figure supplement 1F-I). Even when all four Type II receptors were simultaneously knocked down, we did not observe phenotypes indicative of Nodal loss-of-function (Figure 3D). While head or tail tissues were strongly reduced or only present rudimentarily, cyclopia associated with Nodal loss-of-function (Feldman et al., 1998) could not be detected, and mesendodermal tissues such as heart and somites in the head and trunk region were still present (Figure 3A,D).

Nodal receptors affect Nodal dispersal in zebrafish embryos

During gastrulation, the establishment of the correct range of Nodal signaling is thought to be crucial for normal germ layer patterning (reviewed in Rogers and Müller, 2019). It has previously been hypothesized that the interaction of Nodal with its receptors might control signal propagation (Müller et al., 2012), and the strong affinity of Nodal for its receptor Acvr2b-a has been suggested to shape the Nodal gradient (Wang et al., 2016). Furthermore, Oep is a crucial component of the receptor complex known to bind Nodals, and maternal-zygotic (MZ) *oep* mutants display complete Nodal loss-of-function phenotypes (Gritsman et al., 1999). It has recently been shown that Oep can dramatically alter the Nodal signaling range (Lord et al., 2019), but its effect on the distribution of Nodal ligands themselves has not been assessed. To test whether Nodal receptors can indeed affect the Nodal distribution during germ layer patterning, we mimicked the secretion of endogenous Nodal from the marginal zone by injecting *squint-GFP* or *cyclops-GFP* mRNA (Müller et al., 2012) into the yolk syncytial layer (YSL) (Figure 5A) and then measured the distribution of the tagged proteins in wild type embryos and receptor knockdown conditions (Figure 5B-D).

In wild type embryos, Squint-GFP was secreted from the YSL and at two hours post-injection formed a graded distribution (Figure 5B,C), similar to previously reported gradients that had been generated using localized clones instead of YSL injections (Soh et al., 2020; Wang et al., 2016; Müller et al., 2012). Loss-of-function conditions for the Type I receptor-encoding genes *acvr1b-a* and *acvr1b-b* as well as the co-receptor *oep* led to a broader Squint-GFP distribution (Figure 5B,C). While Squint-GFP is localized relatively diffusely in the extracellular space, the Cyclops-GFP signal is distributed in a punctate pattern and sharply decreases away from its source in wild type embryos (Müller et al., 2012) (Figure 5B,D). Similar to Squint-GFP, loss-of-function conditions for the Type I receptors *acvr1b-a* and *acvr1b-b* or the co-receptor *oep* had a drastic effect on the Cyclops-GFP gradient four hours post-injection, broadening its range and increasing the number of Cyclops-GFP puncta (Figure 5B,D).

Receptor binding influences signal propagation through multiple mechanisms

Receptors can affect signal propagation through embryonic tissues by several mechanisms. First, receptor availability can affect the clearance rate of bound ligands and thereby affect signal propagation by modulating protein stability (reviewed in Rogers and Müller, 2019; Rogers and Schier, 2011). Second, transient receptor binding might slow down signal diffusion (Müller et al., 2013; Müller et al., 2012; Miura et al., 2009; Crank, 1979). Third, positive autoregulation through ligand-receptor interactions can extend a ligand's expression domain by relay signaling (Rogers and Müller, 2019; van Boxtel et al., 2015). To determine whether the receptors affect Nodal propagation by one of these mechanisms, we measured stability and diffusion of Nodal in the presence and absence of receptors, and assessed the range of Nodal signaling with and without positive autoregulation.

It has previously been shown that Nodals bind to the Type II receptor Acvr2b-a with nanomolar affinity in living zebrafish embryos (Wang et al., 2016). To test whether this interaction affects extracellular ligand stability, we used active Squint-Dendra2 and Cyclops-Dendra2 in Fluorescence Decay after Photoconversion (FDAP) assays (Bläßle and Müller, 2015; Rogers et al., 2015; Müller et al., 2012). If binding of Nodals to Acvr2b-a affects ligand stability, elevated Acvr2b-a levels should increase the clearance of Squint-Dendra2 and Cyclops-Dendra2. However, overexpression of *acvr2b-a* did not markedly change Nodal clearance rate constants compared to wild type embryos (Figure 6A). This suggests that the strong interaction between Nodals and Acvr2b-a (Wang et al., 2016) is not sufficient to modulate Nodal protein stability.

To test whether receptor interactions can affect Nodal diffusion, we performed Fluorescence Recovery After Photobleaching (FRAP) assays (Almuedo-Castillo et al., 2018; Bläßle et al., 2018; Soh and Müller, 2018; Pomreinke et al., 2017; Müller et al., 2013; Müller et al., 2012). We assessed the effective diffusivity of active Squint-GFP (Müller et al., 2012) in wild type embryos, in embryos lacking *acvr1b-a*/*acvr1b-b*, and in embryos overexpressing *oep* or the Type II receptor *acvr2b-a* (Figure 6B). Strikingly, the effective diffusivity of Squint-GFP in the absence of *acvr1b-a/acvr1b-b* increased from about 2 $\mu m^2/s$ to ~4 $\mu m^2/s$, consistent with the broader Nodal distribution in the absence of these Type I receptors (Figure 5C). Furthermore, *oep* overexpression reduced the diffusivity of Squint-GFP to ~1 $\mu m^2/s$, consistent with the increased Nodal signaling range (Lord et al., 2019) and broader Nodal distribution in MZ*oep* mutants (Figure 5). In contrast, overexpression of *acvr2b-a* did not markedly change the effective diffusivity of Squint-GFP (Figure 6B), suggesting that the strong interaction between Squint and Acvr2b-a previously shown *in vivo* (Wang et al., 2016) is not sufficient to modulate Squint diffusivity. Together, our results indicate that Oep, Acvr1b-a and Acvr1b-b serve not only to transduce signaling activity but also to regulate the spatial range of the signal itself.

The Nodal signaling pathway features strong autoregulatory feedback by inducing the Nodal ligands Squint and Cyclops as well as the co-receptor Oep and the Type I receptor Acvr1b-a (Figure 1A,E,F) (Dubrulle et al., 2015; Bennett et al., 2007; Dougan et al., 2003; Feldman et al., 2002). However, the role of this positive feedback for the propagation of Nodal signaling is currently unclear (Lord et al., 2019; Rogers and Müller, 2019). We found that the feedback-induced co-receptor Oep and the Type I receptors Acvr1b-a and Acvr1b-b together act as diffusion regulators of Nodal (Figure 5, Figure 6B), implying that the range of Nodal propagation may – paradoxically – be increased in the absence of positive Nodal feedback in surrounding tissues. To test this prediction, we sought to visualize the activity range of endogenous Nodal signals.

Cyclops and Squint have been shown to activate target genes at a distance (Chen and Schier, 2001), and the biophysical properties of tagged zebrafish Nodals support their function as a short-to-mid-range signals (Müller et al., 2012). However, these findings are based on ectopic expression assays and the readout of target genes such as *no tail*, whose transcription is also activated by Nodal-induced FGFs and thus does not directly report Nodal activity (van Boxtel et al., 2015). It has therefore been debated whether endogenous Nodals act directly at a distance as initially proposed (Chen and Schier, 2001) or whether they act exclusively at a short range and require relay through positive feedback on Nodal expression (Rogers and Müller, 2019; van Boxtel et al., 2018; van Boxtel et al., 2015; Rodaway et al., 1999).

To examine whether zebrafish Nodals can directly act on distant cells at endogenous expression levels and to test the relay model, we transplanted cells from the embryonic margin – where endogenous Nodal expression is highest – of H2A.F/Z:GFP embryos (Pauls et al., 2001) into the animal pole – where Nodal expression is absent – of wild type embryos or Nodal mutant embryos (MZ*sqt*$^{-/-}$;*cyc*$^{-/-}$; Figure 6C). Since MZ*sqt*$^{-/-}$;*cyc*$^{-/-}$ embryos cannot produce functional Nodals, there is no Nodal relay in this mutant background allowing us to directly assess the endogenous Nodal signaling range in the absence of Nodal autoinduction or confounding relay effects. To assess Nodal signaling after transplantation, pSmad2/3 immunofluorescence staining was performed on embryos fixed 2 h post-transplantation. pSmad2/3 can clearly be detected in the nuclei of cells outside the transplant in both wild type and mutant backgrounds (Figure 6C). This indicates that Nodals do not require a relay mechanism to signal to distant cells. Interestingly, the pSmad2/3 intensities inside and around the transplants were higher in the MZ*sqt*$^{-/-}$;*cyc*$^{-/-}$ background than in the wild type background (Figure 6 – figure supplement 1A), and pSmad2/3-positive nuclei were found more frequently outside of transplanted clones in the MZ*sqt*$^{-/-}$;*cyc*$^{-/-}$ background (Figure 6C), consistent with our prediction that the range of Nodal propagation should be increased in the absence of positive Nodal feedback in tissues surrounding the Nodal source. However, in the absence of Nodal signaling Leftys are not expressed (van Boxtel et al., 2015; Feldman et al., 2002), which might also contribute to the extended Nodal signaling range in MZ*sqt*$^{-/-}$;*cyc*$^{-/-}$ mutants.

Endogenous Nodal signaling is active at the embryonic margin, and we therefore wanted to assess whether Nodals can also signal over a distance in marginal tissues, where the feedback-regulated receptors Oep and Acvr1b-a are expressed (Figure 1D-F) (Vopalensky et al., 2018). We therefore performed margin-to-margin transplantations of H2A.F/Z:GFP cells into MZ*sqt*$^{-/-}$;*cyc*$^{-/-}$ host embryos and found that Nodals can also act on distant cells at the margin (Figure 6D), where receptor expression is higher than in the animal pole (Figure 1D,F). In agreement with our prediction that the range of Nodal propagation should be increased with dampened positive feedback in tissues surrounding the Nodal source, pSmad2/3-positive nuclei tended to be found more frequently outside of transplants in the MZ*sqt*$^{-/-}$;*cyc*$^{-/-}$ mutant background compared to wild type hosts, with a few cases even showing extremely extended ranges (Figure 6D, Figure 6 – figure supplement 1B). While our findings are consistent with the idea that positive feedback mediated by receptors and co-receptors restricts the range of

Nodal signaling, we cannot rule out that the extended range we observed with margin transplantations in MZ*sqt*$^{-/-}$;*cyc*$^{-/-}$ hosts is also influenced by dampened negative feedback, which will have to be tested in MZ*sqt*$^{-/-}$;*cyc*$^{-/-}$;*lft1*$^{-/-}$;*lft2*$^{-/-}$ quadruple mutants in the future.

Discussion

The Nodal signaling pathway is a key regulator of vertebrate development and important for human disease and regenerative medicine (Tewary et al., 2019; Lee et al., 2010; Schier, 2009; Roessler et al., 2008). Here, we systematically assessed putative Nodal Type I and Type II receptor homologs in zebrafish. We found that the transcripts of most of these putative Nodal receptors are maternally deposited and present during germ layer patterning, indicative for a potential role in early patterning. The Type I receptor Acvr1c (Alk7) is an exception and not expressed until 4 dpf, making it unlikely to be involved in germ layer formation. While single mutants of the Nodal co-receptor Oep and the signal transducer Smad2 display complete loss-of-function phenotypes (Dubrulle et al., 2015; Gritsman et al., 1999), the loss of individual Nodal ligands (Squint and Cyclops) only leads to partial defects (Dougan et al., 2003; Feldman et al., 1998; Rebagliati et al., 1998a; Rebagliati et al., 1998b; Sampath et al., 1998). This redundancy is mirrored in the function of the Type I and Type II receptors. For example, individual loss of *acvr1b-a* and *acvr1b-b* activity does not induce Nodal-related defects, whereas combined loss-of-function conditions for both *acvr1b-a* and *acvr1b-b* lead to a complete Nodal mutant phenotype, suggesting that these Type I receptors redundantly mediate Nodal signaling during early embryogenesis. In contrast to the Type I receptors, knockdown of any of the Type II receptors individually or in combination surprisingly did not phenocopy Nodal loss-of-function. However, our combinatorial knockdown might not completely abolish gene activity, and our findings will have to be validated with quadruple null mutants in the future. It is also possible that another TGF-β Type II receptor, not yet associated with Nodal signaling, could act as a substitute. Receptor promiscuity has already been demonstrated for Acvr2b-a, which can mediate Activin and BMP signaling by recruiting the respective Type I receptor Acvr1b-a or Bmpr1a (Nagaso et al., 1999). Even a direct high-affinity interaction of Nodal with the BMP Type II receptor Bmpr2 has been shown *in vitro* (Aykul et al., 2015). Furthermore, the Type I receptor TGFβr1 can phosphorylate and thereby activate the Type I receptor Acvr1, indicating that Type I receptors can function like Type II receptors under certain conditions (Ramachandran et al., 2018). Whether this dual function of Type I receptors affects endogenous Nodal signaling in zebrafish requires further investigation.

During germ layer patterning, Nodal is first expressed in the YSL, from which it spreads into the embryo to form a signaling gradient. There are currently two major models that can explain the propagation of Nodal signaling in this context. In the hindered diffusion model, Nodal is secreted from source cells and its free diffusion through the embryo is hindered by interactions with immobile diffusion regulators (Rogers and Müller, 2019; Wang et al., 2016; Müller et al., 2013; Müller et al., 2012). In the second model, Nodal ligands only act in a juxtacrine fashion, and propagation of Nodal signaling to adjacent cells is mediated by a relay mechanism involving positive feedback of Nodal expression (Lord et al., 2019; Rogers and Müller, 2019; van Boxtel et al., 2018; van Boxtel et al., 2015). To distinguish between these models, we transplanted cells expressing endogenous Nodal signals into Nodal-mutant backgrounds that are devoid of relay mechanisms involving feedback on Nodal expression. Consistent with the known function of Nodals as short- to mid-range signals (Müller et al., 2012; Chen and Schier, 2001), we found that Nodals do not exclusively act in a juxtacrine manner and can signal to distant cells even in the absence of Nodal relay. The importance of positive Nodal feedback as an additional mechanism to regulate Nodal signaling propagation is supported by the restriction of the Type I receptor Acvr1b-a and the co-receptor Oep to the

marginal zone. This spatial restriction is mediated by Nodal ligands, which are also expressed at the margin (Vopalensky et al., 2018; Dubrulle et al., 2015; Bennett et al., 2007; Feldman et al., 2002; Meno et al., 1999), suggesting a role for positive feedback to limit Nodal signaling to the embryonic margin. Although our data support the idea that Nodals function as classical morphogens and act directly at a distance as master regulators of mesendoderm formation (Chen and Schier, 2001), complex germ layer patterning requires the interaction with other signaling molecules such as FGFs (van Boxtel et al., 2018; Dubrulle et al., 2015; van Boxtel et al., 2015; Bennett et al., 2007), which act as secondary downstream relay factors to induce mesendodermal gene expression at the correct time and place.

The action range of Nodals has been proposed to be restricted by extracellular interactions (Müller et al., 2013; Müller et al., 2012). In this hindered diffusion model, Nodal's free diffusivity of approximately 40 $\mu m^2/s$ (Wang et al., 2016; Müller et al., 2013) would be slowed down by an order of magnitude through interactions with immobile diffusion regulators such as receptors (Wang et al., 2016) or heparin sulfate proteoglycans (Marjoram and Wright, 2011). Here, we *directly* assessed the influence of Nodal receptors and co-receptors on the dispersal of Nodal ligands. We found that embryos with reduced receptor levels displayed broader Nodal gradients. The strongest effect was observed for mutants of the Nodal co-receptor Oep, suggesting that Oep is a major regulator of Nodal propagation. To elucidate whether the Type I receptors Acvr1b-a and Acvr1b-b as well as the co-receptor Oep directly regulate Nodal diffusivity, we used FRAP assays to measure Nodal mobility in intact embryos with modulated receptor levels. Consistent with our gradient analyses, the co-receptor Oep had the largest impact on Nodal diffusivity (Cohen's $d = 1.42$ with $p = 0.003$, see Materials and Methods), indicating its importance not only as a co-factor for the assembly of the Nodal signaling complex, but also as a diffusion regulator during early embryogenesis. In agreement with our findings, a recent report has shown that the Nodal co-receptor Oep restricts the range of Nodal signaling during zebrafish embryogenesis (Lord et al., 2019). Previous research has shown that Oep is critical for Nodal signaling (Gritsman et al., 1999) and indicated that Oep mediates the interaction of Nodal with the Activin receptor complex (Bianco et al., 2002; Yan et al., 2002; Reissmann et al., 2001; Yeo and Whitman, 2001). Moreover, the Oep-Nodal interaction is crucial for the regulation of Nodal signaling, as chimeric Nodals that do not require Oep for signaling activity cannot be inhibited by Lefty (Cheng et al., 2004). In mouse models, Nodal has been shown to directly interact with the Oep homolog Cripto already before secretion and processing of the Nodal protein, and Oep was also found to regulate Nodal endocytosis and subsequent signaling (Blanchet et al., 2008a; Blanchet et al., 2008b). While the influence of Oep/Cripto and the Type II receptors on Nodal propagation could be explained by their direct interaction, the Type I receptor Acvr1b-a is thought to require the presence of the co-receptor Oep/Cripto to interact with Nodal (Reissmann et al., 2001). However, there is evidence that Nodal can also directly interact with Type I receptors (Calvanese et al., 2015; Reissmann et al., 2001). Alternatively, the observed impact of Type I receptor levels on Nodal dispersal might be due to a failure in assembling the full Nodal receptor complex, possibly affecting endocytosis of Nodal (Zhou et al., 2004) and causing Nodal to accumulate in the extracellular space resulting in a broader Nodal gradient.

In summary, we performed a systematic analysis of putative zebrafish Nodal receptors and found that Type I receptors as well as the co-receptor Oep can shape Nodal gradients during early embryogenesis by modulating ligand mobility and dispersal. In the future, it will be interesting to determine the function of receptor redundancy in Nodal signaling, to analyze the role of receptor and co-receptor feedback in robust embryogenesis (Stapornwongkul et al., 2020; Zhu et al., 2020), and to elucidate why only a subset of the Nodal receptors is regulated by positive feedback.

Acknowledgments

We thank Daniel Čapek, Christine Henzler, Sarah Keim, Jens Dominik Maile, Katherine Rogers and Hannah Wild for technical support and discussions. We are grateful to the European Zebrafish Research Center (EZRC) for providing the *acvr2a-a*^{sa34654} and *acvr2a-b*^{sa18285} zebrafish lines. This project has received funding from the European Research Council (ERC) under the European Union's Horizon 2020 research and innovation program (grant agreement No 637840 (QUANTPATTERN) and grant agreement No 863952 (ACE-OF-SPACE)). This work was also funded by the Max Planck Society and the International Max Planck Research School "From Molecules to Organisms".

Materials and Methods

Fish lines and husbandry

All procedures were executed in accordance with the guidelines of the State of Baden-Württemberg and approved by the Regierungspräsidium Tübingen (35/9185.46-5, 35/9185.81-5). MZ*oep*^{tz57} embryos were generated as previously described (Gritsman et al., 1999; Zhang et al., 1998). The wild type strain Tü was used for the generation of the *acvr1c*^{t06pm} mutant allele. For the generation of *acvr1b-a*^{t03pm} and *acvr2b-a*^{t08pm} mutants, the wild type strain TE was used. *acvr2a-a*^{sa34654}, *acvr2a-b*^{sa18285} mutants were obtained from the European Zebrafish Research Center (EZRC). For all experiments, maternal-zygotic receptor mutant embryos were used. H2A.F/Z:GFP embryos were obtained from an incross of GFP-positive H2A.F/Z:GFP fish (Pauls et al., 2001). MZ*sqt*$^{-/-}$;*cyc*$^{-/-}$ embryos were obtained from an incross of *sqt*$^{-/-}$;*cyc*$^{-/-}$ mutants (Feldman et al., 1998; Schier et al., 1996) generated by germline transplantation (Ciruna et al., 2002). The fish strain TE was used as a wild type control in all experiments.

Phylogenetic analysis

For phylogenetic analysis, human and mouse protein sequences of the Type I receptors Acvr1b and Acvr1c as well as protein sequences of the Type II receptors Acvr2a and Acvr2b were used for BLAST queries in Uniprot (RRID: SCR_002380) to identify zebrafish homologs. The alignment of human, mouse and zebrafish sequences was performed using Clustal Omega (RRID: SCR_001591) (Madeira et al., 2019). The phylogenetic tree was calculated with a neighbor-joining algorithm using the blosum62 matrix. Jalview version 2.10.3b1 was used for visualization (RRID: SCR_006459) (Waterhouse et al., 2009). Branch lengths indicate evolutionary distance.

Whole-mount in situ hybridization

To synthesize *acvr1b-a, acvr1b-b, acvr1c, acvr2a-a, acvr2a-b, acvr2b-a* and *acvr2b-b* probes for *in situ* hybridization assays, full-length receptor-encoding sequences amplified from shield stage cDNA were cloned into TOPO Blunt plasmids (Thermo Fisher Scientific 45024) using the following primers:

Receptor	**Forward primer (5'->3')**	**Reverse primer (5'->3')**
acvr1b-a	ATGCTAAGAGATGGGAATGTTGC	TCAGATCTTAATGTCTTCTTGGACG
acvr1b-b	ATGGACCCACGGCAAATC	TCAGATTTTGAGATCCTCGT
acvr1c	ATGTCTCATCCCAGGTGCTCAG	TTCTTTAACATCCTTGACCACAGTCAC
acvr2a-a	ATGGGACCTGCAACAAAGCT	TCATAGACTAGACTCCTTTG
acvr2a-b	ATGGCGAGCCACTGGACAAACT	TCATAGGCTGGACTCTTTAG
acvr2b-a	ATGTTCGCTTCTCTGCTCACTTT	TCAGATGCTGGACTCTTTGGGC
acvr2b-b	ATGTTTGTTCCCTGGCTGGC	TCAGGTGCTGGAGTCTTTGG

For *in situ* probe synthesis, plasmids were linearized using SpeI or NotI restriction enzymes followed by *in vitro* transcription using SP6 or T7 polymerase (Roche) and digoxigenin (DIG)-modified ribonucleotides (Roche). RNA probes were purified using the RNeasy MinElute Cleanup kit (Qiagen 74204) according to the manufacturer's protocol. Embryos fixed in 4% formaldehyde and transferred into methanol for storage were processed for *in situ* staining as previously described (Thisse and Thisse, 2008), but without proteinase K treatment and pre-absorption of the anti-DIG antibody (Sigma-Aldrich, Roche 11093274910).

mRNA synthesis

Full-length receptor-encoding sequences were amplified from cDNA of shield-stage wild type TE embryos using the primers listed in the section *Whole-mount in situ hybridization*. The sequences were then re-amplified and cloned into pCS2+ vectors using the following primers and restriction enzyme (RE) combinations:

Receptor	**Forward primer (5'->3')**	**Reverse primer (5'->3')**	**RE**
acvr1b-a	TCCCATCGATGCCACCATGCTA AGAGATGGGAATGTTGC	AGAGGCCTTGAATTCGATCAG ATCTTAATGTCTTCTTGGACG	ClaI EcoRI
acvr1b-b	GATTCGAATTCGCCACCATGGA CCCACGGCAAATC	AGAGGCTCGAGCCTTCAGATTT TGAGATCCTCGTCCA	EcoRI XhoI
acvr1c	CATGGGATCCGCCACCATGTCT CATCCCAGGTGCTCAG	GAGGCTCGAGTTATTCTTTAAC ATCCTTGACCA	BamHI XhoI
acvr2a-a	AGGATCCCATCGATGCCACCAT GGGACCTGCAACAAAGCT	TCTAGAGGCTCGAGAGGCCTTC ATAGACTAGACTCCTTTG	ClaI StuI
acvr2a-b	ATCCCATCGATGCCACCATGGC GAGCCACTGGACAAACTGGAA GCAGCGAAAATATGGAGGTGC GATTCTGGGCCGCTCG	CCTTGAATTCGATCATAGGCTG GACTCTTTAG	ClaI EcoRI
acvr2b-a	AGGATCCCATCGATGCCACCAT GTTCGCTT	CACTATAGTTCTAGATCAGATG CTGGACTCTT	ClaI XbaI
acvr2b-b	GATCCCATCGATGCCACCATGT TTGTTCCCTGGCTGGC	GAGGCCTTGAATTCGATCAGGT GCTGGAGTCTTTGG	ClaI EcoRI

For mRNA synthesis, plasmids were linearized with NotI-HF (NEB R3189). mRNA was generated using the mMessage mMachine SP6 Transcription Kit (Thermo Fisher Scientific AM1340). Synthesized mRNA was purified with RNeasy Mini kits (Qiagen 74104) and dissolved in nuclease-free water.

Microinjections

For mRNA, sgRNA and morpholino injections, embryos were injected at the 1- or 2-cell stage with the indicated amounts in a total of 1 nl. Injected embryos were incubated at 28˚C, and unfertilized embryos were discarded at 4-5 hpf. For fixation, imaging and YSL injections, embryos were dechorionated using 0.1 mg/ml Pronase (Roche 11459643001) in 5 ml embryo medium (Rogers et al., 2015).

For Nodal gradient analysis, 2 nl of an injection mix containing 100 pg of *squint-GFP* or *cyclops-GFP* and 0.5 ng of Alexa Fluor™ 647 dextran (Invitrogen D22914) were injected into the YSL of sphere-stage embryos. Imaging of YSL-injected embryos was started 2 hours post-injection (hpi) for *squint-GFP* injections and 4 hpi for c*yclops-GFP* injections.

Mutant generation

acvr1b-a, *acvr1c* and *acvr2b-a* mutants were generated using the CRISPR/Cas9 system (Gagnon et al., 2014). Target sequences for guide RNAs were chosen using CHOP-CHOP (Montague et al., 2014). sgRNAs targeting *acvr1b-a* (a mix of sgRNAs targeting GCTACAGCAGTTCGTCGAGG and GGATTACTAGCGGTCGGCGA) and *acvr1c* (AGCGCTGCATCTGAGCACCT) were synthesized as described previously (Gagnon et al., 2014). *acvr2b-a* sgRNA (targeting GTTCGCTTCTCTGCTCACTT) was procured from IDT. 400 pg of Cas9-encoding mRNA (Addgene MLM3613) and 150 pg of sgRNA were co-injected into 1- to 2-cell-stage wild type embryos.

Genotyping

Genomic DNA was isolated from caudal fin tissue of adult zebrafish using the "hotshot" method (Meeker et al., 2007), and regions of interest were amplified using standard PCR conditions and the following primers:

Mutant	**Target**	**Forward primer (5'->3')**	**Reverse primer (5'->3')**
acvr1b-a^{t03pm}	Exon 2	TCGCTTGTCAATATCACACACA	CTCTCTCTCCACACACCATCAG
acvr1c^{t06pm}	Exon 1	TCTGTCTACGTGTTGTCGCTTT	AAAGTTGGTGTGTGCTGACAGT
acvr2a-a^{sa34654}	Exon 2	AACTACAACCCCAGCTTGGAGAA	TTTGAAAATTCTTTGAAATCTTT
acvr2a-b^{sa18285}	Exon 1	TTTCCAGTTGTGTTTGATTCCATGT	ACAAGTTTCCCTCGCAGCAG
acvr2b-a^{t08pm}	Exon 1	GTGGTGTGTGAGAGTGTGTGTG	CAGGAGCATTTTAACAACACGA

PCR amplicons were prepared for direct use in sequencing reactions by treatment with ExoI (NEB M0568) and rSAP (NEB M0371L), and the respective amplification primers were used in separate sequencing reactions. Mutations in the first generation were identified using PolyPeakParser (Hill et al., 2014) and Hetindel (RRID:SCR_018922). Lasergene Seqman Pro 14 was used for subsequent genotyping analysis. Mutants were outcrossed to wild type TE fish at least once before incrossing heterozygotes to obtain homozygous fish.

Morpholino antisense oligonucleotides

For each receptor, several morpholinos targeting splice sites or the region surrounding the ATG start codon were designed. The following morpholinos (ATG start site targets underlined) were obtained from GeneTools (Philomath, OR):

Target	**Morpholino sequence (5'->3')**	**Target site**	**Reference**
acvr1b-a 1	CTGCAACATTCCCATCTCTTAGCAT	ATG start site	(Jaźwińska et al., 2007)
acvr1b-a 2	GTTTGGCCTGTACTGCTACCATTG	e2i2 splice site	
acvr1b-a 3	ATAAACATGCAACTTACCAGACCCT	e3i3 splice site	
acvr1b-b 1	CATCCTTACAGGACTCCCATTGCAC	ATG start site	
acvr1b-b 2	CAAAGATTTGTTTTCAGCACCTCCA	e7i7 splice site	
acvr1c 1	GATGAGACATGACATCTGTCACTTA	ATG start site	
acvr1c 2	TACTATTTTGTCCTGTCTTACCTGG	e2i2 splice site	
acvr1c 3	TTAATGGGCACAGCCAGCTCTCACC	e3i3 splice site	
acvr2a-a 1	GCAGGTCCCATTTTTTCACTCTTCT	ATG start site	(Albertson et al., 2005)
acvr2a-a 2	AGCAGTAGGGAATACCTGTCATAGC	e2i2 splice site	
acvr2a-a 3	TCGCTGAATGGAGCCTTACTCTGAA	e3i3 splice site	
acvr2a-b 1	TCGATGGTCCCCGAGCGGTTCTTC	Putative 5'UTR	
acvr2a-b 2	TGGCTGCACACAAACACAGATTAAT	splice site	(Dogra et al., 2017)
acvr2a-b 3	TGACAGAAGTATTTACCTGTGACGG	e3i3 splice site	
acvr2b-a 1	GCAGAGAAGCGAACATATTCCTTT	ATG start site	(Albertson et al., 2005)
acvr2b-a 2	TGAGCAGAGAAGCGAACATATTCCT	ATG start site	(Dogra et al., 2017)
acvr2b-a 3	AATGTTTAAGAGAGTCACCTGGTTC	e3i3 splice site	
acvr2b-b	AGCCAGCCAGGGAACAAACATATTC	ATG start site	(Dogra et al., 2017)
control	CCTCTTACCTCAGTTACAATTTATA	n.a.	Gene Tools

Embryos were assessed at shield stage and 1 dpf. After each assessment, unfertilized and dead embryos were discarded.

qRT-PCR

For qRT-PCR experiments, single embryos were collected at shield stage, and total RNA was isolated using NucleoZol (Macherey-Nagel 740404.200) according to the manufacturer's protocol. 100 ng of RNA were used for cDNA synthesis with SuperScript™ III Reverse Transcriptase (Invitrogen 18080044) according to the manufacturer's protocol. qRT-PCR was performed with Platinum SYBR Green qPCR SuperMix-UDG (Invitrogen 1173304) on a CFX Connect Real-Time System (Bio-Rad 1855201). 2 µl of 1:5 diluted cDNA were used as a template. The following primers were used for qRT-PCR analysis:

Target	**Forward primer (5'->3')**	**Reverse primer (5'->3')**
eF1α	AGAAGGAAGCCGCTGAGATGG	TCCGTTCTTGGAGATACCAGCC
acvr1b-a	CGCCATGAAAACATCTTGG	GTGTCCATGTGCCATTGTCT
acvr1b-b	CTCTCCACCTCAGGATCAGG	GTACGAGCCACGGTCCTTT
acvr1c	GAGATTATTGGCACCCAAGG	AACCAGGATGTTCTTTGACTTTATG
acvr2a-a	GGTGTCCTCACAACATTG	TCACCGGTCACTCGACAC
acvr2a-b	GTGACACACACGGACAGGTT	AAACTGATCGCTCCTTCCAG
acvr2b-a	CAAACCAGCCATCGCACA	TCACACCAGTCTACGACC
acvr2b-b	ACACGTCGACATCGGACAG	AGGCTTCAGTCCAACCAGAG

Transcript levels were normalized to the expression of the internal control *eF1α* using the $\Delta\Delta C_t$ method. Technical duplicates and biological triplicates were performed for each sample.

pSmad2/3 immunostainings

Embryos were fixed in 4% formaldehyde in PBS overnight at 4˚C, dehydrated in 100% methanol and stored at -20˚C. For pSmad2/3 immunofluorescence stainings, fixed embryos were incubated in acetone for 7 min, washed three times for 5 min with PBST (PBS + 0.1% Tween 20), blocked for at least 1 h with 10% FBS (Biochrom S0415) in PBST and incubated with 1:5000 rabbit anti-phospho-Smad2/Smad3 primary antibody (Cell Signaling Technologies 8828, RRID: AB_2631089) in blocking solution at 4°C overnight. The following day, embryos were washed 8 times for 15 min with PBST, blocked for at least 1 h with blocking solution, and incubated with 1:500 goat anti-rabbit horseradish peroxidase secondary antibody (Jackson ImmunoResearch 111-035-003, RRID: AB_2313567) in blocking solution at 4°C overnight. Embryos were then washed 8 times for 15 min with PBST, incubated in TSA 1× amplification buffer (TSA Plus Fluorescein Kit, Perkin Elmer, NEL741001KT) for 15 min, and stained by incubation in 75 µl 1:75 fluorescein-TSA in 1× amplification buffer for 45 min. Embryos were washed three times for 5 min with PBST, 30 min with methanol and washed twice more with PBST before incubating them in 1:5000 DAPI in PBST at room temperature (RT) for at least 1 h, followed by at least three washes with PBST. Embryos were then transferred into methanol and stored at -20˚C before imaging.

Imaging

Brightfield images for the documentation of embryo morphology were taken using an Axio Zoom.V16 (ZEISS) microscope with a PlanNeoFluar Z 1× objective.

Images of fixed and live embryos were obtained using a Lightsheet Z.1 microscope (ZEISS). For mounting, the samples were taken up in 1.5% low-melting point agarose (Lonza 50080) with a size 3 glass capillary sample holder (ZEISS). If not noted otherwise, embryos were

imaged using a W Plan-Apochromat 20× objective with 0.7× zoom and 5 µm intervals between z-slices. For imaging of pSmad2/3 immunostainings, embryos were imaged from different angles using a 488 nm laser at 2% power with 100 ms exposure time. For DAPI stainings, embryos were imaged using a 405 nm laser at 10% laser power with 70 ms exposure time. For YSL injections, z-stacks comprising 15 slices were imaged using a 405 nm laser with 100% laser power and 70 ms exposure time. For the detection of Alexa Fluor 647 dextran, embryos were imaged with a 638 nm far-red laser at 1% laser power and 20 ms exposure time.

FRAP and FDAP measurements were performed using an LSM 780 NLO confocal microscope (ZEISS) with an LD C-Apochromat 40×/1.1 W Korr objective. Embryos were mounted in 1.5% low-melting point agarose in glass-bottom petri dishes (MatTek Corporation P35G-1.5-20-C). After solidification, the agarose was covered with embryo medium to protect the embryos from drying out. FRAP and FDAP measurements were performed and analyzed as previously described (Bläßle et al., 2018; Soh and Müller, 2018; Bläßle and Müller, 2015; Rogers et al., 2015; Müller et al., 2012). FRAP data sets that were poorly fit by the diffusion-production-clearance model (overall $R^2 < 0.8$, high local variability, linear increase, or severe mismatch between early recovery kinetics) were excluded.

YSL-injection image analysis

Images obtained from embryos that had been YSL-injected with Nodal-encoding mRNA were analyzed using Fiji (Schindelin et al., 2012). To exclude fluorescent signal in the YSL, the far-red channel was converted into a mask with the mean thresholding algorithm in Fiji. Ten marginal z-slices of the GFP channel were then used for a maximum intensity projection. Before the region of interest around the embryo was defined, the maximum intensity projections were rotated, so that the YSL was on the left, parallel to the image margin. Pixels outside of the embryo and bright staining artifacts were set to *n.a.* to avoid distortion of the calculated averages. For Squint-GFP, the *plot profile* function in Fiji was used to extract the averaged intensities from the embryo. Background levels determined by measuring uninjected embryos were subtracted from the gradient profiles. The profiles were normalized following previously described procedures (Rogers et al., 2020; Gregor et al., 2007) with the model $I_n(x) = A_n\bar{c}(x) + b_n$, relating the mean intensity profile $\bar{c}(x)$ of all data points to each embryo's intensity profile $I_n(x)$ through the embryo-specific proportionality constant A_n and the non-specific background b_n. A_n and b_n were determined by minimizing the sum of squared differences between the model and the intensity profiles using the function *fminsearch* in MATLAB 7.10.0 (Rogers et al., 2020).

The Fiji *find maxima* function was used to identify Cyclops-GFP puncta. Uninjected embryos were used to verify that this approach only identified single maxima in order to exclude artifacts. The x- and y-coordinates of the puncta were extracted using the function *measure*, and the distribution of puncta as a function of distance from the YSL was plotted.

Transplantation of marginal cells

Donor embryos were obtained from an H2A.F/Z:GFP incross. Wild type TE as well as MZ*sqt*$^{-/-}$;*cyc*$^{-/-}$ host embryos were collected 1 h later. Only H2A.F/Z:GFP embryos exhibiting strong fluorescence were used as donors. The embryos were transferred to Ringer's solution (116 mM NaCl, 2.9 mM KCl, 1.8 mM $CaCl_2$, 5 mM HEPES pH 7.2) for margin transplantations. Margin cells were taken from donors around the 30-40% epiboly stage and transplanted into the animal pole or the marginal region of hosts (hosts were around sphere stage) using glass needles with an inner tip diameter of ~80-90 µm. Typically, two margin transplants were derived from each donor embryo (taken from opposing regions). In order to

keep the experimental groups as similar as possible, transplantations were performed such that TE and MZ*sqt*$^{-/-}$;*cyc*$^{-/-}$ embryos were used as hosts in an alternating manner. The embryos were kept in Ringer's solution for 30 min at RT, transferred to embryo medium at 28°C and then fixed 2 h post-transplantation in PBS with 4% formaldehyde.

After overnight fixation at 4˚C, embryos were processed for pSmad2/3 immunostainings as described above, and additionally used for GFP immunostainings with 1:1000 anti-GFP antibody (Aves Labs #GFP-1020, RRID: AB_10000240) at 4°C overnight. The samples were briefly rinsed with PBST and then washed six times for 20 min each before blocking with 500 µl blocking solution for 1.5 h. The blocking solution was removed, and a 1:500 dilution of Alexa Fluor 568-conjugated anti-chicken IgY (Abcam 175477) in blocking solution was added to the samples, which were then kept shaking at 4°C overnight. PBST was added to briefly rinse the samples, and the samples were then washed twelve times for approximately 20 min each. They were stored in PBST containing 1 mg/l DAPI at 4°C until imaging on a Lightsheet Z.1 microscope (ZEISS) with a W Plan-Apochromat 20×/1.0 objective. The samples were mounted in 1.5% low-melting point agarose (Lonza) in embryo medium and imaged in water. All samples and controls from one experiment were imaged on the same day to ensure comparable fluorescence between embryos. The embryos were mounted with the animal-vegetal axis orthogonal (margin-to-animal pole transplantations) or parallel (margin-to-margin transplantations) to the agarose column. z-stacks covering 130 µm from the animal pole were acquired (13 slices with 10 µm steps), and maximum intensity projections over 110 µm (ignoring the two animal-most slices) were generated using Fiji (Schindelin et al., 2012). The outline of the transplants was drawn around cells that exhibited immunofluorescence signal for GFP. For each experimental setup, three independent transplantation experiments were performed on two days. All fixed samples per experimental setup were immunostained in parallel.

The pSmad2/3 intensities within the transplants were measured in a circular region of defined size using Fiji (Schindelin et al., 2012). The intensities in Figure 6 – figure supplement 1A are given relative to the mean wild type intensity. To count animal pole-facing pSmad2/3 positive nuclei (Figure 6 – figure supplement 1B), a line parallel to the margin was drawn just above the animal-most transplanted nucleus. pSmad2/3 positive nuclei on the animal side of this line were counted.

Statistical analysis

p-values for differences between experimental conditions were calculated using two-tailed Student's t-tests assuming equal variance in Excel for Figure 1, Figure 4, and Figure 6. Since an F test in R (R-Core-Team, 2017) showed that the two experimental conditions in Figure 6 – figure supplement 1A did not have equal variance, a Student's t-test with unequal variance was performed in Excel for this data set. A Shapiro-Wilk test in R showed that the data in Figure 6 – figure supplement 1B was not normally distributed, and a Wilcoxon rank sum test was therefore performed to calculate a p-value (note that due to the presence of ties, the p-value is not exact in this case but a normal approximation). Cohen's *d* as a measure for effect size was determined using Robert Coe's Effect Size Calculator (Coe, 2002).

p-values for Figure 1E:

oep				
	+ *squint-GFP*	+ *cyclops-GFP*	+ *lefty-D2*	+ SB505124
Uninjected	0.005	< 0.001	0.003	0.631
acvr1b-a				
	+ *squint-GFP*	+ *cyclops-GFP*	+ *lefty-D2*	+ SB505124
Uninjected	< 0.001	< 0.001	0.003	0.001

acvr1b-b				
	+ *squint-GFP*	+ *cyclops-GFP*	+ *lefty-D2*	+ SB505124
Uninjected	0.503	0.587	0.395	0.980
acvr2a-a				
	+ *squint-GFP*	+ *cyclops-GFP*	+ *lefty-D2*	+ SB505124
Uninjected	0.188	0.401	0.419	0.705
acvr2a-b				
	+ *squint-GFP*	+ *cyclops-GFP*	+ *lefty-D2*	+ SB505124
Uninjected	0.014	0.278	0.777	0.883
acvr2b-a				
	+ *squint-GFP*	+ *cyclops-GFP*	+ *lefty-D2*	+ SB505124
Uninjected	0.108	0.110	0.182	0.920
acvr2b-b				
	+ *squint-GFP*	+ *cyclops-GFP*	+ *lefty-D2*	+ SB505124
Uninjected	0.101	0.260	0.897	0.797

p-values for Figure 4B:

	acvr1b-a$^{-/-}$	*acvr1b-b* MO-1	*acvr1b-a*$^{-/-}$ *acvr1b-b* MO-1	*acvr1b-b* MO-1 *acvr1b-a* mRNA	*acvr1b-a*$^{-/-}$ *acvr1b-b* MO-1 *acvr1b-a* mRNA	*acvr1b-b* MO-1 *acvr1b-b* mRNA	*acvr1b-a*$^{-/-}$ *acvr1b-b* MO-1 *acvr1b-b* mRNA
Wild type	0.203	0.785	< 0.001	0.783	0.041	0.286	0.097

p-values and Cohen's *d* for Figure 6A:

	Squint-Dendra2	**Cyclops-Dendra2**
	+ *acvr2b-a* mRNA	+ *acvr2b-a* mRNA
Wild type	0.200, 0.68	0.586, 0.43

p-values and Cohen's *d* for Figure 6B:

	Squint-GFP		
	+ *oep* mRNA	*acvr1b-a*$^{-/-}$ + *acvr1b-b* MO-1	+ *acvr2b-a* mRNA
Wild type	0.003, 1.42	0.028, 1.03	0.531, 0.31

p-value and Cohen's *d* for Figure 6 – figure supplement 1A:

	MZ*sqt*$^{-/-}$;*cyc*$^{-/-}$
Wild type	< 0.001, 2.21

p-value and Cohen's *d* for Figure 6 – figure supplement 1B:

	MZ*sqt*$^{-/-}$;*cyc*$^{-/-}$
Wild type	0.148, 0.56

Figure Legends

Figure 1. Multiple Nodal receptor candidates are expressed during early zebrafish development. (A) Nodal signaling requires the recruitment of a receptor complex comprising the co-receptor Oep (Tdgf1 homolog) as well as Type I and Type II Activin receptors (Acvr) to induce phosphorylation and nuclear translocation of the signal transducer pSmad2/3 for the induction of Nodal target genes. **(B)** Phylogenetic neighbor-joining alignment tree of Type I and Type II receptor protein sequences from human, mouse and zebrafish. Bootstrap values are listed at the nodes and indicate evolutionary distances. **(C)** Temporal expression analysis of putative Nodal receptors at different developmental stages. TPM: Transcripts per million. dpf: day(s) post-fertilization. Data adjusted from (White et al., 2017). **(D)** Spatial expression analysis of Type I and Type II receptors at 2-cell and shield stages revealed by *in situ* hybridization. Except for *acvr1c*, all receptor-encoding transcripts are maternally deposited. At shield stage, *acvr1b-a* is the only receptor that is not uniformly expressed but restricted to the embryonic margin. **(E)** Nodal signaling controls the expression of *acvr1b-a* and *oep*. Fold change of Nodal receptor expression calculated from qRT-PCR experiments comparing the overexpression of 30 pg *squint-GFP* mRNA, 30 pg *cyclops-GFP* mRNA, 30 pg *lefty2-Dendra2* mRNA and exposure to 10 µM SB-505124 Nodal inhibitor to untreated embryos at 6 hours post-fertilization (hpf). Each point is the mean fold change of an individual embryo compared to an untreated embryo. Error bars represent standard deviation. **(F)** *In situ* hybridization analysis of *acvr1b-a* with increased (+ *squint-GFP*) or decreased (+ SB-505124) Nodal signaling. Scale bars represent 250 µm. See the Figure 1 – source data file for source data.

Figure 1 – source data. Source data for Figure 1.

Figure 1 – figure supplement 1. Protein domains identified in putative Nodal receptors. (A-G) Amino acid sequences of the putative Nodal receptors Acvr1b-a, Acvr1b-b, Acvr1c, Acvr2a-a, Acvr2a-b, Acvr2b-a and Acvr2b-b. The signal peptide is marked in bold, the activin receptor domain in red, the transmembrane domain is underlined, the GS domain is marked in blue, and the protein kinase domain is shown in italics.

Figure 2. Single Nodal receptor mutants have no obvious patterning defects and are viable. (A-F) Left panels: Schematic diagram of typical full-length Type I and Type II receptor proteins (A) and predicted receptor protein truncations resulting from the *acvr1b-a*^{t03pm}, *acvr1c*^{t06pm}, *acvr2a-a*^{SA34654}, *acvr2a-b*^{SA18285} and *acvr2b-a*^{t08pm} mutant alleles (B-F). Mutated nucleic acid sequences and resulting protein lengths in amino acids (aa) are indicated. Right panels: Lateral views of embryos at approximately 27-31 hpf are shown for wild type and single receptor homozygous mutants. Scale bars represent 250 µm. aa: amino acids; SP: Signal peptide; RD: Receptor domain; TM: Transmembrane domain; GS: GS domain; Kinase: Kinase domain; Black: Putative non-sense sequence between frameshift mutation and new stop site.

Figure 2 – figure supplement 1. Phenotypes of embryos 1 day after morpholino-mediated knockdown of putative Type I and Type II Nodal receptors. (A) Phenotype classification categories (same as in Figure 3). **(B-I)** Injection of control (B), *acvr1b-a* (C), *acvr1b-b* (D), *acvr1c* (E), *acvr2a-a* (F) *acvr2a-b* (G), *acvr2b-a* (H), and *acvr2b-b* (I) morpholinos into wild type embryos at the indicated amounts in ng. n indicates the number of analyzed embryos. See the Figure 2 – figure supplement 1 – source data file for source data.

Figure 2 – figure supplement 1 – source data. Source data for Figure 2 – figure supplement 1.

Figure 3. Phenotypes of 1 day-old embryos with combinatorial removal of different Nodal receptor candidates using morpholinos and mutants. If not indicated otherwise, embryos were injected with the indicated amount (in ng) of a mix of transcription start site and splice site targeting morpholinos (see Materials and Methods). n indicates the number of analyzed embryos. **(A)** Phenotype classification categories (same as in Figure 2 – figure supplement 1). **(B)** Phenotype distributions after injection of *acvr1b-a* and *acvr1b-b* morpholino mix into wild type embryos. **(C)** Phenotype distributions after injection of *acvr1b-b* transcriptional start site (MO-1) and *acvr1b-b* splice site (MO-2) targeting morpholinos into maternal-zygotic *acvr1b-a*$^{t03pm/t03pm}$ embryos. **(D)** Phenotype distributions after injection of morpholino combinations targeting the Type II receptors *acvr2a-a*, *acvr2a-b*, *acvr2b-a* and *acvr2b-b* in wild type embryos. **(E)** Phenotype distributions after injection of *acvr2b-b* morpholino into maternal-zygotic *acvr2b-a*$^{t08pm/t08pm}$ mutant embryos. See the Figure 3 – source data file for source data.

Figure 3 – source data. Source data for Figure 3.

Figure 4. The Type I receptors Acvr1b-a and Acvr1b-b redundantly mediate Nodal signaling. (A,B) Influence of *acvr1b-a* and *acvr1b-b* on the Nodal signaling range at shield stage. The range of Nodal signaling in wild type, knockdown and rescued embryos was determined by counting the maximum number of nuclei tiers positive for pSmad2/3 immunostaining from the embryonic margin towards the animal pole. *acvr1b-a*$^{t03pm/t03pm}$ mutants and 0.4 ng *acvr1b-b* MO-1 were used for receptor loss-of-function conditions. Receptor loss-of-function was rescued with 50 pg of *acvr1b-a* or 25 pg of *acvr1b-b* mRNA. Data was obtained from 3 independent replicate experiments. n indicates the number of analyzed embryos. Averages are displayed in red, and error bars show standard deviation. **(C)** Rescue of Type I receptor function after combinatorial mutation/knockdown using *acvr1b-a* and *acvr1b-b* mRNA. To deplete the Type I receptors, the *acvr1b-a*$^{t03pm/t03pm}$ mutant was used in combination with 0.4 ng *acvr1b-b* MO-1. mRNA amounts are given in pg. n indicates the number of analyzed embryos. Note that strong overexpression of Acvr1b-a receptor-encoding mRNA leads to high lethality or tissue aggregates that eventually disintegrate (termed "Nodal gain-of-function"). See the Figure 4 – source data file for source data.

Figure 4 – source data. Source data for Figure 4.

Figure 5. Nodal receptors and co-receptors can shape the distribution of Nodal ligands in zebrafish embryos. (A) Schematic of the YSL-injection assay to create local Nodal sources in a native context. 100 pg of Squint-GFP or Cyc-GFP-encoding mRNA were injected into the YSL of sphere-stage embryos, which were subsequently imaged at 2 or 4 hours post-injection (hpi), respectively, to measure Nodal distributions. **(B)** Lateral views of Squint-GFP (2 hpi) and Cyclops-GFP (4 hpi) signals in wild type compared to MZ*oep*$^{tz57/tz57}$ embryos. **(C)** Quantification of Squint-GFP distributions with modulated receptor and co-receptor levels at 2 hpi. The mean background-subtracted GFP signal as a function of distance from the YSL is plotted, and the shaded regions indicate SEM. The number of measured embryos is indicated in parentheses. Injections of Squint-GFP were analyzed in untreated embryos, *acvr1b-a*$^{t03pm/t03pm}$ mutant embryos injected with 0.4 ng *acvr1b-b* MO-1, or MZ*oep* mutant embryos. **(D)** Nodal receptors and co-receptors shape the distribution of Cyclops-GFP. 100 pg of *cyclops-GFP* mRNA were injected into the YSL of sphere-stage embryos, and embryos were imaged at approximately 4 hpi. The distance and the number of Cyclops-GFP

puncta from the YSL were measured, and the mean number of puncta every 5 µm is plotted. Shaded regions indicate SEM. The number of measured embryos is indicated in parentheses. Injections of *cyclops-GFP* mRNA were analyzed in untreated embryos, in *acvr1b-a*$^{t03pm/t03pm}$ embryos injected with 0.4 ng *acvr1b-b* MO-1, or MZ*oep* mutant embryos. See the Figure 5 – source data file for source data.

Figure 5 – source data. Source data for Figure 5.

Figure 6. Influence of Nodal receptors on Nodal stability, diffusivity and autoregulatory signal propagation. (A) Impact of *acvr2b-a* overexpression on Squint- and Cyclops-Dendra2 clearance rate constants using FDAP measurements. For overexpression, 100 pg *acvr2b-a* mRNA were injected into wild type embryos at the one-cell stage. Mean extracellular clearance rate constants are displayed in red, and individual measurements are shown as black dots. Error bars represent standard deviation. **(B)** Influence of receptor levels on Squint- and Cyclops-GFP diffusivities determined using FRAP measurements. For overexpression, either 50 pg *oep* mRNA or 100 pg *acvr2b-a* mRNA were injected into wild type embryos at the one-cell stage. *acvr1b-a* mutants and 0.4 ng *acvr1b-b* MO-1 were used for receptor loss-of-function conditions. The mean diffusion coefficients are displayed in red, and individual measurements are shown as black dots. Error bars represent 95% confidence intervals. **(C)** Margin-to-animal pole transplantations show that Nodals at endogenous expression levels can signal to distant cells. Top panel: Experimental setup of the margin-to-animal pole transplantations, in which MZ*sqt*$^{-/-}$;*cyc*$^{-/-}$ embryos that lack Nodal relay were used as hosts. Bottom panel: Immunofluorescent stainings show that pSmad2/3-positive nuclei are detected outside of the transplanted clones in both wild type (top row) and MZ*sqt*$^{-/-}$;*cyc*$^{-/-}$ (bottom row) hosts. **(D)** Margin-to-margin transplants show that Nodals at endogenous expression levels can signal to distant cells at the embryonic margin. Top panel: Experimental setup. Bottom panel: Representative maximum intensity projections of immunofluorescent stainings. Transplantations into wild type embryos (top row) and MZ*sqt*$^{-/-}$;*cyc*$^{-/-}$ embryos (bottom row) are shown. Scale bars represent 200 µm. See the Figure 6 – source data file for source data.

Figure 6 – source data. Source data for Figure 6.

Figure 6 – figure supplement 1. Increased pSmad2/3 intensities and ranges within transplants in Nodal-mutant hosts compared to wild type hosts. (A) pSmad2/3 intensities within margin transplants normalized to the mean signal in wild type embryos. Mean intensities are displayed in red, and individual measurements are shown as black dots. Error bars represent 95% confidence intervals. **(B)** Number of pSmad2/3-positive nuclei extending from the distal-most end of margin-to-margin transplants in wild type and MZ*sqt*$^{-/-}$;*cyc*$^{-/-}$ hosts. Mean intensities are displayed in red, and individual measurements are shown as black dots. Error bars represent 95% confidence intervals. See the Figure 6 – figure supplement 1 – source data file for source data.

Figure 6 – figure supplement 1 – source data. Source data for Figure 6 – figure supplement 1.

References

Albertson, R.C., Payne-Ferreira, T.L., Postlethwait, J., and Yelick, P.C. (2005). Zebrafish acvr2a and acvr2b exhibit distinct roles in craniofacial development. Dev Dyn 233, 1405-18.

Almuedo-Castillo, M., Bläßle, A., Mörsdorf, D., Marcon, L., Soh, G.H., Rogers, K.W., Schier, A.F., and Müller, P. (2018). Scale-invariant patterning by size-dependent inhibition of Nodal signalling. Nat Cell Biol 20, 1032-1042.

Attisano, L., and Wrana, J.L. (2002). Signal transduction by the TGF-β superfamily. Science 296, 1646-7.

Aykul, S., Ni, W., Mutatu, W., and Martinez-Hackert, E. (2015). Human Cerberus prevents Nodal-receptor binding, inhibits Nodal signaling, and suppresses Nodal-mediated phenotypes. PLoS One 10, e0114954.

Bennett, J.T., Joubin, K., Cheng, S., Aanstad, P., Herwig, R., Clark, M., Lehrach, H., and Schier, A.F. (2007). Nodal signaling activates differentiation genes during zebrafish gastrulation. Dev Biol 304, 525-40.

Bianco, C., Adkins, H.B., Wechselberger, C., Seno, M., Normanno, N., De Luca, A., Sun, Y., Khan, N., Kenney, N., Ebert, A., et al. (2002). Cripto-1 activates Nodal- and ALK4-dependent and -independent signaling pathways in mammary epithelial cells. Mol Cell Biol 22, 2586-97.

Blanchet, M.H., Le Good, J.A., Mesnard, D., Oorschot, V., Baflast, S., Minchiotti, G., Klumperman, J., and Constam, D.B. (2008a). Cripto recruits Furin and PACE4 and controls Nodal trafficking during proteolytic maturation. EMBO J 27, 2580-91.

Blanchet, M.H., Le Good, J.A., Oorschot, V., Baflast, S., Minchiotti, G., Klumperman, J., and Constam, D.B. (2008b). Cripto localizes Nodal at the limiting membrane of early endosomes. Sci Signal 1, ra13.

Bläßle, A., and Müller, P. (2015). PyFDAP: automated analysis of fluorescence decay after photoconversion (FDAP) experiments. Bioinformatics 31, 972-4.

Bläßle, A., Soh, G., Braun, T., Mörsdorf, D., Preiß, H., Jordan, B.M., and Müller, P. (2018). Quantitative diffusion measurements using the open-source software PyFRAP. Nat Commun 9, 1582.

Calvanese, L., Sandomenico, A., Caporale, A., Foca, A., Foca, G., D'Auria, G., Falcigno, L., and Ruvo, M. (2015). Conformational features and binding affinities to Cripto, ALK7 and ALK4 of Nodal synthetic fragments. J Pept Sci 21, 283-93.

Chen, Y., and Schier, A.F. (2001). The zebrafish Nodal signal Squint functions as a morphogen. Nature 411, 607.

Cheng, S.K., Olale, F., Brivanlou, A.H., and Schier, A.F. (2004). Lefty blocks a subset of TGFβ signals by antagonizing EGF-CFC coreceptors. PLoS Biol 2, E30.

Ciruna, B., Weidinger, G., Knaut, H., Thisse, B., Thisse, C., Raz, E., and Schier, A.F. (2002). Production of maternal-zygotic mutant zebrafish by germ-line replacement. Proc Natl Acad Sci U S A 99, 14919-24.

Coe, R. (2002). It's the effect size, stupid - What effect size is and why it is important. Annual Conference of the British Educational Research Association (University of Exeter, England).

Crank, J. (1979). The mathematics of diffusion (Oxford: Clarendon Press)

DaCosta Byfield, S., Major, C., Laping, N.J., and Roberts, A.B. (2004). SB-505124 is a selective inhibitor of transforming growth factor-β type I receptors ALK4, ALK5, and ALK7. Mol Pharmacol 65, 744-52.

Dogra, D., Ahuja, S., Kim, H.-T., Rasouli, S.J., Stainier, D.Y.R., and Reischauer, S. (2017). Opposite effects of Activin type 2 receptor ligands on cardiomyocyte proliferation during development and repair. Nature Communications 8, 1902.

Dougan, S.T., Warga, R.M., Kane, D.A., Schier, A.F., and Talbot, W.S. (2003). The role of the zebrafish *nodal*-related genes *squint* and *cyclops* in patterning of mesendoderm. Development 130, 1837-51.

Dubrulle, J., Jordan, B.M., Akhmetova, L., Farrell, J.A., Kim, S.H., Solnica-Krezel, L., and Schier, A.F. (2015). Response to Nodal morphogen gradient is determined by the kinetics of target gene induction. Elife 4, e05042.

El-Brolosy, M.A., Kontarakis, Z., Rossi, A., Kuenne, C., Gunther, S., Fukuda, N., Kikhi, K., Boezio, G.L.M., Takacs, C.M., Lai, S.L., et al. (2019). Genetic compensation triggered by mutant mRNA degradation. Nature 568, 193-197.

Feldman, B., Concha, M.L., Saude, L., Parsons, M.J., Adams, R.J., Wilson, S.W., and Stemple, D.L. (2002). Lefty antagonism of Squint is essential for normal gastrulation. Current Biology 12, 2129-2135.

Feldman, B., Gates, M.A., Egan, E.S., Dougan, S.T., Rennebeck, G., Sirotkin, H.I., Schier, A.F., and Talbot, W.S. (1998). Zebrafish organizer development and germ-layer formation require nodal-related signals. Nature 395, 181-5.

Funkenstein, B., Krol, E., Esterin, E., and Kim, Y.S. (2012). Structural and functional characterizations of activin type 2B receptor (acvr2b) ortholog from the marine fish, gilthead sea bream, Sparus aurata: evidence for gene duplication of acvr2b in fish. J Mol Endocrinol 49, 175-92.

Gagnon, J.A., Valen, E., Thyme, S.B., Huang, P., Akhmetova, L., Pauli, A., Montague, T.G., Zimmerman, S., Richter, C., and Schier, A.F. (2014). Efficient mutagenesis by Cas9 protein-mediated oligonucleotide insertion and large-scale assessment of single-guide RNAs. PLoS One 9, e98186.

Garg, R.R., Bally-Cuif, L., Lee, S.E., Gong, Z., Ni, X., Hew, C.L., and Peng, C. (1999). Cloning of zebrafish activin type IIB receptor (ActRIIB) cDNA and mRNA expression of ActRIIB in embryos and adult tissues. Mol Cell Endocrinol 153, 169-81.

Gregor, T., Tank, D.W., Wieschaus, E.F., and Bialek, W. (2007). Probing the limits to positional information. Cell 130, 153-64.

Gritsman, K., Zhang, J., Cheng, S., Heckscher, E., Talbot, W.S., and Schier, A.F. (1999). The EGF-CFC protein one-eyed pinhead is essential for nodal signaling. Cell 97, 121-32.

Gu, Z., Nomura, M., Simpson, B.B., Lei, H., Feijen, A., van den Eijnden-van Raaij, J., Donahoe, P.K., and Li, E. (1998). The type I activin receptor ActRIB is required for egg cylinder organization and gastrulation in the mouse. Genes Dev 12, 844-57.

Hill, C.S. (2018). Spatial and temporal control of NODAL signaling. Curr Opin Cell Biol 51, 50-57.

Hill, J.T., Demarest, B.L., Bisgrove, B.W., Su, Y.C., Smith, M., and Yost, H.J. (2014). Poly peak parser: Method and software for identification of unknown indels using Sanger sequencing of polymerase chain reaction products. Dev Dyn 243, 1632-6.

Jaźwińska, A., Badakov, R., and Keating, M.T. (2007). Activin-βA signaling is required for zebrafish fin regeneration. Current Biology 17, 1390-1395.

Kosaki, R., Gebbia, M., Kosaki, K., Lewin, M., Bowers, P., Towbin, J.A., and Casey, B. (1999). Left-right axis malformations associated with mutations in ACVR2B, the gene for human activin receptor type IIB. Am J Med Genet 82, 70-6.

Lee, C.C., Jan, H.J., Lai, J.H., Ma, H.I., Hueng, D.Y., Lee, Y.C., Cheng, Y.Y., Liu, L.W., Wei, H.W., and Lee, H.M. (2010). Nodal promotes growth and invasion in human gliomas. Oncogene 29, 3110-23.

Leerberg, D.M., Hopton, R.E., and Draper, B.W. (2019). Fibroblast growth factor receptors function redundantly during zebrafish embryonic development. Genetics 212, 1301-1319.

Li, Y.F., Canario, A.V.M., Power, D.M., and Campinho, M.A. (2019). Ioxynil and diethylstilbestrol disrupt vascular and heart development in zebrafish. Environ Int 124, 511-520.

Lord, N.D., Carte, A.N., Abitua, P.B., and Schier, A.F. (2019). The pattern of Nodal morphogen signaling is shaped by co-receptor expression. bioRxiv, 2019.12.30.891101.

Macias-Silva, M., Abdollah, S., Hoodless, P.A., Pirone, R., Attisano, L., and Wrana, J.L. (1996). MADR2 is a substrate of the TGFβ receptor and its phosphorylation is required for nuclear accumulation and signaling. Cell 87, 1215-24.

Madeira, F., Park, Y.M., Lee, J., Buso, N., Gur, T., Madhusoodanan, N., Basutkar, P., Tivey, A.R.N., Potter, S.C., Finn, R.D., et al. (2019). The EMBL-EBI search and sequence analysis tools APIs in 2019. Nucleic Acids Res 47, W636-W641.

Marjoram, L., and Wright, C. (2011). Rapid differential transport of Nodal and Lefty on sulfated proteoglycan-rich extracellular matrix regulates left-right asymmetry in Xenopus. Development 138, 475-485.

Matzuk, M.M., Kumar, T.R., and Bradley, A. (1995). Different phenotypes for mice deficient in either activins or activin receptor type II. Nature 374, 356-60.

Meeker, N.D., Hutchinson, S.A., Ho, L., and Trede, N.S. (2007). Method for isolation of PCR-ready genomic DNA from zebrafish tissues. Biotechniques 43, 610, 612, 614.

Meno, C., Gritsman, K., Ohishi, S., Ohfuji, Y., Heckscher, E., Mochida, K., Shimono, A., Kondoh, H., Talbot, W.S., Robertson, E.J., et al. (1999). Mouse Lefty2 and zebrafish Antivin are feedback inhibitors of Nodal signaling during vertebrate gastrulation. Mol Cell 4, 287-98.

Meyer, A., and Van de Peer, Y. (2005). From 2R to 3R: evidence for a fish-specific genome duplication (FSGD). Bioessays 27, 937-45.

Miura, T., Hartmann, D., Kinboshi, M., Komada, M., Ishibashi, M., and Shiota, K. (2009). The cyst-branch difference in developing chick lung results from a different morphogen diffusion coefficient. Mech Dev 126, 160-72.

Montague, T.G., Cruz, J.M., Gagnon, J.A., Church, G.M., and Valen, E. (2014). CHOPCHOP: a CRISPR/Cas9 and TALEN web tool for genome editing. Nucleic Acids Res 42, W401-7.

Müller, P., Rogers, K.W., Jordan, B.M., Lee, J.S., Robson, D., Ramanathan, S., and Schier, A.F. (2012). Differential diffusivity of Nodal and Lefty underlies a reaction-diffusion patterning system. Science 336, 721-4.

Müller, P., Rogers, K.W., Yu, S.R., Brand, M., and Schier, A.F. (2013). Morphogen transport. Development 140, 1621-38.

Nagaso, H., Suzuki, A., Tada, M., and Ueno, N. (1999). Dual specificity of activin type II receptor ActRIIb in dorso-ventral patterning during zebrafish embryogenesis. Development Growth & Differentiation 41, 119-133.

Oh, S.P., and Li, E. (1997). The signaling pathway mediated by the type IIB activin receptor controls axial patterning and lateral asymmetry in the mouse. Genes Dev 11, 1812-26.

Pauls, S., Geldmacher-Voss, B., and Campos-Ortega, J.A. (2001). A zebrafish histone variant H2A.F/Z and a transgenic H2A.F/Z:GFP fusion protein for in vivo studies of embryonic development. Dev Genes Evol 211, 603-10.

Pomreinke, A.P., Soh, G.H., Rogers, K.W., Bergmann, J.K., Blässle, A.J., and Müller, P. (2017). Dynamics of BMP signaling and distribution during zebrafish dorsal-ventral patterning. Elife 6, e25861.

R-Core-Team (2017). R: A language and environment for statistical computing. R Foundation for Statistical Computing, Vienna, Austria. URL https://www.R-project.org/.

Ramachandran, A., Vizan, P., Das, D., Chakravarty, P., Vogt, J., Rogers, K.W., Müller, P., Hinck, A.P., Sapkota, G.P., and Hill, C.S. (2018). TGF-β uses a novel mode of receptor activation to phosphorylate SMAD1/5 and induce epithelial-to-mesenchymal transition. Elife 7, e31756.

Rebagliati, M.R., Toyama, R., Fricke, C., Haffter, P., and Dawid, I.B. (1998a). Zebrafish nodal-related genes are implicated in axial patterning and establishing left-right asymmetry. Dev Biol 199, 261-72.

Rebagliati, M.R., Toyama, R., Haffter, P., and Dawid, I.B. (1998b). cyclops encodes a nodal-related factor involved in midline signaling. Proc Natl Acad Sci U S A 95, 9932-7.

Reissmann, E., Jörnvall, H., Blokzijl, A., Andersson, O., Chang, C., Minchiotti, G., Persico, M.G., Ibanez, C.F., and Brivanlou, A.H. (2001). The orphan receptor ALK7 and the Activin receptor ALK4 mediate signaling by Nodal proteins during vertebrate development. Genes Dev 15, 2010-22.

Renucci, A., Lemarchandel, V., and Rosa, F. (1996). An activated form of type I serine/threonine kinase receptor TARAM-A reveals a specific signalling pathway involved in fish head organiser formation. Development 122, 3735-43.

Rodaway, A., Takeda, H., Koshida, S., Broadbent, J., Price, B., Smith, J.C., Patient, R., and Holder, N. (1999). Induction of the mesendoderm in the zebrafish germ ring by yolk cell-derived TGF-β family signals and discrimination of mesoderm and endoderm by FGF. Development 126, 3067-78.

Roessler, E., Ouspenskaia, M.V., Karkera, J.D., Velez, J.I., Kantipong, A., Lacbawan, F., Bowers, P., Belmont, J.W., Towbin, J.A., Goldmuntz, E., et al. (2008). Reduced NODAL signaling strength via mutation of several pathway members including FOXH1 is linked to human heart defects and holoprosencephaly. Am J Hum Genet 83, 18-29.

Rogers, K.W., Bläßle, A., Schier, A.F., and Müller, P. (2015). Measuring protein stability in living zebrafish embryos using fluorescence decay after photoconversion (FDAP). J Vis Exp, 52266.

Rogers, K.W., ElGamacy, M., Jordan, B.M., and Müller, P. (2020). Optogenetic investigation of BMP target gene expression diversity. Elife 9, e58641.

Rogers, K.W., Lord, N.D., Gagnon, J.A., Pauli, A., Zimmerman, S., Aksel, D.C., Reyon, D., Tsai, S.Q., Joung, J.K., and Schier, A.F. (2017). Nodal patterning without Lefty inhibitory feedback is functional but fragile. Elife 6.

Rogers, K.W., and Müller, P. (2019). Nodal and BMP dispersal during early zebrafish development. Dev Biol 447, 14-23.

Rogers, K.W., and Schier, A.F. (2011). Morphogen gradients: from generation to interpretation. Annu Rev Cell Dev Biol 27, 377-407.

Rossi, A., Kontarakis, Z., Gerri, C., Nolte, H., Holper, S., Krüger, M., and Stainier, D.Y. (2015). Genetic compensation induced by deleterious mutations but not gene knockdowns. Nature 524, 230-3.

Sampath, K., Rubinstein, A.L., Cheng, A.M., Liang, J.O., Fekany, K., Solnica-Krezel, L., Korzh, V., Halpern, M.E., and Wright, C.V. (1998). Induction of the zebrafish ventral brain and floorplate requires cyclops/nodal signalling. Nature 395, 185-9.

Schier, A.F. (2009). Nodal morphogens. Cold Spring Harb Perspect Biol 1, a003459.

Schier, A.F., Neuhauss, S.C., Harvey, M., Malicki, J., Solnica-Krezel, L., Stainier, D.Y., Zwartkruis, F., Abdelilah, S., Stemple, D.L., Rangini, Z., et al. (1996). Mutations affecting the development of the embryonic zebrafish brain. Development 123, 165-78.

Schindelin, J., Arganda-Carreras, I., Frise, E., Kaynig, V., Longair, M., Pietzsch, T., Preibisch, S., Rueden, C., Saalfeld, S., Schmid, B., et al. (2012). Fiji: an open-source platform for biological-image analysis. Nature Methods 9, 676-682.

Shen, M.M. (2007). Nodal signaling: developmental roles and regulation. Development 134, 1023-34.

Shi, Y., and Massagué, J. (2003). Mechanisms of TGF-β signaling from cell membrane to the nucleus. Cell 113, 685-700.

Soh, G.H., and Müller, P. (2018). FRAP analysis of extracellular diffusion in zebrafish embryos. Methods Mol Biol 1863, 107-124.

Soh, G.H., Pomreinke, A.P., and Müller, P. (2020). Integration of Nodal and BMP signaling by mutual signaling effector antagonism. Cell Rep 31, 107487.

Stapornwongkul, K.S., de Gennes, M., Cocconi, L., Salbreux, G., and Vincent, J.P. (2020). Patterning and growth control in vivo by an engineered GFP gradient. Science 370, 321-327.

Tewary, M., Dziedzicka, D., Ostblom, J., Prochazka, L., Shakiba, N., Heydari, T., Aguilar-Hidalgo, D., Woodford, C., Piccinini, E., Becerra-Alonso, D., et al. (2019). High-throughput micropatterning platform reveals Nodal-dependent bisection of peri-gastrulation-associated versus preneurulation-associated fate patterning. PLoS Biol 17, e3000081.

Thisse, C., and Thisse, B. (1999). Antivin, a novel and divergent member of the TGFβ superfamily, negatively regulates mesoderm induction. Development 126, 229-40.

Thisse, C., and Thisse, B. (2008). High-resolution in situ hybridization to whole-mount zebrafish embryos. Nat Protoc 3, 59-69.

van Boxtel, A.L., Chesebro, J.E., Heliot, C., Ramel, M.C., Stone, R.K., and Hill, C.S. (2015). A temporal window for signal activation dictates the dimensions of a Nodal signaling domain. Dev Cell 35, 175-85.

van Boxtel, A.L., Economou, A.D., Heliot, C., and Hill, C.S. (2018). Long-range signaling activation and local inhibition separate the mesoderm and endoderm lineages. Dev Cell 44, 179-191 e5.

Vopalensky, P., Pralow, S., and Vastenhouw, N.L. (2018). Reduced expression of the Nodal co-receptor Oep causes loss of mesendodermal competence in zebrafish. Development 145, dev158832.

Wang, Y., Wang, X., Wohland, T., and Sampath, K. (2016). Extracellular interactions and ligand degradation shape the Nodal morphogen gradient. Elife 5, e13879.

Waterhouse, A.M., Procter, J.B., Martin, D.M., Clamp, M., and Barton, G.J. (2009). Jalview Version 2--a multiple sequence alignment editor and analysis workbench. Bioinformatics 25, 1189-91.

White, R.J., Collins, J.E., Sealy, I.M., Wali, N., Dooley, C.M., Digby, Z., Stemple, D.L., Murphy, D.N., Billis, K., Hourlier, T., et al. (2017). A high-resolution mRNA expression time course of embryonic development in zebrafish. Elife 6, e30860.

Yan, Y.T., Liu, J.J., Luo, Y., E, C., Haltiwanger, R.S., Abate-Shen, C., and Shen, M.M. (2002). Dual roles of Cripto as a ligand and coreceptor in the Nodal signaling pathway. Mol Cell Biol 22, 4439-49.

Yeo, C., and Whitman, M. (2001). Nodal signals to Smads through Cripto-dependent and Cripto-independent mechanisms. Mol Cell 7, 949-57.

Zhang, J., Talbot, W.S., and Schier, A.F. (1998). Positional cloning identifies zebrafish one-eyed pinhead as a permissive EGF-related ligand required during gastrulation. Cell 92, 241-51.

Zhou, Y., Scolavino, S., Funderburk, S.F., Ficociello, L.F., Zhang, X., and Klibanski, A. (2004). Receptor internalization-independent activation of Smad2 in Activin signaling. Mol Endocrinol 18, 1818-26.

Zhu, Y., Qiu, Y., Chen, W., Nie, Q., and Lander, A.D. (2020). Scaling a Dpp morphogen gradient through feedback control of receptors and co-receptors. Dev Cell 53, 724-739 e14.

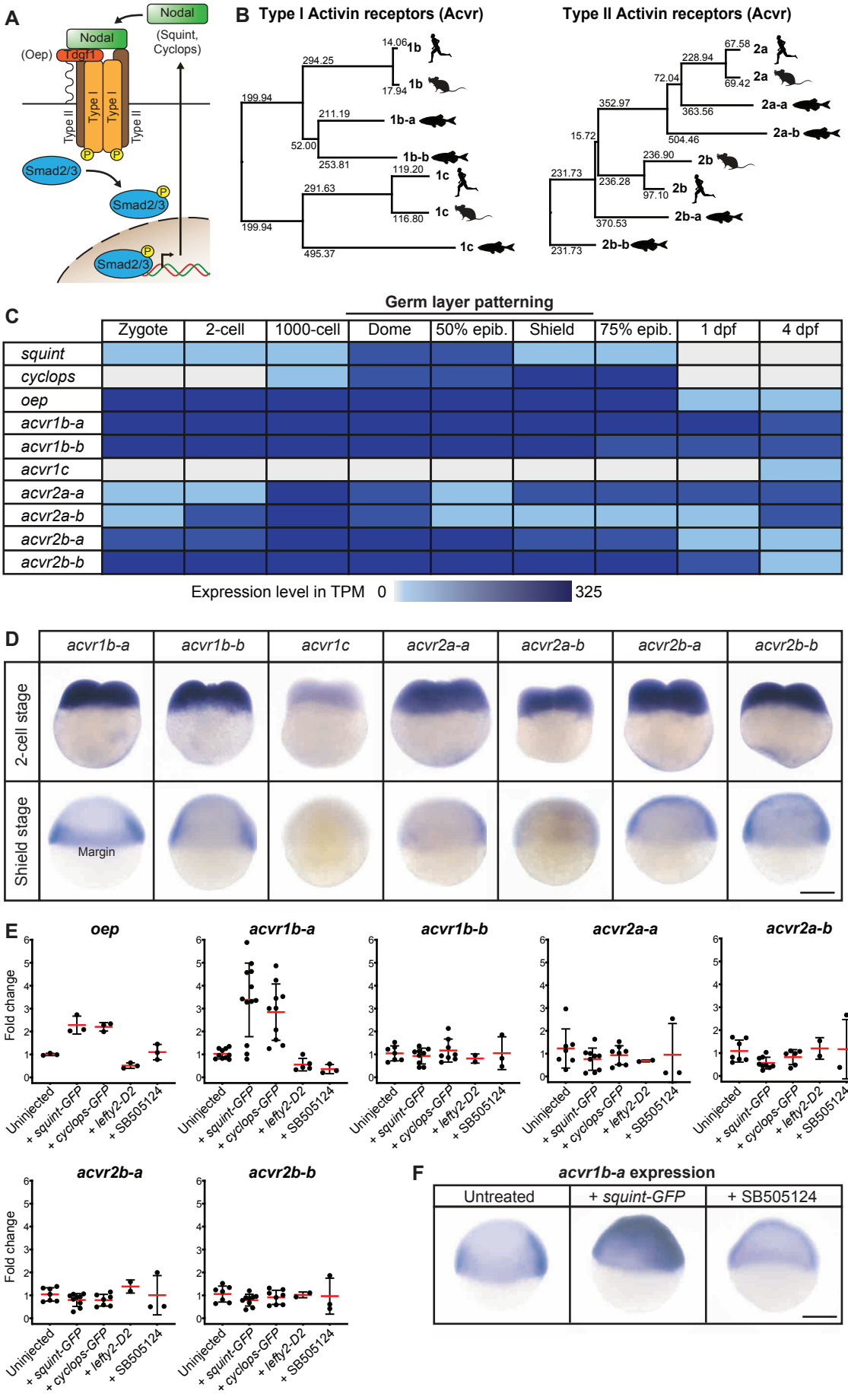
A
Nodal
Nodal
(Oep)
Tdgf1
(Squint, Cyclops)
Type II
Type I
Type I
Type II
P
P
Smad2/3
Smad2/3
P
Smad2/3
P
B Type I Activin receptors (Acvr)
14.06
1b
294.25
17.94
1b
199.94
211.19
1b-a
52.00
253.81
1b-b
119.20
1c
291.63
116.80
1c
199.94
495.37
1c
Type II Activin receptors (Acvr)
67.58
2a
228.94
72.04
69.42
2a
352.97
2a-a
363.56
15.72
504.46
2a-b
236.90
2b
231.73
236.28
2b
97.10
2b-a
370.53
231.73
2b-b
C
Germ layer patterning
Zygote
2-cell
1000-cell
Dome
50% epib.
Shield
75% epib.
1 dpf
4 dpf
squint
cyclops
oep
acvr1b-a
acvr1b-b
acvr1c
acvr2a-a
acvr2a-b
acvr2b-a
acvr2b-b
Expression level in TPM 0
325
D
acvr1b-a
acvr1b-b
acvr1c
acvr2a-a
acvr2a-b
acvr2b-a
acvr2b-b
2-cell stage
Shield stage
Margin
E
oep
acvr1b-a
acvr1b-b
acvr2a-a
acvr2a-b
acvr2b-a
acvr2b-b
Fold change
Uninjected
+ squint-GFP
+ cyclops-GFP
+ lefty2-D2
+ SB505124
F
acvr1b-a expression
Untreated
+ squint-GFP
+ SB505124

Figure 1

A **Acvr1b-a**

MLRDGNVAVMPPRRTAVALLALCGLLAVGDALKCNCTACESTGYVCETDGACMASTSYINGQEEQQVRICIPRVSLVPPGQPIYCL
SAKGLLNTHCCYTDFCNSINLQIPNGIADGKGGSWGPVELVAVIAGPVFLFCLLLIVGVLLFQHHQRNYNHRQRLDVEDPSCDHLYLA
KDKTLQDLIFDLSTSGSGSGLPLFVQRTVART*IVLQEIIGKGRFGEVWRGRWRGGDVAVKIFSSREERSWFREAEIYQTIMLRHENIL
GFIAADNKDNGTWTQLWLVSDYHEHGSLFDYLNHYSVTIEGMIKLSLSAASGLAHLHMEILGTQGKPGIAHRDLKSKNILVKKNGTC
AIADLGLAVRHESITDTIDIAPNQRVGTKRYMAPEVLDETINMKHFDSFKCADIYALGLVYWEIARRCNAGGIHEDYQLPYYDLVPSDP
SIEEMRKVVCDQRLRPNVPNWWQSYEALRVMGKIMRECWYANGAARLTALRIKKTLSQL*SVQEDIKI

B **Acvr1b-b**

MDPRQILRILIVLSGLNGVCDALLCNCTAPHCERDGFKCETNGACVASTSVIEGQEQHVRLCIHKEKLVPPGQPFYCLSAEGLMNTH
CCYTDYCNSIDLRLPIVTNGPGAGQDWGPVELTAVVAGPVFVLCVLVLLGLFLFQHHQRAYGHRQRLEVEDPSTEHMFLAKDKTLQ
DLIYDLSTSGSGSGLPLFVQRTVART*IVLQEIIGKGRFGEVWRGKWRGGDVAVKIFSSREERSWFREAEIYQTIMLRHENILGFIAAD
NKDNGTWTQLWLVSDYHENGSLFDYLNRYSVTIEGMIKLALSAASGLAHLHMEILGTQGKPGIAHRDLKSKNILVKKNCTCAIADLGL
AVRHESITDTIDIAPNQRVGTKRYMAPEVLEESINMRHFDSFKCADIYALGLVYWEIARRCNAGGIHEEYQLPYYDLVPSDPSIEEMR
KVVCDQRLRPNIPNWWQSYEALRVMGKIMRECWYANGAARLTALRIKKTLSQLSVDEDLKI

C **Acvr1c**

MSHPRCSDAALFIFTFVQLTAALKCVCHLCVNHTCETEAEGACWNSVMLINGKEETVKSCVSPSELKGQVFCYSSRNVSKRNCCF
TDFCNNETLHLNPEQPPEDSGWSQLEVAAVILVPSCLVCVGVMLGVCAIQNLRCTHIKSLKQDPEEPLDDPTLVSPDKCLKELIYDM
STSGSGSGLPLLVQRTIART*IVLQETIGKGRFGEVWRGKWRGEDVAVKIFSSRDERSWFREAEIYQTIMLRHDNILGFIAADNKDNGS
WTQLWLVSEYHEHGSLFDYLNRFTVSVEGMIVLALSIASGIAHLHMEIIGTQGKPAIAHRDIKSKNILVKKNGAAVIADLGLAVKHDSNT
NTIDIPINHRVGTKRYMAPEILDDSINMSSFESFKRADIYSLSLVFWELARRCSIQGIHEDFQLPYYDQVQSDPSLDDMRRVVCEQKL
RPNIPNQWQSCEALRVMGKIMRECWHANPAARLTALRVKKTISQVTVVKDVKE

D **Acvr2a-a**

MGPATKLAFGVFLISCSSGAILGRSETQECVFYNYNPSLENRGNRSGIEPCVGDKDKRLHCFATWRNVSGTVEIVKQGCWLDDVN
CYDSTECVEKKEDPDVFFCCCEGNMCNEKFFYNPNTAPVQTTSNPLTQKPPLFSTLLYSIVPIMGIAAIVLLSFWMYRHHKLAYPPVL
VPTQDPGPMPPSPTLVQKP*LQLLEIKARGRFGCVWKAQLLNDYVAVKIFPIQDKLSWQNEYDIYNIPGMRHENILQFIGAEKRGSNL
DIELWLITAYHEKSSLTDYLKANVVTWNELCHIAQTMARGLAYLHSDFPGHRDGHKPAIAHRDFKSKNVLLKTNLTACIADFGLALKFE
AGKSAGDTHGQVGTRRYMAPEVLEGAINFQRDAFLRIDMYAVGLVLWELAARCTASDGPVDEYMLPFEEEVGQHPTLEDMQEVVV
HKKLRPTLRECWQKHPGLAMLCETIEECWDHEAEARLSAGCVEERVV*QMQRQTSVSAPEEIVTVVTMVTNVDYPPKESSL

E **Acvr2a-b**

MASHWTNWKQRKYGGAILGRSETQECVYYNVSWEKDGTNRSGTESCYGEKDKRRHCFSTWKNRSGTIEMVKQGCWLDDVNCY
DSSECVERKENIDVFFCCCEGNLCNQKFHYNPETVEPTLNPVPPKPDLFPTLLYSLLPIMAVAVILFISFWMYRHLKLTYPPLLVPSQD
PGLTPPSPLLGQKP*LQLLELKARGRFGCVWKAQLLSEAVAVKIFPVQNKQSWQNEYEIYNASGMKHENLLHFIGAEKRGNGVDIEL
WLITTYHEKGSLTDFLKANVLSWNELCLIAQTFVRGLAYLHEDIPNLKDGHKPAIAHRDIKSKNVLLKSDLTACIADFGLALKFEAGKST
GDTHGQVGTRRYMAPEVLEGAISFQRDAFLRIDMYAAGLVLWELATRCTAADGPVDEFCLPFEEEAGLHPSLEDMQDVVVHKKLR
PIFREHWLKHTGLSLLCETMEECWDHEAEARLSAGCVEERII*SMQRSTSIISPDDILSVVTMVTNLDFPPKESSL

F **Acvr2b-a**

MFASLLTLALLLATFAADPSHGEVETRECLYYNVNWEVEKTNRSGVERCEGEKDKRSHCYASWRNNSGSIQLVKKGCWLDDFNC
YDRQECVATEENPQVFFCCCEGNFCNERFTHLPDISGPVISPPPVSPSLLNVLVYSLLPLSMLSMAVLLAFWMYRHRKPPYGHVDV
NEDPGPSPPSPLVGLKPLQLLEVKARGRFGCVWKAQMINEYVAVKIFPIQDKLSWQNEREMFSTPGMKHDN*LLRFIAAEKRGSNLE
MEFWLITEFHERGSLTDYLKGNAVSWADLCVIAESMACGLAYLHEDVPRSKGEGPKPAIAHRDFKSKNVMLKMDLTAVIGDFGLAVR
FEPGKPPGDTHGQVGTRRYMAPEVLEGAINFQRDSFLRIDMYAMGLVLWELVSRCKAADGPVDEYMLPFEEEIGQHPSLEDLQDA
VVHKKLRPAFKDCWLKHSGLCQMCETMEECWDHDAEARLSAGCVQERISQIRRV*SSSTSDCLFSMVTSLTNVDLPPKESSI

G **Acvr2b-b**

MFVPWLAFALVWCTGVSHAEVATRECVYYNDNWRTEKTNQSGFERCEGEKDKRLHCYASWLNSTGTIRLVKKGCWLDDFNCYD
RQECVATEESPQVFFCCCEGNYCNEKFTHLPEAIAPAVKIQPPQPGPSLFGILVYSLLPLAILSLALVLACWTYHQRKPPYRHVDIGQ
DAGLPPPSPLVGLKP*LQLLELKARGRFGCVWKAQLLSEYVAVKIFPIQDKQSWQNERDIYLTEGFKHENILHYISAEKRGTNLQMEL
WLVTEFHERGSLTDYLKGNVVSWPQLCHISASMSRGLAYLHEDLPYRAEGPKPAIAHRDFKSKNVLLKMDLTAVIADFGLAVRFEPG
KPPGDTHGQVGTRRYMAPEVLEGAINFQRDSFLRIDMYALGLVLWELVSRCTASDGPVGEYQLPFEEEVGQHPSLEDLQDAVVHK
KMRPVFKDCWVKHQGLSQLCETIEECWDHDAEARLSAGCVEERIST*SKSNNTLNTSTSECLLSMLTSHSDTDLPPKDSST

Bold: Signal peptide
Red: Activin receptor domain
Underlined: Transmembrane domain
Blue: GS domain
Italics: Protein kinase domain

Figure 1 – figure supplement 1

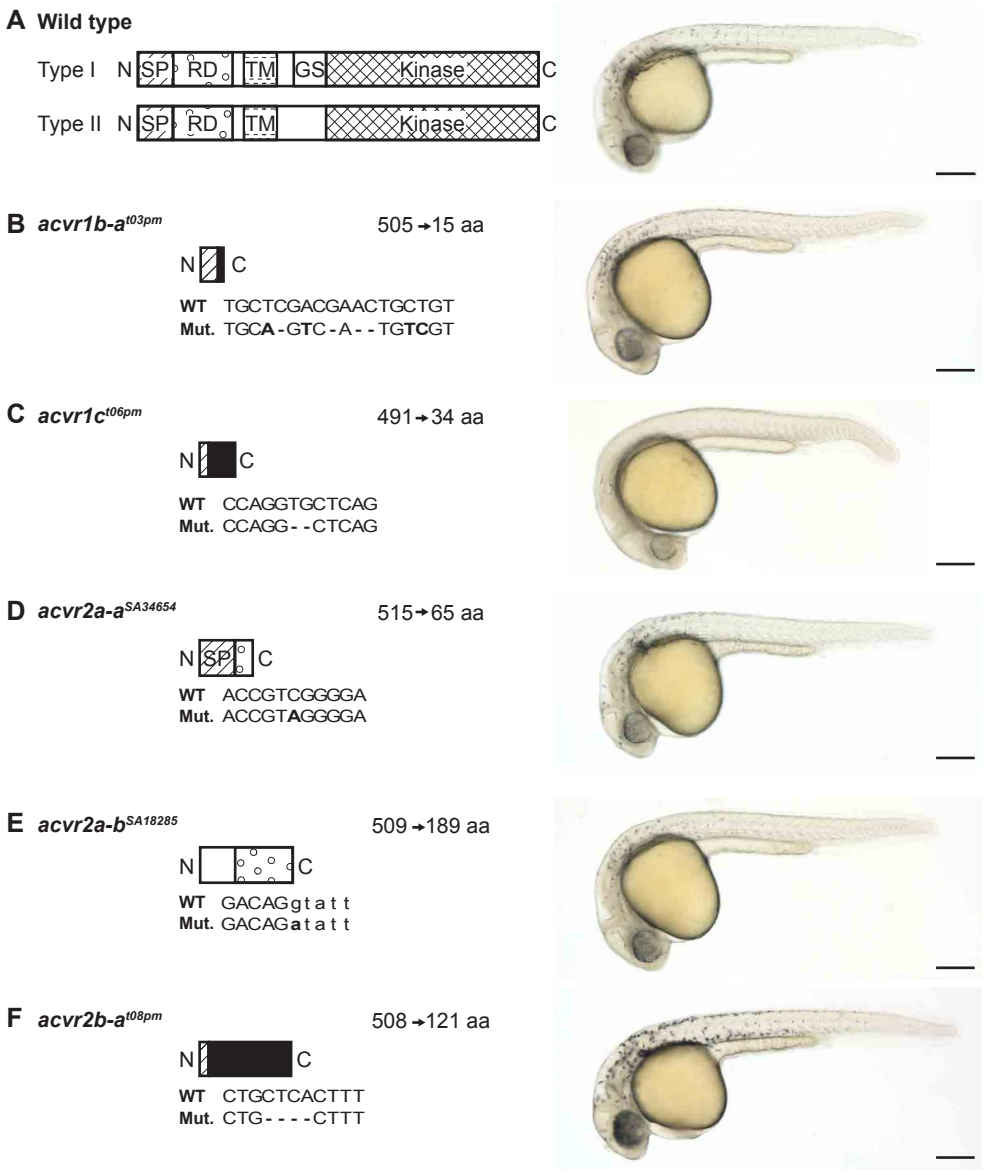
A Wild type
Type I N SP RD TM GS Kinase C
Type II N SP RD TM Kinase C
B acvr1b-a t03pm
505 → 15 aa
N C
WT TGCTCGACGAACTGCTGT
Mut. TGCA-GTC-A--TGTCGT
C acvr1c t06pm
491 → 34 aa
N C
WT CCAGGTGCTCAG
Mut. CCAGG--CTCAG
D acvr2a-a SA34654
515 → 65 aa
N SP C
WT ACCGTCGGGGA
Mut. ACCGTAGGGGA
E acvr2a-b SA18285
509 → 189 aa
N C
WT GACAGgtatt
Mut. GACAGatatt
F acvr2b-a t08pm
508 → 121 aa
N C
WT CTGCTCACTTT
Mut. CTG----CTTT

Figure 2

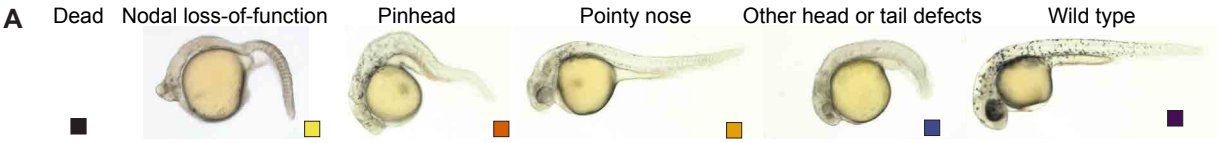

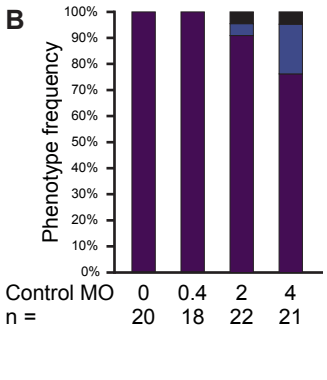

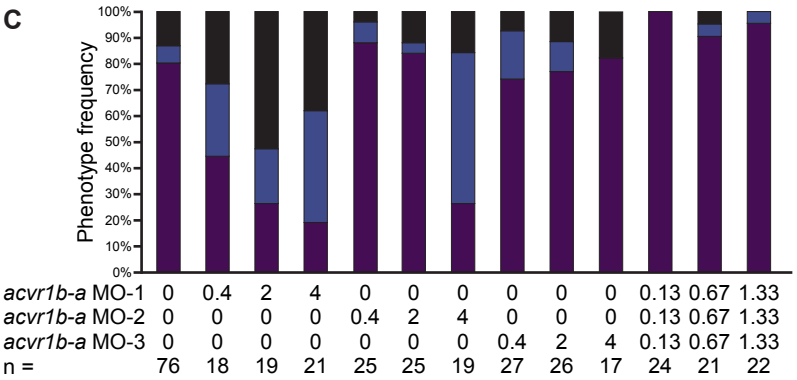

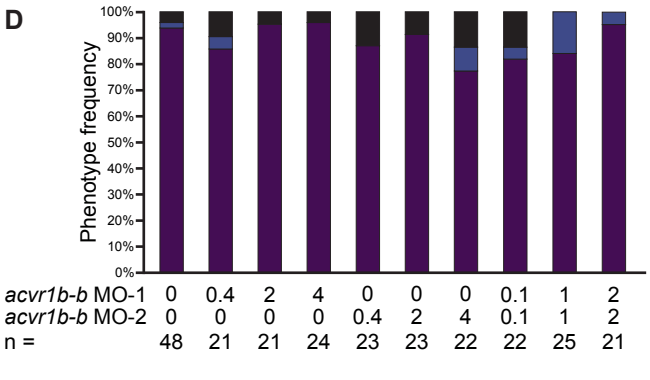

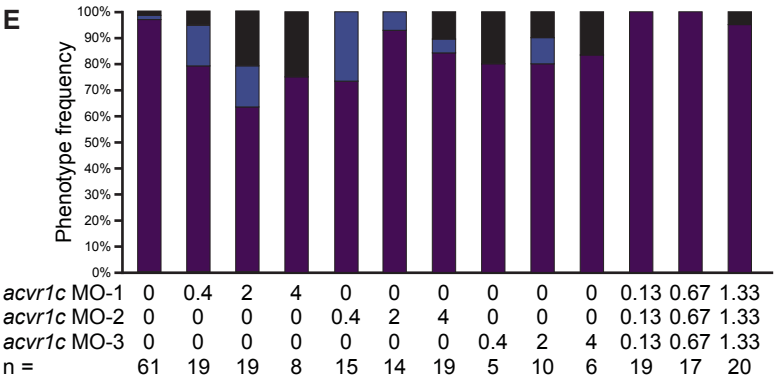

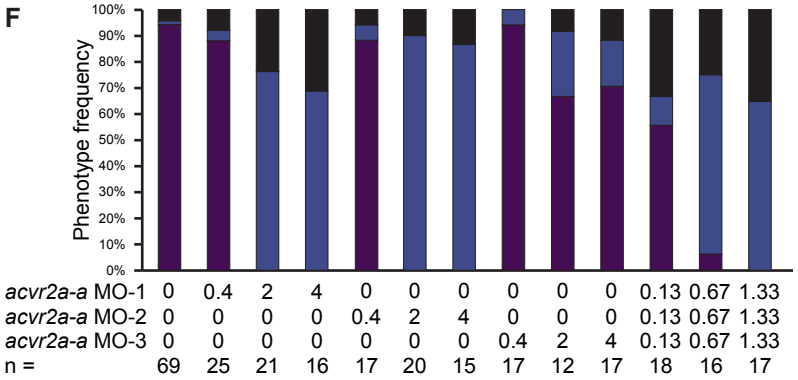

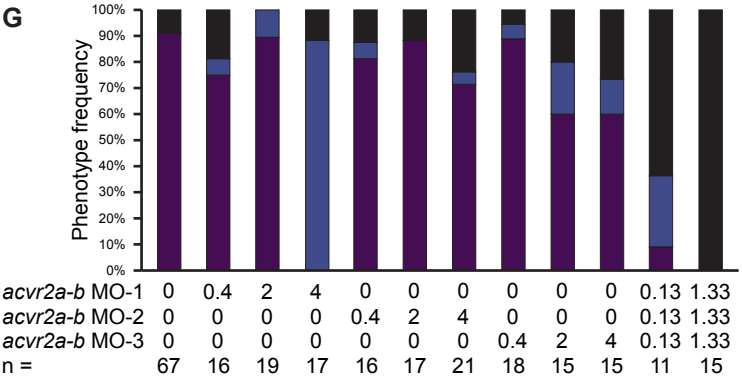

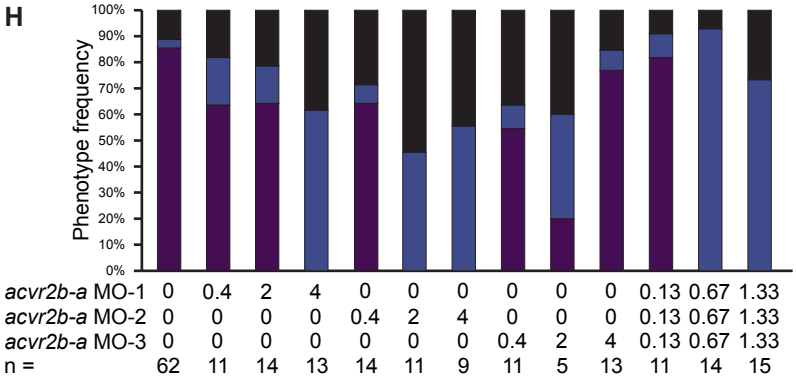

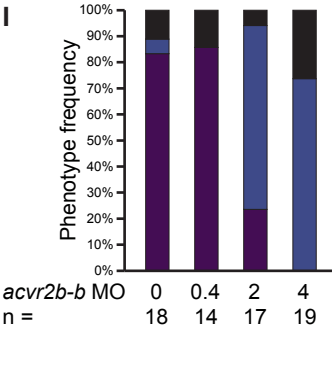

Figure 2 – figure supplement 1

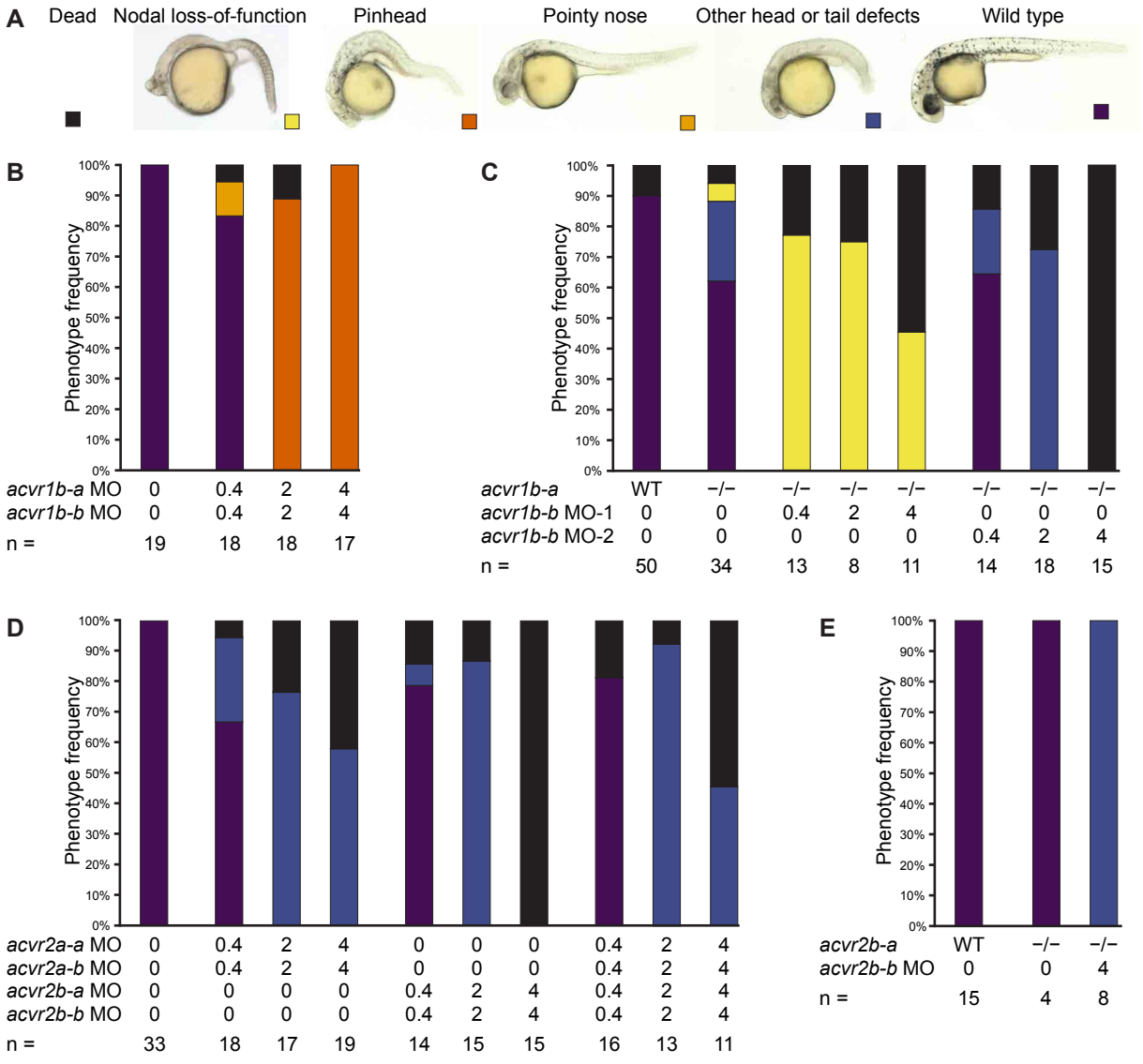
A
Dead
Nodal loss-of-function
Pinhead
Pointy nose
Other head or tail defects
Wild type
B
Phenotype frequency
100%
90%
80%
70%
60%
50%
40%
30%
20%
10%
0%
acvr1b-a MO 0 0.4 2 4
acvr1b-b MO 0 0.4 2 4
n = 19 18 18 17
C
Phenotype frequency
acvr1b-a WT −/− −/− −/− −/− −/− −/− −/−
acvr1b-b MO-1 0 0 0.4 2 4 0 0 0
acvr1b-b MO-2 0 0 0 0 0 0.4 2 4
n = 50 34 13 8 11 14 18 15
D
Phenotype frequency
acvr2a-a MO 0 0.4 2 4 0 0 0 0.4 2 4
acvr2a-b MO 0 0.4 2 4 0 0 0 0.4 2 4
acvr2b-a MO 0 0 0 0 0.4 2 4 0.4 2 4
acvr2b-b MO 0 0 0 0 0.4 2 4 0.4 2 4
n = 33 18 17 19 14 15 15 16 13 11
E
Phenotype frequency
acvr2b-a WT −/− −/−
acvr2b-b MO 0 0 4
n = 15 4 8

Figure 3

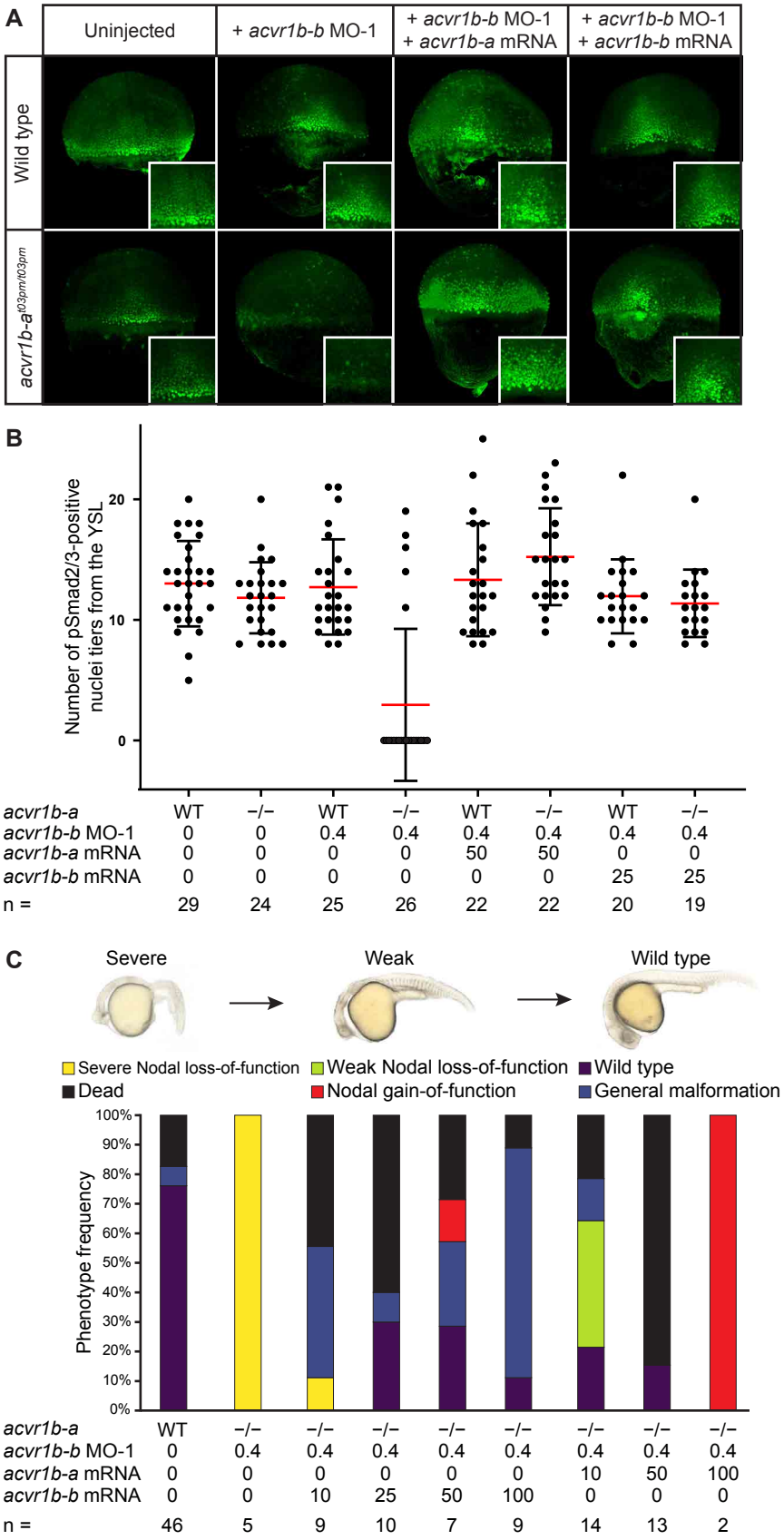
A
Uninjected
+ acvr1b-b MO-1
+ acvr1b-b MO-1
+ acvr1b-a mRNA
+ acvr1b-b MO-1
+ acvr1b-b mRNA
Wild type
acvr1b-a t03pmr/t03pm
B
Number of pSmad2/3-positive nuclei tiers from the YSL
20
10
0
acvr1b-a WT −/− WT −/− WT −/− WT −/−
acvr1b-b MO-1 0 0 0.4 0.4 0.4 0.4 0.4 0.4
acvr1b-a mRNA 0 0 0 0 50 50 0 0
acvr1b-b mRNA 0 0 0 0 0 0 25 25
n = 29 24 25 26 22 22 20 19
C
Severe
Weak
Wild type
Severe Nodal loss-of-function
Weak Nodal loss-of-function
Wild type
Dead
Nodal gain-of-function
General malformation
Phenotype frequency
100%
90%
80%
70%
60%
50%
40%
30%
20%
10%
0%
acvr1b-a WT −/− −/− −/− −/− −/− −/− −/− −/−
acvr1b-b MO-1 0 0.4 0.4 0.4 0.4 0.4 0.4 0.4 0.4
acvr1b-a mRNA 0 0 0 0 0 0 10 50 100
acvr1b-b mRNA 0 0 10 25 50 100 0 0 0
n = 46 5 9 10 7 9 14 13 2

Figure 4

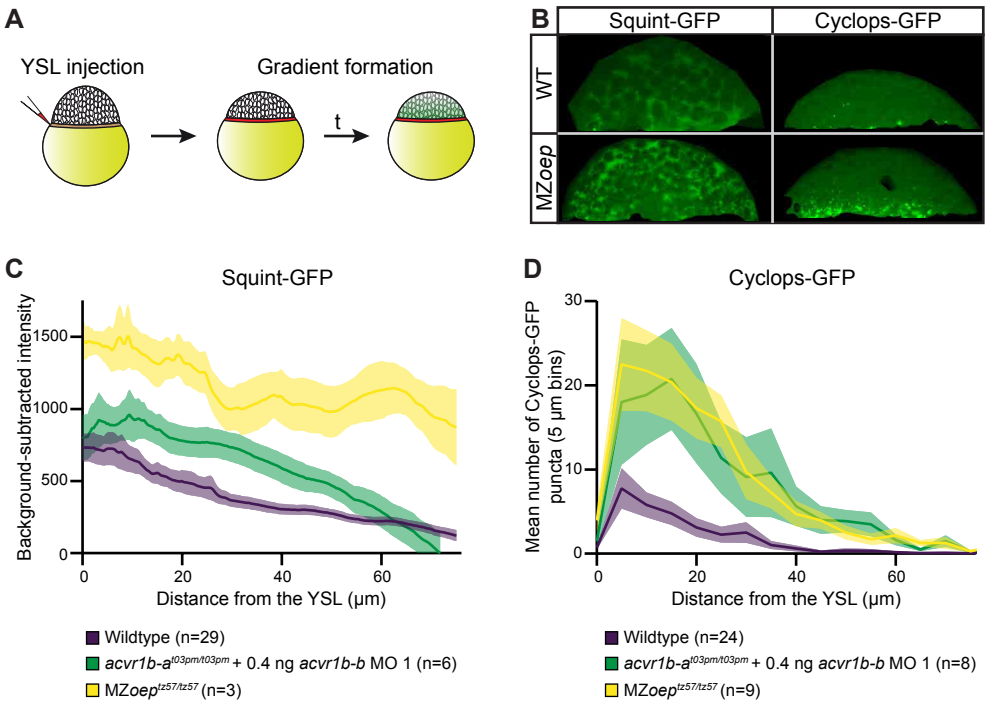
A
YSL injection
Gradient formation
t
B
Squint-GFP
Cyclops-GFP
WT
MZoep
C
Squint-GFP
Background-subtracted intensity
1500
1000
500
0
0
20
40
60
Distance from the YSL (µm)
Wildtype (n=29)
acvr1b-a t03pm/t03pm + 0.4 ng acvr1b-b MO 1 (n=6)
MZoep tz57/tz57 (n=3)
D
Cyclops-GFP
Mean number of Cyclops-GFP puncta (5 µm bins)
30
20
10
0
0
20
40
60
Distance from the YSL (µm)
Wildtype (n=24)
acvr1b-a t03pm/t03pm + 0.4 ng acvr1b-b MO 1 (n=8)
MZoep tz57/tz57 (n=9)

Figure 5

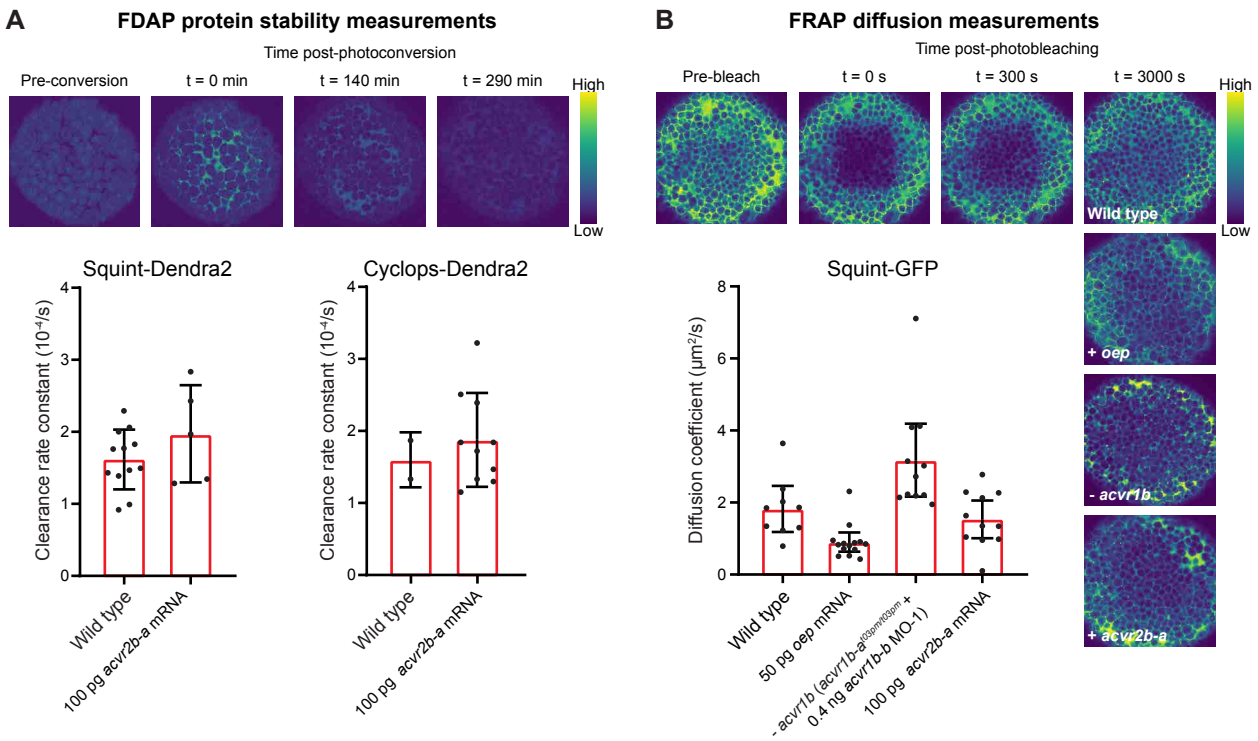
A
FDAP protein stability measurements
Time post-photoconversion
Pre-conversion
t = 0 min
t = 140 min
t = 290 min
High
Low
Squint-Dendra2
Clearance rate constant (10-4/s)
Wild type
100 pg acvr2b-a mRNA
Cyclops-Dendra2
Clearance rate constant (10-4/s)
Wild type
100 pg acvr2b-a mRNA
B
FRAP diffusion measurements
Time post-photobleaching
Pre-bleach
t = 0 s
t = 300 s
t = 3000 s
High
Low
Wild type
+ oep
- acvr1b
+ acvr2b-a
Squint-GFP
Diffusion coefficient (µm2/s)
Wild type
50 pg oep mRNA
- acvr1b (acvr1b-a tm303pm/tm303pm + 0.4 ng acvr1b-b MO-1)
100 pg acvr2b-a mRNA

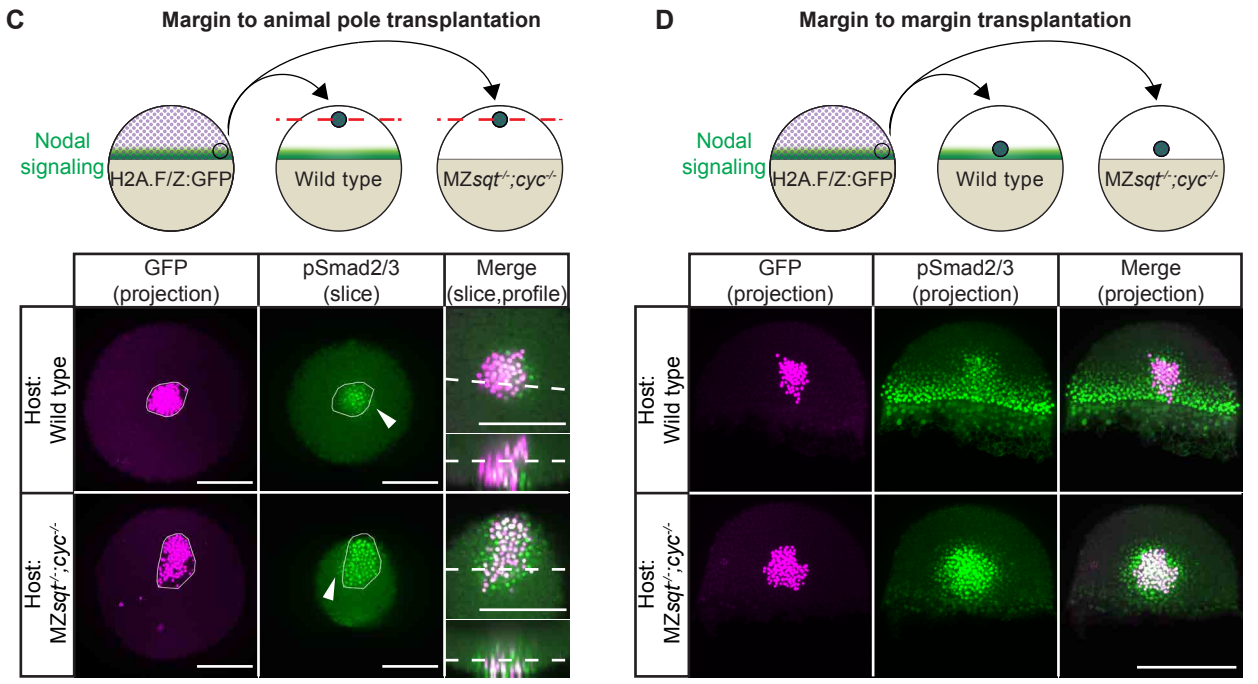
C
Margin to animal pole transplantation
Nodal signaling
H2A.F/Z:GFP
Wild type
MZsqt-/-;cyc-/-
GFP (projection)
pSmad2/3 (slice)
Merge (slice,profile)
Host: Wild type
Host: MZsqt-/-;cyc-/-
D
Margin to margin transplantation
Nodal signaling
H2A.F/Z:GFP
Wild type
MZsqt-/-;cyc-/-
GFP (projection)
pSmad2/3 (projection)
Merge (projection)
Host: Wild type
Host: MZsqt-/-;cyc-/-

Figure 6

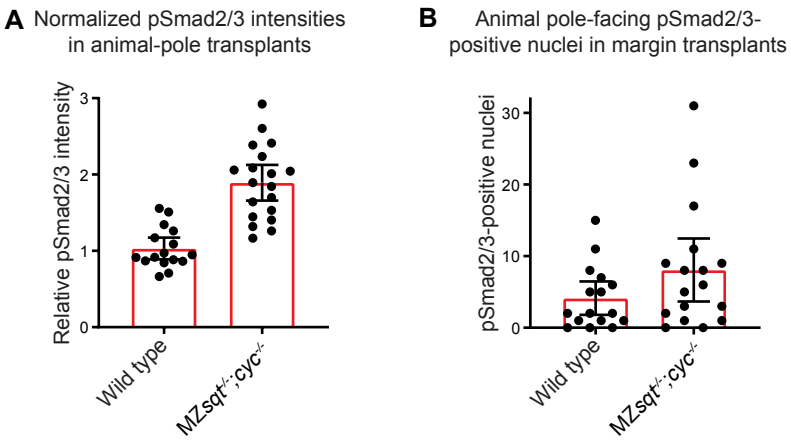

Figure 6 – figure supplement 1